Reconstructing Oxide Surfaces

A DISSERTATION
SUBMITTED TO THE FACULTY OF THE GRADUATE SCHOOL
OF THE UNIVERSITY OF MINNESOTA
BY

Jessica Lori Riesterer

IN PARTIAL FULFILLMENT OF THE REQUIREMENTS
FOR THE DEGREE OF
DOCTOR OF PHILOSOPHY

Advisor: Prof. C. Barry Carter

May 2009

Acknowledgements

I would like to thank Prof. C. Barry Carter for his help and support over the many years I've worked toward my Ph.D. at the Universities of Minnesota and Connecticut. Dr. Emmanuelle Marquis was also a wonderful source for advise and support during my time at Sandia National Laboratory-Livermore, CA.

Several people have supported me through the years with aid in my research. Dr. Stuart McKernan was invaluable. My group members all influenced me and helped me through graduate school. I would like to specially thank Drs. Arzu Altay, Chris Perrey, Shelley Gilliss and Julia Nowak. Prof. N. Ravishankar has also given me much insight.

My collaborators, Profs. Eva Olsson, Mehmet Gülgün, and N. Ravishankar, allowed me to travel to the world to work with them. Drs. Jeff Farrer and Zhenting Jiang allowed me to extensively use their EBSD equipment.

A very special thank you needs to go to Janet McKernan. She kept me sane during a very difficult few years. She also has excellent lab-packing skills. I will forever be indebted to her. Susan Soucy needs to be recognized for her help in getting our group settled at UConn. I really enjoyed the conversations I had with her when I needed a break from unpacking.

I am blessed to have great friends who helped me to figure out what is important in life. I certainly would not have had as much fun during my graduate school years without Bill Mook, Mindy Harvath and Megan Cordill.

Finally, I must thank my parents and sister. Abby often reminded me that life will get easier exactly when I needed it. My mom, Renae, and dad, Glen, have been so supportive throughout the years. Even though they may not always understand what I was doing, they were always there for a shoulder to cry on and to celebrate my successes.

This research has been supported by the U. S. Department of Energy through grants DE-FG02-92ER45465-A004 and DE-FG02-01ER45883. The 3M Harry Heltzer Endowed chair gave support while at the University of Minnesota and the National Physical Sciences Consortium (NPSC) assisted in funding while at Sandia National Laboratory-Livermore, CA. The University of Connecticut funded all other work.

Abstract

The work presented here is concentrated on surfaces and interfaces in alumina (Al_2O_3), anorthite ($CaAl_2Si_2O_8$), silica (SiO_2) and rutile (TiO_2). While each of these materials have different crystal structures and measurable properties, they all exhibit similar mechanisms for fundamental behavior.

The topics researched and discussed lead into each other. Faceting describes the movement of atoms to a lower energy configuration. While faceting of the surface is only considered, grain boundaries can be faceted. In cross-section, facets resemble grain boundary grooves. Grooves and ridges form where a grain boundary intersects the surface of a material. The grooves facilitate grain boundary migration and diffusion. The surface tension at the groove is governed by Young's equation, which balances the interfacial forces between the solid and vapor. Glass films can wet or dewet the surface a grain boundaries. Whether the film wets or dewets depends on the surface energy of the surface and the liquid. Capillary forces determine the type of dewet patterns formed on the surface. Again, the surface-vapor-liquid interfaces are governed by Young's equation. Liquid films at grain boundaries facilitate densification and grain boundary migration. Liquid phase sintering (LPS) uses capillary forces and the dissolution/reprecipitation process to sinter green compacts to a high density at lower temperatures. Capillary forces and surface tension can also cause the liquid film to penetrate or exude from the grain boundary. Various forms of microscopy have been used to characterize and relate these phenomena.

Table of Contents

Acknowledgements i
Abstract ii
Table of Contents iii
List of Tables vii
List of Figures viii

Chapter 1: Introduction 1
1.1 How does it fit together? 1
1.2 General Considerations for Ceramic Research 7
1.3 Processing Ceramics 10
1.4 Possible Pinning Mechanisms in Dynamic Processes 12
1.5 Characterization Techniques and Limitations 13
1.6 Summary 19
References 19
Figures 24

Chapter 2: Using AFM to Monitor Alumina Surface Facets 33
2.1 Introduction 33
2.2 Background 34
2.3 Experimental 47
2.4 Results 49
2.5 Discussion 52
2.6 Summary and Future Work 57
References 58
Tables 62
Figures 63

Chapter 3: Thermal Grooving at Grain Boundaries and Triple Junctions 82
3.1 Introduction 82
3.2 Background 84
3.3 Experimental 94
3.4 Results 96
3.5 Discussion 96
3.6 Summary and Future Work 99
Appendix 3.1 Chemical Grooving 99
Appendix 3.2 Grooving by Ion Bombardment 101
Appendix 3.3 The Role of Triple Junctions 102
Appendix 3.4 Materials Used by Two-Phase SOFCs 103
References 105
Figures 108

Chapter 4: Dewetting of SiO_2 on TiO_2 124
4.1 Introduction 124
4.2 Background 126
4.3 Experimental 133
4.4 Results 135
4.5 Discussion 136
4.6 Summary and Future Work 140
Appendix 4.1 TiO_2 is Hot 141
Appendix 4.2 TiO_2/SiO_2 Mirrors & the Interface 142
Appendix 4.3 TiO_2-SiO_2 Phase Diagram 143
References 144
Figures 148

Chapter 5: Exudation and Penetration of Glass 171
5.1 Introduction 171
5.2 Background 172
5.3 Experimental 184
5.4 Results 185
5.5 Discussion 187
5.6 Summary and Future Work 192
Appendix 5.1 Surface Energy vs. Surface Tension 194
Appendix 5.2 Liquid-Metal Embrittlement 194
References 196
Tables 200
Figures 202

Chapter 6: EBSD Study of GBM and AGG in Alumina in the Presence of a Liquid Phase 223
6.1 Introduction 223
6.2 Background 224
6.3 Experimental 231
6.4 Results 232
6.5 Discussion 233
6.6 Summary and Future Work 236
Appendix 6.1 Exaggerated vs. Abnormal Grain Growth 237
Appendix 6.2 Lath-Like Grains 238
Appendix 6.3 Texture 239
Appendix 6.4 Surface Preparation 240
Appendix 6.5 Grain Growth in 3D 243
Appendix 6.6 Composition of Liquid Phases 245
References 248
Figures 252

Chapter 7: Summary and Future Work 263
7.1 Conclusions and Summary of Work 263
7.2 Development of New Characterization Techniques 265
7.3 Future Experiments 267
7.4 Review of How This Work Fits Together 270
References 271

Bibliography 272

List of Tables

Table 2.1: Common low-index planes in alumina and their corresponding simplified nomenclature, lattice spacing and surface energies. p. 62

Table 5.1: Colors produced by Glass Dopants p. 200

Table 5.2: Mean Thermal Expansion Coefficients of Selected Ceramics p. 201

List of Figures

Figure 1.1: Surface features, such as a terrace or facet, may create localized charge imbalances referred to as space charge. In addition, planar surfaces are not electronically neutral at the local scale due to unsatisfied bonds. p. 24

Figure 1.2: Examples of calculated arbitrary Wulff Plots by R. F. Sekerka.[31] p. 25

Figure 1.3: An agate geode with a quartz center.[35] The reaction layers between different compositions can be clearly seen. p. 26

Figure 1.4: SEM image of a SiO_2-based diatom showing the instrument's large depth of focus and topographic imaging abilities. The diatoms were harvested from St. Croix Lake in Minnesota. Diatoms self-assemble into remarkable structures. p. 27

Figure 1.5: Sintering begins with particles in a green compact (a) just touching and forming a grain boundary when brought to temperature (b). A neck (c) forms between the particles via surface diffusion. Pores form when necks do not fully close (d). p. 28

Figure 1.6: Pulsed-laser deposition (PLD) uses a laser beam to ablate a target material. A plasma plume of the desired film composition is formed and deposited onto a heated substrate. p. 29

Figure 1.7: The interaction volume produces when an electron beam strikes a sample surface is responsible for many different types of signals. The total volume is approximately 100 μm^3. p. 30

Figure 1.8: The focused-ion beam (FIB) tool geometry is similar to an SEM. The ion column is 52˚ to the electron column. Accessories, such as GIS deposition needles and micromanipulators, fit in remaining ports. p. 31

Figure 1.9: (a) SPM geometry involves reflecting a laser off of a moving cantilever to measure various signals on the sample surface. (b) The cantilever scans back and forth over the surface, similar to how a record player operates (c). p. 32

Figure 2.1: Surface reconstruction may form two different morphologies: (a) Terrace-&-Ledges and (b) Hill-&-Valley structures. p. 63

Figure 2.2: The theoretical morphology of surface reconstruction consists of facets made from a simple and complex plane. The simple plane is a low-energy, low-index plane, while the complex has higher surface energy and larger crystallographic indices.p. 64

Figure 2.3: The rhombohedral alumina crystal structure is commonly described using the hexagonal unit cell, illustrated in (a). Relationships between low-index planes are shown in (b). p.65

Figure 2.4: Highlighted in yellow are the unrelaxed surface terminations of (a) the (0001) *c*-plane and (b) the $(10\bar{1}0)$ *m*-plane of alumina. The unit cell is outlined in black. p. 66

Figure 2.5: Facet orientation with respect to the hexagonal unit cell for alumina. The complex plane is in blue, while the simple plane is in red. The *m*-plane is in grey. p. 67

Figure 2.6: Fiducial markers were made using a hardness tester. The markers allow the same area to be returned to using both (a) VLM and (b) AFM. p. 68

Figure 2.7: Samples rested on a single-crystal Al_2O_3 slab inside two Al_2O_3 crucibles during heat treatment. Al_2O_3 powder was packed between the crucibles and placed in Al_2O_3 boats to act as impurity getters. p. 69

Figure 2.8: A fiducial marker, (just out of the image in the bottom-right corner), was used to measure from and locate the region of interest. The facets surrounding the indent can be clearly seen. p. 70

Figure 2.9: AFM of the as-received surface shows that the surface is initially flat. p. 71

Figure 2.10: The facets marked with cursors in (a) have begun to coalesce with the smaller facets to the right, respectively, seen in (b). p. 72

Figure 2.11: Facet tips act like kinks when they meet other facet tips. By watching the same set of facet tips after (a) 10 min, (b) 12 min and (c) 14 min at 1400˚C the morphology change is evident. p. 73

Figure 2.12: The facet tips are responsible for lengthening the entire facet and allowing coalescences by forming kinks. p. 74

Figure 2.13: Vicinal surfaces (upper-left corner) must form first and evolve into fully formed facets (bottom-right corner). p. 75

Figure 2.14: The vicinal surfaces have a regular shape just like facets when sectioned perpendicularly (a). When the vicinal surfaces are sectioned parallel to themselves, the surfaces lack structure. p. 76

Figure 2.15: Secondary facets coarsen in the same manner as primary facets with time. p. 77

Figure 2.16: The same facet changes with further exposure to 1400˚C. The facet grows in height and additional facets form in the regions around it. p. 78

Figure 2.17: Significant coarsening has occurred on the *m*-plane surface after 30 min at 1400˚C. p. 79

Figure 2.18: Indents acting as fiducial markers were monitored as they healed. (a) No facets present in the as-indented surface. (b) After only 6 min at 1400˚C, significant healing has happened and large facets have formed. p. 80

Figure 2.19: An originally miscut surface (a) must pass through a minor cusp in the energy plot to form vicinal surfaces before moving to a major cusp (b) and the equilibrium structure. p. 81

Figure 3.1: The FIB tool uses an ion column aligned 52˚ to the SEM column to mill site-specific cross-sections in bulk material. p.108

Figure 3.2: (a) illustrates surface diffusion from the grain boundary to the free surface in order to form a thermal groove and ridges. (b) defines the necessary terms that describe the process. p.109

Figure 3.3: When a remnant groove forms, a grain boundary moves from its original position (a) by having the subsurface portion of the grain boundary lead in front of the thermal groove (b). After a critical condition is reacted, the thermal groove snaps into alignment with the grain boundary and leaves a remnant groove behind (c). p. 110

Figure 3.4: Balance of surface tensions at a triple junction triple-phase point. p. 111

Figure 3.5: Pore shrinkage within the bulk is a removal of vacancies. In order to accommodate vacancies diffusing out of the material, thermal grooves form at the grain boundaries. p.112

Figure 3.6: Samples were kept clean during annealing by using two crucibles and alumina powder as an impurity getter. p. 113

Figure 3.7: The presence of glass allows larger grain boundary grooves to form beneath the glass. The bare surface did not experience accelerated groove formation. p. 114

Figure 3.8: VLM mapping of the surface (a) allows the same grains to be found using the VLM optics of the AFM (b). The canitilvers can be seen above the region of interest (out of focus) in (b). p. 115

Figure 3.9: A grain boundary is in the middle of migrating and leaving its remnant groove behind. p. 116

Figure 3.10: Section analysis perpendicular to the migrating grain boundary. p.117

Figure 3.11: Section analysis parallel to the migrating grain boundary. p. 118

Figure 3.12: Thermal groove depth and width is dependent on time at the anneal temperature. p.119

Figure 3.13: (a) Thermal grooves form by surface diffusion from where the grain boundary meets the free surface. (b) Glass at the free surface accelerates grooving since diffusion through the liquid may occur. p. 120

Figure 3.14: Triple junctions can move in conjunction with grain boundaries and leave behind a remnant triple junction at the original position. p. 121

Figure 3.15: The remnant groove (green) section is much more shallow and wider than the actual grain boundary (red). p. 122

Figure 3.16: Grains of different orientation in Cu have been etched at different rates within the FIB tool. p. 123

Figure 4.1: The (001) planes of a) anatase, b) rutile and c) brookite TiO_2. p. 148

Figure 4.2: Rutile TiO_2 surface projections in the a) [001]- b) [100]- and c) [110]-directions. p. 149

Figure 4.3: Diagram displaying the different polymorphs of SiO_2. p. 150

Figure 4.4: Amethyst (purple) and quartz (clear) crystals are forms of SiO_2. p. 151

Figure 4.5: Young's equation describes the SLV triple junction and the balance of forces. p. 1.52

Figure 4.6: A triple phase point (a) has similar geometry and force balances as a grain boundary thermal groove (b). p. 153

Figure 4.7: Contact angle measurements need to be carefully made. When the surface is assumed to be flat, an apparent contact angle is measured. However, the actual angle may be very different if small surface features exist. p. 154

Figure 4.8: Marangoni convection involves the motion of material from the bottom of the material to the top due to a temperature, composition or viscosity gradient. p. 155

Figure 4.9: Hexagonal Bénard cells form from motion of material from the center of the cell outwards. A dimple forms in the center of the cell. p. 156

Figure 4.10: Rayleigh Instability forms after an initially flat,, continuous film breaks apart and forms droplets on top of surface features. p. 157

Figure 4.11: Films heated in a Pt crucible form Bénard cells of uniform size. p. 158

Figures 4.12: High magnification images of the Bénard cells. p. 159

Figure 4.13: Sections of the Bénard cells show that there is dimple in the center and a skirt surrounds the cells. p. 160

Figure 4.14: Pt Surface pits in surfaces annealed in a Pt crucible are seen in an enhanced AFM height image. p. 161

Figure 4.15: Scanning artifacts produce tiny undulations in the section analysis that may be mistaken as real features. The enhanced AFM height image shows that noise in the scan lines are creating the undulations. p. 162

Figure 4.16: Films heated in an Al_2O_3 crucible had the SiO_2 film disappear and irregular surface facets form. p. 163

Figure 4.17: Section analysis of samples heated in an Al_2O_3 crucible shows surface facets and large depressions on the surface. p. 164

Figure 4.18: Small surface pits covered the surface of those samples exposed to Al_2O_3. p. 165

Figure 4.19: When film thickess is increased to 100 nm ,contaminated droplets undergo the Rayleigh instability. p. 166

Figure 4.20: A dewetting front was observed via (a) VLM and (b) AFM of a 200 nm thick film that underwent the identical anneal as thinner films. p. 167

Figure 4.21: (a) HRTEM and (b) schematic of a FIB cross-section showing the reaction layer of Al_2O_3 contaminates. p. 168

Figure 4.22: SiO_2-TiO_2 phase diagram p. 169

Figure 4.23: Al_2O_3-TiO_2 phase diagram p. 170

Figure 5.1: Materials Science in pottery includes topics like (a) crazing, (b) spherulites and (c) oxidation in Raku glazes and other glazes. p. 202

Figure 5.2: (a) If the liquid droplet at the surface is large compared to a pore within the GB, the liquid will penetrate the GB. (b) If there is more liquid in the pore, the liquid will exude from the GB in an effort to balance partial pressures. (c) An equilibrium GB wetting condition will exist when the pressures balance between the external surface droplet and the internal pore. p. 203

Figure 5.3: Curvature of the particles' surfaces drives the initial sintering of particles. Once a grain boundary forms between two particles, a neck forms via surface diffusion. Pores forms from a gap between particles. p. 204

Figure 5.4: Interfacial tension geometry for the triple-phase boundary has similar geometry to the phase boundary within the grain boundary. The force balance of the internal phase boundary can be approximated by a meniscus (inset). p. 205

Figure 5.5: (a) During migration material from the purple interface dissolves in the liquid and reprecipitates at the orange interface. (b) A droplet is left on the left side of the original grain boundary position from the formation of the thermal ridge. The droplet marks where the grain boundary had been. p. 206

Figure 5.6: The sample surface (a) After polishing, but before annealing in the presence of anorthite powder. (b) After first anneal showing the glass droplet reservoir and the exuded droplets. p. 207

Figure 5.7: Prior to annealing (a) anorthite powder was sprinkled into the dimple. On heating (b) the glass melted and infiltrated the grain boundaries. p. 208

Figure 5.8: CAS-Al_2O_3 phase diagram p. 209

Figure 5.9: Highlighted areas are those where changes can be clearly seen with the VLM. In particular, Ostwald ripening and grain boundary migration has occurred. p. 210

Figure 5.10: EBSD point analysis showing that droplet patterns are dependent surface orientation. The spot was not indexed because the film was too thick. p. 211

Figure 5.11: Droplet patterns depend on the underlying grain surface orientation. In addition, droplets align themselves along grain boundaries. p. 212

Figure 5.12: (a) AFM and (b) SEM showing the decoration of a remnant groove. p. 213

Figure 5.13: Comparison of a decorated remnant groove after (a) 6 min and (b) 12 min at 1650˚C. p. 214

Figure 5.14: Section analysis of remnant groove after 6 min at 1650˚C. p. 215

Figure 5.15: Section analysis of remnant groove after 12 min at 1650˚C. p. 216

Figure 5.16: EDS of droplets confirmed qualitatively that the glass is anorthite. The large droplet at the edge of the specimen was used to get composition data. p. 217

Figure 5.17: Completely wet grain away from any sample edges. In (a) the grain of interest is in the center of the VLM image and Newton's rings can be used to see the thickness difference of the droplet. The AFM image in (b) shows the finer detail of the droplet at the grain boundaries. p. 218

Figures 5.18: The grain is originally wet all the way to the grain boundaries. (b) After more time at temperature, the glass is pulling away, i.e. dewetting, from the thermal grooves. p. 219

Figure 5.19: The droplet over the TJ has gone back into the GB. The large droplet on the grain to right is starting to pull away from the GB, exposing facets at the thermal grooves. The GBs initially had glass at at them, but now they are widely etched and dry. In (b) the right-hand grain shows the fine detail of the thermal grooves where a droplet has pulled away from the grain boundary. p. 220

Figure 5.20: Clearly a droplet is at the GB initially and disappears after the second anneal to form a groove at the TJ. The other GB initially has glass at the GB, but forms a wide groove with further heat treatment. p. 221

Figure 5.21: Two other possible sample geometries to further this would be a) bicrystals made from substrates of material with a glass film of material B at the interface and b) multilayers materials A and B deposited via pulsed-laser deposition (PLD) onto a substrate of material A. The interface would have known orientations, simplifying analysis. p. 222

Figure 6.1: Phillips XL-30 SEM chamber showing how the EBSD detector is aligned with SEM column with respect to the sample. p. 252

Figure 6.2: As-received pure alumina was polished to 0.5-μm finish for EBSD. Average grain size was measured to be ~3 μm. p. 253

Figure 6.3: VLM shows large abnormal grains with small grains trapped at the grain boundaries and within the matrix. The surface is covered with remnant grooves. p. 254

Figure 6.4: (a) EBSD maps of the surface are of poorer quality than (b) maps if polished bulk material. p. 255

Figure 6.5: EBSD orientation maps show how the surface evolves from small 3 μm grains to large abnormal grains several hundred μm in size. p. 256

Figure 6.6: After (a) 20 hr and (b) 80 hr, smaller grains were found to be trapped with abnormal grains. The trapped grains have an interface relationship with the alumina (0001). p. 257

Figure 6.7: EDS of grains trapped in a grain boundary between two abnormal grains shows that Si resides at the triple pockets and not with in the matrix. Ca was also found, but due to printing resolution, is not shown here. p. 258

Figure 6.8: (a) An exaggerated grain in an alumina tube. The grain is fairly equiaxed. (b) Abnormal grains in alumina have a lath-like shape. p. 259

Figure 6.9: When looking at the sample in plan-view, the blue grain appears to be larger than the red grain. But if a cross-section is made along the green line, one can clearly see that the red grain is larger than the blue grain. p. 260

Figure 6.10: Depending on how the grain is diced, a misleading grain shape may result at the surface when polished. In this example, a hexagonal grain is diced in two different directions. When viewed from the new surfaces, the blue grain looks very different from the red one. p. 261

Figure 6.11: A FIB-prepared Cu atom-probe tomography (APT) needle has a radius of curvature of < 50 nm. p. 262

Chapter 1: Introduction

1.1 How the topics fit together

1.1.1 The Importance of Basic Science Research

While research usually follows funding trends, basic science research is always important. In recent years funding from government agencies for the most fundamental research has been significantly decreased or entirely cut. Science is defined as "the effort to understand, or understand better" and is derived from the Latin word *scientia*, meaning "knowledge."[1] However, by reducing funding levels in the United States,[2] scientists are choosing to do research on topics that are heavily funded rather than what needs to be understood. The glamorous topics that are attracting support still need basic research to fully understand the topic; if the most basic materials and phenomena are not understood, comprehending more complicated situations is impossible.

This dissertation is an effort to understand some fundamental behavior in ceramic materials. Surface and interface behaviors in common ceramics have been studied using several different microscopy techniques. Alumina, silica and rutile are common materials found in whitewares, abrasives, catalysis, electronics and geology[3]. While these materials have been in common use for decades, some of their behaviors are not yet understood.

1.1.2 Why is now the time to be studying this?

This type of basic research on ceramics has been going on for decades. Recent advances in characterization tools and modeling have allowed more detailed studies. Questions that could not be answered years earlier are now starting to be solved using computers with more memory and higher processing speeds. Improvements in resolution and data collection speed allow better data to be collected. For example, within the last ten years, spherical aberration (C_s) within electron microscopes has been significantly corrected.[4,5]

In addition, within the last five years, C_s-correctors and monochromators have become affordable options on TEMs used in typical research laboratories.

The world is also becoming more global. In the past, distance, cultural differences and military conflicts kept researchers from collaborating or even accessing journal articles. Work presented in this dissertation was completed by collaborating with other scientists in California[*, **], Utah[***], Sweden[^], Turkey[^^] and India[^^^]. By pooling efforts and equipment, research problems can be solved in a more efficient, accurate way.

1.1.3 History of Ceramic Characterization

Ceramics are subject to surface energy and capillary forces. These topics have been studied for hundreds of years. Newton,[6] Young,[7] Rayleigh[8] and even Da Vinci[6] all studied how energy and capillary forces affect common situations. These famous scientists unknowingly laid the way for ceramic research today by studying behaviors of alcoholic beverages and other ordinary materials.

---

[*] A. Minor, National Center for Electron Microscopy, Lawrence Berkeley National Laboratory, Berkeley, CA

[**] E. A. Marquis and D. L. Medlin, Sandia National Laboratories, Livermore, CA

[***] J. K. Farrer, Dept. of Physics and Astronomy, Brigham Young University, Provo, UT

[^] E. Olsson, Dept. of Applied Physics, Chalmers University, Göteborg, Sweden

[^^] M. A. Gülgün, Dept. of Materials Science and Engineering, Sabancı University, Istanbul, Turkey

[^^^] N. Ravishankar, Materials Research Centre, Indian Institute of Science, Bangalore, India

Most of the early research was done on pure metals. Metals are usually less complicated than ceramics since cubic metals are much more common than cubic ceramics. Metallic bonding is not directional and reduces the number of special structure formations due to bonding considerations.[9] All of the early dislocation, point defect and dislocation studies were done on metals.[10, 11] Sample preparation is faster and processing conditions are less extreme for metals than ceramics. Obviously, studying metals is not a substitute for studying ceramics, but can be used to guide research. Alloys can have complicated structures, but bonding is still less complicated than that for ceramics.

Beginning in the mid-1900s, three researchers have made significant progress in understanding ceramic behavior. In the 1950s, Burke assembled some of the best ceramists at the time to work at the General Electric Research Laboratories. The ceramics and metallographic group that he put together was able to solve many of the materials science's fundamental questions.[12] Coble made great headway in understanding ceramics by applying the techniques used for metals characterization to ceramics. Before his work at General Electric Research Laboratories and MIT, ceramic characterization was done in similar manner to geologic characterization using thin sections.[12] One of Coble's greatest contributions to materials science was his development of Lucalox™, a fully dense alumina for use in sodium-vapor lamps.[13] Kronberg was another researcher at General Electric and worked out the crystal structure and deformation mechanisms of sapphire.[14]

Mullins did an enormous amount of work on surface energy-driven phenomena within materials while working at Carnegie Mellon University over 40 years. He developed some of the early theories on the formation of thermal grooving,[15] surface reconstruction,[16] capillary forces[17, 18] and grain boundary migration.[19]

Kingery worked mostly at MIT and was a co-author of the first comprehensive textbook on ceramics.[3] He has been credited with bringing the ceramic industry up-to-date and into mainstream research.[20] His focus on studying the fundamentals of sintering and

thermal conductivity of traditional ceramics, such as clay bricks and whitewares, brought separate areas of research and art together.

1.1.4 How are the presented projects experimentally similar?

The work presented here is concentrated on surfaces and interfaces in alumina (Al_2O_3), anorthite ($CaAl_2Si_2O_8$), silica (SiO_2) and rutile (TiO_2). While these materials have different crystal structures and measurable properties, they all exhibit similar mechanisms for fundamental behavior. Surface reconstruction is dominated by surface energy no matter the material.[16] Point defects, diffusion and capillary forces behave the same way in all ceramics because of the mix of ionic and covalent bonding.[3, 21]

The topics researched and discussed here lead into each other. Faceting describes the movement of atoms to a lower energy configuration.[16] While faceting of the surface is only considered, grain boundaries can be faceted. In cross-section, facet morphology resembles grain boundary grooves. Grooves and ridges form where a grain boundary intersects an interface.[15] The grooves facilitate grain boundary migration and diffusion. The surface tension at the groove is governed by Young's equation[7], which balances the interfacial forces between the solid and vapor. Glass films can wet or dewet the surface and grain boundaries on heating above the glass melting temperature. Whether the film wets or dewets depends on the surface energy of the surface and the liquid. Capillary forces determine the type of dewet patterns formed on the surface. Again, the surface-vapor-liquid interfaces are governed by Young's equation. Liquid films at grain boundaries facilitate densification and grain boundary migration. Liquid-phase sintering (LPS) uses capillary forces and the dissolution/reprecipitation process to sinter green compacts to a high density at lower processing temperatures. Capillary forces and surface tension can also cause the liquid film to penetrate or exude from the grain boundary. To summarize, orientation, surface energy and capillary forces govern all of the behaviors investigated within this dissertation.

1.1.5 'Real-World' Applications

When someone is asked to name a ceramic component, toilets, whitewares, light bulbs and windowpanes are often the first things mentioned. These traditional uses for ceramics inspired early research, but ceramics have become significantly more 'high tech' with time.

Today's energy crisis and the threat of global warming have required alternative energy to come to the forefront of research efforts. Fuel cells are a promising technology for solving these problems. Fuel cells use a layered structure to pull H_2O out of the atmosphere and split the molecule into H_2 and O^{2+} to power electronics, automobiles and industrial applications. The only bi-products produced are eco-friendly gases and water vapor. The electrolyte layers within fuel cells are made from ceramic materials and are often wet with Pt films. Perovskite- and fluorite-structured materials are the materials of choice for this application.

Nanotechnology has been the biggest research area in the last decade and continues to be an important topic. Nano-sized ceramics are important in gas sensing devices, microelectronics, catalysis and biological applications. Nanoparticles are also found in everyday life, such as air particulates, steam and water precipitates. While nanoparticles have been around for ages, only within the last several decades have the characterization tools been available to understand and perform systematic research on them. A particularly interesting application is the manipulation of nanostructures to pattern and perform specific tasks.

Sintering to achieve dense material using less extreme processing conditions is a classic topic of ceramics study.[3] Whitewares, pottery and lighting require dense materials. However, processing ceramics is difficult and costly. Understanding how ceramics sinter and mechanisms to speed or lower processing temperatures can make sintering more economical and less energy-intensive. Applications operating at small length-scales require a finer understanding of sintering.

Ceramics are being used increasingly in biological applications. Joint replacements, dental implants and bone graphs all require biocompatible ceramic materials. The ceramics used in these applications exhibit all of the same behavior as when they are *ex vitro*, but when *in vitro* they are also subjected to a highly corrosive environment. How the body will interact with the prostheses needs to be understood. In addition, the replacement components must sufficiently match the body's original properties in order to prevent damage to other body parts and limit the number of invasive surgeries.

Diatoms and sea sponges have ceramic skeletons that naturally form in complex patterns.[21] The aquatic organisms have silicate-based structures and have been found to have excellent mechanical and optical properties that currently can not be matched by any man-made materials.

Geology is closely linked to materials science.[22] The same block of material will be labeled a 'ceramic' by a materials scientist, but a 'mineral' by a geologist.[23] Geologists will mine the field for specimens formed in nature and try to replicate the behavior in the lab. Geodes are an example of reaction and diffusion kinetics. Water, vapor, temperature and pressure all contribute to a mineral or gemstone's formation.[24]

Crystal growth requires a strong understanding of mass transport. Single crystals can be grown from melt, deposition and evaporation/condensation methods. All of these methods use convective flow to propel material motion. Crystal growth rates depend on diffusion and surface energy. Material will diffuse along preferred crystallographic directions, and preferred planes will grow while others will be hindered. Atmosphere, chemistry and temperature are other factors that drive or inhibit growth. During growth, atoms will attach to specific points on the crystal surface. Kinks and terrace edges will grow faster than the flat ledge regions, similar to facet formation.[3]

Using the principles of crystal growth, optical fibers can be grown for use in communications applications. The fibers rely on easy growth in a low-energy direction and hindered growth in directions perpendicular to the easy-growth direction. This same

principle is used for the growth of nano-sized fibers and rods. If crystallinity is not a concern for fibers, glass can be drawn to produce very fine fibers from the melt.

Microelectronics relies on thin films of insulators for several applications. The interface between the layers is becoming more important to understand as length-scales become smaller. Composition, orientation and stresses at the interface will all affect electronic transport properties and slow devices or cause them to fail. In addition, the films are subject to liquid- and solid-state wetting depending on the processing and service conditions.

Pottery and art glass are little considered applications of ceramic engineering. Glazes rely on the same principles as spreading and dewetting of liquid films and crystallization of thin films to create the interesting colors and patterns at the surface.[25] Reduction reactions between the clay, glaze and metal ions create brilliant colors.[26] Glazes also experience stress at the interface with the clay. The stress is similar to lattice misfit in epitactic films. Crazing results when cracks form within the glaze and can be an added ornament or a detrimental point of weakness. Pottery is cast using liquid slip, which is subject to composition and thermal gradients creating convection.[3] Stoneware and pottery rely on the same sintering principles as green compacts. Pores can cause a piece to explode within a kiln.

1.2 General Considerations for Ceramic Research

1.2.1 Crystal Structure

Anisotropy in structure, chemistry and bonding exist in most ceramics. The crystal structure depends on the valence of the material and the type of bonds that the ions are capable of making. Covalent bonds will lead to a more rigid and open crystal structure. Structures that are more ionically bonded will be tighter, but able to relax more if ions are removed. Linus Pauling[27] defined a set of rules to help the researcher determine what the crystal structure of a ceramic should be, based on the coordination number,

valence and atom size of the material. The coordination number may be predicted based on the atoms size and charge.[28]

1.2.2 Space Charge

Space charge describes local electronic structure. While an entire crystal may be electrically neutral, local features may not be. Surfaces are the best example of this behavior. The surface must be terminated in specific atomic arrangement to satisfy energy balances. However, kinks, terraces and facets all create pointed features that are not balanced electronically.[28] Figure 1.1 illustrates how these surface features can create localized charge; the terrace edge is negatively terminated, creating a local negative charge imbalance. Likewise, the facet tip is positively charged, despite the crystal having the proper atomic arrangement. The planar surface is more electronically neutral, but each atom has an unsatisfied bond at the surface. The space charge allows impurities to easily settle on to the surface and bond to the bulk. During processing, surface vacancies can be produced that will also accommodate impurities and alter charge transport. In the bulk, grain boundaries will form in a way to balance the space charge from each of the interface planes depending on orientation, often leading to coincident-site lattice (CSL) boundaries.

1.2.3 Orientation

Herring[29] used Wulff's theory[30] to derive a model for surface energy plots of materials. Each material has a unique set of surface energies depending on the specific crystal structure and the resulting crystallographic orientations. Some orientations are lower in energy than others, making them more stable and preferred planes for growth and motion. Higher energy planes will reconstruct to form lower energy planes if the energy reduction makes up for the energy needed to create more surface area. The Wulff plot is a graphic representation of the material's surface energy. Low-energy cusps indicate which planes have the lowest energy. Because surface energy depends on the crystal orientation, any behavior that is driven by surface energy will, therefore, depend on orientation. Sekerka's[31] calculated Wulff shapes for an arbitrary anisotropic material are

presented as an example of Wulff plots in figure 1.2. With electron backscatter diffraction (EBSD) becoming more accessible in recent years, orientation considerations can be more easily considered.

Within the materials science field, two schools of thought exist. Some researchers believe that the surface drives most of the material's behaviors, while other researchers believe that the bulk and sub-surface features control what is happening. The work presented here will illustrate that the two are not mutually exclusive. Researchers can gain insight by studying one and applying the results to the other. In some cases, as in chapter 5 of this dissertation, the surface and grain boundary orientations influence wetting behavior of each other. Therefore, while research may be isolated to only one type of feature within a material, the other must be kept in mind.

1.2.4 Chemistry

Valence differences of a particular ion lead to local space charge and will change the way it behaves and what reactions it will undergo. Small amounts of additives or impurities will change the behavior of a ceramic. The mobility of grain boundaries depends on what type of atom is residing in the boundary and where it is within the boundary.[32] The classic example of alumina reaching theoretical density with the addition of a few ppm of magnesia shows the importance of chemistry.[13] Point defects will change local chemistry and introduce strain within the lattice. Local chemistry changes within a component can be a source of failure.

1.2.5 Mass Transport

Measuring diffusion coefficients is difficult, since several forms of diffusion exist that are not easily separated from each other. Diffusion rates are different for the same migrating species in the same bulk material depending on whether the species is moving at the surface, in a grain boundary or within the bulk.[33] Under different processing conditions, one type of diffusion may dominate while another dominates at a different value.[34] A change in processing temperature is one example where the diffusion

mechanism will change. Discrepancies between measured and calculated diffusion coefficients also need to be resolved.

Traditional chemical engineering concepts are becoming more important in materials science. As this dissertation will show, convection and fluid flow are important concepts that are not well understood in ceramic processing. Convection occurs due to the formation of either a temperature or composition gradient. In this work thermal and concentration gradients are addressed. Capillary forces drive wetting of liquid phases on substrates and grain boundary infiltration. The same forces that make extrusion of polymers possible allow ceramics to be processed.

1.3 Processing Ceramics

Ceramics can be processed in a variety of ways. Man has been producing ceramics for thousands of years by using hot fires to make primitive pottery. In modern times, sophisticated equipment has been developed to produce high-tech ceramics. Nature can self-assemble molecules to create beautifully intricate structures.

1.3.1 Naturally

Geodes are naturally occurring rocks that form via diffusion couples. An example of an agate geode with a quartz center is shown in figure 1.3. Layers of different chemical composition can be clearly seen in the image. [35] The layers form by material counter diffusion across the interfaces. Each layer has nearly the same chemistry, but often has a different crystal structure. For some geodes, an inside cavity is lined with crystallites of one or more minerals.[23]

Skeletons of small marine life forms, called diatoms, are particularly interesting ceramic structures. Once the diatom has died, its skeleton is left behind and continues to float in the water or settles into the sand. As can be seen in figure 1.4, these skeletons are small and incredibly intricate. Researchers collect specimens from all over the globe, noting the water temperature, composition and seasonal changes;[36, 37] however, little is known

about how the biomineralization actually occurs. Only recently, mother-of-pearl (a.k.a. aragonite) was proposed to form via a combination of columnar and layer growth.[38] The quality of nature's self-assembly can not currently be duplicated by man.[39]

1.3.2 Powder Processing, Sintering & Grain Size

The most common methods for ceramic processing typically involve some sort of powder precursor. Traditionally, powders are pressed to form a green body. Sometimes this is done with the help of heat or a binder. The green body has a very low density and poor mechanical properties, and must be sintered to form the final compact. The final density depends on the initial powder size, degree of pressing and the sintering conditions. Figure 1.5 illustrates how sintering between powder particles occurs to form grains. Material will diffuse along the surface of the particle to form a neck, which bridges an adjoining particle. Diffusion is driven by capillary forces and particle curvature.[3, 21] Pores are left behind where the necks do not fully close the gap between particles. Often, small amounts of additives will be introduced to densify the compact further.[13] The final grain size will be roughly the same as the initial powder size.

1.3.3 Making Thin Films & PLD

Thin films are responsible for laptops, magnetic recording and solar cells. Several deposition techniques are used to grow films on substrates. The most popular methods are molecular-beam epitaxy (MBE),[40] chemical vapor deposition (CVD)[40] and pulsed-laser deposition (PLD). All of these methods require a substrate to be under vacuum and deposition chambers to be extremely clean.

Since only PLD was used in this work, this growth technique will be the only one discussed here.[41, 42] The reader is referred elsewhere for a detailed description of other thin-film deposition methods.[40-42] PLD uses an excimer laser that is pulsed between 1-100 Hz with a user-defined energy/pulse, usually several hundreds of mJ/pulse. The pulse travels through a beam path into a high or ultrahigh vacuum chamber, illustrated in figure 1.6. The pulse strikes a bulk target that is the exact composition of the desired

film. The energy from the laser pulse needs to be great enough for the material ablated from the target to form plasma. The plasma plume then travels from the target to the substrate's surface. The plasma condenses into a solid phase film on the substrate's surface. The substrate is often heated as high as 1000˚C in order to promote the film's crystallization. Low substrate temperature and high pulse rate tend to form amorphous films, while the opposite deposition conditions can lead to completely crystalline films. Annealing after deposition may cause the film to fully crystallize and relieve strain at the interface. Film thicknesses can range from only several nanometers to microns. Multilayers can easily be made by having a rotating target carousel allowing the substrate to remain under vacuum when changing deposition materials. Stoichiometry is maintained by introducing O_2 or N_2 into the deposition chamber.[41, 42]

1.4 Possible Pinning Mechanisms in Dynamic Processes

1.4.1 Pores at grain boundaries and in the lattice

Pores within the bulk can act as a second phase and impede grain boundary migration and dislocation motion.[43] Pores alter the local chemistry in a similar manner to lattice vacancies. Grain boundaries need to absorb and transport voids to the surface in order to densify the material. Pores can also become sinks for contamination and hold gas phases. Burke[43] was one of the first to study pores in alumina. In particular, he looked at how sintering and grain boundary migration is effected by pore dissolution and migration. Studies have been done on faceting of pores to determine the equilibrium shape of materials.

1.4.2 Additives at grain boundaries and in the lattice

Additives in the lattice can help sintering, but impede grain boundary motion. Contamination at the surface can also change the local surface energy. Wetting and surface reconstruction behavior will be altered as a result.[44] Additives are believed to promote lattice diffusion to create a more dense compact during sintering.[43] Lattice diffusion is favored at higher temperatures than surface diffusion.[33] Additives can lower

the temperature needed to induce lattice diffusion. While this may ease grain boundary migration, any impurities present will also move easier. Precipitates can easily form and pin dislocations, facets and grain boundaries.[10] This processing trick has been put to use in LPS of ceramics, but can result in early component failure.[3]

1.4.3 Point Defects and Dislocations

Point defects are single lattice points that are either missing, chemically different, electronically different or pushed into an interstitial site.[11] Point defects can alter the local chemistry and create a pinning point for grain boundaries. In addition, grain boundaries tend to be sinks for point defects. As the grain boundary concentration changes, the mobility also changes. The point defects can coalesce and form voids within the bulk, leading to behaviors described earlier.

Dislocations are half-planes of atoms that have either been inserted, removed or sheared within the lattice.[10] The lattice becomes strained to accommodate the disruption and a stress gradient radiating from the dislocation core results. Dislocations can tangle within the lattice, dissociate and create stacking faults. Grain boundaries are a network of dislocations. The excess stress, dislocation tangles and change in lattice stacking can halt grain boundary motion if the grain boundary does not have enough energy to pass through or around the entanglements.[10, 11]

1.5 Characterization Techniques and Limitations

1.5.1 Visible-Light Microscopy

Visible-light microscopy (VLM) refers to traditional bench-style microscopes. 'Visible-light' is used to describe the technique rather than 'optical' because all microscopes have some type of optics! But in this case, visible light is being used to form an image, rather than UV, infrared or electron light. Anthony Leeuvenhoek[45] was the first person to grind and polish his own lenses precisely enough to magnify bacteria with visible light. Today's bench-top models have changed little since his work around 1700. The

microscope uses a series of glass lenses that are precisely ground to specific curvatures. By combining convex and concave lenses, aberrations can be corrected. Visible light is used in transmission or reflection modes, and can be coupled with polarizers to enhance specific features of interest. The polarizers enable different orientations in metals and precipitations to be identified. By using the change in focus, height information may be determined. VLMs are now coupled with CCD cameras to allow videos of behavior and digital images to be captured.[46] VLMs can also be equipped with heating and cooling stages to allow *in situ* monitoring.[47]

1.5.2 Electron Microscopy

1.5.2a Transmission Electron Microscopy

Electron microscopy was first successfully used by Ernst Ruska in the 1930's.[48] Transmission electron and scanning electron microscopes, (TEM and SEM, respectively), were made commercially available in the late 1950s. Some of the first microscope manufacturers included RCA and Siemens.[49]

TEM uses highly accelerated electrons, 100 kV – 1.25 MV, to pass through a thin sample and strike an imaging medium.[48] A series of electromagnetic lenses control and focus the electrons within the microscope column to produce a meaningful image or diffraction pattern. The electrons interacting with the specimen as they pass through the material produce the collected data. Both particle and wave natures of the electrons contribute to the signal produced. Structure, orientation and chemistry can be determined using TEM.

Specific techniques within the TEM allow precise measurements to be made at the atomic level. The current resolution world record is less than 1 Å. High-resolution TEM allows the lattice to be directly imaged and point-to-point data of atomic columns to be measured. High-angle annular dark field (HAADF) imaging allows chemistry to be determined to be determined using atomic number contrast, also known as *z*-contrast. When HAADF is coupled with energy-dispersive spectroscopy (EDS), quantitative

compositions can be determined. Electron energy-loss spectroscopy (EELS) can determine the chemistry, valence and bonding of specific ions within a sample. Heating, cooling and straining are only a few *in situ* studies that can now be done within the TEM. Electron diffraction patterns are gathered using selected-area and convergent-beam diffraction methods, SAD and CBED respectively.

While TEM is a powerful characterization tool, limitations do exist.[48] The sample thickness needs to be less than 100 nm thick to be electron transparent. The thin samples may not be representative of the bulk. In addition, making these samples is difficult and very time consuming. Sample preparation needs to be done with care, since the thin samples are easily damaged during preparation, possibly altering the data. Aberrations, such as C_s, exist that can not be completely corrected. Contrast mechanisms need to be carefully considered to understand the images, often requiring image simulation. Finally, the TEM takes a long time to learn and is expensive to maintain.

1.5.2b Scanning Electron Microscopy

SEM uses electron optics in a similar manner to TEM; electrons are focused using electromagnetic lenses, but are scanned rather than transmitted using scan coils within the microscope column.[50] Most electrons within a SEM are accelerated between 100 mV-30 kV, much less than within the TEM. The electron beam is sensitive to the top most 100 μm^3 of the sample, referred to as the interaction volume and can be seen in figure 1.7. Several types of signals can be gathered when an electron beam strikes the surface: secondary electrons, backscattered electrons, Auger electrons, X-rays and fluorescent light. While SEM does not have the same resolution as TEM, images have a 3D-quality that may give more straightforward analysis.

Within the SEM, several techniques exist to compliment the detailed images.[50] While secondary electrons give topography information, backscattered electrons give chemical and orientation images. Electron backscatter diffraction (EBSD) measures the orientation of the backscattered electrons striking the detector.[51] By measuring intensity,

angles and distances of the Kikuchi patterns formed by the backscattered electrons, orientation and phase information at the surface can be gathered. EDS allows chemistry to be mapped on the surface of the material.[50] Quantitative values of concentration can be measured using the characteristic X-ray intensities striking the EDS detector. Cathodoluminesence detectors are able to determine if visible light is emitted from the material. As in the TEM, several types of *in situ* stages have been designed for the SEM.

SEM is subject to limitations, also. The same aberrations in the TEM exist in the SEM. The large beam spot size and current cause the resolution to be much less than in TEM. Non-conducting samples easily charge when exposed to the beam. To counteract the charging, conductive coatings need to be applied to the surface, possible altering or inhibiting data collection.

1.5.2c Focused-Ion Beam Tool

The focused-ion beam (FIB) tool has become widely available in recent years. The FIB is attached to a SEM at a 52˚ angle from the SEM column.[50] The machines are often referred to as "dual-beams" since two microscope columns are attached to one imaging chamber. A typical dual-beam FIB setup can be seen in figure 1.8. Single-beams do exist but are primarily used for ion-beam patterning and not characterization.[52] The FIB uses metal ions to mill away material at the surface of the sample. The metal used needs to be a metal close to room temperature; therefore, Ga and In ions are typically used.[53] Site-specific regions can be milled to understand the sub-surface structure and behavior of particular features.[52] TEM cross-section samples can be made much quicker and with better accuracy of specific regions of interest. The FIB column can be operated at different beam currents and accelerating voltages between 1—30 kV. By changing the conditions, the beam size can be changed and the amount of damage caused by the heavy ions can be minimized. The ion beam and electron beam can also be combined with gas injection sources (GIS) to deposit material, such as Pt, W or SiO_2, onto surfaces in a CVD process.[52]

Besides the SEM column, a FIB tool can be coupled with EBSD and EDS. By doing serial sectioning with the FIB followed by subsequent imaging, tomography can be done of specific sample regions. The same technique can be combined with EBSD and EDS to get 3D reconstructions of both structure and chemistry at the surface and in cross-section. Unfortunately, this is a destructive technique.

FIB tools have the same limitations as a SEM with some additional issues. The metal ions easily damage the surface and change the structure. Ga ions are easily implanted within the sample. The limited amount of stage tilt allowed within the imaging chamber can inhibit the type of structures created. Similar to the TEM, FIB tools are difficult to learn and are very expensive to purchase and maintain.

1.5.3 Scanning Probe Microscopy

Scanning probe microscopy (SPM) is a relatively new set of characterization tools. Invented by Binnig, Quate and Gerber in the 1980's,[54] several types of signals can be probed at the atomic level by scanning a special stylus over surfaces. The first type of SPM was the scanning tunneling microscope (STM), and Binnig, Quate and Gerber were awarded the Nobel Prize for the invention. STM uses a biased tip to probe the surface structure of conductive materials. The tip is scanned over the surface in a similar manner as a stylus moving over a record, illustrated in figure 1.9. The biased tip is deflected by either the attractive or repulsive surface charge. Reflecting a laser off of the tip's backside into a four-quadrant piezodetector monitors the deflection of the tip. The change in voltage bias within the detector is converted to height and deflection measurements in order to map the surface topography.

Several other techniques based on the SPM technique have developed over the years.[55] Atomic force microscopy (AFM) is the most common SPM technique. AFM works in the same manner as STM, but the samples can be non-conducting and the tip can be allowed to touch the surface. Lateral force microscopy (LFM) measures the friction forces between the surface and tip, while scanning thermal microscopy (SThM) measures the surface's thermal conductivity. Electric conductivity and surface charge

can be monitored using electrostatic force and Kelvin-probe microscopes, (EFM and KPM, respectively). Magnetic domains can be easily measured using magnetic force microscopy (MFM).

SPM techniques need to be carefully considered.[55] Chemistry can not be directly determined from the images. The size of the tip creates artifacts in the images. Large tip radii may not be able to reach high-aspect-ratio trenches or may overshoot tall features. When imaging sharp points, the tip may be imaged rather than the sample. While scanning over the material, surface debris may cling statically to the tip and reduce the image quality. The tip may also alter the surface, itself be damaged, by pushing material around or scratching the surface.

1.5.4 Feature Identification

While much of the work presented here has been looked at before in a similar manner, this work is unique in that the same regions of samples have been observed throughout processing. Ceramics need to be processed at high temperatures that do not allow *in situ* studies to be performed. Therefore, a series of abbreviated thermal treatments must be used to 'stop' the behavior, monitor it *ex situ* and repeat until the desired end point is reached. This work allows the exact same feature to be monitored throughout.

Two techniques for returning to the same sample features repeatedly have been used in this work. The first was making detailed maps of the features using VLM and AFM. The maps of the initial stage were returned to after subsequent stages to identify and monitor the exact same feature and how it behaves with time. Munoz[56] was the first to use this technique successfully in polycrystalline ceramics. The other method for identification was to mark surfaces with indentations using a gravity-loaded hardness tester. These indents could easily be found using the VLM. The same force and Vickers-type tip were used for each indent, giving an easy reproducible marking method. The markers allowed quick identification of surface features. In addition, indents do not heal quickly when surfaces are processed at high temperatures and can be returned to after several heat treatments before they have healed.

1.6 Summary

In the following chapters, fundamental ceramic surface studies will be presented. Chapter 2 describes monitoring the same set of facets from nucleation to significant coarsening in order to fully understand how surface reconstruction occurs. AFM is the primary tool used for this study. AFM is also used to study thermal grooving in chapter 3. Thermal groove formation and motion of triple junctions were monitored. The triple-phase point between dewet droplets, bulk surfaces and air and other characteristics of glass films after annealing were monitored in chapter 4, while glass exuding from grain boundaries is discussed in chapter 5. Finally, chapter 6 looks at abnormal grain growth in the presence of glass. EBSD was used to monitor surface morphology changes. The common theme between these topics is how does surface energy/tension change with crystal orientation after the oxide is subjected to a thermal treatment.

References

[1] Science, community encyclopedia, http://en.wikipedia.org/wiki/Science, (May 30).

[2] R. L. Meeks, Federal R&D funding by budget function: Fiscal years 2003-2005, (2004).

[3] W. D. Kingery, H. K. Bowen, D. R. Uhlmann, Introduction to Ceramics, John Wiley & Sons New York, (1960).

[4] P. E. Batson, N. Dellby, O. L. Krivanek, "Sub-angstrom resolution using aberration corrected electron optics" Nature, **418** [6898] 617-620 (2002).

[5] M. A. O'Keeffe, E. C. Nelson, Y. C. Wang, A. Thust, "Sub-angstrom resolution of atomistic structures below 0.8 A" Phil. Mag. B, **81** [11 SPEC] 1861-1878 (2001).

[6] A. Marmur, in: M. E. Schrader, G. Loeb (Eds.), Modern Approach to Wettability: Theory and Applications, New York, (1991), pp. 327-358.

[7] T. Young, "An Essay on the Cohesion of Fluids" Phil. Trans. R. Soc. Lon. 65-87 (1805).

[8] L. Rayleigh, "On the Instability of Jets" Proc. Lon. Math. Soc., **10** 4-13 (1878).

[9] R. E. Reed-Hill, R. Abbaschian, Physical Metallurgy Principles, PWS Publishing Company Boston, (1973).

[10] D. Hull, D. J. Bacon, Introduction to Dislocations, Butterworth Heinemann Oxford, (1965).

[11] J. Weertman, J. R. Weertman, Elementary Dislocation Theory, Oxford University Press New York, (1964).

[12] C. A. Handwerker, R. M. Cannon, R. H. French, "Robert L Coble: A retrospective" J. Am. Ceram. Soc., **77** [2] 293-297 (1994).

[13] R. L. Coble, Transparent alumina and method of preparation, U. S. P. Office, United States, (1962).

[14] M. L. Kronberg, "Plastic Deformation of single Crystals of Sapphire: Basal Slip and Twinning" Acta Metall., **5** 507-524 (1957).

[15] W. W. Mullins, "Theory of thermal grooving" J. Appl. Phys., **28** [3] 333-339 (1957).

[16] W. W. Mullins, "Theory of Linear Facet Growth During Thermal Etching" Phil. Mag., **6** [71] 1313-1341 (1961).

[17] W. W. Mullins, "Flattening of a nearly plane solid surface due to capillarity" J. Appl. Phys., **30** [1] 77-83 (1959).

[18] W. W. Mullins, "Stochastic theory of particle flow under gravity" J. Appl. Phys., **43** [2] 665-677 (1972).

[19] W. W. Mullins, "Two-dimensional motion of idealized grain boundaries" J. Appl. Phys., **27** [8] 900-904 (1956).

[20] R. J. Brook, "Obituary: W. David Kingery (1926-2000)" Nature, **406** [6796] 582 (2000).

[21] C. B. Carter, M. G. Norton, Ceramic Materials: Science and Engineering, Springer New York, NY, (2007).

[22] D. J. Vaughan, R. A. D. Pattrick (Eds.), Mineral Surfaces, Chapman & Hall, London, p. 370, (1995).

[23] C. W. Chesterman, K. E. Lowe, National Audubon Society Field Guide to Rocks and Minerals, Alfred A. Knopf, Inc. New York, (1979).

[24] A. Thomas, The Gemstones Handbook: Properties, Identification and Use, Barnes & Noble New York, (2008).

[25] J. Britt, The Complete Guide to High-Fire Glazes: Glazing & Firing at Cone 10, Lark Books New York, NY, (2004).

[26] C. Hess, K. Wight, Looking at Glass: A Guide to Terms, Styles and Techniques, The J. Paul Getty Museum Los Angeles, (2005).

[27] L. Pauling, "The Principles Determining the Structure of Complex Ionic Crystals" J. Amer. Ceram. Soc., **51** 1010-1026 (1929).

[28] C. Noguera, Physics and Chemistry at Oxide Surfaces, Cambridge University Press Cambridge, UK, (1996).

[29] C. Herring, "Some Theorems on the Free Energies of Crystal Surfaces" Phys. Rev., **82** [1] 87-93 (1951).

[30] G. Wulff, "Regarding the question of the speed at which crystals grow and shrink" Z. Krist., **34** 449-530 (1901).

[31] R. F. Sekerka, "Analytical criteria for missing orientations on three-dimensional equilibrium shapes" J. Crys. Growth, **275** 77-82 (2005).

[32] B. L. Adams, D. Kinderlehrer, W. W. Mullins, A. D. Rollett, S. Ta'asan, "Extracting the relative grain boundary free energy and mobility functions from the geometry of microstructures" Scripta Mater., **38** [4] 531-536 (1998).

[33] P. Shewmon, Diffusion in Solids, The Minerals, Metals & Materials Society Warrendale, Pennsylvania, (1989).

[34] R. L. Coble, "Sintering Crystalline Solids. II. Experimental Test of Diffusion Models in Powder Compacts" J. Appl. Phys., **32** [5] 793-799 (1961).

[35] H. Friedman, Geode, webpage, http://www.minerals.net/mineral/silicate/tecto/quartz/images/geode4.htm, (20 January).

[36] M. Ferrario, D. U. Hernández-Becerril, I. Garibotti, "Morphological study of the marin planktonic diatom Chaetoceros castranei Karsten (Bacillariophyceae) from Antarctic waters, with a discussion on its possible taxonomic relationships" Botanica Marina, **47** 349-355 (2004).

[37] C. E. Stickley, J. Pike, A. Leventer, "Productivity events of the marine diatom *Thalassiosira tumida* (Janisch) Hasle recorded in deglacial varves from the East Antarctic Margin" Mar. Micropaleontol., **59** 184-196 (2006).

[38] R. A. Metzler, M. Abrecht, R. M. Olabisi, D. Ariosa, C. J. Johnson, B. H. Frazer, S. N. Coppersmith, P. U. P. A. Bilbert, "Architecture of Columnar Nacre, and Implications for Its Formation Mechanism" Phys. Rev. Lett., **98** (2007).

[39] E. Pouget, E. Dujardin, A. Cavalier, A. Moreac, C. Valéry, V. Marchi-Artzner, T. Weiss, A. Renault, M. Paternostre, F. Artzner, "Hierarchial architectures by synergy between dynamical template self-assembly and biomineralization" Nat. Mater., **6** 434-439 (2007).

[40] S. A. Campbell, The Science and Engineering of Microelectronic Fabrication, Oxford University Press New York, (2001).

[41] D. Bäuerle, Laser Processing and Chemistry, Springer Berlin, (2000).

[42] K. Seshan (Ed.) Handbook of Thin-Film Depositin Processes and Techniques, Noyes Publications/William Andrew Publishing, Norwich, NY, p. 629, (2002).

[43] J. E. Burke, "Role of grain boundaries in sintering" J. Am. Ceram. Soc., **40** [3] 80-85 (1957).

[44] E. D. Williams, N. C. Bartelt, "Surface Faceting and the Equilibrium Crystal Shape" Ultramicroscopy, **31** 36-48 (1989).

[45] Microbus, History of the Microscope, web page, www.microscope-microscope.org/basic/microscope-history.htm, (August 15).

[46] L. Microsystems, Camera Systems, webpage, http://www.leica-microsystems.com/website/products.nsf?open&path=/website/products.nsf/(allids)/89d748f7e7a47026c12574560026bd89, (20 January).

[47] O. A. Inc., Olympus Microscopy Resource Center, webpage, http://www.olympusmicro.com/, (20 January).

[48] D. B. Williams, C. B. Carter, Transmission Electron Microscopy: A Textbook for Materials Science, Plenum New York, (1996).

[49] S. J. B. Reed, Electron Microprobe Analysis and Scanning Electron Microscopy in Geology, Cambridge University Press Cambridge, Great Britain, (1996).

[50] J. Goldstein, D. Newbury, D. Joy, C. Lyman, P. Echlin, E. Lifshin, L. Sawyer, J. Michael, Scanning Electron Microscopy and X-ray Microanalysis, Kluwer Academic/Plenum Publishers New York, (2003).

[51] A. J. Schwartz, M. Kumar, B. L. Adams (Eds.), Electron Backscatter Diffraction in Materials Science, Kluwer Academic/Plenum Publishers, New York, p. 339, (2000).

[52] L. A. Giannuzzi, F. A. Stevie, Introduction to Focused Ion Beams: Instrumentations, Theory, Techniques and Practice, Springer New York, (2005).

[53] M. W. Phaneuf, "Applications of focused ion beam microscopy to materials science specimens" Micron, **30** 277-288 (1999).

[54] G. Binnig, C. F. Quate, C. Gerber, "Atomic Force Microscope" Phys. Rev. Lett., **56** [9] 930-933 (1986).

[55] R. Howland, L. Benatar, A Practical Guide to Scanning Probe Microscopy, Park Scientific Instruments Sunnyvale, CA, (1993).

[56] N. E. Munoz, S. R. Gilliss, C. B. Carter, "The monitoring of grain-boundary grooves in alumina" Phil. Mag. Lett., **84** [1] 21-26 (2004).

Chapter 1
Figures:

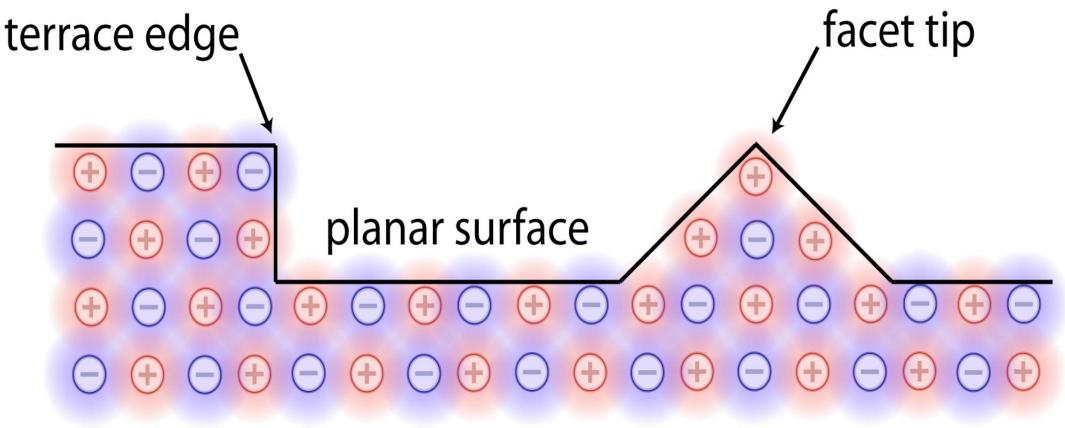

Figure 1.1: Surface features, such as a terrace or facet, may create localized charge imbalances referred to as space charge. In addition, planar surfaces are not electronically neutral at the local scale due to unsatisfied bonds.

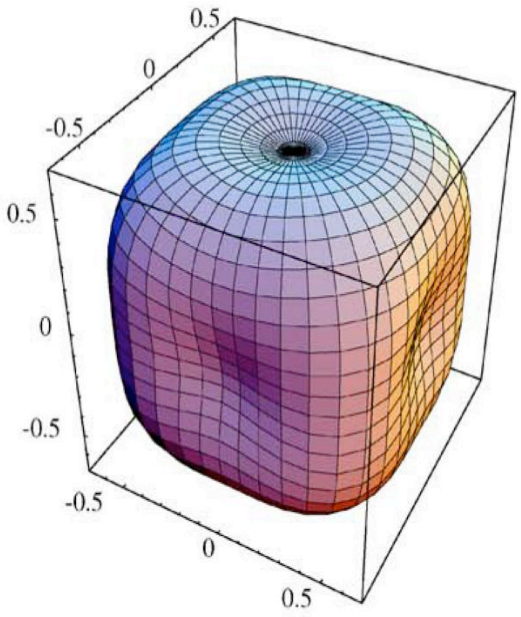

γ-plot for $a = -0.4$

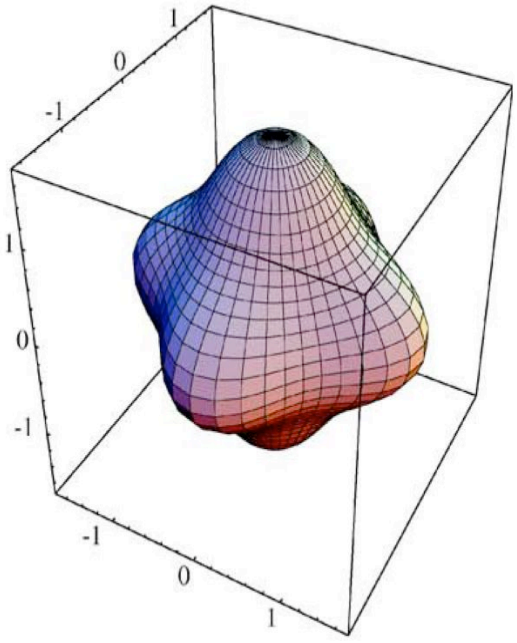

1/γ-plot for $a = -0.4$

Figure 1.2: Examples of calculated arbitrary Wulff Plots by R. F. Sekerka.[31]

Figure 1.3: An agate geode with a quartz center.[35] The reaction layers between different compositions can be clearly seen.

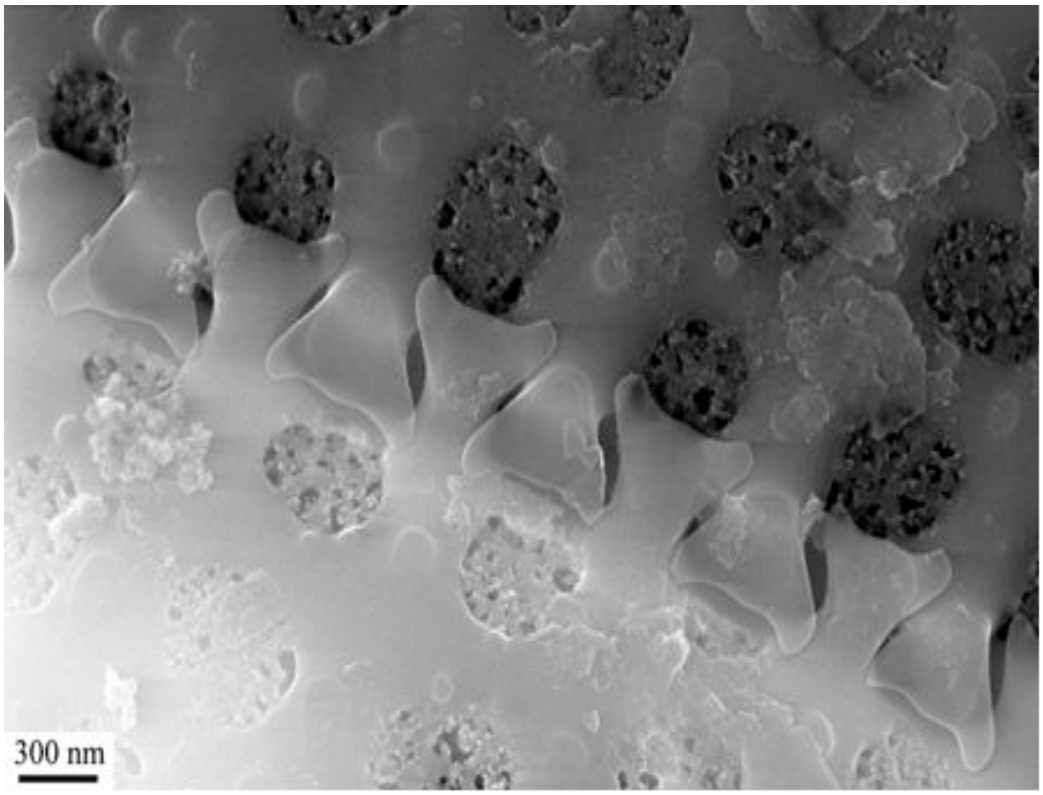

Figure 1.4: SEM image of a SiO_2-based diatom showing the instrument's large depth of focus and topographic imaging abilities. The diatoms were harvested from St. Croix Lake in Minnesota. Diatoms self-assemble into remarkable structures.

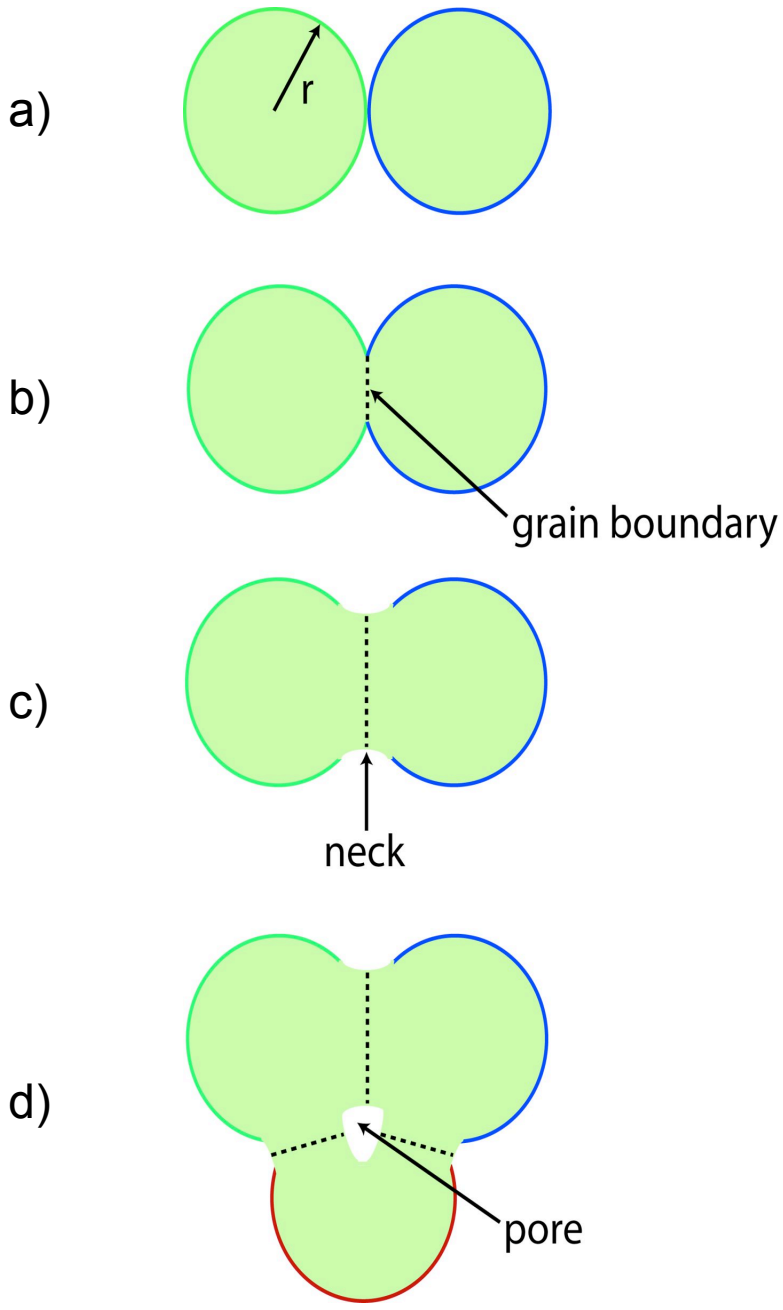

Figure 1.5: Sintering begins with particles in a green compact (a) just touching and forming a grain boundary when brought to temperature (b). A neck (c) forms between the particles via surface diffusion. Pores form when necks do not fully close (d).

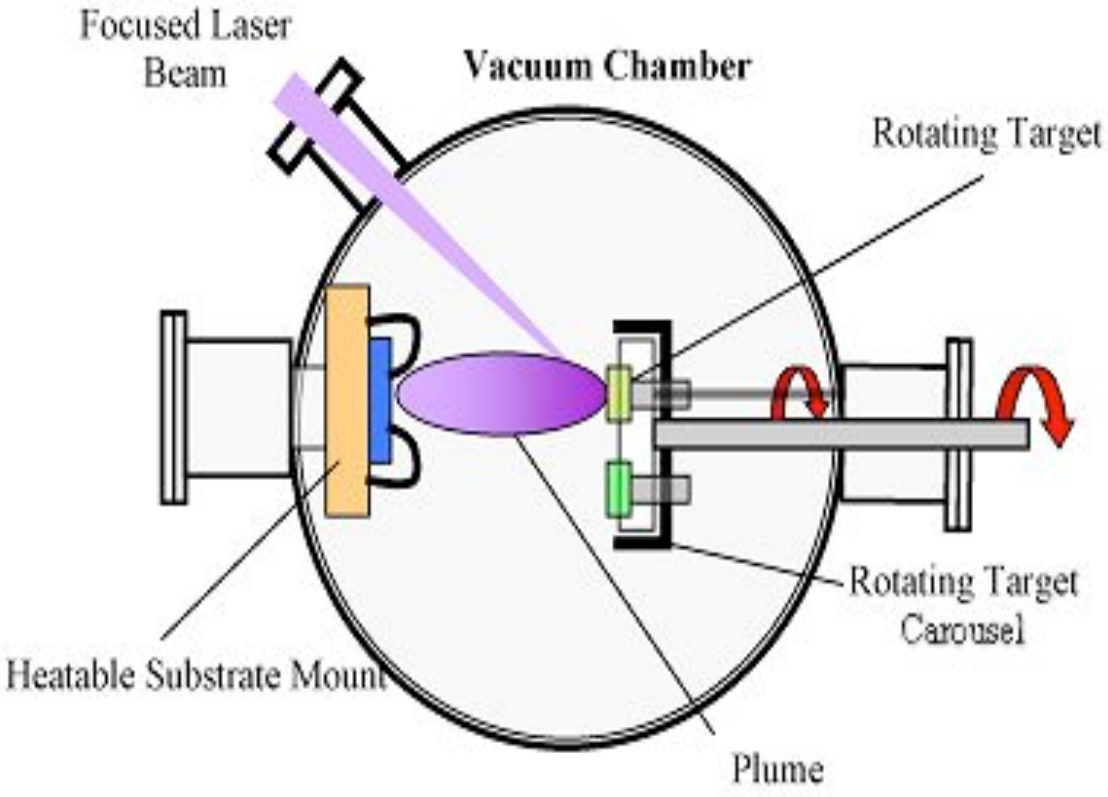

Figure 1.6: Pulsed-laser deposition (PLD) uses a laser beam to ablate a target material. A plasma plume of the desired film composition is formed and deposited onto a heated substrate.

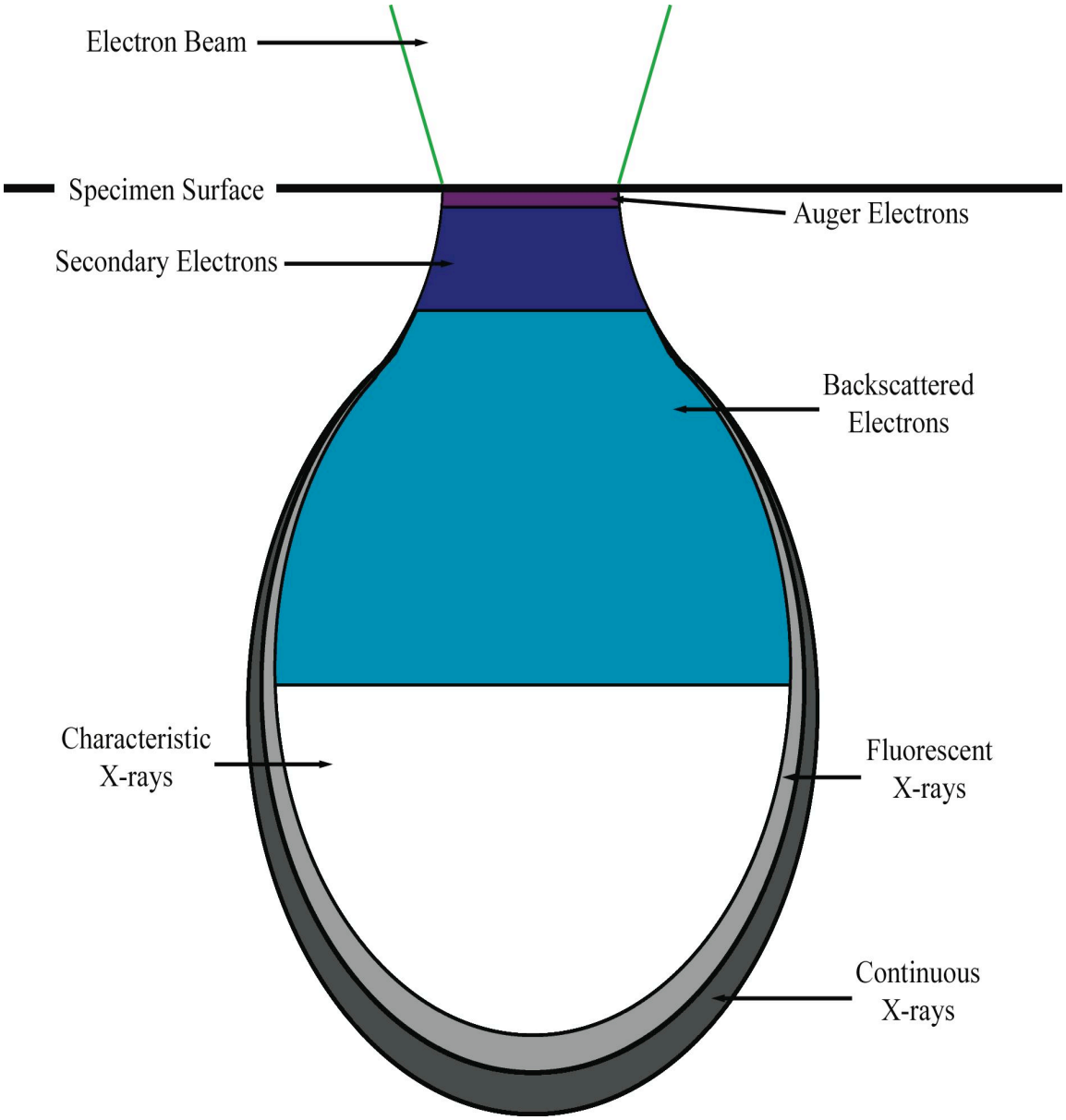

Figure 1.7: The interaction volume produces when an electron beam strikes a sample surface is responsible for many different types of signals. The total volume is approximately 100 μm^3.

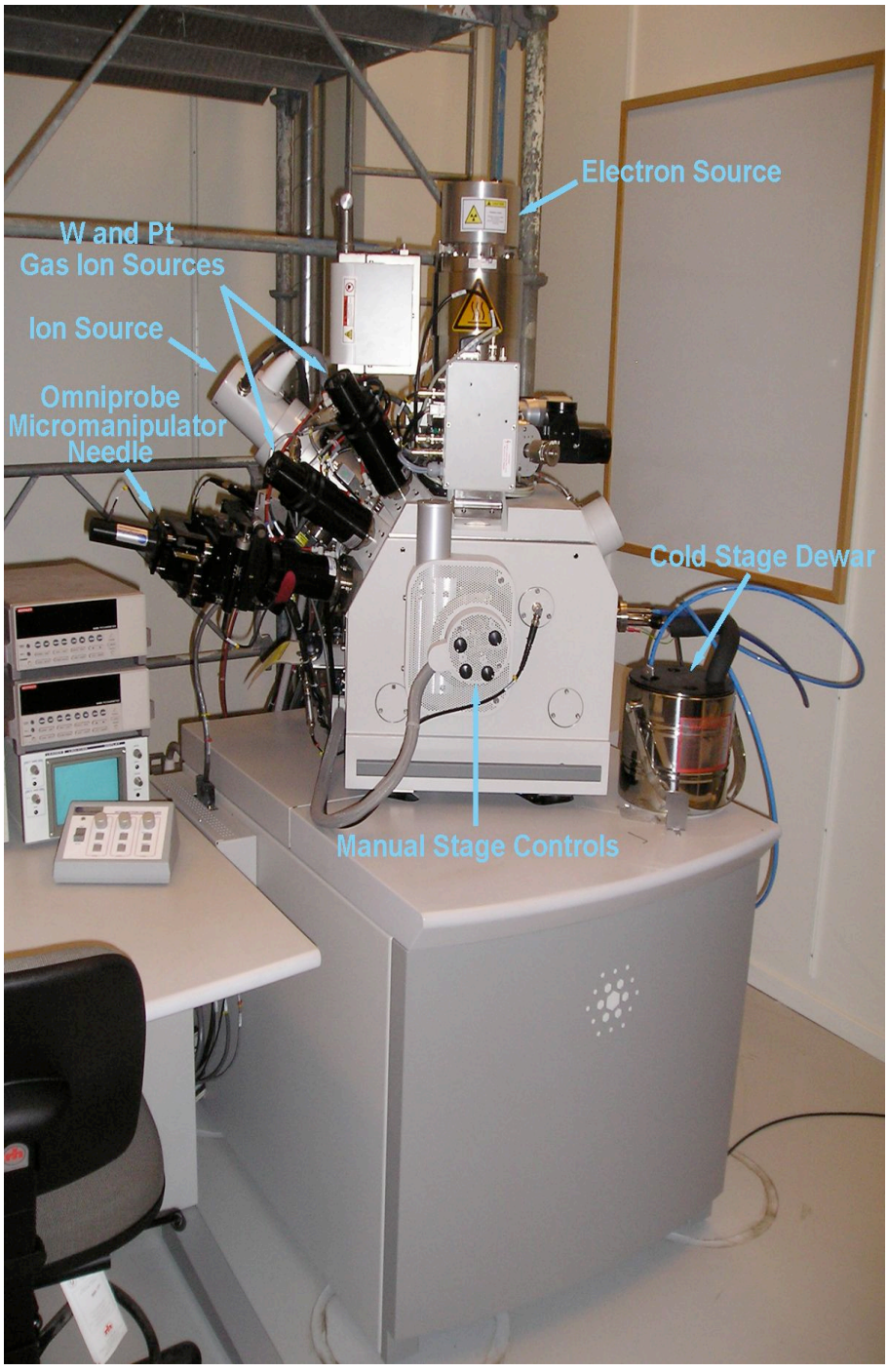

Figure 1.8: The focused-ion beam (FIB) tool geometry is similar to an SEM. The ion column is 52˚ to the electron column. Accessories, such as GIS deposition needles and micromanipulators, fit in remaining ports.

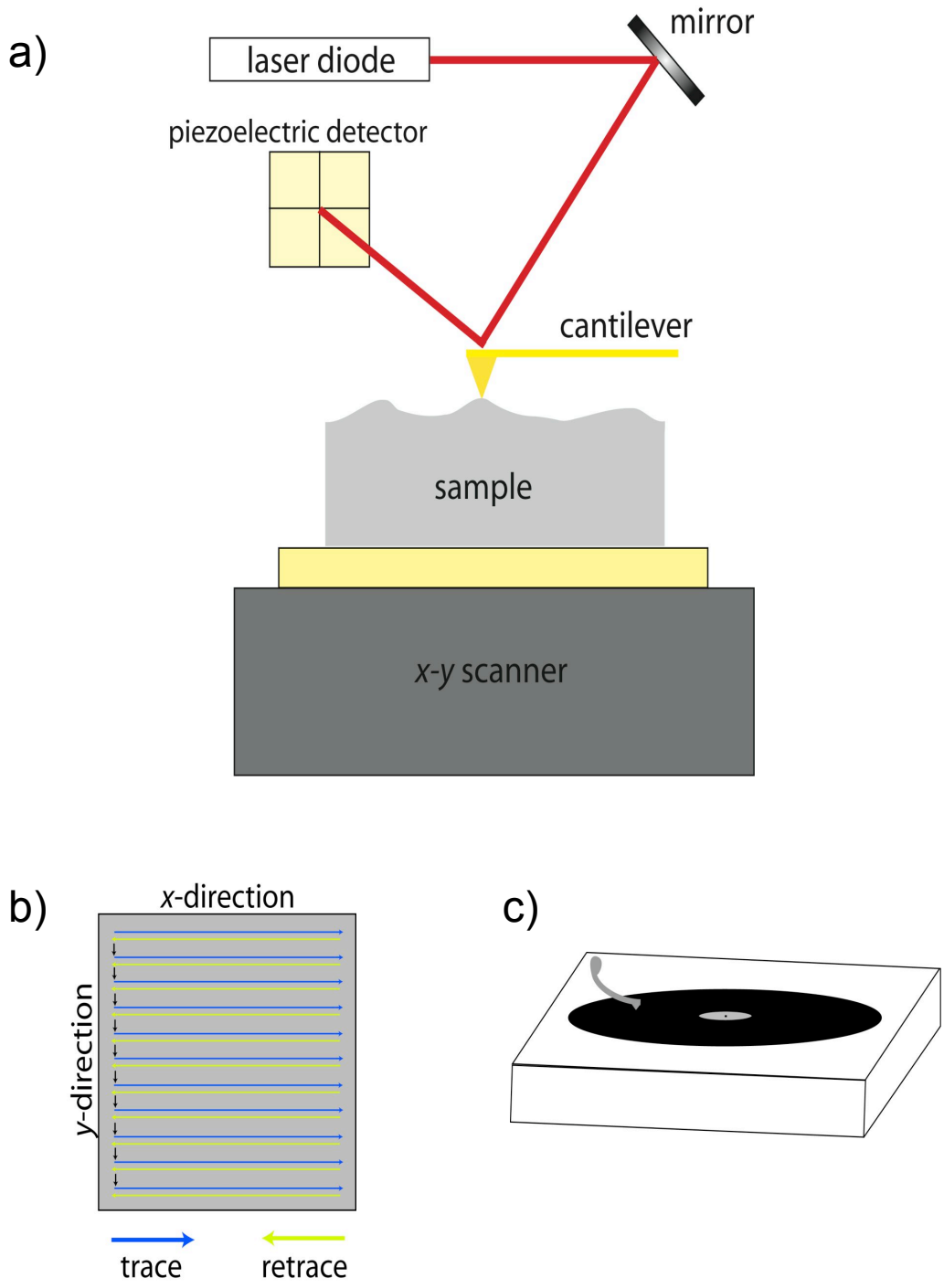

Figure 1.9: (a) SPM geometry involves reflecting a laser off of a moving cantilever to measure various signals on the sample surface. (b) The cantilever scans back and forth over the surface, similar to how a record player operates (c).

Chapter 2: Using AFM to monitor alumina surface facets

2.1 Introduction

Upon first look, faceting and surface reconstruction seem to be relatively straightforward concepts in materials science. Despite decades of research, faceting is not well understood in ceramics. Mullins[1] long ago proposed a theory for facet formation, but to date, has yet to be confirmed. Surface faceting can lead to an understanding of mass and energy transport within a material. Transport properties are especially important in understanding surface reactions, catalysis and gas absorption in fuel cells. Grain boundaries are often faceted and the presence of facets can alter the transport rate along grain boundaries and change grain boundary migration.

The theme of this dissertation is surface energy-driven mass transport. Alumina was chosen as the material of interest, since it is a model ceramic. Al_2O_3 is a two-component oxide with high anisotropy and has a mix of ionic and covalent bonds. The point where the vapor is in contact with the edge formed by two crystallographically different planes is the simplest form of a triple point. When equilibrium is reached, all of the forces acting at that point will be balanced. When the forces are out of balance, mass transfer will occur in an attempt to regain equilibrium.

This chapter establishes two techniques for the rest of the dissertation. The first being mapping with both visible-light microscopy (VLM) and atomic-force microscopy (AFM) in order to return to the exact region of a specimen after a series of heat treatments. With each mapping, the same set of magnifications are used to aid in finding the features of interest. VLM mapping before AFM imaging allows the same feature to be found using the visible-light optics coupled with the AFM. The second technique is the use of fiducial markers to return to the same features that are smaller than conventional VLM resolution. Here, a gravity-loaded hardness tester was used to place indents in a square array on single-crystal alumina. The indentation force and Vickers-

type tip used were always the same, making the fiducial markers reproducible. The as-received wafer has been polished, so no features are visible with VLM. The fiducial markers are large enough to be seen in the VLM and can be seen after a series of heat treatments, since the indents are too deep to heal quickly.

2.2 Background

Ceramics are difficult to understand because of their unique bonding characteristics. Each ceramic structure consists of a different combination of ionic and covalent bonding. In addition, a more covalently-bonded structure will be more rigid due to the directionality of the bonds. The ionic-to-covalent bond ratio determines how reactive the oxide will be.[2] Thus, each ceramic material has unique surface characteristics, making generalizations of ceramics impossible. While the overall ceramic must be neutral to maintain charge and stoichiometric balance, local space charge may exist. Impurities attracted to the localized charge can dramatically change behaviors that occur at surfaces; surface reconstruction and second-phase wetting are two examples.

Facets can form on ceramic surfaces in order to lower the overall energy of the surface. Each surface has an associated surface energy. Surfaces will have a particular crystal termination and associated surface energy. Crystal termination is defined by surface preparation and stability critieria.[2] The most stable surface planes are those which have the fewest bonds broken and are the most densely packed. Surfaces can relax, rumple or reconstruct in order to lower the surface energy.[2] All three of these processes create more surface area, which is usually unfavorable. However, if newly formed planes have a total lower energy than the original surface, despite the formation of more surface area, the surface will reconstruct into facets. Relaxation and rumpling occur to accommodate the local charge and stoichiometry. Facets are made of two or more crystallographic planes and form in one of two morphologies: (A) terraces-and-ledge or (B) hill-and-valley, illustrated in Figure 2.1.

Surface energy dictates the equilibrium shape of crystals at all length-scales, including nanostructures. For example, whiskers are one-dimensional structures that have a low

surface energy on one plane, but a large surface energy on a plane 90° to the first.[3] Crystal growth is restricted in the direction perpendicular to the high-energy plane, but favored in the direction perpendicular to the low-energy plane. As a result, long one-dimensional structures form.

As mentioned above, impurities can be attracted to the localized charge and dangling bonds, and likewise, alter local surface energy. [4] Cleanliness is therefore an important factor when considering ceramic processing. Surfaces can have different local structure than the bulk, since the atoms at the surface are constrained in only two directions and may relax in the third.[2] Impurities can either obstruct or promote the relaxation. The atmosphere in which surfaces are exposed to also affects relaxation and rumpling by allowing gas species, such as hydroxyl groups, to satisfy local surface-charge imbalances.[5]

Sintering is the act of two crystals of material thermally treated in order to join the crystals and create bulk material.[6] Diffusion at interfaces and surfaces allow the individual crystals to join and reduce the overall energy of the system. The initial surface-to-volume ratio is one factor that determines the rate of sintering. Grains will grow, porosity is reduced and material strength improves during sintering.[7] Sintering allows the joining of ceramic parts at a large production scale. Facets at interfaces play a crucial role in the diffusion of material during sintering.

These behaviors in occur at high temperatures. Few characterization techniques are capable of monitoring surfaces at high enough temperature while the surface behavior is occurring. During the time necessary to reach temperature, surface behavior can begin or be different than that at the desired temperature. The same is true for when a surface is cooled to room temperature from a high temperature. Thermally quenching the ceramic and observing the surface *ex situ* is the only method available to observe high temperature behaviors. The behavior must be locked-in during the quench to insure the behavior is not be altered during cooling.

Epitactic growth of materials on ceramic substrates often occurs at temperatures higher than room temperature. Elevated temperatures during deposition can initiate surface reconstruction on unstable planes and change the resulting film quality.[8] Specific planes of substrate materials are used at surfaces to promote growth of particular orientations of the deposited material with the least amount of misfit. The lattice misfit is usually small and results in few dislocations and defects in the growing film. Facets produce nucleation points for further growth during traditional crystal growth from melts. As Ling, et al.[9] showed, in order to grow pristine films, interactions at the new interface must be understood.

Studying surface behavior can provide a clue to what occurs in the bulk at grain boundaries, phase boundaries and dislocations. Surface studies are usually much easier to conduct, since the behavior occurs over an area and not within a volume.

2.2.1 Surface energy and faceting

Surface tension is defined as the energy needed to form the surface.[3] Surface tension and energy are often used synonymously when discussing solid bulk ceramics, but one should use care when interchanging the terms. While surface tension and energy have the same units of energy per area, the terms describe two different things. The Eötvos rule states that as temperature increases, surface energy will decrease.[3] Liquids have a lower surface energy than solids, but do not have an associated surface tension. Surface tension implies that a force is present at the surface due to the stress locked within the crystal. Surface energies are nearly always positive and are calculated by combining Madelung interactions and short-range repulsion between atom pairs.[2] Relaxation of these terms changes the surface energy of planes and changes which crystallographic orientations are the most stable.

Wulff[10] and Herring[11] are reported to give detailed explanations regarding how crystal reconstruction is governed by surface energy. As described previously, reconstruction describes the process of a high-energy surface orientation changing into two or more different orientations to lower the total surface energy, even at the expense of forming

more surface area. Herring described why the terrace-and-ledge morphology may be preferred over hill-and-valley formation based on the Wulff construction of the surface energy (γ) plot for a crystal.[11] The Wulff plot of a material is a three-dimensional representation of surface energy plotted against orientation.[12] Moore[13] further defines stepped surface morphologies by defining "simple" and "complex" planes; the facet plane of low-index orientation is defined as simple, while the other plane, usually of random orientation, is defined as complex. In addition, the simple plane has the lowest energy, while the complex plane is of lower energy than the original surface, but not as low as the simple plane. Figure 2.2 illustrates the lowest energy facet configuration. Because of the energy change, Williams and Bartelt[4] and Straumal, et al[14] considered faceting at surfaces and grain boundaries to be a type of phase transformation.

Moore[13] used these definitions and the original surface normal of the as-received surface in silver to predict whether {100} or {111} simple planes would form after thermal etching. He concluded that the angle made between the original surface and the low-index poles would determine which type of simple plane would form. Further, the angle (β) in which the complex plane makes with the original surface plane can be used to measure the ratio between the total surface energy per area of the complex plane (γ_c) after thermal etching to the surface energy before etching (γ_t), as seen in equation 2.1. With equation 2.2, Moore also postulated that the simple angle (α) could predict whether surface reconstruction would occur at all. The surface energy per area of the simple plane (γ_s) is compared to the surface energy of the complex plane after thermal treatment.

$$\frac{\gamma_t}{\gamma_c} = \frac{\cos(\alpha+\beta)\sin\beta + \sin\alpha}{\sin(\alpha+\beta)} = \cos\beta \qquad [2.1]$$

$$\alpha > \arccos\frac{\gamma_s}{\gamma_c} \qquad [2.2]$$

Others have looked at the surface reconstruction behavior of additional alumina surface orientations. Antonik and Lad[15] found that the cleaved $(10\bar{1}2)$ surface forms jogged facet edges corresponding to the cation-anion bond coordination.

Mullins[1] proposed the theory of surface facet formation. The theory is based from experimental observations of Ag, including Moore's[13] study, and related faceting to Mullins' previous work on thermal grooving.[16] He derived the governing equations for surface facet nucleation and growth for three cases based on orientation, surface energy and the Wulff plot[10]: 1) evaporation and condensation, 2) surface diffusion and 3) volume diffusion. Mullins recognized that the environment and vapor pressure in which annealing took place could potentially change the faceting behavior or lead to facet decay. He also believed that surface diffusion dominated the beginning stages of faceting, and diffusion on the simple surface occurred at a different rate than that of the complex surface. Surface diffusion would be facilitated through vacancy transport. Mullins considered diffusion across the facet and along the length of the facet, and proposed that the limiting condition governing transport could be determined by the rate of facet growth and the facet profile. Nucleation of facets was proposed to occur at local fluctuations of orientation at the surface and further growth was localized. He made three assumptions in his calculations: 1) only a single facet was considered and facet domains had not yet formed, 2) the facet is long and slender and can be treated in two-dimensions and 3) the slope of the complex surface with respect to the original surface is small, leading to semi-quantitative results.

Mullins also proposed that facet lengthening occurs at the facet tips, but that widening occurred at an ever-decreasing velocity. The widening velocity depends on the distance from the tip. In addition, the facet width or wavelength was defined as X^*. With small X^*, surface diffusion would dominate. When facets have grown large enough, evaporation and condensation becomes the dominating transport mechanism. Volume diffusion is thought to not dominate in any regime.

However, surface defects may change the local space charge of surfaces and surface steps.[17] To date, no one has been able to account for point defects in models to determine the exact effect on the surface energy since an infinite number of possibilities exist.

Impurities tend to segregate to surfaces, since the energy of sitting on a surface is lower than sitting in the bulk.[17] The impurities will change the local surface energy and charge. Therefore, cleanliness is key when studying surface reconstruction.

2.2.2 Vicinal surfaces

Vicinal surfaces are defined to be those cut only a few degrees away from a stable, low-index orientation.[4] The off-cut may be from imperfect dicing of the boule or formed during annealing the surface to correct polishing damage. Vicinal surfaces typically form a terrace-and-ledge morphology when thermally treated to form the equilibrium crystal shape (ECS). At low temperatures relative to the roughening transition, vicinal surfaces appear stable. However, at high temperature, vicinal surfaces want to lower their energy and roughen in the same manner as high-index surfaces. When vicinal surfaces reconstruct, a high vapor pressure and/or surface diffusion rate must be present to facilitate large-scale changes. Sub-surface damage at may facilitate the diffusion.

Prestipino, et al.[18] modeled the formation of vicinal surfaces as having a preroughening state based on the interactions and repulsions of surface kinks. In their model, vicinal surfaces were found to be either flat, preroughened due to short-range repulsion between parallel surface kinks, or exhibit long-range reconstruction and driven by surface energy. Kurnosikov, et al.[19] proposed a step bunching mechanism as a precursor to faceting on the (0001) alumina surface when heated to 1500˚C for as much as 4 h. Step bunching is described as "a local change in step density." The step bunching eventually disappears by forming a new step at equilibrium. Newly formed steps are smaller in height than the step bunches that form the facet.

Facet appearance in the *x*-*y* plane (straight or wavy) may be predicted by the facet-surface orientation relationship and the wafer miscut angle.[19] The larger the miscut angle, the more wavy the (0001)-surface facets became, deviating from the sharp terrace and ledge morphology[19]. Therefore, the resulting surface energy moves away from a low-energy cusp on the surface energy plot.[11] However, miscut [0001]-surface normal samples still favor the $[11\bar{2}0]$ or $[10\bar{1}0]$ direction.[19] Homogeneous and local faceting may occur. In addition, the resulting morphology of surface reconstruction is dependent on the atmosphere in which the thermal etching occurred.[20]

2.2.3 Uses of faceted surfaces

Faceted surfaces can be used in the microelectronics field[14, 21] to produce ordered nanostructures. Self-assembly of nanoparticles and structures on surfaces often require a template. Templated growth is an alternative, less expensive method to lithography. Ravishankar, et al.[22] have used facets on the *m*-plane of alumina as a template for vapor deposition of Pt nanoparticles in a regular array on the facet ridges. The solid-state droplets are uniform in size and equally spaced. Other non-reactive metals have been deposited on alumina surfaces and shown to order depending on the surface orientation.[23] By using $(10\bar{1}0)$ (*m*-plane) α-Al_2O_3 as a substrate, Fe nanostructures can be made to self-assemble. These nanostructures have magnetic properties dependent on substrate orientation.[21] Nanopatterning in this manner has exciting possibilities for catalysis and magnetic recording. The local charge and dangling bonds at a facet tip and/or ridge can provide the necessary conditions for catalysis. The faceted surfaces can also give a better epitactic relationship for thin-film growth.[24]

Faceted basal plane alumina has also been used to grow ordered ceramic structures and induce twin boundaries in epitactic NiO, Cu_2O and TiO_2 films grown using pulsed-laser deposition (PLD).[25] Faceting and surface reconstruction can begin to describe faceting at grain boundaries and the resulting complex grain boundary structure.[14]

2.2.4 Growth of faceted surfaces

Facet growth and coalescence is proposed to occur by material diffusing along the step edges[19] or along the length of the simple surface plane to and from the complex planes.[13] Impurities, orientation inhomogeneities and dislocations are believed to be nucleation sites for facet development.[13] Kinetics at the surface ultimately decide the facet size.[4] Along with temperature, the diffusion length atoms need to traverse will define the facet size. Similar to dislocation lines[3], kinks form on the surface, allow steps to move and provide nucleation points.

2.2.5 Alumina

2.2.5a Crystallography

Al_2O_3 has many properties that make it a desirable material for several applications. Al_2O_3 is commonly referred to as alumina or corundum. When doped with Cr^{3+}, single crystal Al_2O_3 becomes ruby; sapphire results when Ti^{2+}, Ti^{4+} and Fe^{2+} are used to dope the single-crystal.[3] Alumina has a high hardness (9 on the Mohs Hardness scale)[3], making it an excellent material for watch bearings and polishing media.[3] The high melting point, ~2020˚C, makes alumina a good choice for refractory applications and crucibles. Electronic devices contain alumina as an insulating layer and dielectric material. Sodium-vapor lamps are made from MgO-doped polycrystalline alumina. The $(\bar{1}012)$ plane of alumina is used for Si growth, since the lattice mismatch is minimal.

Alumina has a rhombohedral crystal structure (Figure 2.3) and belongs to the $R\bar{3}c$ space group. The lattice parameters are a = 5.1284Å and $\alpha = 55.28^{\circ}$.[26] The density of alumina has been measured to be 3.96 g/cm^3.[3] Traditionally, alumina is described in the hexagonal coordinate system; the positions of the oxygen ions in the lattice cause the hexagonal coordinates to be more convenient than the rhombohedral system for describing the structure in most cases. When the structure is converted to a hexagonal unit cell, the lattice parameters are a = 4.7589Å and c = 12.991Å.[26] As a consequence,

Miller-Bravais indices, a.k.a. 4-index notation, is used rather than the traditional 3-index Miller indices to describe directions and planes in the unit cell. Table 2.1 and figure 2.3b describe the planes in alumina most often used and lists commonly used notation. The oxygen sublattice fills the hexagonal unit cell atom positions. The Al^{3+} ions sit in the octahedral interstitial sites. To satisfy stoichiometry, only two-thirds of the octahedral positions are filled. To compensate for the charge imbalance, the Al^{3+} cations sit slightly off of the exact octahedral sites.[3] As a result of the Al^{3+} cations trying to charge compensate and move far away from each other, surface relaxation occurs. Relaxation of surfaces results in lower surface energy and is different for each crystallographic plane, i.e. (A) *c*-plane (Figure 2.4a), (B) *m*-plane (Figure 2.4b). Bench, et al.[25] summarize the possible surface terminations of the basal plane and propose two possible Al^{3+} terminations to be the lowest-energy at the surface.

2.2.5b Alumina surfaces studies

The basal plane of alumina is known to facet in a terrace-and-ledge morphology, made of the $\{11\bar{2}0\}$ and $\{10\bar{1}2\}$ planes. Planes making up facets at grain boundaries or in the presence of a liquid- or glass-phase can be different from a faceted surface in ambient conditions due to the change of surface energy, despite having the same nominal vicinal surface initially. The large anisotropy alumina has creates different facet behavior on the major crystallographic planes. The low-index planes of alumina have a range of unrelaxed surface energies, with the *m*-plane having the highest surface energy. (Table 2.1)[17] The high surface energy implies that the *m*-plane is the least stable and will reconstruct into planes with lower energy. The simple plane formed during the *m*-plane reconstruction is the $(10\bar{1}2)$,[27] which relaxes the least and is the most stable plane in alumina.[17]

Above 1200˚C, alumina has been found to form surface vacancies, which may facilitate reconstruction.[5] Hartman[28] calculated the attachment energy for each of the major planes in alumina. The attachment energy is related to the surface energy and is obviously an important factor during crystal growth.

The average surface diffusion for alumina was determined by collecting data from several researchers using different experimental conditions.[29] The surface diffusion coefficient, D_s, given in equation 2.3, can only be considered an average, since diffusing material will move at different rates on different surface orientations.

$$D_s\ (cm^2\ sec^{-1}) = 4.05 \times 10^5 \exp -(452\ kJ\ mol^{-1}/RT) \qquad [2.3]$$

Recently, faceting behavior of different planes of alumina was studied when exposed to wet atmospheres. The behavior was shown to drastically change depending on the humidity levels and the degree of hydroxylation.[5] This observation agrees with previous studies,[30] since hydroxyl groups act similar to impurities.

2.2.7 Previous faceting studies

2.2.7a LEED

Low-energy electron diffraction (LEED) has been used to monitor the stability of surface orientations.[4] LEED allows surface periodicities to be interpreted as a projection of the bulk unit cell in reciprocal space. However, LEED does not allow direct observation of surface evolution, and therefore, is unsuitable for the present work. Surfaces also need to be sputtered under UHV conditions before imaging, which will alter surface structures. In addition, LEED requires extensive quantitative modeling performed in parallel to confirm surface terminations.[2]

2.2.7b TEM

Using transmission electron microscopy (TEM), Susnitsky and Carter[31] have shown that surface structure for the low-index planes of alumina may have a different surface structure than expected from the bulk. They attributed the difference to possible contamination on the surface, introduced during TEM sample preparation, and a difference in processing temperature. In addition to traditional methods of measuring step thickness using thickness fringes in the TEM, convergent-beam electron diffraction

(CBED) may also be used to measure step heights.[27] Susnitsky and Carter[27] extended their work to complimentary TEM and reflective electron microscopy (REM) analysis. They confirmed the preferred facet planes for the (0001), (11$\bar{2}$0), (10$\bar{1}$2) and (10$\bar{1}$0) planes, summarized in table 2.1. Contrast in REM is obtained from geometric shadowing, phase contrast and step distortions, making the technique difficult. Image foreshortening from the glancing electron beam adds to complicated REM image interpretation.

Morrissey and Carter[32] showed that steps bow around surface particles, similar in manner to dislocations, by using a unique TEM sample preparation method. By growing alumina films on aluminum and chemically etching the metal away, damage-free TEM samples were made. Further heat treatment in vacuum allowed grain growth, phase transformation and step motion to be observed. They also proposed that the facets and steps facilitated grain growth.

Bench, et al.[25] used TEM to determine preferred growth morphologies of ceramic thin-films and used bright-field contrast to determine step heights of basal plane terraces. Step heights were found to equal three times the unit cell height.

TEM using a 400kV accelerating voltage by Bursill, et al.[4] found that the electron beam irradiation of alumina was capable of inducing surface reconstruction. The electron beam also induced positive polarity at the surface. However, the TEM can still be used to determine the surface-termination of the reconstructed surfaces if a lower kV microscope is used.[33]

In situ heating of vicinal surfaces to form facets would be the ideal experiment. However, the maximum temperature heating-holders for conventional TEMs can reach is only 1300˚C.[34] In addition to this and possible beam damage, the kinetics governing diffusion in alumina are too slow to perform experiments in a reasonable time frame. Also, since the surface energy will be altered by being in a different environment, the reducing atmosphere inside the TEM column is often not desirable for surface studies.

2.2.7c AFM

Atomic force microscopy (AFM) has been a popular surface imaging technique, since the technique does not require difficult sample preparation, is non-destructive and is ideally suited for surface-topography analysis. In addition, using AFM does not alter any intermediate surface reconstruction by inducing beam damage or requiring any surface-energy-altering coatings.

Several groups have used AFM to determine surface morphologies on alumina surfaces. Antonik and Lad[15] used AFM to look at the surface reconstruction of the $(10\bar{1}2)$ alumina plane. Steps were measured to be 3.5 Å high and 800Å wide. However, the evolution of facet formation was not monitored and anneals were done in vacuum at 500˚C. Barth and Reichling[20] used dynamic scanning force microscopy, a technique related to AFM, to look at the reconstructed (0001) alumina surface. Atomic resolution confirmed the $(\sqrt{31} \times \sqrt{31})R+9^{\circ}$ (0001)-surface structure and determined that defects terminating at the surface stabilize the surface. Kurnosikov, et al.[19] used AFM to show the effect of surface miscut on the terrace-and-step morphology of the basal alumina plane. They found that misorientation of the vicinal surface by less than 4˚ significantly alters the resulting step structures. Step-bunching was also found to occur before step faceting.

2.2.7d Key observations of changes

Chalmers, King and Shuttleworth[35] reported some of the first observed surface facets in Ag. Faceting occurred when Ag was heated in oxygen, but disappeared when reheated in nitrogen atmosphere. Because of the reversibility, early theories proposed that surface oxidation was driving facet formation. However, the fact that the annealing atmosphere changes the surface free energy was later correctly proposed.[35] In addition, damage remaining after mechanical polishing was thought to nucleate faceting. Processing temperature was shown to affect the facet morphology, but the original surface orientations were not known for a conclusive comparison. Studies performed

before the wide availability of electron microscopy were unable to determine surface orientations of specific grains in a nondestructive manner. *In situ* heating of Ag showed that faceting began when held at temperature and not during cooling.[35] The facets were shown to lie parallel to specific crystallographic directions using polarized visible light.

Mullins[1] gave an extensive theory of how facets form, but based his calculations on Ag surfaces. He did not treat ceramic surfaces in his model, nor did he look at facet domains. His model only described a single facet before additional facets nucleated to create a facet domain.

Heffelfinger, et al.[36] was the first to look at the *m*-plane surface and propose a method of surface faceting in ceramics. Faceting was monitored after thermal anneals of varying time (no more than 8 hours). The simple plane of facet structures was determined by cross-section TEM to be $(1\bar{1}02)$. Several stages during the faceting process were proposed: 1) nucleation and growth of individual facets, 2) formation of facet domains and 3) coalescence and coarsening. Random areas of the surface were looked at and used to infer the faceting mechanism. The facet width X^* was shown to behave differently than expected from Mullins'[1] theoretical work. Facet domains were proposed to nucleate from surface undulations near individual facets. In particular, the undulation opposite the groove formed by the simple side of the facet was proposed to be the nucleation point for the next facet. This facet/groove geometry was later modeled to be a stable kink-antikink formation mechanism in surface-tension-anisotropy-induced surface reconstruction.[37] As the facet grows in size, a facet domain with kink/anti-kinks must form to maintain the dynamic reconstruction process.

Heffelfinger[36] proposed the complex plane gradually changes until the $(10\bar{1}\bar{1})$ plane forms and a hill-and-valley surface morphology results, implying that β is not at equilibrium. Facets were anticipated to lengthen at the facet tips until additional facet domains were reached. Facet alignment, in the [0001] direction, and coalescence could then take place. With further annealing, the entire surface forms a hill-and-valley structure. Figure 2.5 illustrates the equilibrium hill-and-valley structure with respect to

the Al_2O_3 hexagonal unit cell. Coalescence and growth continues at this point, but at a much slower rate, suggesting that the facet tips are responsible for the surface reconstruction. The finite-sized facets eventually cover the surface and result from the nucleation and eventual impingement of additional facets on the original facet.[38] However, the same individual facet or facet domain was never returned to after a series of thermal treatments to confirm the proposed model.

Heffelfinger, et al.[39] also looked at surface-step formation on the vicinal (0001) plane of alumina using AFM. Early observation (after 10 min at 1400˚C) of surface annealing showed the formation of terraces and ledges with an average height of 0.21 nm, corresponding to a *c*/6 ratio (*c* is the unit cell height in the [0001]). With further annealing, these surface steps grow to have heights 2 or 3 times that of *c*. Saw[40] later confirmed his work.

While many studies[19, 20, 26, 41] have looked at the (0001) (*c*-plane) orientation of α-Al_2O_3, little has been done on the (*m*-plane).[24, 26, 36] A study of alumina for substrates confirmed Heffelfinger's results using TEM and selected-area diffraction (SAD).[24]

2.3 Experimental

2.3.1 Sample surface preparation

As-received polished single-crystal alumina wafers (supplied by Crystal Systems or Union Carbide), with a nominal $\{10\bar{1}0\}$ surface orientation, were etched using aqua regia (50% HCl: 50% HNO_3) for a minimum of 2 hr. The wafers were diced into 2x2 mm^2 pieces using a diamond-embedded wafering saw. Cut samples were marked using a Buehler gravity-loaded hardness tester. Four Vickers-type indents, spaced 30 μm apart, were made to form a squared-off area using 25 g of force. (Figure 2.6) Prior to every thermal treatment, surfaces were cleaned in acetone and methanol baths for 10 minutes, respectively, using an ultrasonic cleaner. Surface cleanliness is necessary for this study. Any residue or impurities on the surface will affect the surface tension, and

thus, the resulting surface reconstruction. This procedure is identical to the one followed by Heffelfinger, et al.[36]

2.3.2 Thermal treatment

Each thermal treatment of samples was conducted in the same manner, but the length of thermal treatment varied. The sample was placed on top of a large piece of single crystal inside an alumina crucible inside a box furnace. This crucible was placed inside another alumina crucible and packed with high-purity alumina powder. Boats of alumina powder were placed in the furnace near the crucibles and served as an impurity getter. Figure 2.7 illustrates the crucible set-up used inside the box furnace. The temperature was ramped to 1400˚C at 20˚/min. The furnace was kept in air atmosphere. The initial thermal treatment was programmed to last 10 minutes. However, because of the time lag between the controller and furnace, the actually time at 1400˚C was only 6 minutes. Immediately after the controller shut off, the samples were air-quenched to lock-in the high-temperature behavior. Subsequent thermal treatments lasted only for 1 or 2 minutes, where dwell time did not start until the temperature was stable at 1400˚C. Samples were, again, quenched in air. The short initial thermal anneals allow the vicinal surface and facet nucleation to be observed before significant growth and coarsening occurs. Prior to the first heat treatment, wafer orientation was confirmed using traditional XRD and GADDS.

2.3.3 AFM used in this study

AFM imaging was used before any thermal treatments and after every subsequent treatment to monitor changes on the surface. Two types of AFMs were used in contact mode: 1) Digital Instruments Multimode using Nanoscope 5 software and 2) Park Systems XE-70 using XEP data collection and XEI data analysis software. Images were collected using Si cantilevers with a minimum force constant of 0.25 N/m, 30˚ cone angle and <10.0 nm tip radius of curvature. The cantilevers were backside-coated with Al to improve reflectivity.

Marking the surface allowed the same region, and therefore, the same facets to be watched as they form and develop through a series of thermal treatments. Three regions of each sample surface were monitored after each thermal treatment; two regions were those marked using Vickers indents and one region of the surface was randomly chosen. When doing AFM, the marked regions were first found using the visible-light optics built into the AFM. A large Vickers indent was made using 100 g of force approximately 100 μm from the square region of interest. The large indent aided in finding the region of interest, as illustrated in figure 2.8.

The XE-70 AFM is particularly good for this type of study. Large scans need to be initially made to find the region of interest and the scan size gradually decreased to characterize the surface reconstruction. However, traditional tube scanners often create a "bowing" or "pendulum" artifact in the image causing the image edges appear to be higher than the center. The XE-70 has a linear *z* scanner decoupled from the *x*-*y* scanner eliminating this type of artifact. In addition, the laser and visible-light optics follow identical paths and are aligned parallel with the *z* scanner, allowing for more precise alignment of the laser. Finally, the XE-70 *z* scanner may be operated in both open- and closed-loop modes. This feature allows high-resolution images of small features to be collected in addition to large scans with little noise.

2.4 Results

Samples from several *m*-plane wafers were monitored for their surface behavior. While all samples experienced accelerated facet formation, the kinetics for each sample at the beginning of surface reconstruction were different depending on the local miscut of the surface, resulting in different behaviors observed in the initial stages of reconstruction. Figure 2.9 proves the as-received surface was initially flat.

2.4.1 Primary facet formation

In most regions, faceting began as small hill-and-valley shaped facets after the first heat treatment. Only primary facets were observed at all stages. The facets were observed to

lengthen and grow in height with further heat treatment. Section analysis indicated that the facets initially have a rounded appearance. As a facet grows in size with further heat treatment, the simple and complex structure that is characteristic of *m*-plane facets becomes more evident.

The initial facets were found to behave similarly, but at slightly different stages across the sample surface depending on local miscut and distance from fiducial markers. Significantly smaller facets appeared to reside between large facets. These small facets were eventually absorbed as additional heat treatments were conducted by larger facets lying next to them. Figure 2.10 shows the disappearance of one facet, while a nearby facet grows in width. The facets continue to lengthen until the tips meet other facet tips. When they meet, one facet forms a bump while the adjacent facet tapers towards the original surface. With time the bump becomes jagged and eventually wraps itself around the adjoining facet. Figure 2.11 shows the actual process, while figure 2.12 illustrates the coarsening mechanism.

2.4.2 Secondary facets and vicinal surface formation

Where local miscut from a perfect $(10\bar{1}0)$-surface was greater than at other regions on the wafers, secondary facets formed in addition to the primary *m*-plane facets that are expected. By monitoring the exact same set of facets after a series of heat treatments, the secondary facets were shown to form vicinal surfaces before the primary facets formed. Figure 2.13 shows how the surface changed. The regions close to indents faceted quicker (bottom-right corner) than areas far away from the indents (top-left corner) due to the subsurface damage near the indents.

After the first heat treatment, an 'orange-peel' structure was observed. The surface had flat terraces where the edge protruding from the surface was rounded. Step bunching of tiny facets were observed where these terraces met. Section analysis of this morphology is shown in figure 2.14.

With an additional minute at 1400˚C, the 'orange-peel' structure had completely disappeared and facets were observed over the entire surface. These facets had a short length and were roughly 1.75 nm in height. Section analysis of the same facets showed that the facets had a rounded appearance, rather than a sawtooth morphology. The facet being monitored throughout heat treatment was shown to grow to roughly 7.0 nm in height after an additional minute at temperature (8 min total thermal treatment). All of the facets in the surrounding area were observed to grow in height and length, and still had a rounded appearance. Figure 2.15 shows the time series and morphology development of the same region, while figure 2.16 shows the section analysis after each anneal.

After monitoring the same region after a total heat treatment of 30 min, the short step bunches had completely disappeared and the expected *m*-plane surface morphology was observed. (See figure 2.17) Similar to surfaces that only exhibited primary faceting, small facets were observed to be present between the large facets. Section analysis of the region of interest showed the facets had grown to about 10.0 nm in height and had begun to take on the more expected sawtooth appearance. Significantly fewer small facets exist and long facets with sharp facet tips, similar to Heffelfinger's observations,[38] existed.

2.4.3 Healing of fiducial markers

The fiducial markers were monitored using AFM and were found to heal with thermal treatment. Prior to heat treatment, radial cracks were observed to propagate from all four of the Vickers indent corners into the bulk single crystal material for every indent. In some instances additional cracks were observed roughly 45˚ to the corner cracks and perpendicular to the sides of the indent. Figure 2.17 shows what a typical fiducial marker looked like before and after an anneal. The radial cracks were observed to completely heal quickly if the crack was parallel to the facet direction, i.e. the crack occurred on the {0001}. The hillocks surrounding the indent were found to become smaller with time and the indents appear to heal.

Faceting was first observed to occur near the indentations. In particular, the area surrounding the radial cracks reconstructed before the initially smooth surface in the center of the marked region.

The radial cracks not aligned with a particular crystallographic direction healed much slower. The cracks also provided a model sample to study thermal groove formation. More on thermal grooves can be found in chapter 3 of this dissertation.

2.5 Discussion

Because of tip artifacts during AFM, measurements of heights and angles are not precise.[42] However, the measurements give the general behavior and are easily compared to similar work by others using AFM.

Lee and Lagerlof's[26] review paper gives all of the required crystallography information for alumina. In particular, they calculated the angles made by the $(10\bar{1}0)$ *m*-plane with the simple $(10\bar{1}2)$ *r*-plane and the complex $(10\bar{1}\bar{1})$ planes to be 32.4˚ and 17.6˚, respectively, illustrated in figure 2.5. All crystallographic parameters used here where taken from this paper.

Surface reconstruction of the *c*-plane was proposed to be aluminum terminated, creating a local positive surface charge.[41] The short Al-O bond is the most stable surface configuration. The surface terminations shown in figure 2.4 will have an effect on surface reconstruction. Dangling bonds will try to move in order to lower the overall surface energy.

2.5.1 Primary facet formation

Samples that exhibited primary faceting only allowed monitoring of facet coalescence. For the first time, a model can be proposed, based on experimental observation of the same set of facets, describing how facets coalesce over time at elevated temperature. Facets were also found to grow at the expense of neighboring facets. These observations

give insight into the earliest stages of surface reconstruction. Part of surface reconstruction is the widening of facets with time. Figure 2.10 shows how this process occurs. The marked facets in 2.10a consume the small facets to the left of the markers to form one wider facet in 2.10b. The complex plane is dynamic, and therefore can move to combine with the complex plane of the neighboring facet.

Williams and Bartelt[4] describe two possible geometries for facets: 1) sharp edges and 2) rounded edges. As the temperature increases, rounded edges are preferred. The transition from sharp to rounded facet edges implies that a distinct roughening transition temperature does not exist; reconstruction to form the equilibrium crystal shape (ECS) at the surface occurs within a temperature range. The section analysis in figure 2.16 shows that the facets evolve from a sharp facet with a corresponding groove to rounded facets. The original sharp facet's groove is a nucleation point for more facets.[36] The rounded facets are indicative of the surface transitioning from a vicinal surface to a faceted surface. This transition is confirmed in figure 2.17, where the facets have formed into the expected hill-and-valley structure.

2.5.2 Facet junctions and coalescence

Figure 2.12 illustrates the model proposed here for facet coalescence. Facet tips that meet during lengthening in opposite directions on the *m*-plane surface have been observed to join using a kink-motion method, similar to how dislocations move through a bulk sample on the glide plane.[43] The AFM images in Figures 2.11 show the same set of facets moving through a serious of heat treatments and confirm the following model.

After facets nucleate, lengthening begins. The lengthening eventually leads to facet tips forming in opposite directions to meet. In order to continue reconstruction to the ECS, the facets must coalesce. In some cases one or both facets must shift in order to have the facet pair in registry with each other. To achieve this, one of the facet tips will form into a kink. With longer time at temperature, this kink becomes more jagged until the facet tip meets the edge of the adjacent facet. The facet kink can then migrate along the edge of the facet, appearing to wrap itself around the other facet. The complex plane of

one facet is able to easily merge with the simple plane of the other facet, allowing the facets to coalesce. The result is a single facet that has a width equal to the distance between the outside simple plane and the other facet's outside complex plane. The overall height will be equal to or lower than the initial height in order to compensate for the increased width. The kink-motion mechanism allows facet coalescence and motion on the surface without requiring the entire facet to move in one energetically unfavorable process along the [0001] crystal direction.

This observation agrees well with theory. Williams[30] believes that facet motion occurs via step kinks migrating. She has proposed that the surface is under stress because of the atoms near the surface attempting to retain the crystal structure. The kink motion is driven by the release of this stress. Thus, certain orientations will experience more stress than others and the resulting reconstructed surfaces will be more mobile than surfaces experiencing a lower stress. As the temperature approaches the melting point, the surface is able to relax and kink motion is less likely. Prestipino, et al.[18] modeled the preroughening of vicinal surfaces with interactions and repulsions of kinks. Savina, et al.[37] showed that the groove which formed next to a facet, as described in section 2.5.1, was formed by a kink/anti-kink balance.

2.5.3 Secondary facets and vicinal surface formation

In some instances, vicinal surfaces must form prior to facet formation. The surface is locally slightly off of a low-index plane and must form this plane before faceting can occur. Vicinal surfaces observed in this case had an "orange-peel" appearance, and can be seen in figures 2.13 and 2.14. When section analysis is performed perpendicular to the regular surfaces, a periodic structure exists, shown in figure 2.14a. Where the vicinal surface ledges meet, facets can nucleate. Figure 2.14b shows that when section analysis of the vicinal surfaces is taken parallel to them, the vicinal surface ledges have no real form, but facets can be clearly seen to be nucleating.

As time goes on these facets evolve into expected surface reconstruction behavior. Because of subsurface damage, the area surrounding an indent serving as fiducial

marker will begin surface reconstruction much faster than an area far away from the indent in an effort to heal the damage. Figure 2.13 is unique in that it shows the time evolution from vicinal surface formation in the top-left corner to significant surface reconstruction near the indent in the bottom-right corner.

Similar to Heffelfinger, et al.'s[39] observation of small facet pairs on the *c*-plane of alumina, small initial facets were first observed on the alumina *m*-plane before formation of large facets. However, a related study[38] reports a smoothing of the *m*-plane surface when subjected to 1 h anneals at 1400˚C. The results reported here contradict this and imply that the off-cut of the nominal surface needs to be corrected by first forming a terrace-and-ledge vicinal surface. The formation of vicinal surfaces implies that the local surface tension must move through a minor energy cusp on the Wulff plot, resulting in secondary facets or vicinal surfaces, before the major energy cusp can be reached, visually represented in figure 2.19. Minor cusps on the plot describe a local energy minimum. When the surface tension has reached the lowest energy configuration at the major energy cusp, primary facets in the hill-and-valley structure will have formed. As the surface tension is lowered, intermediate step bunching begins where the vicinal ledges meet. The step bunching is the precursor to fully formed facets. The study by Kurnosikov, et al.[19] agrees with the intermediate step-bunching before facet formation. Their study on the *c*-plane is in agreement that vicinal surfaces need to be formed to correct the surface miscut prior to the formation of facets.

Mullins[1] did not consider secondary faceting in much detail. He believed that the secondary facets, which lie perpendicular to the primary facets, do not affect the primary faceting. Secondary faceting was proposed to occur much later than primary faceting because primary facets have a larger driving force and do not interrupt the secondary facets. A roughening transition temperature is believed to exist, where the formation of vicinal surfaces changes over to surface reconstruction. Nozières and Gallet have derived the equations governing this transition.[44] The presence of second-order faceting may form enough local curvature to cause the edges and corners of facets to determine the facet domain size for the initial primary facet formation.[37]

2.5.4 Healing of fiducial markers

The indents in this study had radial cracks coming from each corner. These cracks are believed to serve as nucleation points for surface reconstruction, since facets were always first observed next to the cracks.

The same technique of marking samples with Vickers-type indents using a microhardness tester has been used previously to monitor polishing depth in phase boundary studies.[45] The work presented here is the first known to use indents to return to the same region of interest. A Vickers tip is a square pyramid with an included angle of 138˚. The indentation depth is related to the diagonal length through equation 2.4.

$$h = \frac{d}{2}\tan 68^{\circ} \qquad [2.4]$$

By monitoring the healing of the indentations, we can have a better understanding of where the material from the markers is going and how the added stress accelerates the surface reconstruction. In addition, the radial cracks provide a model system for studying thermal grooving in alumina. More on this topic can be found is chapter 3 of this dissertation.

Facet formation was accelerated in this study compared to prior observations.[36] Figure 2.18 shows the significant facet formation near the indent after only 6 min at 1400˚C. The extent of surface reconstruction is determined by an incubation time dependent on the wafer's angle of miscut,[19] giving one explanation to the accelerated nucleation and coarsening. The nature of the hillocks creates more local miscut closer to the indent than far away. In addition, the indentations used as fiducial markers on the surface would create sub-surface damage, promoting surface reconstruction at a faster rate. Molecular dynamics simulations of the reconstruction of Au near the melting point found that reconstruction began in as little as 7 ps.[46] Thus, the acceleration observed here is not unreasonable.

2.4.5 Other considerations

Impurities at the surface may alter the surface energy enough that high-index planes may become much more stable than when the surface is clean.[4] However, great care was taken during this study to prevent contamination.

One critical parameter that has not been considered here is the effect of water on the *m*-plane surface. Previous studies have shown that hydroxyl groups will cluster on the *c*-plane surface[20] and alter the surface reconstruction depending on temperature and how much water vapor is present.[5] Determination of water effects during high-temperature surface reconstruction is currently not possible at temperature in atmospheric conditions, since AFM stage heating is limited to roughly 400˚C.

2.6 Summary and Future Work

Several experimental observations were seen for the first time in this study leading to important conclusions to be drawn about the surface reconstruction process. Facet kink motion allows coalescence of two adjacent facets. Local misorientation of surfaces creates dramatically different surface behavior. In cases of smaller local miscut, vicinal surfaces must form prior to the reconstructed equilibrium surface. Finally, fiducial markers can be used to monitor the same set of facets throughout their lifetime and accelerate surface reconstruction by providing nucleation points for facets.

Further work is necessary on surface reconstruction. FIB sections should be made to confirm orientations and for use in *in situ* TEM studies. The same work should be repeated in vacuum to determine how atmosphere changes surface reconstruction. Finally, purposefully miscut surfaces, of known miscut angle, should be used to study vicinal surface formation further.

References

[1] W. W. Mullins, "Theory of Linear Facet Growth During Thermal Etching" Phil. Mag., **6** [71] 1313-1341 (1961).

[2] C. Noguera, Physics and Chemistry at Oxide Surfaces, Cambridge University Press Cambridge, UK, (1996).

[3] C. B. Carter, M. G. Norton, Ceramic Materials: Science and Engineering, Springer New York, NY, (2007).

[4] E. D. Williams, N. C. Bartelt, "Surface Faceting and the Equilibrium Crystal Shape" Ultramicroscopy, **31** 36-48 (1989).

[5] R. Chandrasekharan, L. Zhang, V. Ostroverkhov, S. Prakash, Y. Wu, Y.-R. Shen, M. A. Shannon, "High-temperature hydroxylation of alumina crystalline surfaces" Surf. Sci., **602** 1466-1474 (2008).

[6] W. D. Kingery, H. K. Bowen, D. R. Uhlmann, Introduction to Ceramics, John Wiley & Sons New York, (1960).

[7] A. G. Evans, Y. Fu, in: W. D. Kingery (Ed.), Structure and Properties of MgO and Al_2O_3 Ceramics, Columbus, OH, (1984), pp. 697-719.

[8] J. R. Heffelfinger, C. B. Carter, "The effect of surface structure on the growth of ceramic thin films" Phil. Mag. Lett., **76** [3] 223-232 (1997).

[9] W. L. Ling, N. C. Bartelt, K. F. McCarty, C. B. Carter, "Twin boundaries can be moved by step edges during film growth" Phys. Rev. Lett., **95** (2005).

[10] G. Wulff, "Regarding the question of the speed at which crystals grow and shrink" Z. Krist., **34** 449-530 (1901).

[11] C. Herring, "Some Theorems on the Free Energies of Crystal Surfaces" Phys. Rev., **82** [1] 87-93 (1951).

[12] A. R. Roosen, R. P. McCormack, C. W. Carter, "Wulffman: A tool for the calculation and display of crystal shapes" Comp. Mater. Sci., **11** 16-26 (1998).

[13] A. J. W. Moore, "The Influence of Surface Energy on Thermal Etching" Acta metall. mater., **6** 293-304 (1958).

[14] B. B. Straumal, V. G. Sursaeva, S. A. Polyakov, "Faceting and Roughening of the Asymmetric Twin Grain Boundaries in Zinc" Interface Sci., **9** 275-279 (2002).

[15] M. D. Antonik, R. J. Lad, "Faceting, Reconstruction, and Defect Microstructure at Ceramic Surfaces Revealed by Atomic Force Microscopy" Journal of Vacuum Science & Technology a-Vacuum Surfaces and Films, **10** [4] 669-673 (1992).

[16] W. W. Mullins, "Theory of thermal grooving" J. Appl. Phys., **28** [3] 333-339 (1957).

[17] P. W. Tasker, in: W. D. Kingery (Ed.), Structure and Properties of MgO and Al_2O_3 Ceramics, Columbus, OH, (1984), pp. 176-189.

[18] S. Prestipino, E. A. Jagla, E. Tosatti, "Can one have preroughening of vicinal surfaces?" Surface Science, **454** 652-656 (2000).

[19] O. Kurnosikov, L. Pham Van, J. Cousty, "High-Temperature transformation of vicinal (0001) Al_2O_3-α Surfaces: an AFM Study" Surf. Interface Anal., **29** 608-613 (2000).

[20] C. Barth, M. Reichling, "Imaging the atomic arrangements on the high-temperature reconstructed α-Al_2O_3(0001) surface" Nature, **414** 54-57 (2001).

[21] J. Oster, M. Huth, L. Wiehl, H. Adrian, "Growth of Fe nanostructures" J. Magn. Magn. Mater., **272-276** 1588-1589 (2004).

[22] N. Ravishankar, V. B. Shenoy, C. B. Carter, "Electric Field Singularity Assisted Nanopatterning" Adv. Mater., **16** [1] 76-80 (2004).

[23] N. Ravishankar, C. B. Carter, "Ordered nanostructures by site-specific heterogeneous nucleation" Phil. Mag. Lett., **85** [10] 523-531 (2005).

[24] L. Wiehl, J. Oster, M. Huth, "High-resolution transmission electron microscopic investigations of molybdenum thin films on faceted α-Al_2O_3" J. Appl. Cryst., **38** 260-265 (2005).

[25] M. W. Bench, P. G. Kotula, C. B. Carter, "Influence of the nature of the (0001) alumina surface on thin film growth" Surf. Sci., **391** 183-195 (1997).

[26] W. E. Lee, K. P. D. Lagerlof, "Structural and Electron Diffraction Data for (a-Al_2O_3)" J. Elect. Microsc. Techn., **2** 247-285 (1985).

[27] D. W. Susnitzky, C. B. Carter, "Surface Morphology of Heat-Treated Ceramic Thin Films" J. Am. Ceram. Soc., **75** [9] 2463-2478 (1992).

[28] P. Hartman, "The attachment energy as a habit controlling factor III. Application to Corundum" J. Crys. Growth, **49** 166-170 (1980).

[29] A. R. Gaddipati, W. D. Scott, "Surface mass transport of alumina" J. Mater. Sci., **21** 419-423 (1986).

[30] E. D. Williams, "Surface steps and surface morphology: understanding macroscopic phenomena from atomic observations" Surf. Sci., **299/300** 502-524 (1994).

[31] D. W. Susnitzky, C. B. Carter, "Identification of α-alumina surface structures by electron diffraction" J. Am. Ceram. Soc., **69** [9] C217-C220 (1986).

[32] K. J. Morrissey, C. B. Carter, "Surface steps on α-alumina films" Journal, **41** [Issue] 137-142 (Year).

[33] M. A. O'Keeffe, "News and Views: Edge effects" Nat. Mater., **419** 28-29 (2002).

[34] D. B. Williams, C. B. Carter, Transmission Electron Microscopy: A Textbook for Materials Science, Plenum New York, (1996).

[35] B. Chalmers, R. King, R. Shuttleworth, "The thermal etching of silver" Proc. Roy. Soc. A, **193** [1035] 465-483 (1948).

[36] J. R. Heffelfinger, M. W. Bench, C. B. Carter, "On the faceting of ceramic surfaces" Surf. Sci. Let., **343** L1161-L1166 (1995).

[37] T. V. Savina, A. A. Golovin, S. H. Davis, A. A. Nepomnyashchy, P. W. Voorhees, "Faceting of a growing crystal surface by surface diffusion" Phys. Rev. E, **67** [21] (2003).

[38] J. R. Heffelfinger, C. B. Carter, "Mechansms of surface faceting and coarsening" Surf. Sci., **389** 188-200 (1997).

[39] J. R. Heffelfinger, M. W. Bench, C. B. Carter, "Steps and the structure of the (0001) a-alumina surface" Surf. Sci., **370** L168-L172 (1997).

[40] K. G. Saw, "Surface reconstruction of α-(0001) sapphire: An AFM, XPS, AES and EELS investigation" J. Mater. Sci., **39** 2911-2914 (2004).

[41] L. A. Bursill, P. J. Lin, D. J. Smith, "Surface Faceting and Polarity of Alumina" Ultramicroscopy, **23** 223-228 (1987).

[42] N. E. Munoz, S. R. Gilliss, C. B. Carter, "The monitoring of grain-boundary grooves in alumina" Phil. Mag. Lett., **84** [1] 21-26 (2004).

[43] D. Hull, D. J. Bacon, Introduction to Dislocations, Butterworth Heinemann Oxford, (1965).

[44] P. Nozières, F. Gallet, "The roughening transition of crystal surfaces. I. Static and dynamic renormalization theory, crystal shape and facet growth" J. Physique, **48** [3] 353-367 (1987).

[45] J. D. Mun, A. P. Sutton, B. Derby, "Grain growth and texture changes in a Ni foil during diffusion bonding to ZrO2" Phil. Mag. A, **76** [2] 289-305 (1997).

[46] G. Bilalbegovic, F. Ercolessi, E. Tosatti, "High-temperature surface faceting" Surf. Sci. Let., **258** L676-L678 (1991).

Tables

Table 2.1: Common low-index planes in alumina and their corresponding simplified nomenclature, lattice spacing and surface energies.

Surface	Nomenclature	Lattice spacing[3] (nm)	Unrelaxed surface energy[17] ($J\ m^{-2}$)	Relaxed surface energy[17] ($J\ m^{-2}$)
(0001)	c or basal	0.2165	6.53	2.97
$(10\bar{1}2)$	r	0.1740	3.55	2.57
$(11\bar{2}0)$	a	0.2379	5.17	2.65
$(10\bar{1}0)$	m	0.1375	6.87	2.89
$(11\bar{2}3)$	n	0.1147	n/a	n/a
$(10\bar{1}1)$	s		6.41	3.27

Chapter 2 Figures

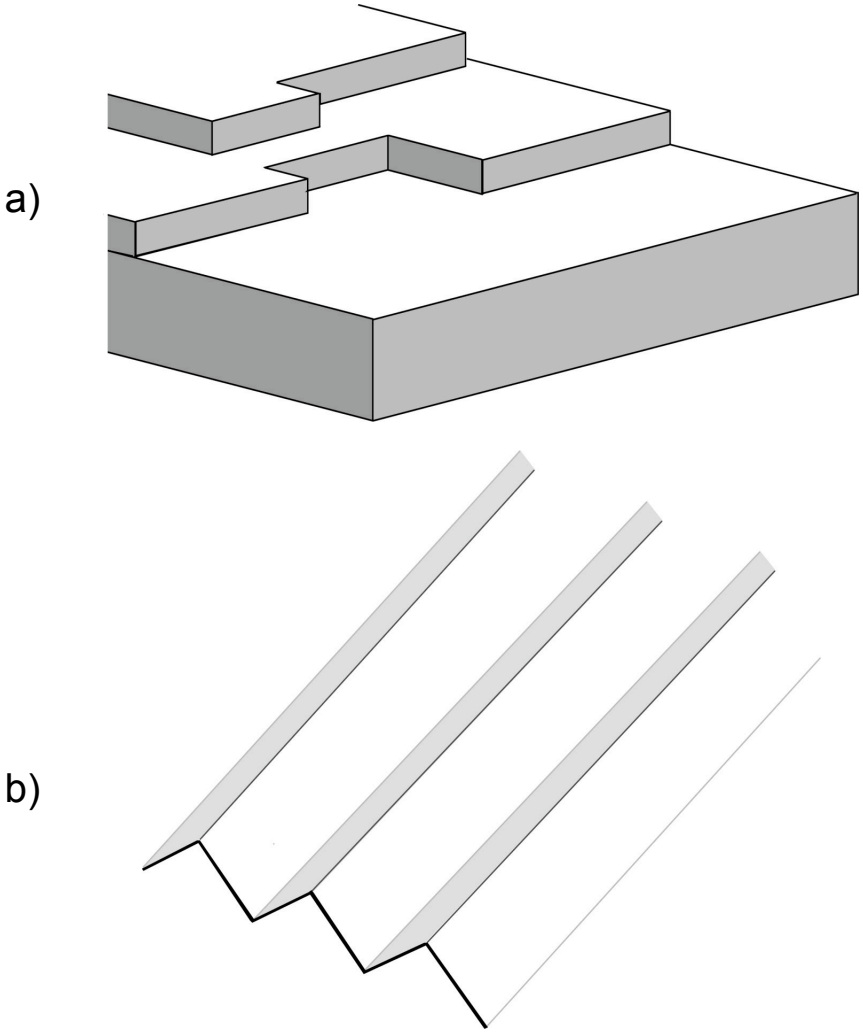

Figure 2.1: Surface reconstruction may form two different morphologies: (a) Terrace-&-Ledges and (b) Hill-&-Valley structures.

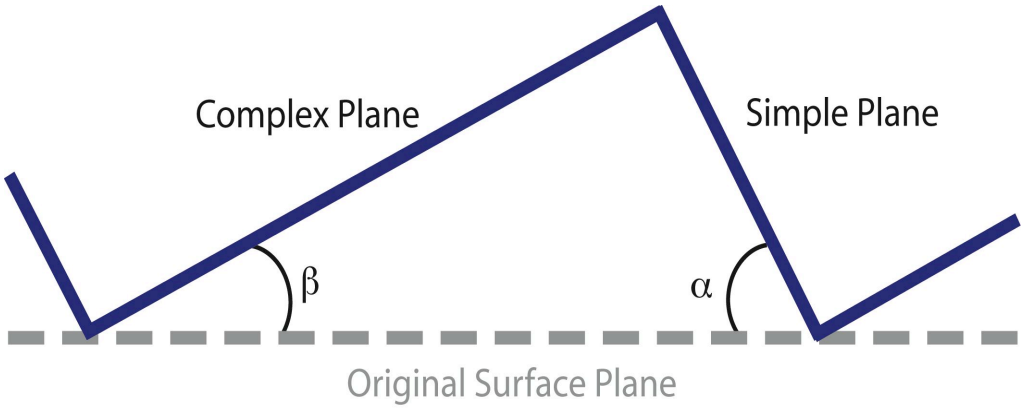

Figure 2.2: The theoretical morphology of surface reconstruction consists of facets made from a simple and complex plane. The simple plane is a low-energy, low-index plane, while the complex has higher surface energy and larger crystallographic indices.

a)

b)

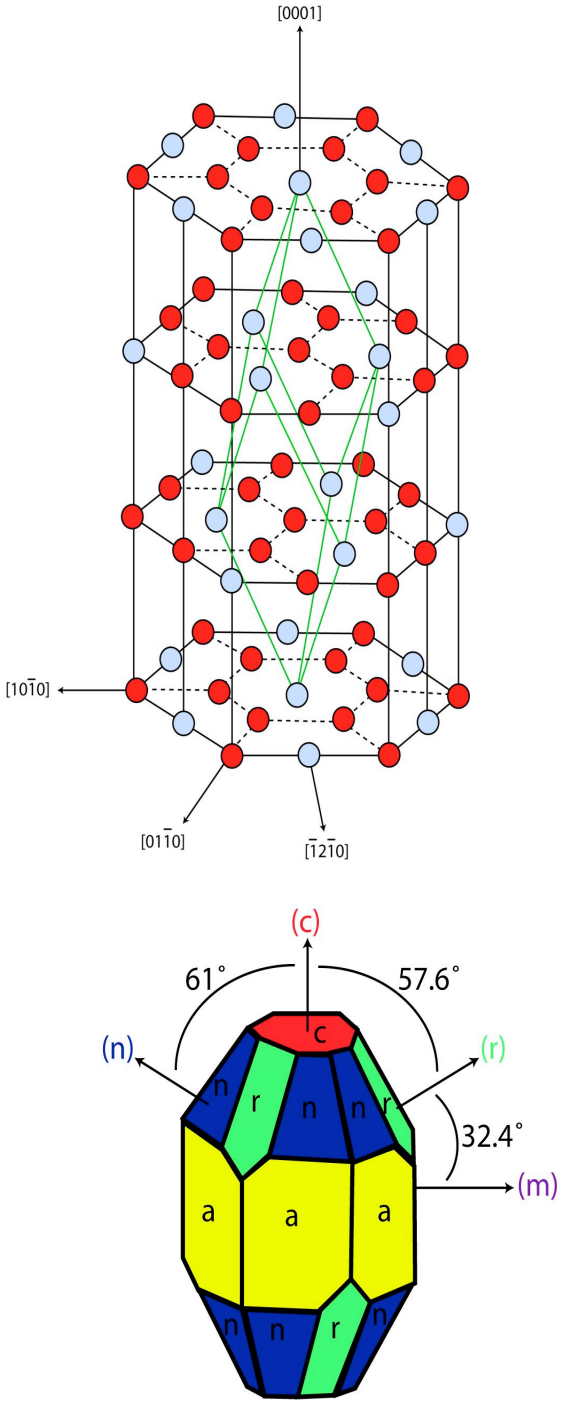

Figure 2.3: The rhombohedral alumina crystal structure is commonly described using the hexagonal unit cell, illustrated in (a). Relationships between low-index planes are shown in (b).

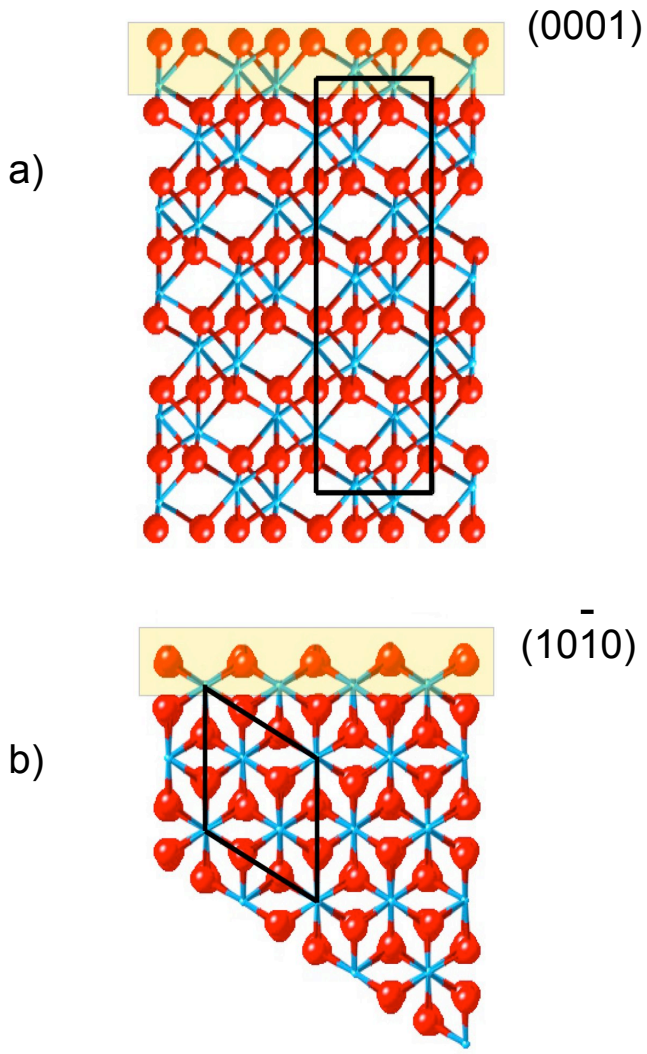

Figure 2.4: Highlighted in yellow are the unrelaxed surface terminations of (a) the (0001) *c*-plane and (b) the (10$\bar{1}$0) *m*-plane of alumina. The unit cell is outlined in black.

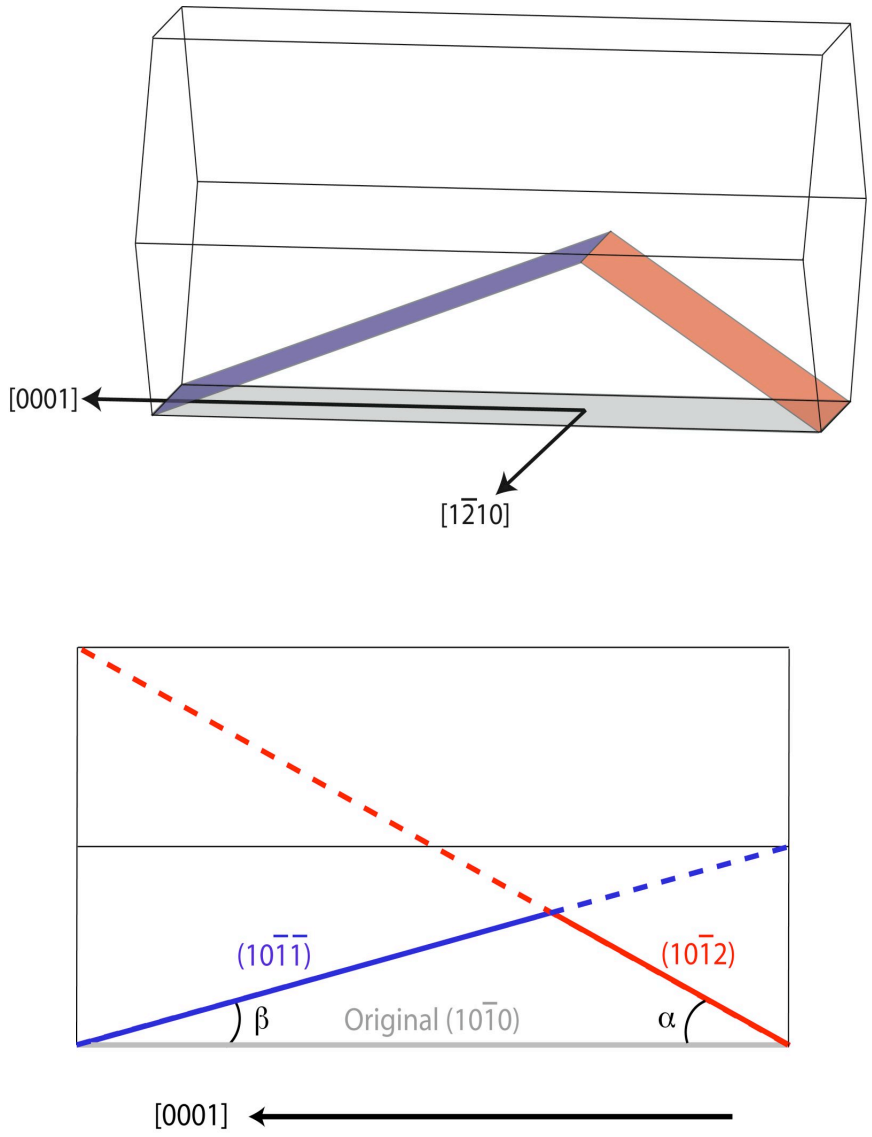

Figure 2.5: Facet orientation with respect to the hexagonal unit cell for alumina. The complex plane is in blue, while the simple plane is in red. The *m*-plane is in grey.

a)

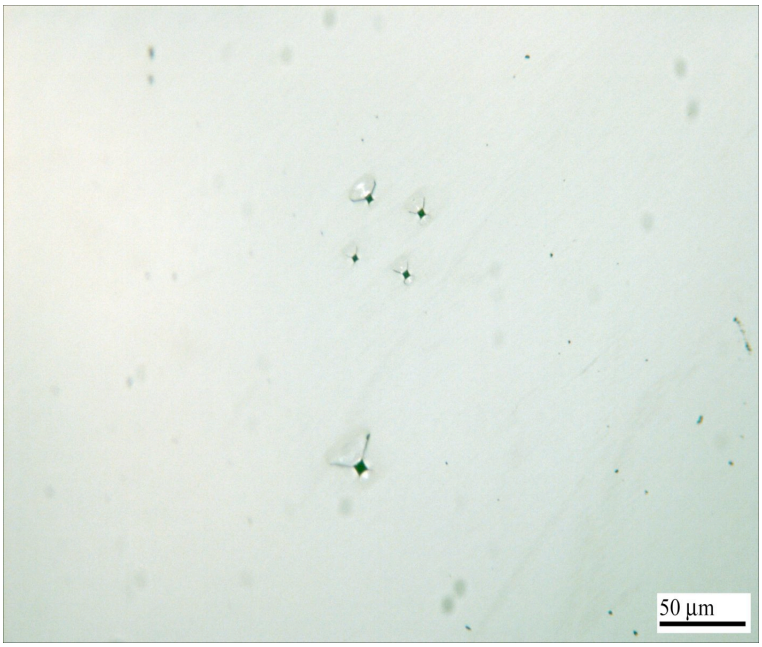

b)

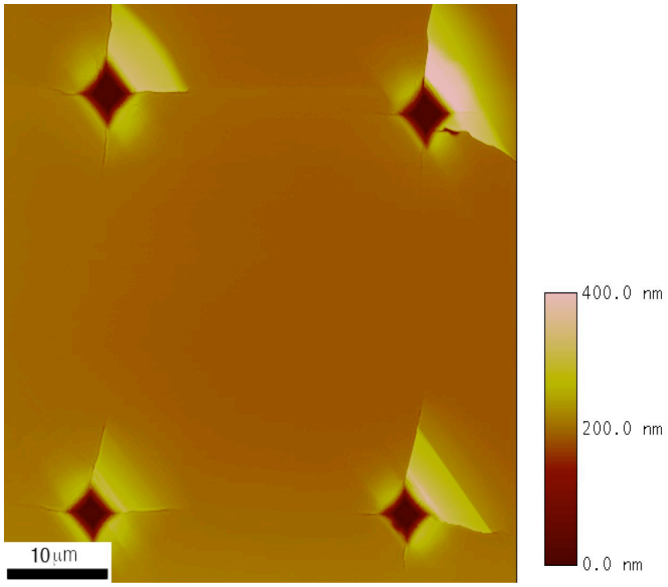

Figure 2.6: Fiducial markers were made using a hardness tester. The markers allow the same area to be returned to using both (a) VLM and (b) AFM.

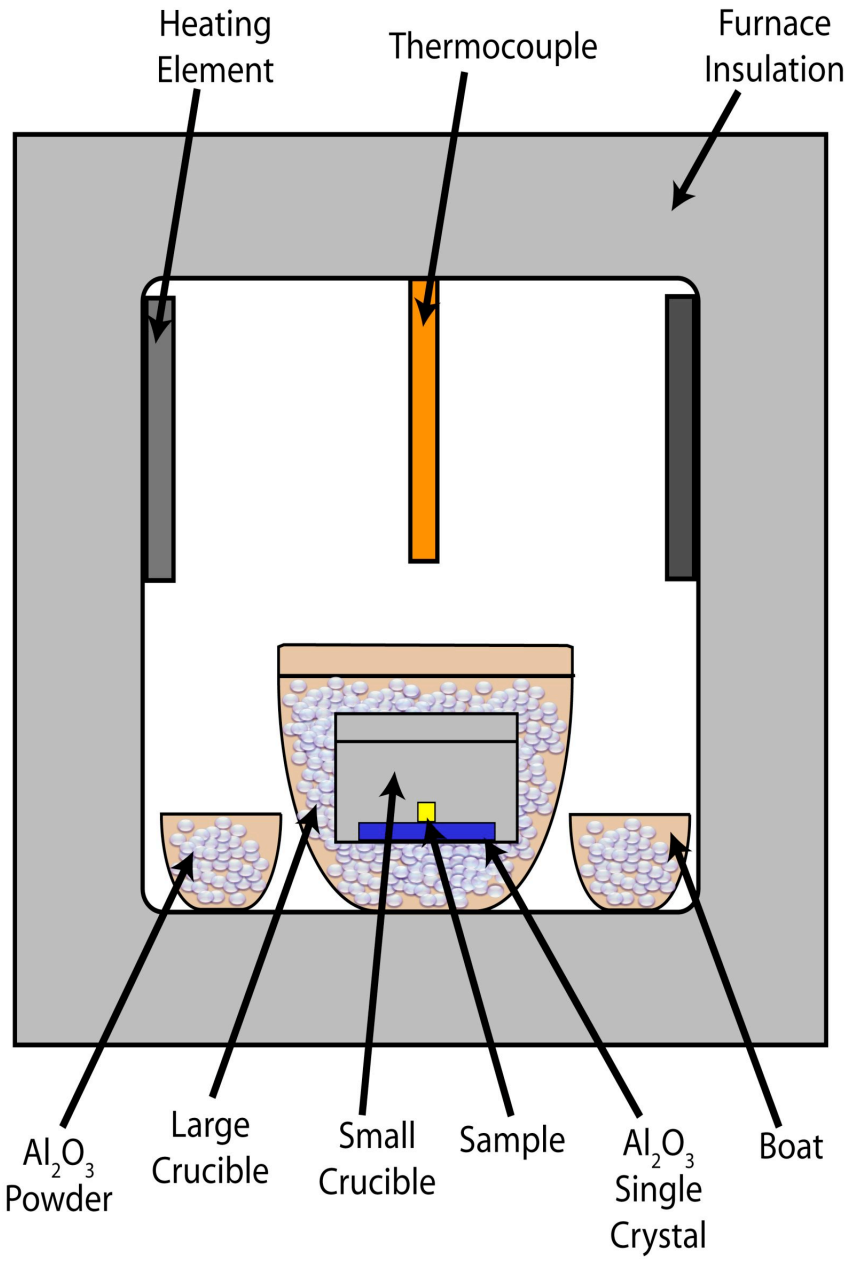

Figure 2.7: Samples rested on a single-crystal Al_2O_3 slab inside two Al_2O_3 crucibles during heat treatment. Al_2O_3 powder was packed between the crucibles and placed in Al_2O_3 boats to act as impurity getters.

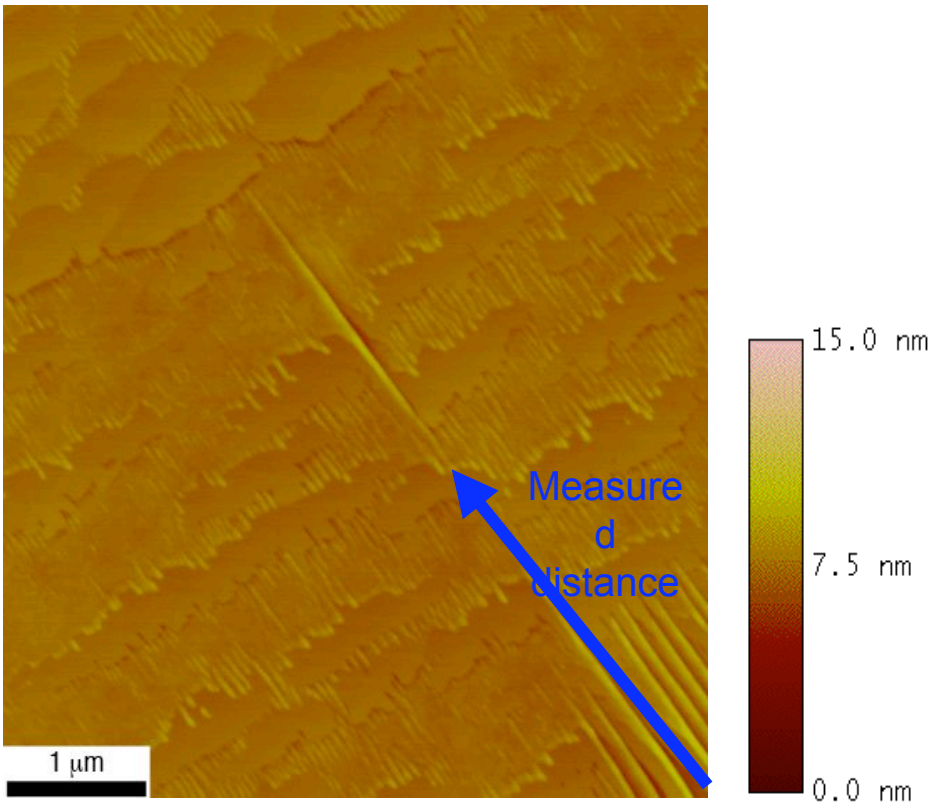

Figure 2.8: A fiducial marker, (just out of the image in the bottom-right corner), was used to measure from and locate the region of interest. The facets surrounding the indent can be clearly seen.

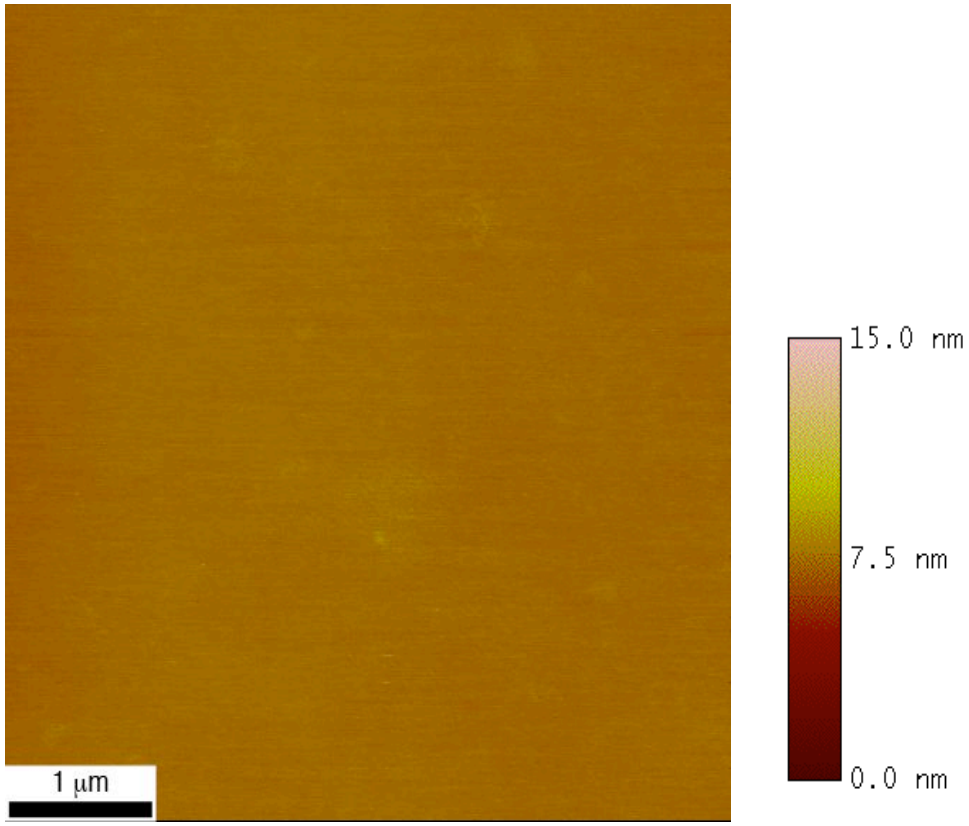

Figure 2.9: AFM of the as-received surface shows that the surface is initially flat.

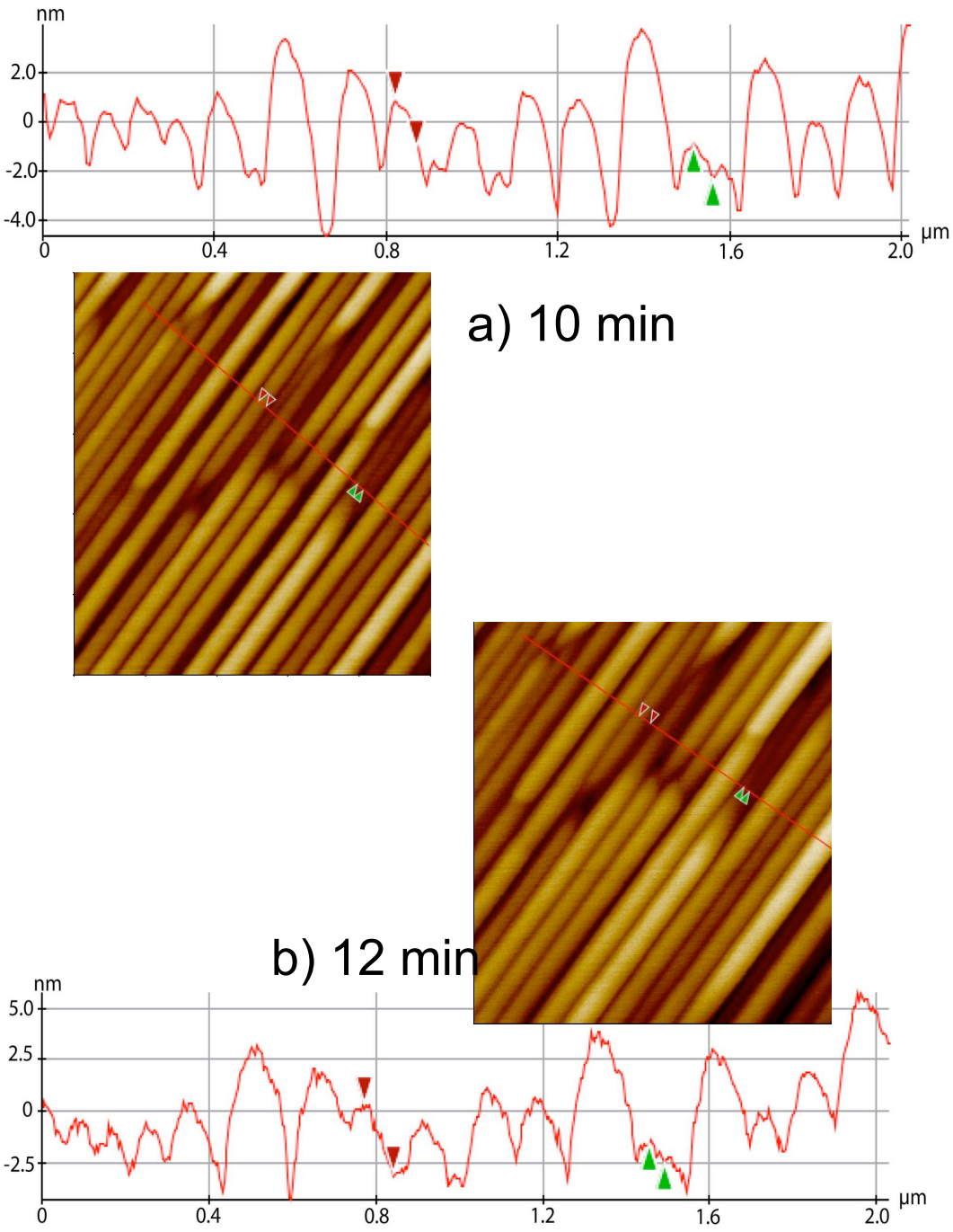

Figure 2.10: The facets marked with cursors in (a) have begun to coalesce with the smaller facets to the right, respectively, seen in (b).

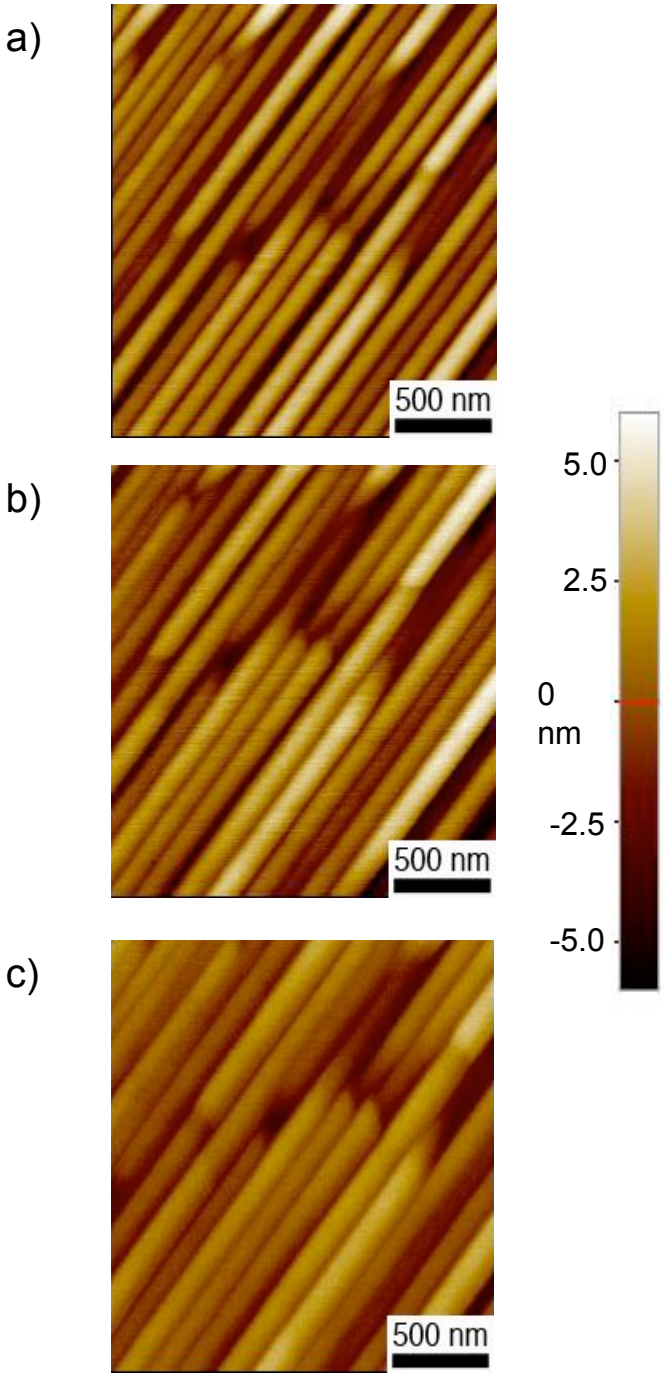

Figure 2.11: Facet tips act like kinks when they meet other facet tips. By watching the same set of facet tips after (a) 10 min, (b) 12 min and (c) 14 min at 1400˚C the morphology change is evident.

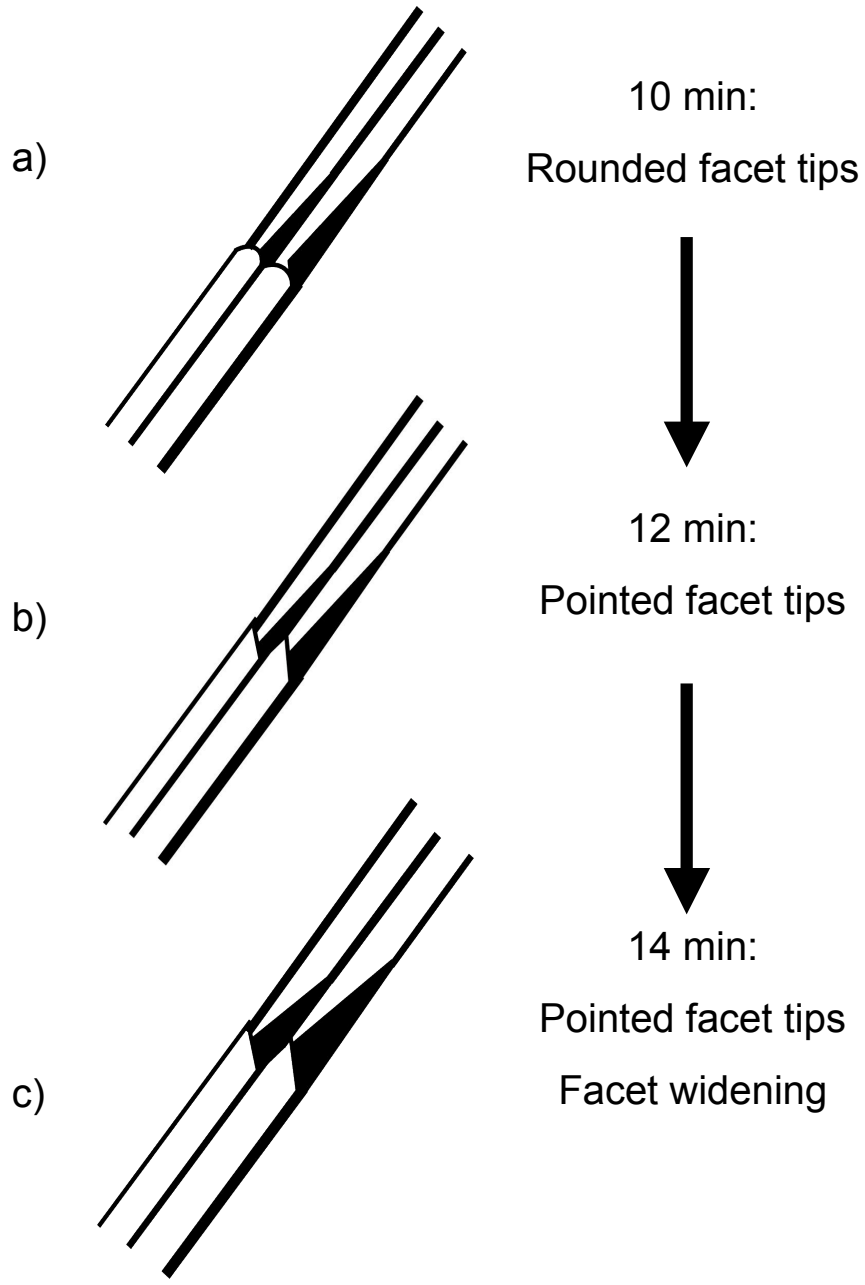

Figure 2.12: The facet tips are responsible for lengthening the entire facet and allowing coalescences by forming kinks.

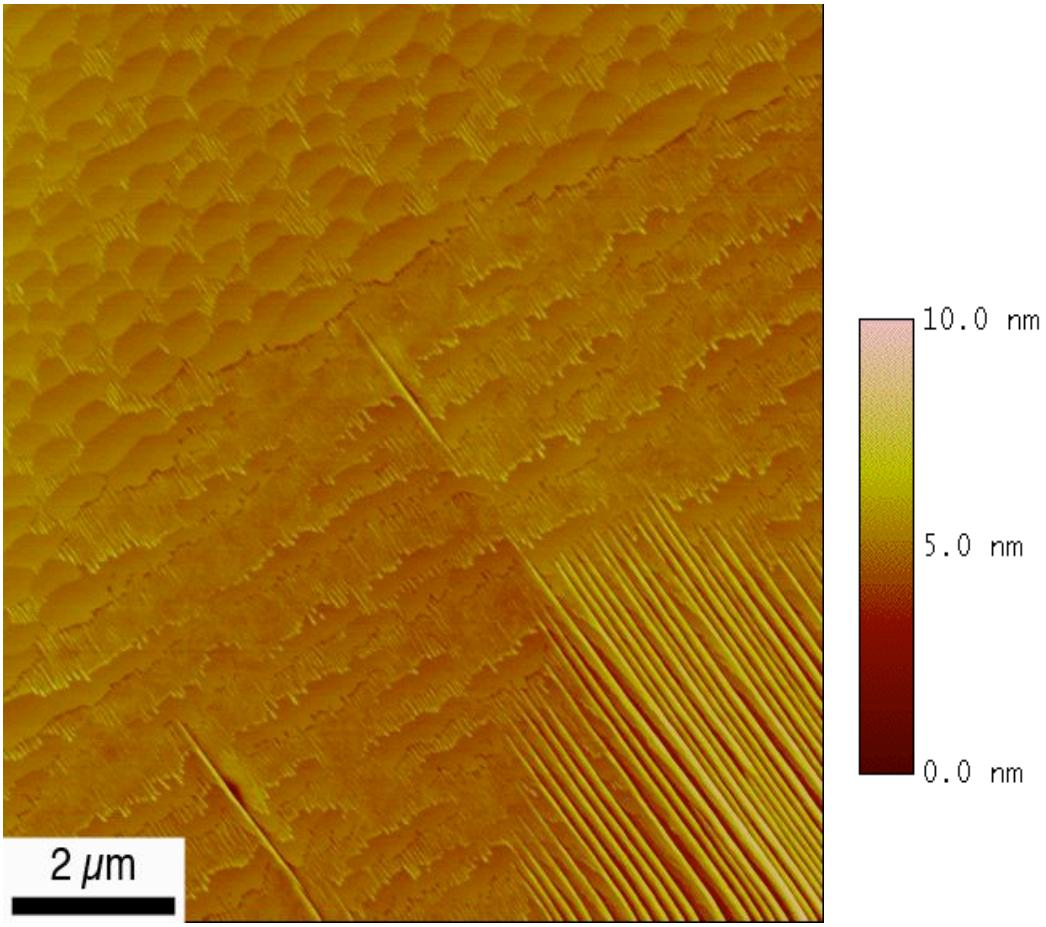

Figure 2.13: Vicinal surfaces (upper-left corner) must form first and evolve into fully formed facets (bottom-right corner).

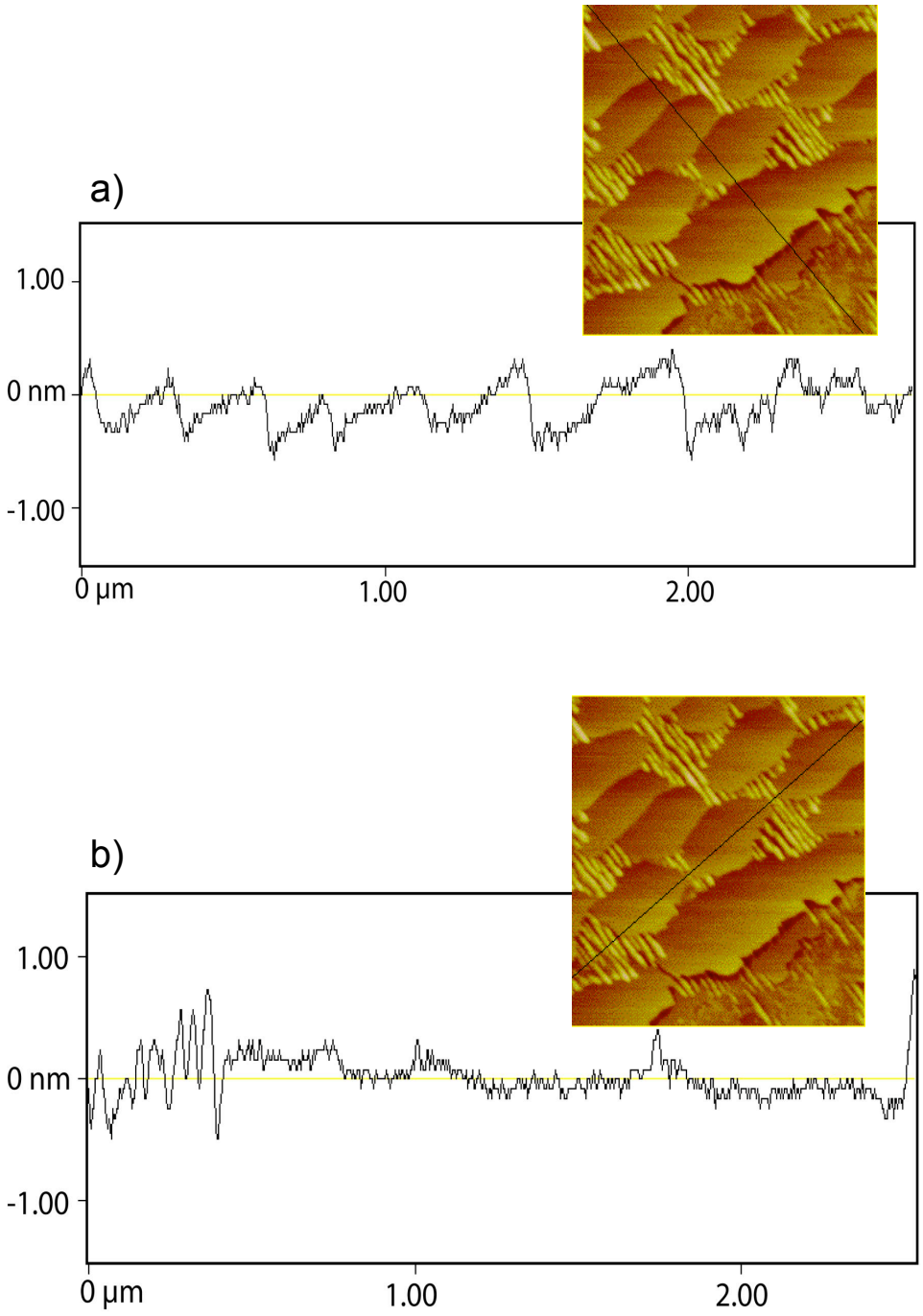

Figure 2.14: The vicinal surfaces have a regular shape just like facets when sectioned perpendicularly (a). When the vicinal surfaces are sectioned parallel to themselves, the surfaces lack structure.

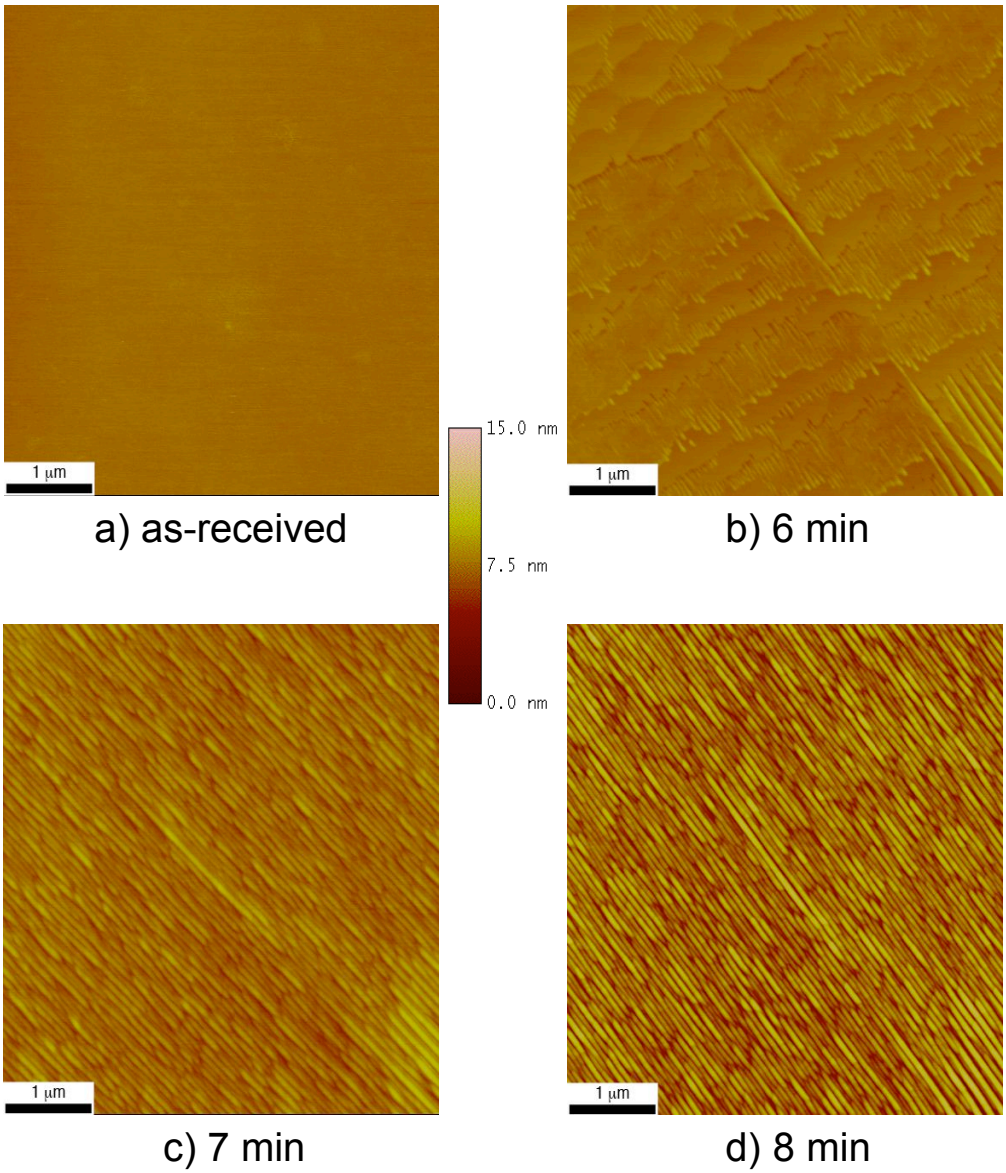

Figure 2.15: Secondary facets coarsen in the same manner as primary facets with time .

a) 6 min

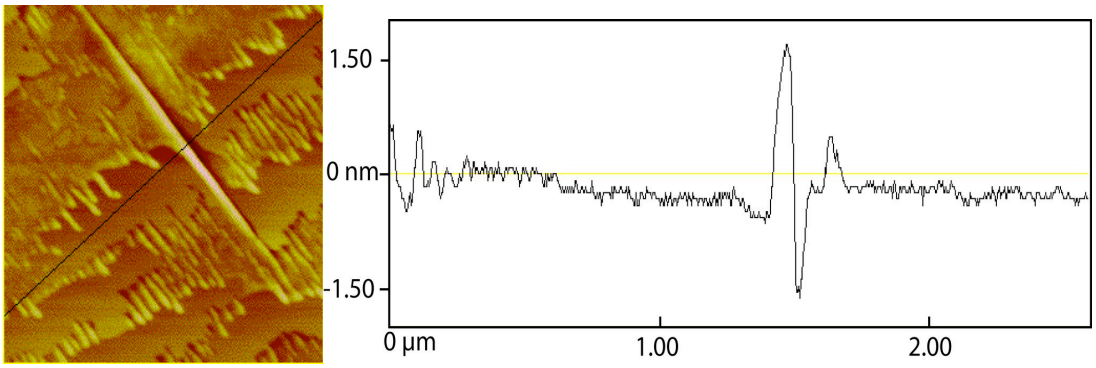

b) 7 min

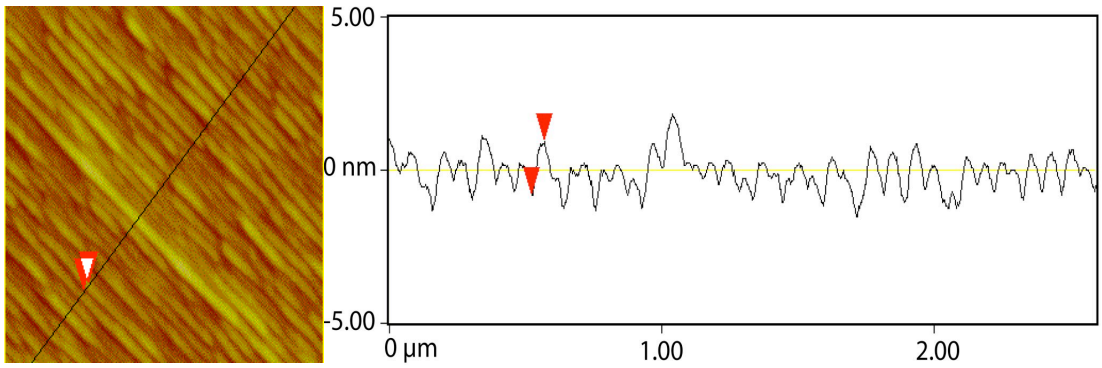

c) 8 min

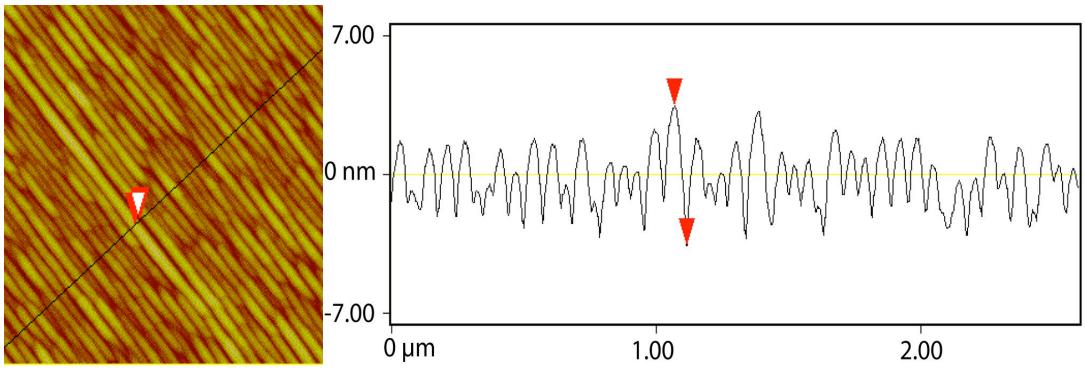

Figure 2.16: The same facet changes with further exposure to 1400˚C. The facet grows in height and additional facets form in the regions around it.

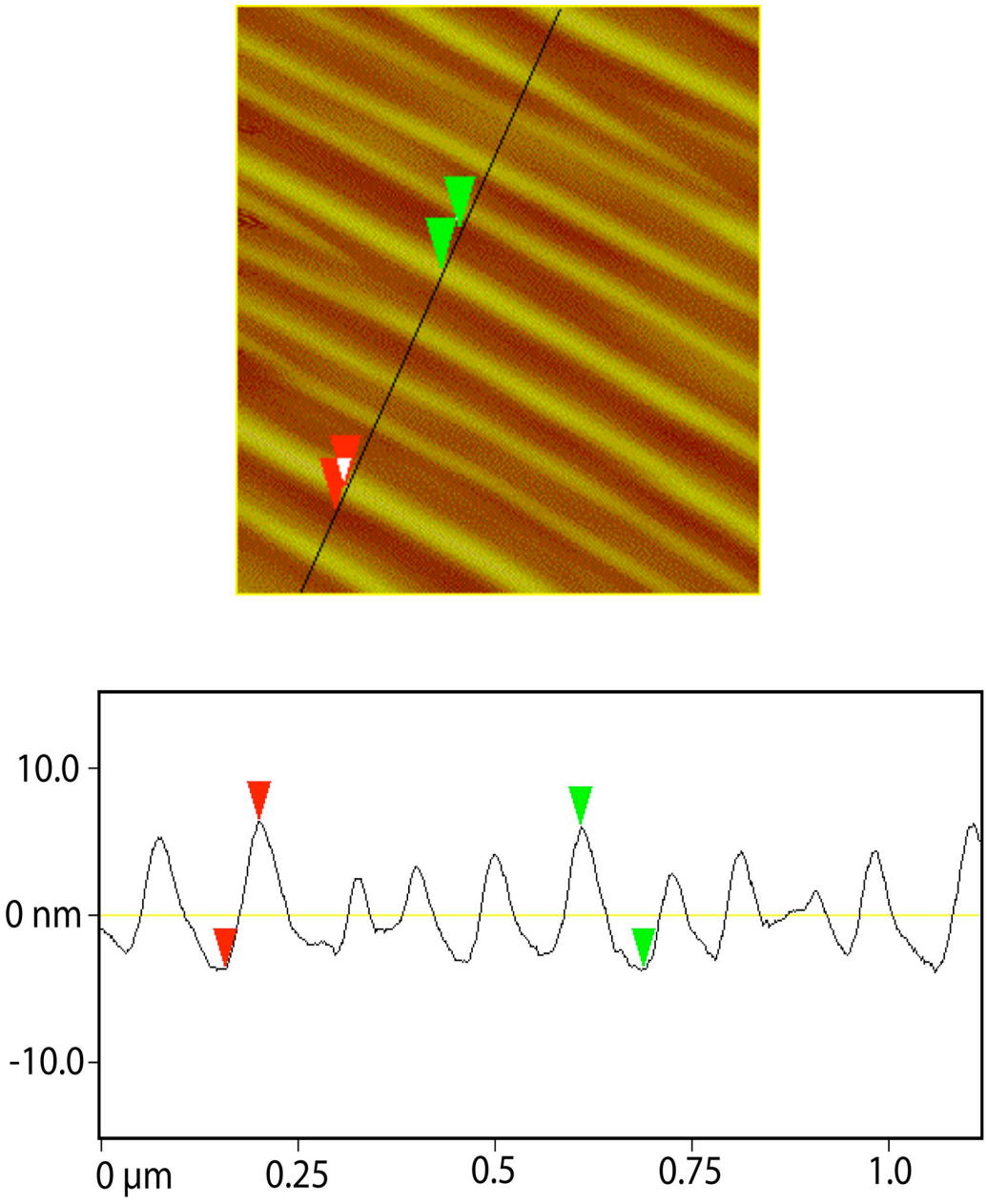

Figure 2.17: Significant coarsening has occurred on the *m*-plane surface after 30 min at 1400˚C

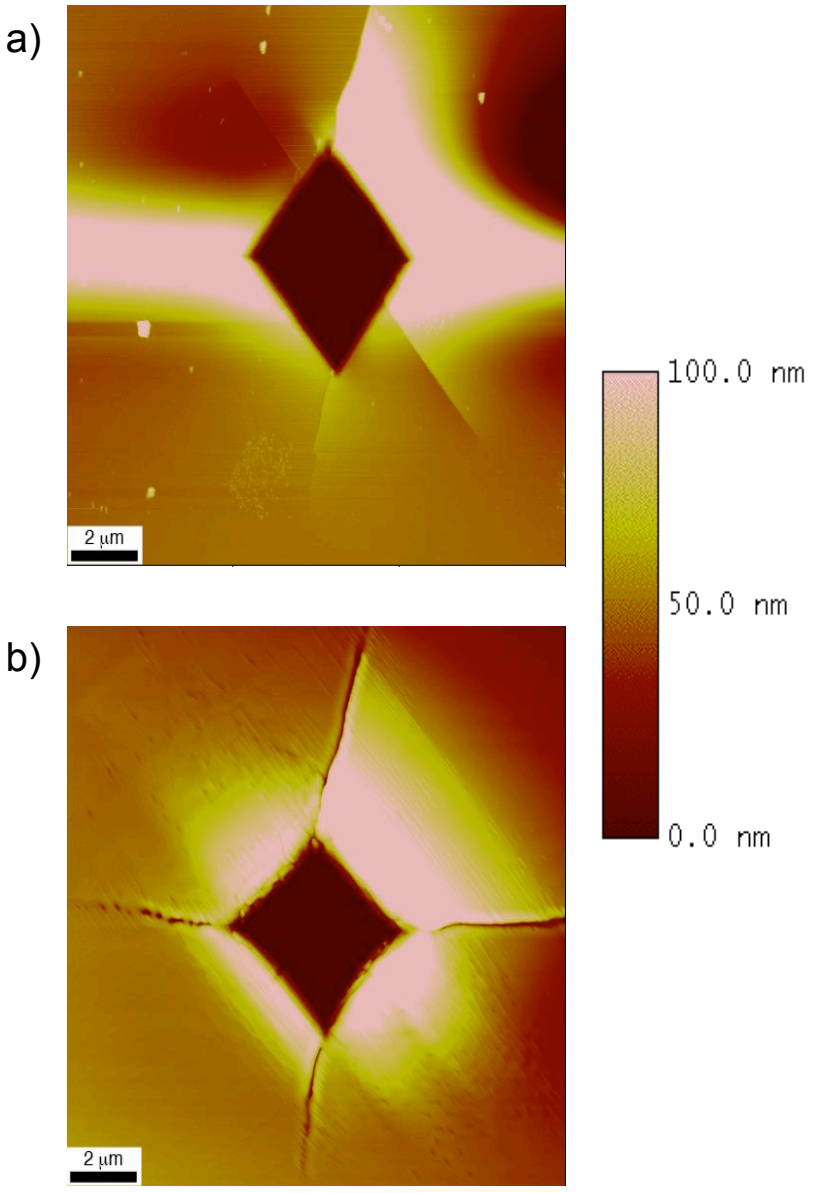

Figure 2.18: Indents acting as fiducial markers were monitored as they healed. (a) No facets present in the as-indented surface. (b) After only 6 min at 1400˚C, significant healing has happened and large facets have formed.

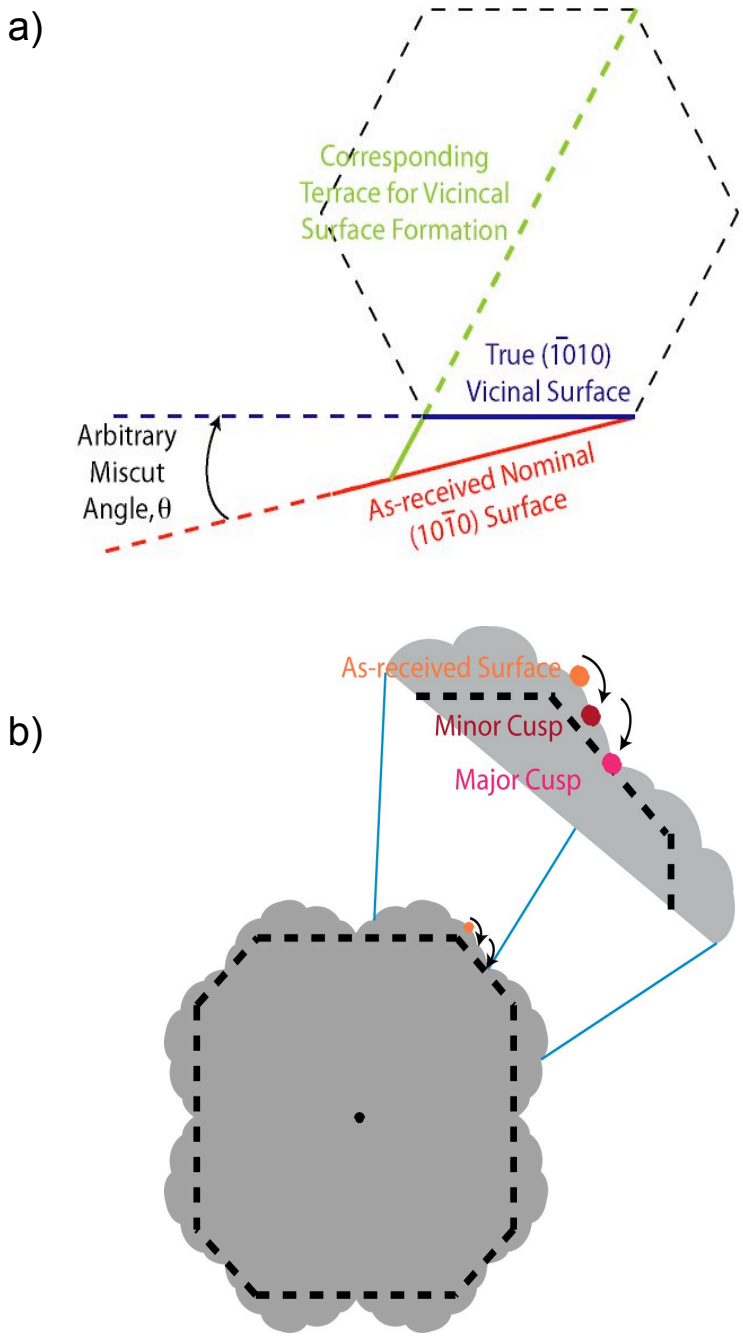

Figure 2.19: An originally miscut surface (a) must pass through a minor cusp in the energy plot to form vicinal surfaces before moving to a major cusp (b) and the equilibrium structure.

Chapter 3: Thermal Grooving at Grain Boundaries and Triple Junctions

3.1 Introduction

Grain boundaries in polycrystalline materials are responsible for many materials properties. Grain boundaries act as impurity getters and are often the location for electronic transport. Grain boundary sliding decreases mechanical strength, but high grain boundary density can be likened to a work-hardened material.

Grain boundary migration in ceramics is still not understood. The lack of three-dimensional characterization techniques limits how grain boundaries can be studied. Experimentalists are limited to data in two-dimensions and have to infer what is going on sub-surface. The best-case scenario is that cross-section samples may be made after the boundaries have moved. However, the behavior in the same sample cannot be watched further after the cross-section is made. Often a ring of pores may be used to monitor grain boundary migration.[1] However, this technique is limited in that the pores may also be mobile, consequently, giving inaccurate migration distances and rates. In addition, pores may inhibit grain boundary migration by acting as a second phase and pinning the grain boundary.[2]

Development of the focused-ion beam (FIB) tool has allowed easier cross-section analysis. Dual-beam FIB tools are a scanning electron microscope (SEM) with a gas-ion source (GIS) column attached to the same chamber 52˚ from the SEM column. (Figure 3.1) The GIS, usually a Ga^{+3} source, uses ions to mill specific areas of the sample surface while being monitored with the SEM column. Cross-section SEM and transmission electron microscope samples (TEM) may be prepared much quicker than traditional methods. When combined with energy-dispersive spectroscopy (EDS) and

electron backscatter diffraction (EBSD), serial sectioning with the FIB can produce three-dimensional images with chemical and orientation information for each section milled. However, the ions can be implanted or create an amorphous region at the surface. The damage layer in Si is approximately 20 nm thick at the surface using Ga^{+3} ions. If surface features are in the region of interest, the ion beam will most likely damage the feature unless a protective coating of significant thickness is sputtered onto the surface first.

Therefore, a more reliable and less damaging method of monitoring grain boundary migration is needed. Munoz, et al.[3] developed a method of using thermal grooves to monitor boundary migration. Surfaces form thermal grooves on interfaces at the location of grain boundaries. The groove forms into the boundary. The material removed from the groove forms ridges on either side of the groove. (Figure 3.2) When a grain boundary migrates, the groove takes time to heal and can often be seen as a shadow next to the next to the new position of the grain boundary. (Figure 3.3) The remnant groove, or ghost boundary, is an exact marker of where the grain boundary's original position had been.

In addition to migration, thermal grooves can be used to monitor grain growth and shrinkage. Mullins[4] derived equation 3.1, called the Von Neumann-Mullins relation, which describes the rate of grain area increase or decrease, and therefore the grain boundary migration speed, determined entirely by the grain's number of sides, *n*. The constant *k* is related to the temperature-dependent activation energy and mobility.

$$\frac{dA}{dt} = k\left[\frac{\pi}{3}\right](n-6) \qquad [3.1]$$

Grains with greater than six sides will grow, while grains with fewer than six sides will shrink. However, the presence of triple junctions, the points where three grain boundaries meet, and their effect on grain boundary migration was not considered in this relation. Gottstein and Shvindlerman[5] showed that the triple junction drag significantly changes grain boundary kinetics. Appendix 3.3 explains the influence of

triple junction drag in greater detail. Crystal orientation was also not considered. Rollett and Mullins considered how abnormal grain growth and grain boundary migration is affected by the number of grain sizes.[6]

Grain boundary energies may be measured by measuring the dihedral angle of the thermal grooves at the boundary.[7] Grain boundary energy is a function of tilt angle of the boundary. Remnant grooves may be used to measure the grain boundary mobility.[8]

Ceramics are known to often have a glassy layer at the grain boundary. Impurities often prefer to sit in the spacious grain boundaries, rather than the bulk. The grain boundaries act as a capillary for intergranular films.[9] Exaggerated or abnormal grain growth has been proposed to be initiated by local equilibrium fluctuations such as grain boundary curvature and thermal grooves.[10] Lath-like grains have been reported[11] to have non-equilibrium dihedral angles at the grain boundary grooves, suggesting the presence of a wetting liquid phase. Therefore, impurities may drastically change grain boundary behavior and thermal grooving. Cleanliness during sample preparation is of utmost importance.

In recent years, a growing interest in triple-phase boundaries has emerged. Research in fuel cell technology has shown that understanding interfaces and triple points is crucial in making more efficient fuel cells. The triple-phase boundary between the atmosphere, anode and electrolyte is suspected of being the critical point for the absorption of hydrogen atoms. Little is understood of the exact absorption mechanism or even the structure of the triple point.

3.2 Background

3.2.1 Theory of Thermal Grooving

Surface tension and surface energy are often used interchangeably. However, these terms are only equivalent when referring to liquids in equilibrium. Care needs to be taken during analysis.

Grooving at grain boundaries has been looked at for nearly a century, but very little is understood about groove formation. Chalmers, King and Shuttleworth[12] were some of the first to study thermal grooving and proposed the cornerstones for future formation theories. This early work was done on electrolytically polished Ag that was annealed at several different temperatures for 11 hours. In addition to thermal grooving, this work was some of the first monitoring surface reconstruction. The same experiments were performed in air, oxygen, nitrogen and vacuum atmospheres and showed that atmosphere dramatically changes the surface behavior and groove formation. While faceting was observed when surfaces were annealed in air or oxygen, remnant grooves were only present when annealed in nitrogen. *In situ* heating determined that thermal grooves form while at temperature and not during the cooling process. Thermal grooves were also noted to move with the grain boundaries.

While Mullins'[13] classic theory on groove formation ignored orienation, Chalmers, King and Shuttleworth[12] realized that the different surface energies from crystallographically-different surface planes were important. They even proposed that the surface energy must change depending on which environment the material was annealed in. They argued that thermal treatment in vacuum was not an equilibrium condition, since the vapor from evaporation would not be allowed to condense back onto the surface. Prior to electron microscopy, straining the crystal a small amount and creating slip bands allowed crystallographic directions to be determined in real samples.[12]

The free energy of the surface at a thermal groove was divided into the following parts: 1) the free energy of the atom sitting in the lattice, 2) the additional energy required to sit at the surface, 3) the additional energy to sit near or on a grain boundary. Consideration 1 will always be a constant value, but considerations 2 and 3 will have a different values depending on the crystallographic plane the atom resided on. The combination of these free energies would create three surface tensions to form where a grain boundary met a surface: one force acting on the grain boundary (τ_{AB}) and two acting on the individual surfaces of each grain (τ_A and τ_B). (Figure 3.4) Grooves should

form on the surface where all three forces are balanced. This geometry is directly applicable to triple junctions of three grains, also. (See Appendix 3.3) However, while the force balance in equation 3.2 describes the groove angles, it does not describe the groove depth. Chalmers, King and Shuttleworth proposed[12] that the width depended on the grain size, but did not give any argument for this hypothesis.

$$\frac{T_{AB}}{\sin\gamma} = \frac{T_A}{\sin\beta} = \frac{T_B}{\sin\alpha} \qquad [3.2]$$

Mullins[13] proposed a theory and derived governing equations based on the Gibbs-Thompson (equation 3.3) and Nernst-Einstein equations (equation 3.4) for thermal grooving. The terms are defined as: p is the vapor pressure, p_o is the equilibrium vapor pressure, K is the curvature, γ is the surface free energy per unit area, Ω is the molecular volume, D_s is the surface diffusion coefficient, s is the arc length, V is the average velocity of surface atoms and kT is Boltzmann's constant and temperature. He treated the problem as having three possible diffusion mechanisms: 1) evaporation-condensation, 2) surface diffusion and 3) volume diffusion. Chalmers, King and Shuttleworth[12] also argued that slip could be a possible material transfer mechanism, but the forces needed to slip a portion of the grain would be much larger than the surface tension. The groove ridges trying to flatten via evaporation-condensation and surface diffusion was proposed to be the source for evaporation and condensation of the groove. Volume diffusion was not treated in Mullins' discussion, since he argued that surface diffusivity was much higher than volume diffusivity, and therefore, negligible unless the temperature was near the material's melting point or the thermal grooves were large. Surface diffusion was later determined to be the governing grooving method for alumina by collecting data from several researchers using different methods of monitoring surface grooves.[14]

$$\ln\left(\frac{p}{p_o}\right) = K\left[\frac{\gamma\Omega}{kT}\right] \qquad [3.3]$$

$$V = -\left[\frac{D_s \gamma \Omega}{kT}\right]\frac{\partial K}{\partial s} \qquad [3.4]$$

The following assumptions were made in Mullins' theory of thermal grooving:[13]

a Surface energies of the material are isotropic.

b The grain boundary is stationary and perpendicular to the initially flat surface.

c The grain-boundary energy is independent of the tangent plane.

d Crystal defects at the surface can be ignored.

e Torque terms ($\partial\gamma_i/\partial\theta_i$) due to grain boundary curvature are negligible.

Mullins was able to use equation 3.3 for evaporation-condensation and equation 3.4 for surface diffusion and solve for the groove depth, d_e and d_s, with time for the respective regimes, where t is time, v is the atoms per unit area, M is the weight of the molecule and θ is the partial angle of the groove. For surface diffusion, the groove width, w, was also derived.

$$d_e = -1.13\tan(90-\theta)(At)^{\frac{1}{2}} \qquad [3.5]$$

$$d_s = 0.973\tan(90-\theta)(Bt)^{\frac{1}{4}} \qquad [3.6]$$

$$w = 4.6(Bt)^{\frac{1}{4}} \qquad [3.7]$$

$$A = \frac{p_o \gamma \Omega^2}{(2\pi M)^{\frac{1}{2}}(kT)^{\frac{3}{2}}} \qquad [3.8]$$

$$B = \frac{D_s \gamma \Omega^2 v}{kT} \qquad [3.9]$$

In order to determine whether evaporation-condensation or surface diffusion was the dominant formation mechanism for the material, the ratio σ was, defined in equation 3.10, using equations 3.8 and 3.9. A larger σ would imply that surface diffusion ruled while evaporation-condensation would be forming the groove for small values. In general, surface diffusion dominates with short time, but becomes less important as the groove forms, since the groove becomes an evaporation source and condensation may occur on the groove ridges. However, some argument exists[12] as to whether evaporation is easier at a groove or if the vapor pressure at the groove would cause immediate condensation. Evaporation-condensation will occur at higher processing temperatures, when the atoms are less bound to the surface. The activation energy needed for surface diffusion of cations is much less than that needed for evaporation-condensation.[12] Inert atmospheres during processing will favor surface diffusion. Ultimately, the vapor pressure, *p*, of the material is what determines which mechanism is controlling groove formation.

$$\sigma = 0.36 \frac{B^{\frac{1}{2}}}{A} t^{-\frac{1}{2}} \qquad [3.10]$$

Burke's[2] work on monitoring pores during sintering alumina confirmed that surface and interface diffusion are more dominant than evaporation-condensation and volume or lattice diffusion. As figure 3.5 shows, diffusion of vacancies to eliminate pores is most likely to occur at grain boundaries or surfaces. Vacancies traveling to the surface at a grain boundary will cause shrinking at the grain boundaries and densification of the entire compact. The microstructure that results resembles thermal grooving.

Mullins[10] argued that all steady-state grooves were uniform in shape, and only differ in scale. Only the partial angle of the groove was the critical parameter, while groove size, boundary curvature, migration velocity, local surface roughness and orientation does not play a role in the boundary's behavior.

For isotropic materials, ridges should be nearly the same size and shape for all boundaries. Munoz, et al.[3] showed that for alumina, which is highly anisotropic, the

ridges are asymmetric in size at migrating boundaries and symmetric at stationary boundaries. Local instabilities cause a slight asymmetry at stationary boundaries. Using a FIB-prepared TEM sample, migrating boundaries were found to be inclined sub-surface in the direction of migration and towards the larger of the two surface ridges, i.e. the smaller partial angle. Using these results, Young's equation (equation 11) was found to be valid only for stationary boundaries. The energy and grain boundary location also affect the groove profiles. This important observation reiterates that the groove is only in local equilibrium.

$$\gamma_{GB} = 2\gamma_S \cos\theta_S \qquad [3.11]$$

The study continued by watching the smoothing of the remnant grooves.[15] Equation 2 was modified to equations 3.12 and 3.13 and accounts for anisotropy and that grain boundaries are not necessarily perpendicular to the surface. In addition, if the boundary migrates, local equilibrium is destroyed and equation 3.11 becomes invalid. The partial angles are now defined as θ_1 and θ_2 for the respective sides of the groove. The surface energy of each grain measured at the groove base becomes γ_1 and γ_2, respectively. The angle of the grain boundary makes with the originally flat surface is defined as θ_{GB} and γ_{GB} is still the interfacial energy of the grain boundary. Figure 3.2 illustrates the modifications.

$$\gamma_{GB} \cos\theta_{GB} = \gamma_1 \cos\theta_1 + \gamma_2 \cos\theta_2 \qquad [3.12]$$

$$\gamma_{GB} \sin\theta_{GB} = \gamma_1 \sin\theta_1 - \gamma_2 \sin\theta_2 \qquad [3.13]$$

With further heat treatment, remnant grooves will begin to heal. The sharp groove base becomes rounded and shallow. Healing occurs at a much slower rate than grain boundary migration, and therefore, remnant grooves are excellent markers of the original grain boundary position.

Mullins[10] proposed that migrating boundaries are pinned by thermal grooves. The boundary will not migrate sub-surface until a critical θ_{GB} is passed. If the boundary lies

somewhere between 90˚ and θ_{GB} to the surface, the boundary would have to lengthen in order to move, illustrated in figure 3.4. Since this creates more interfacial area, lengthening is highly unfavorable. If the angle is greater than the critical angle to the surface, then the boundary can escape its groove and migrate. The intersection point of the boundary and the surface can then snap into a new position 90˚ to the surface. The process continues in the same manner over and over. The groove depth does not play a roll in anchoring the grain boundary; only the critical angle determines whether the boundary is pinned or mobile. Grain boundary mobility is thought to depend on the vacancy concentration. The motion at the surface occurs quickly enough that no thermal grooves form. As the boundary jumps along, remnant grooves are left behind to form a serrated morphology at the surface. However, early work[12] in Ag only showed remnant grooves when annealed in inert environments. The reason for this is not completely clear.

3.2.2 Previous Studies on Single-Phase Grooving

As described above, Munoz, et al.[3] studied groove profiles in alumina using the AFM and VLM mapping. However, surfaces slow-cooled in the furnace versus quenched grain boundaries were not compared to see if the cooling rate has an effect on migration and groove formation. Shin, et al.[16] also used AFM confirm thermal groove formation via surface diffusion and to determine the surface diffusion coefficient in polycrystalline alumina. However, measurements were only taken after one thermal treatment. The same area was not monitored after subsequent heat treatments. A large AFM tip diameter (~50 nm) was used for imaging and discrepancies in measured angles, found in Munoz's[3] paper, were ignored. In addition, no orientation considerations were made.

The rate of smoothing of remnant grooves was found to depend on the surface orientation.[15] This important point is one that Mullins[13] assumed was negligible. Different grain orientations were identified by the different faceting behavior of each

grain at the surface.[17] However, exact orientations were not measured with EBSD or selected-area diffraction (SAD).

Nomarski optical interferometers have been used to characterize thermal grooves of grain boundaries at the surface of metals[10] and ceramics,[18] mostly before the invention of AFM. However, The experimental error of this technique has been shown to be as much as 40%![18] Therefore, quantitative analysis using this technique should be viewed critically.

Other techniques previously used to study grain boundary grooving include, surface prolifometry, carbon reference line and metal reference line.[19]

The TEM is an obvious characterization tool for grain boundaries. The Fresnel-fringe and dark-field diffuse scattering techniques are most commonly used to identify boundaries and measure their thickness.[20] Contrast from grooved boundaries in the TEM was carefully looked at by Rasmussen, et al.[21] Grooved boundaries with and without a glassy layer in the boundary were found to give similar contrast in some instances, implying that image simulation is a necessary step in observing boundaries in the TEM.

In situ monitoring of ceramic thermal grooves is not possible at this time. Heating stages for the VLM and AFM only reach ~400˚C in air. Thermal grooves are tens of nanometers tall. Since TEM specimen thicknesses are of the same order of magnitude[20], *in situ* TEM would not exhibit behavior representative of the bulk. In addition, techniques used for preparing traditional and cross-section TEM specimens often alter the sample. For example, ion milling to the final thickness for electron transparency often preferentially etches grain boundaries.[9] However, *in situ* monitoring of metal surfaces is possible. Chalmers, King and Shuttleworth[12] were able to watch Ag surfaces with a custom built furnace that reached at least 950˚C under various atmospheres.

Thermal grooves of ZrO_2 have been shown to be suppressed when allowed to form in MgO-atmosphere compared to in air.[18] In this case, surface diffusion must be

controlling sintering and the presence of MgO suppresses the ZrO_2 surface diffusion coefficient, allowing densification to occur more readily.

AFM was used to determine the dihedral angles, groove width and surface diffusion coefficients of ceria.[19] When measuring groove width, asymmetric thermal ridges were noted at some grain boundaries. However, a standard procedure for measuring groove width at these boundaries was not made. In addition, "small grooves" were found on the surface, but were probably remnant grooves. No distinction between thermal and remnant grooves is made.

3.2.3 Grooving at Phase Boundaries

Phase boundaries are interfaces between two crystallographically and chemically different species. They are two or more component systems. Very few studies have looked at phase boundary behavior. Those who have studied phase boundaries have done so from interest in thermal barrier coatings and metal-ceramic interfaces. Studies have always looked at a fracture surface between the interface and never at the triple-phase boundary between the two solid components and the atmosphere.

While grain boundary curvature is thought to play a negligible role in grain boundary grooving and migration, Mullins[10] proposed that the curvature would be of some importance. The curvature would create a large plastic strain at the boundary, similar to epitactic growth. Mullins also proposed that a second phase would limit the maximum grain size of the compact.

Second-phase particles will cause discontinuous grain growth.[2] The particles or grains of a second phase, including pores, pin the grain boundary similar to how a dislocation is pinned. Continuous grain growth will stop when equation 3.14 is true. In this case, D is the average diameter of grains, d is the average diameter of inclusions or pores and f is the volume fraction of pores present.

$$D = \frac{d}{f} \qquad [3.14]$$

3.2.4 Previous Studies on Two-Phase Grooving

Many studies of metal-ceramic interfaces have been performed. Interfaces between different phases that are not soluble in one another are expected to be more or less stationary to conserve mass.[22] Thermal grooving at these interfaces were shown to be controlled by interfacial and volume[22, 23] diffusion, in contrast to single-phase systems. Pore formation at metal-ceramic interfaces are common.[22-24] Grooves at the metal-ceramic interfaces were monitored by fracturing the specimens at the interface. The triple-phase metal-ceramic-atmosphere was not monitored in any study.

Ni foils diffusion bonded onto ZrO_2 were found to grain grow quickly in the early stages of diffusion bonding, while the ZrO_2 did not experience any grain growth.[22] The Ni foil texture was found to change from the (100) to (111) preferred interface plane during diffusion bonding, but did not change if the Ni was not in contact with ZrO_2; the ZrO_2 orientation did not matter. Parallel diffusion between Ni and ZrO_2 is necessary to get grooves to form in the Ni. Since ZrO_2 is the slow-diffusing species, grooves are expected to form in the Ni long before ZrO_2 grooves. Therefore, a low-energy interface orientation must exist which is different from the low-energy surface orientation for Ni.

Reimanis[23] studied diffusion-bonded Nb-Al_2O_3 interfaces and was able to return to the same area using interference optical microscopy. Grooving was found to form during the diffusion bonding process. The fracture surface was characterized using SEM. This study also found that preferred Nb growth occurred despite different alumina orientations. The Nb grain boundaries in contact with Al_2O_3 had larger thermal grooves than those that did not contact the Al_2O_3, where specific grain boundary misorientations gave rise to larger thermal ridges than others. Reimanis proposed that the thermal grooves were the first points of contact at the interface and served as material sources for diffusion to bond the Nb-Al_2O_3 interface.

Metal-Metal multilayers[24] were also found to thermally groove. However, one metal was found to form larger ridges than the other.

The only study to date of two-phase ceramic systems has been by Marshall, et al.[25] They studied grooving at the interface between alumina and monazite by fracturing the sample at the interface and looking at the corresponding halves with the AFM. The dihedral angle was measured and the interfacial energies were discussed. The study showed that the alumina interfacial energy is more isotropic than alumina surfaces. Asymmetric grooving at the alumina-monazite interface were found, similar to Munoz's[3] work on alumina boundaries. While qualitative relationships between the fracture energy and interfacial energy were made, quantitative numbers for interfacial energy were not determined in the study.

3.3 Experimental

3.3.1 Alumina Surface Preparation

Alumina samples were prepared by dicing a Lucalox™ tube (Al_2O_3 doped with 0.5 wt% MgO to inhibit abnormal grain growth) into pieces 2 mm x 3 mm using a diamond-embedded wafering saw. The inside surface of the initially curved samples was polished flat using 30 μm diamond lapping film. The outside surface was polished flat, but to a 0.5 μm finish using diamond lapping film. Polishing the surface flat eliminated the driving force caused by surface curvature. Sample surfaces were cleaned in acetone and methanol baths for 10 minutes, respectively, using an ultrasonic cleaner.

3.3.2 Alumina Thermal Treatment

Samples were thermally etched in a box furnace in air at 1650˚C for 30 minutes or 16 hours and allowed to cool at 150˚C/min to 1300˚C and 40˚C/min to room temperature. The furnace was initially ramped to 1650˚C at 20˚C/min. Samples were placed in a high-purity alumina crucible packed inside another alumina crucible with alumina powder between the crucibles during thermal etching, illustrated in figure 3.6. The short length of time allowed the thermal grooves to just form and little grain boundary migration to be induced. Subsequent thermal treatments were performed in the same manner for 30 minutes.

3.3.3 Thermal Grooving in the Presence of Glass

Alumina substrates polished in the same manner as above were dimpled on one side until the center of the sample was roughly 10 μm thick. Anorthite (CAS or $CaAl_2Si_2O_8$) powder was sprinkled in the dimple and allowed to form a glass when the sample was brought to 1650˚C. The temperature was held for 6 min before the furnace cooled naturally. The sample geometry can be seen in figure 3.7 and more on the experimental procedure can be found in chapter 5 of this dissertation.

3.3.4 Characterization of Thermal Grooves

Visible-light microscopy (VLM) was used to map the surface after the initial thermal etch for all samples. The VLM map, shown in figure 3.8, assisted in finding recognizable grains with the CCD camera on the Park Systems XE-70 AFM. The same group of grains was monitored after each thermal treatment with the AFM using the XEP data acquisition software. Groove profiles were measured with the XEI data analysis software. This technique gave non-destructive observation of subsequent grooving behavior.

Contact-mode AFM tips used were provided by MikroMasch and were backside Al-coated Si with a tip radius of <10 nm, cantilever length of 110 μm and spring constant of 0.95 N/m. However, tip artifacts are inevitable during AFM imaging. Munoz, et al.[15] give an extensive description of possible artifacts in AFM images and measurements. The same considerations were taken in this study. The same scanning direction was used for all measurements and tips that gave consistent measurements based on a standard groove were used. Measurements from scan profiles were taken at the same magnification for the set of grooves. Therefore, any scanning artifacts in the data collected here would be systematic and would not alter the qualitative data. Marshall, et al.[25] describe a very good tip radius correction procedure, if needed.

3.4 Results

3.4.1 Grooving in Alumina

A grain boundary in the middle of separating from its remnant groove can be seen in figure 3.9-11. Bridges of material form over the original thermal groove as the boundary moves. Figures 3.10 and 3.11 show that the dark regions in the AFM height image are the thermal groove and that a thermal ridge on the opposite side of the boundary has already formed. The bridges form at a periodic spacing of roughly 2 μm.

The time dependence on groove formation is evident in figure 3.12. Samples held at temperature for only 30 min had grooves much thinner and not as deep as sample surfaces held at 1650˚C for 16 hr. Both show classic thermal groove formations.

3.4.2 Grooving in the Presence of Glass

When the alumina surface was exposed to glass for a short amount of time, the grain boundaries that resided under the glass droplets had larger thermal grooves than grain boundaries that were not under a droplet, as shown in the VLM image in figure 3.7.

3.4.3 Triple Junction Migration

For the first time, remnant triple junctions were observed in samples held at temperature for 16 hr. Figure 3.14 shows that the remnant triple junction has moved with two out of three grain boundaries that connect to it. The grain boundaries have also left remnant grooves behind. The section analysis in figure 3.15 proves that a remnant boundary exists opposite the actual triple junction from a real grain boundary.

3.5 Discussion

Sata and Sasamoto[26] found that alumina does not vaporize unless exposed to high temperatures (≥1800˚C) or under vacuum (10^{-2}-10^{-3} Pa). Therefore, the study presented here assumes that the only mass transport mechanism working to form the thermal

grooves in the alumina is surface diffusion. In addition, AFM measurements of partial angles have found to be inaccurate, and should only be used as estimates.[3] The finite tip radius causes underestimates of high-aspect ratio grooves.

3.5.1 Grooving in Alumina

The migrating boundary shown in figure 3.9 is a unique observation. A boundary during migration has not been observed before. The quenched behavior shows that a groove must move across the surface to meet the grain boundary, as proposed in figure 3.3. The bridges indicate that surface diffusion is moving material. It is yet unclear what species are diffusion, but Al-O surface diffusion of stoichiometric units rather than individual atoms has been proposed.[19]

While early work[12] on Ag showed that grooves move with the grain boundary and remnant grooves are not often left behind, the bonding in metals may allow boundary migration with the corresponding groove to occur easier than that of ionic and covalently bonded ceramics. The boundary would be more mobile, and therefore, grooves would have less time to form at the surface before the boundary moved, again. In addition, the previous work[12] was not thermally cycled to see if remnant grooves developed after grain boundaries were pinned during cooling.

The fact that the size of thermal grooves changes with exposure time to high temperatures shows that the entire system is takes a long time to achieve equilibrium. After 16h, shown in figure 3.12, the grain boundaries, thermal grooves and thermal ridges are still dynamic.

Using AFM measurements of partial angle, groove depth and groove width, Mullins'[13] theory of surface diffusion at thermal grooves may be proved or disproved by comparing the measured values to the expected values based on equation 3.15.

$$\frac{w}{d_s} = \frac{4.73}{\tan(90 - \theta_s)} \qquad [3.15]$$

Again, using experimentally obtained data, the surface energy, γ_s, and the surface diffusion coefficient, D_s, may be backed out using equation 3.10 from Mullins.[13] Surface diffusion is expected to be the dominant groove formation mechanism, since the processing temperature was considerably below the melting point of alumina and thermal treatment in air is considered an inert atmosphere for oxides. Shin, et al.[16] measured a surface diffusion coefficient for pure alumina of $8.22 \times 10^{7} \exp[-577/RT]$ using the same technique.

3.5.2 Grooving in the Presence of Glass

The VLM image in figure 3.7 clearly shows that grain boundary grooving is accelerated when exposed to glass. The grooves can be easily seen with the VLM after only 6 min at 1650˚C, opposed to 30 min when no glass is present. Diffusion occurs faster through a liquid medium than at the surface. The material can move through the glass when it is in liquid form and deposit onto the thermal ridges, as illustrated in figure 3.13. This observation confirms that surface diffusion, with or without glass present, is the dominant formation mechanism for thermal grooves.

3.5.3 Triple Junction Migration

Remnant triple junctions were observed in the AFM height images in figure 3.14. The triple junction has migrated along with two grain boundaries. In order to maintain the force balance at the triple junctions, more than one boundary must move simultaneously. The curvature of the interface at the real triple junction, seen in figure 3.15, and the boundary parallel to the remnant groove is pointed towards the direction of triple junction motion. The analogy that the triple junction is being pulled along the grain boundary can be made.

The faceting on either side of the remnant grooves is the same or beginning to change over to same as the rest of the grain. The surface reconstruction is another indication, in addition to the shallow section analysis in figure 3.15, that the broad boundaries are actually remnant grooves.

3.6 Summary and Future Work

For the first time, a grain boundary in the midst of migrating and leaving its remnant groove behind was observed. In addition, remnant triple junctions were also observed. The fact that these features were observed after short and long periods of time at temperature proves that thermal grooving is a non-equilibrium condition. Grooving is accelerated when the boundary is exposed to glass at the surface.

Further work needs to be completed in order to fully understand thermal grooves. Crystal orientation plays a roll in the type of thermal grooves formed.[3] EBSD should be used to along with cross-section analysis in the TEM to determine orientations of the surface and the interface. A preferred direction of motion may also be found for migrating triple junctions. Finally, more thermal treatments held for varying times and cooling rates may better elucidate the thermal groove formation mechanism.

Appendix 3.1: Chemical Grooving

The use of chemical etchants to expose subsurface features of crystalline materials is not new. The method is particularly useful for monitoring dislocation climb and glide and to determine slip systems of materials. Since grain boundaries are made-up of networks of dislocations, the basic science studies of dislocations are relevant.[27] Etch pits have been used to locate where dislocations emerge at the crystal surface for years. Gilman and Johnston[28] were the first to really look at the structure of etch pits and used to them to monitor migrating dislocations. The same dislocation in LiF was monitored before and after annealing or straining the LiF crystals. Their work showed that etch pits at dislocations have a pyramidal shape, but etch pits that are left after the dislocation have flat bottoms. In addition, the shape of the etch pit can indicate whether the dislocation is edge or screw character.

The etch pit geometry closely resembles a grain boundary groove. The groove attached to the boundary is sharp in profile, but remnant grooves become shallow as the boundary migrates away and healing begins. Gilman and Johnston[28] even noted that

when a dislocation moved during etching, a groove formed rather than a single etch pit. They also noted[29] that etch pits form faster at an edge dislocation than at a screw dislocation, implying that crystallography is important in groove formation.

Surface faceting also resembles thermal grooving of grain boundaries.[30] Facets form at the same time as thermal grooves and their morphology depends on orientation, surface energy and annealing atmosphere. When facets have hill-and-valley morphology, a sharp groove exists with asymmetric humps on either side. The humps nucleate more facets. Facets also have the ability to move on the surface, similar to thermal grooves. In addition, thermal grooves themselves can be faceted.

Munoz[15] has done some preliminary work on chemical etching grain boundary grooves, but no quantitative analysis has been done to date.

The etching rate is determined by the type of acids used and the length of time the crystal is exposed to the etchant.[29] Etchants are usually complex recipes of acids and have a limited useful lifetime. Eventually the etching reagent is saturated with the material etched away and the process slows or stops.[29] In parallel, thermal grooves stop or are slow to form when the atmosphere during the anneal is incorrect or the partial pressure of the material is reached. Preferred orientations will etch faster than others.[28] Second-phase particles will also etch at different rates.

Similarly to how facets and thermal grooves form, growth and dissolution during chemical etching is thought to happen at step or kink edges at the surface.[29] Chemical etching can preferentially etch compositions, as well. For instance, anorthite droplets can be etched away with hydrofluoric acid to reveal the alumna substrate's faceting structure underneath the droplet.[31]

Chemical polishing relies on using strong acids to etch the entire sample surface. The technique is often combined with mechanical polishing for chemical-mechanical polishing (CMP). The technique is often used in preparation of microelectronics, since materials can be polished to a nearly damage-free surface. Recipes used in industry are

often proprietary, so finding data on etch rates of particular recipes is often difficult. Chemical polishing can be used on materials that are defect free or have defects impervious to chemical etching. If care is not taken, preferential etching of specific features will occur, as described earlier. As previously alluded to, chemical polishing rates depend on the chemical recipe and the material being polished. A recipe that works well on Si may not do anything on Al_2O_3 or polish Al much too quickly. The chemicals used for polishing are usually strong acids and bases; therefore, safety becomes a concern.

Appendix 3.2: Grooving by Ion Bombardment

Ion milling is a common thinning and polishing technique for TEM sample preparation.[20] Ion milling with Ar is a typical final step to remove any mechanical damage from mechanical polishing. Conventional ion mills operate in a range from 0—5kV and can be roughly focused to regions on the surface. The ions bombard the surface and knock-off or sputter the material away from the surface in order to thin the sample. However, specimen heating, knock-on damage and ion implantation are all possible problems with the technique.

The FIB tool has become an invaluable tool for TEM sample preparation. Using the same concept as traditional ion milling, metal ions are accelerated between 0—30kV within an SEM. By combining a liquid-metal ion source with the SEM column, specific regions of the bulk can be thinned to electron transparency. The tool has eliminated most of the luck needed when making a TEM specimen. However, the FIB has the same limitations as traditional ion milling. The ion implantation and knock-on damage is even worse with the FIB, since the ions are accelerated much more, and thus, surface coatings are needed to protect any important surface features. Preferred milling of grains of different orientation can occur, and an example may be seen in figure 3.19.

In addition to the limitations given above, ion bombardment can preferentially etch materials and features within the sample in both traditional and FIB milling. In particular, grain boundaries have been shown to etch quicker than the bulk material.

Appendix 3.3: The Role of Triple Junctions

As described in figure 3.4 and equation 3.2, triple junctions of grains are balanced by three surface tensions. However, in this case, the vapor is another grain. Chalmers, King and Shuttleworth[12] proposed that the only way in which grain growth could proceed is if the overall surface energy was reduced. The only way this was possible was to reduce the grain boundary energy. At a grain-boundary triple-junction, when all of the surface tensions are exactly balanced, the angles $\gamma, \alpha,$ and β will each equal 120˚ and the boundaries will be straight. Boundary migration is the system's attempt at reaching this equilibrium. Grooving will occur at the point where everything balances. Grain boundary grooves are constant far away from triple junctions, but dramatically change at the triple point in order for the interfacial energies of the intersecting grain boundaries to be accommodated.[32]

Thermally grooved Cu was looked at using scanning tunneling microscopy.[32] The triple junction grooves were approximated to be tetrahedrons and were assumed to be 33% deeper than the corresponding grain boundary grooves. The tetrahedral shape of the triple junction grooves was based on the following approximations: 1) 120˚ grain boundary intersection angles, 2) constant triple line tension, 3) constant grain boundary groove angles and 4) the absence of interfacial torques. However, these approximations identify only equilibrium. Systems not meeting equilibrium conditions were found to have positive triple line tensions. Measured triple line tensions were found to be two orders of magnitude larger than line dislocations in a Cu lattice, which may indicate that triple lines have character similar to disclinations.

Grain boundary migration models do not usually consider triple junctions do to the difficulty in measuring triple junction properties. A steady-state triple junction mobility in two-dimensions has been proposed by Gottstein, Shvindlerman and coworkers.[33] The angle of grain boundary intersection is the main driving force for grain boundary and triple junction migration. The group proposed that the triple junctions will drag the grain boundaries if the triple junction mobility is smaller than the grain boundary

mobility. The grain boundaries become more mobile and govern the migration rate. The grain boundaries will try to establish the equilibrium grain boundary intersection angle of 120˚. However, if the triple junction mobility is larger than the grain boundary mobility, the triple junctions will determine the rate of grain boundary migration and the intersection angles will approach 0˚. As temperature increases, triple junction mobility was found to become larger and promote equilibrium grain boundary morphologies. Grain size was also found to affect whether the triple junctions or grain boundaries govern migration.[5] Unfortunately, measuring the triple junction mobility is impossible at this time, so quantitative growth rates for materials can not be determined.

Gottstein and Shvindlerman[5] also applied these observations to the Von-Neumann-Mullins relation[4] (equation 3.1). Triple junctions were found to slow the rate at which grains with n<6 shrink and grains with n>6 grow. In addition, they determined that regular shaped polyhedral grains would be in equilibrium and cease to grow, even if the grains were not hexagons, in contrary to what Mullins[4] proposed, as long as the grain was not shaped in a triangle. However, if the grains were not regular polyhedrons, the angle of the intersecting grain boundaries would provide the necessary driving force for grain boundary migration. A larger grain size, measured by the grain's perimeter was argued to increase the rate of grain boundary migration. Grain boundary inclination, which is the case for all migrating boundaries,[3] was not accounted for in the group's model. The misorientation across grain boundaries was also not considered in any models describing triple junctions.

Appendix 3.4: Materials used in Two-Phase SOFCs

Solid-oxide fuel cells (SOFCs) require intimate contact between several phases. A triple-phase boundary results. This point is the least understood, but most important part of a SOFC. Several traditional oxides have been used in SOFC fabrication.

Cubic zirconia (CZ), c-ZrO_2, has the fluorite structure where the oxygen ions fill the face-centered cubic lattice and zirconium ions fill all eight tetrahedral positions in the unit cell.[9] CZ is only stable at high temperatures or when stabilized. The most common

stabilizing agent is Y_2O_3. Zirconia's melting point of 2677˚C makes it an important refractory material. CZ is also commonly used as a diamond-simulant, but is rarely found in nature. Zirconia is also biologically inert and can be used in joint replacements.

CZ has long been known to be a good candidate for fuel-cell applications. The necessary requirements are: 1) high density (>93%), 2) prevent gas permeation, 3) high ionic conductivity and 4) adequate strength and resistance to thermal shock for real-world applications.[18] CZ has a high ionic conductivity, especially when stabilized. Stabilization with other cations creates oxygen vacancies in the lattice.[9] The same property makes zirconia a good choice for oxygen sensing. YBCO can be grown on ZrO_2 substrates.

Zirconia needs to be stabilized. Solid-solution additives, such as Y_2O_3, CaO and MgO, have been found to stablize and densify zirconia. Several liquid-phase forming additives have also been used to densify zirconia, but the second-phase at grain boundaries degrades the electrical conductivity. Sintering of zirconia is thought to rely on the presence of the stabilizing species by increasing the vacancy concentration, which provides an easier diffusion path through the lattice.

When zirconia is added to Al_2O_3, which are immiscible, the high-temperature tetragonal ZrO_2 phase changes to monoclinic and toughens the Al_2O_3.[9]

Ceria, CeO_2, is also a material used in fuel-cell applications. Like CZ, ceria also has the fluorite structure; the Ce^{4+} ions sit at the tetrahedral interstices while the O^{2-} ions fill the FCC lattice.[9] However, Ce^{3+} can also be present and creates interesting electronic structures and properties in ceria.

Ceria is a common abrasive and is often used in polishing pads for chemical-mechanical polishing. An emerging application for ceria is using it as a catalyst for diesel fuel and to convert carbon monoxide to carbon dioxide in engine exhaust.[9]

References

[1] R. D. Monahan, J. W. Halloran, "Single-Crystal Boundary Migration in Hot-Pressed Aluminum Oxide" J. Am. Ceram. Soc., **62** [11-12] 564-567 (1979).

[2] J. E. Burke, "Role of grain boundaries in sintering" J. Am. Ceram. Soc., **40** [3] 80-85 (1957).

[3] N. E. Munoz, S. R. Gilliss, C. B. Carter, "The monitoring of grain-boundary grooves in alumina" Phil. Mag. Lett., **84** [1] 21-26 (2004).

[4] W. W. Mullins, "Two-Dimensional Motion of Idealized Grain Boundaries" J. Appl. Phys., **27** [8] 900-904 (1956).

[5] G. Gottstein, L. S. Shvindlerman, "Triple junction drag and grain growth in 2D polycrystals" Acta Mater., **50** 703-713 (2002).

[6] A. D. Rollett, W. W. Mullins, "On the Growth of Abnormal Grains" Scripta Mater., **36** [9] 975-980 (1997).

[7] Y. Ikuhara, N. Shibata, T. Watanabe, F. Oba, T. Yamamoto, T. Sakuma, "Grain boundary characters and structures in structural ceramics" Ann. Chim. Sci. Mat., **27** [1] S21-S30 (2002).

[8] S. J. Dillon, M. P. Harmer, "Mechanism of "solid-state" single-crystal conversion in alumina" Journal of the American Ceramic Society, **90** [3] 993-995 (2007).

[9] C. B. Carter, M. G. Norton, Ceramic Materials: Science and Engineering, Springer New York, NY, (2007).

[10] W. W. Mullins, "Effect of thermal grooving on grain boundary motion" Acta Metall., **6** [6] 414-424 (1958).

[11] S. J. Bennison, M. P. Harmer, "Grain-growth kinetics for alumina in the absence of a liquid phase" J. Am. Ceram. Soc., **68** [1] C22-C24 (1985).

[12] B. Chalmers, R. King, R. Shuttleworth, "The thermal etching of silver" Proc. Roy. Soc. A, **193** [1035] 465-483 (1948).

[13] W. W. Mullins, "Theory of thermal grooving" J. Appl. Phys., **28** [3] 333-339 (1957).

[14] A. R. Gaddipati, W. D. Scott, "Surface mass transport of alumina" J. Mater. Sci., **21** 419-423 (1986).

[15] N. E. Munoz, S. R. Gilliss, C. B. Carter, "Remnant grooves on alumina surfaces" Surf. Sci., **573** [3] 391-402 (2004).

[16] W. Shin, W. Seo, K. Koumoto, "Grain-boundary grooves and surface diffusion in polycrystalline alumina measured by atomic force microscope" J. Eur. Ceram. Soc., **18** [6] 595-600 (1998).

[17] D. W. Susnitzky, C. B. Carter, "Identification of α-alumina surface structures by electron diffraction" J. Am. Ceram. Soc., **69** [9] C217-C220 (1986).

[18] S. Wu, E. Gilbart, R. J. Brook, in, Science of Ceramics, Italy, (1983), pp. 371-380.

[19] M. Jin, E. Shimada, Y. Ikuma, "Atomic force microscopy study of surface diffusion in polycrystalline CeO_2 via grain boundary grooving" J. Ceram. Soc. JPN, **108** [5] 456-461 (2000).

[20] D. B. Williams, C. B. Carter, Transmission Electron Microscopy: A Textbook for Materials Science, Plenum New York, (1996).

[21] D. R. Rasmussen, Y. K. Simpson, R. Kilaas, C. B. Carter, "Contrast Effects at Grooved Interfaces" Ultramicroscopy, **30** 52-57 (1989).

[22] J. D. Mun, A. P. Sutton, B. Derby, "Grain growth and texture changes in a Ni foil during diffusion bonding to ZrO2" Phil. Mag. A, **76** [2] 289-305 (1997).

[23] I. E. Reimanis, "Pore Removal During Diffusion Bonding of Nb-Al2o3 Interfaces" Acta Metall. Mater., **40** S67-S74 (1992).

[24] D. Srinivasan, P. R. Subramanian, "Kirkendall porosity during thermal treatment of Mo-Cu nanomultilayers" Mater. Sci. Eng. A-Struct., **459** [1-2] 145-150 (2007).

[25] D. B. Marshall, J. R. Waldrop, P. E. D. Morgan, "Thermal grooving at the interface between alumina and monazite" Acta Mater., **48** [18-19] 4471-4474 (2000).

[26] T. Sata, T. Sasamoto, in: W. D. Kingery (Ed.), Structure and Properties of MgO and Al_2O_3 Ceramics, Columbus, OH, (1984), pp. 541-552.

[27] D. Hull, D. J. Bacon, Introduction to Dislocations, Butterworth Heinemann Oxford, (1965).

[28] J. J. Gilman, W. G. Johnston, "Observations of dislocation glide and climb in lithium fluoride crystals" J. Appl. Phys., **27** [9] 1018-1022 (1956).

[29] J. J. Gilman, W. G. Johnston, G. W. Sears, "Dislocation etch pit formation in lithium fluoride" J. Appl. Phys., **29** [5] 747-754 (1958).

[30] J. R. Heffelfinger, M. W. Bench, C. B. Carter, "On the faceting of ceramic surfaces" Surf. Sci. Let., **343** L1161-L1166 (1995).

[31] S. Ramamurthy, H. Schmalzried, C. B. Carter, "Interaction of Silicate Liquid with a Sapphire Surface" Phil. Mag. A, **80** [11] 2651-2674 (2000).

[32] P. Fortier, G. Palumbo, G. D. Bruce, W. A. Miller, K. T. Aust, "Triple line energy determination by scanning tunneling microscopy" Scripta Metall. Mater., **25** 177-182 (1991).

[33] U. Czubayko, V. G. Sursaeva, G. Gottstein, L. S. Shvindlerman, "Influence of triple junctions on grain boundary motion" Acta Mater., **46** [16] 5863-5871 (1998).

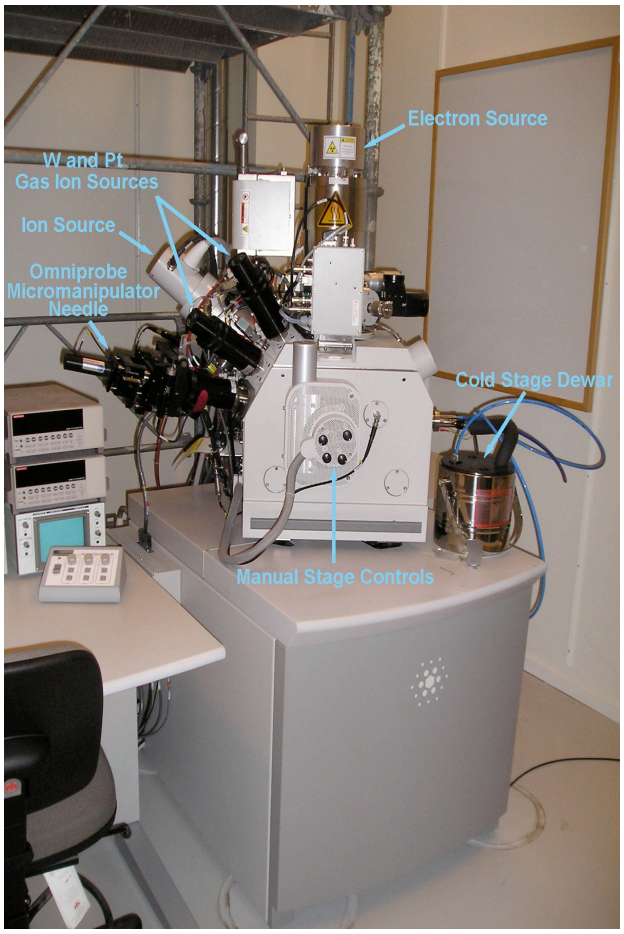

Figure 3.1: The FIB tool uses an ion column aligned 52˚ to the SEM column to mill site-specific cross-sections in bulk material.

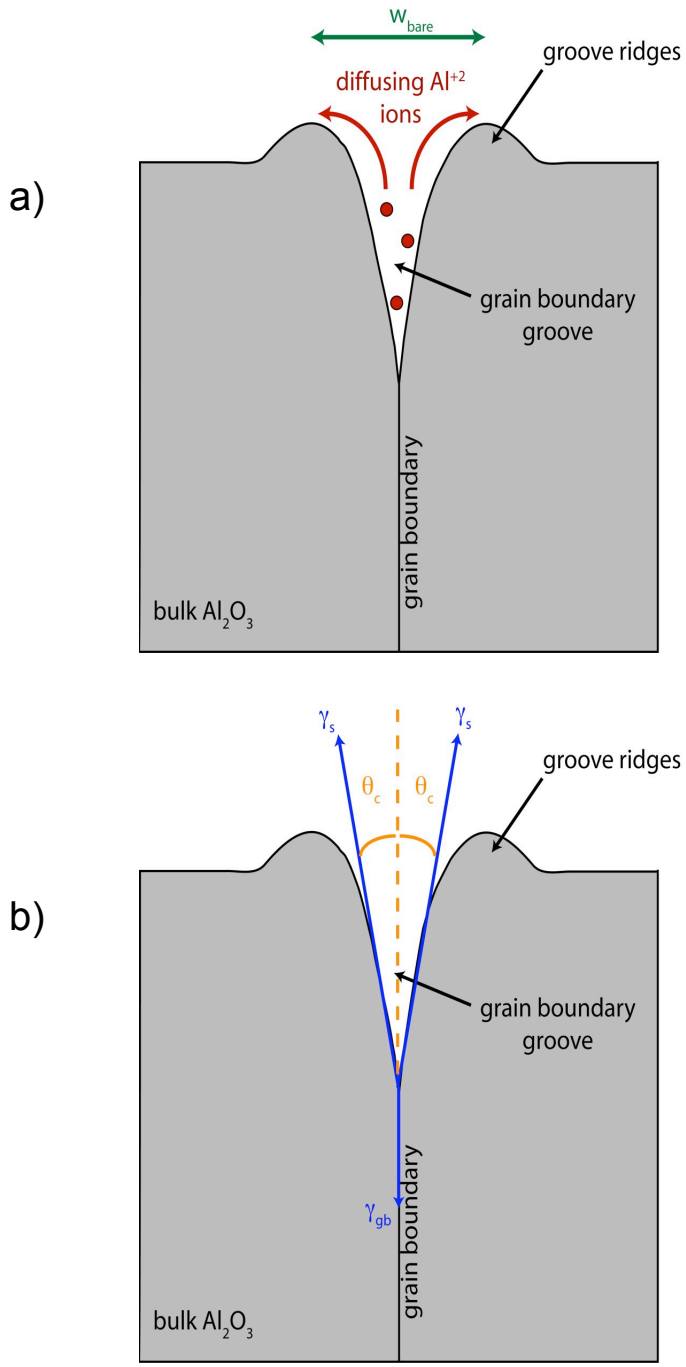

Figure 3.2: (a) illustrates surface diffusion from the grain boundary to the free surface in order to form a thermal groove and ridges. (b) defines the necessary terms that describe the process.

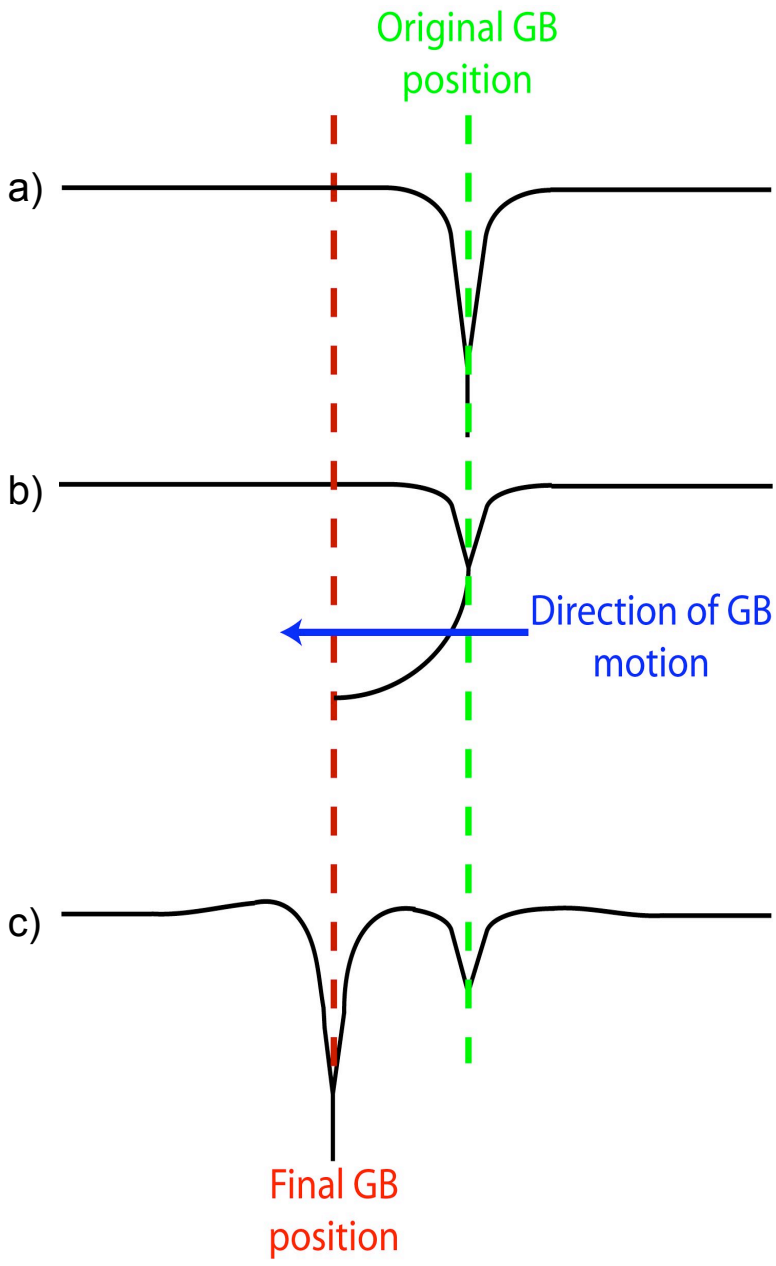

Figure 3.3: When a remnant groove forms, a grain boundary moves from its original position (a) by having the subsurface portion of the grain boundary lead in front of the thermal groove (b). After a critical condition is reacted, the thermal groove snaps into alignment with the grain boundary and leaves a remnant groove behind (c).

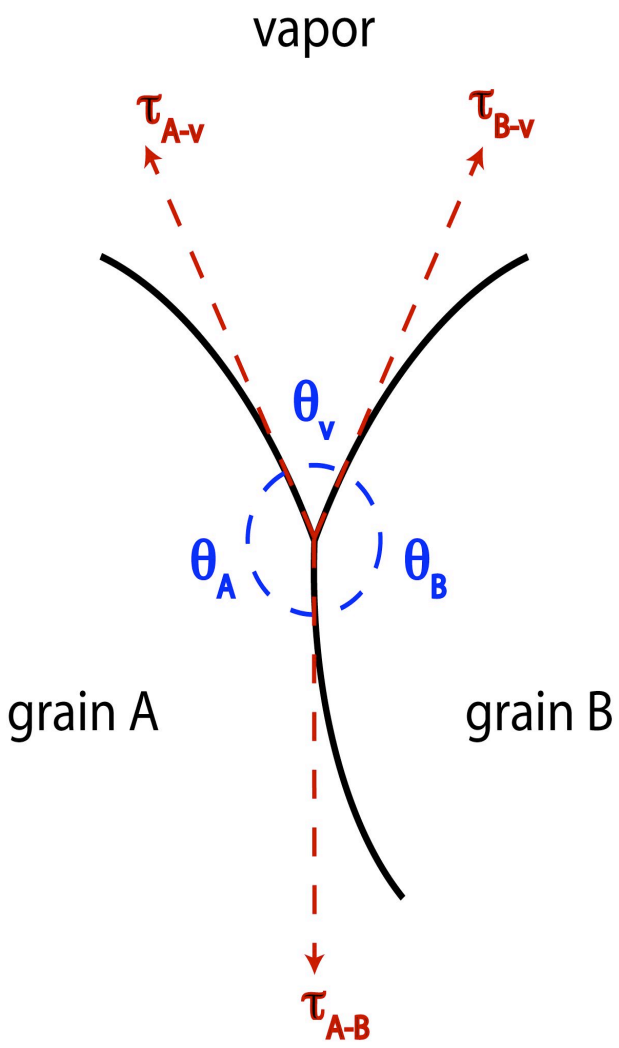

Figure 3.4: Balance of surface tensions at a triple junction triple-phase point.

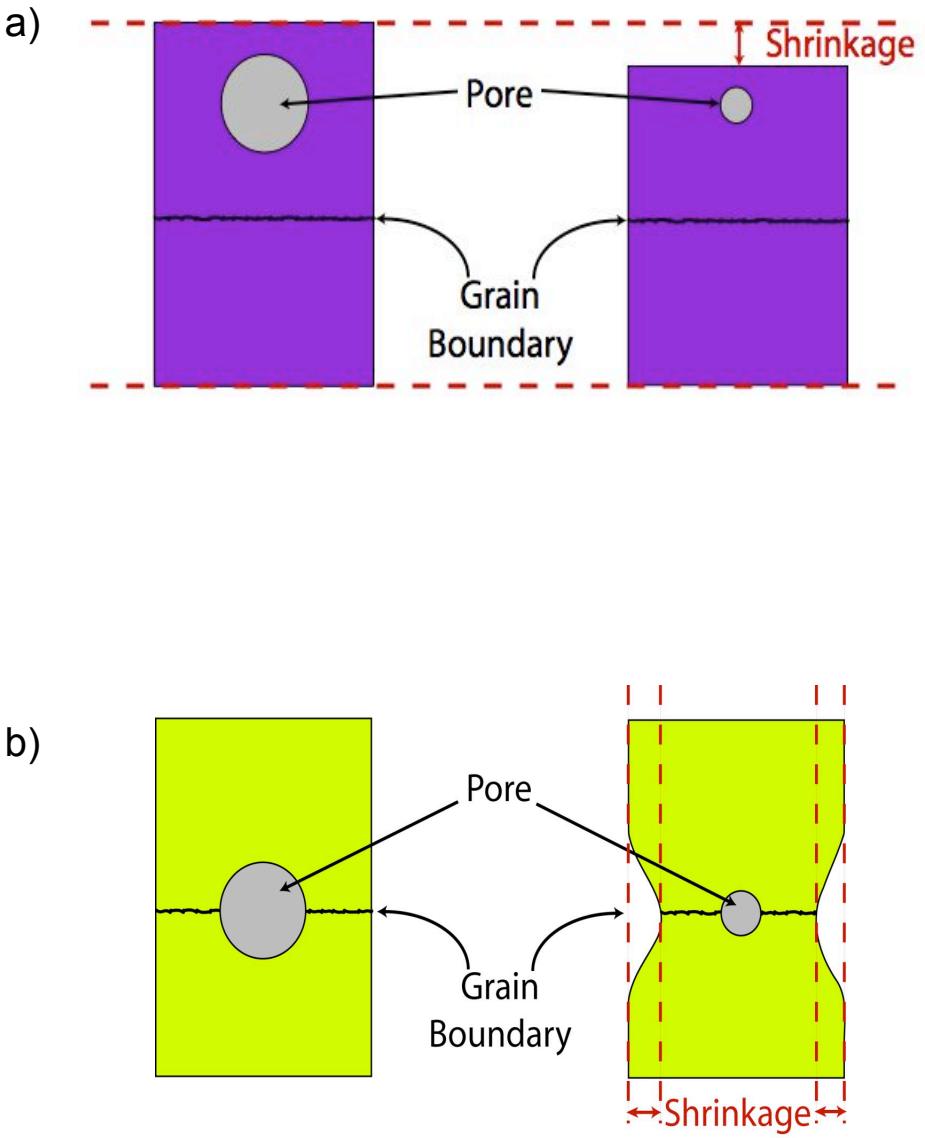

Figure 3.5: Pore shrinkage within the bulk is a removal of vacancies. In order to accommodate vacancies diffusing out of the material, thermal grooves form at the grain boundaries.

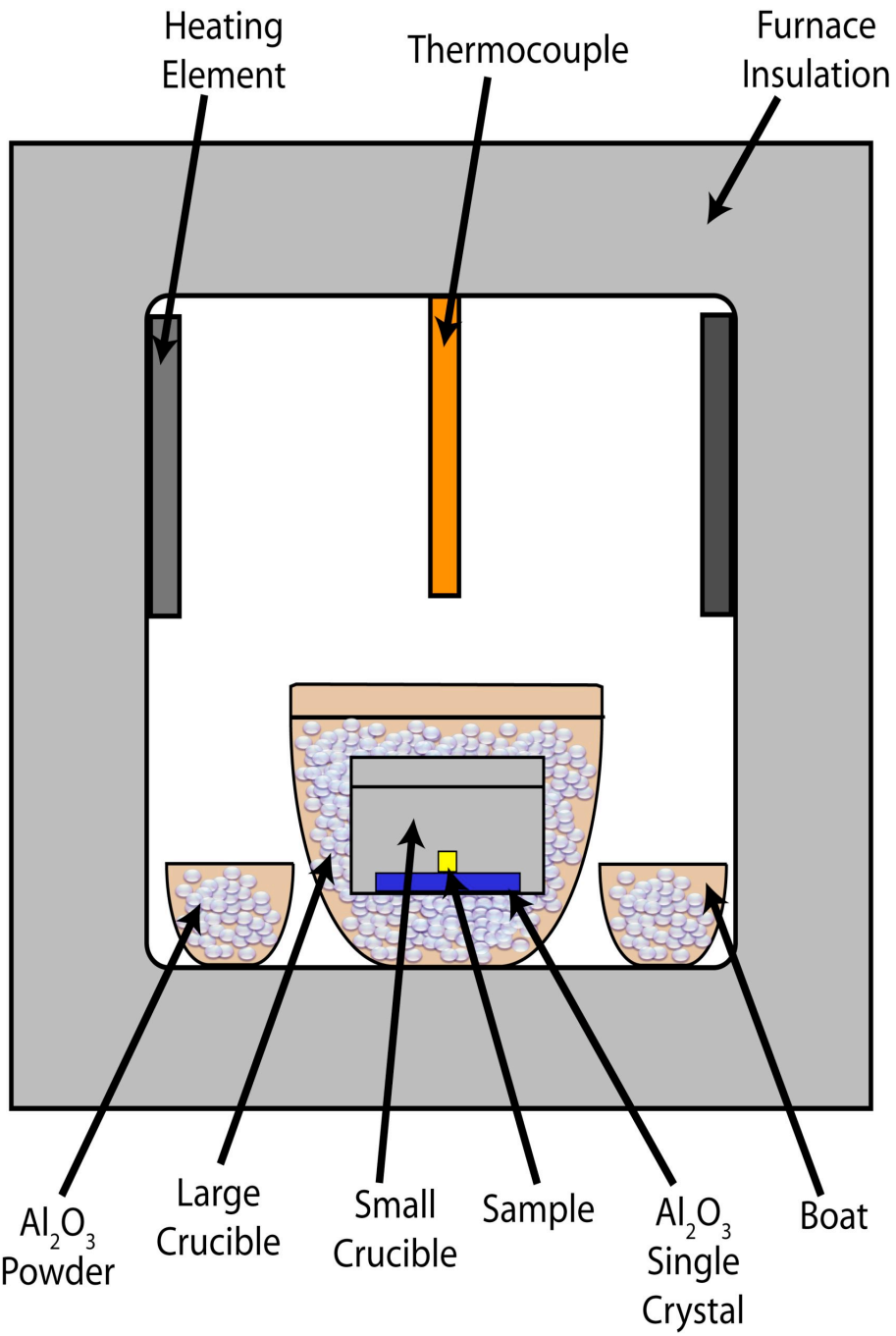

Figure 3.6: Samples were kept clean during annealing by using two crucibles and alumina powder as an impurity getter.

a)

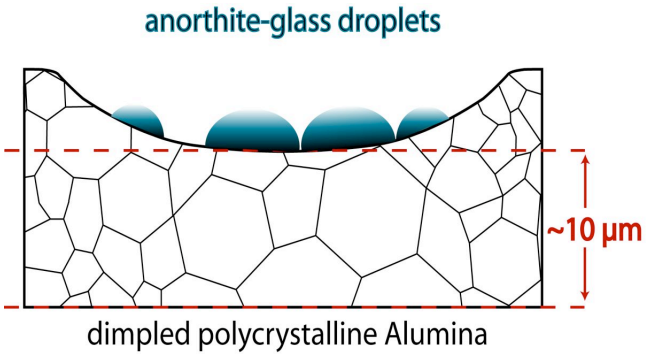

b)

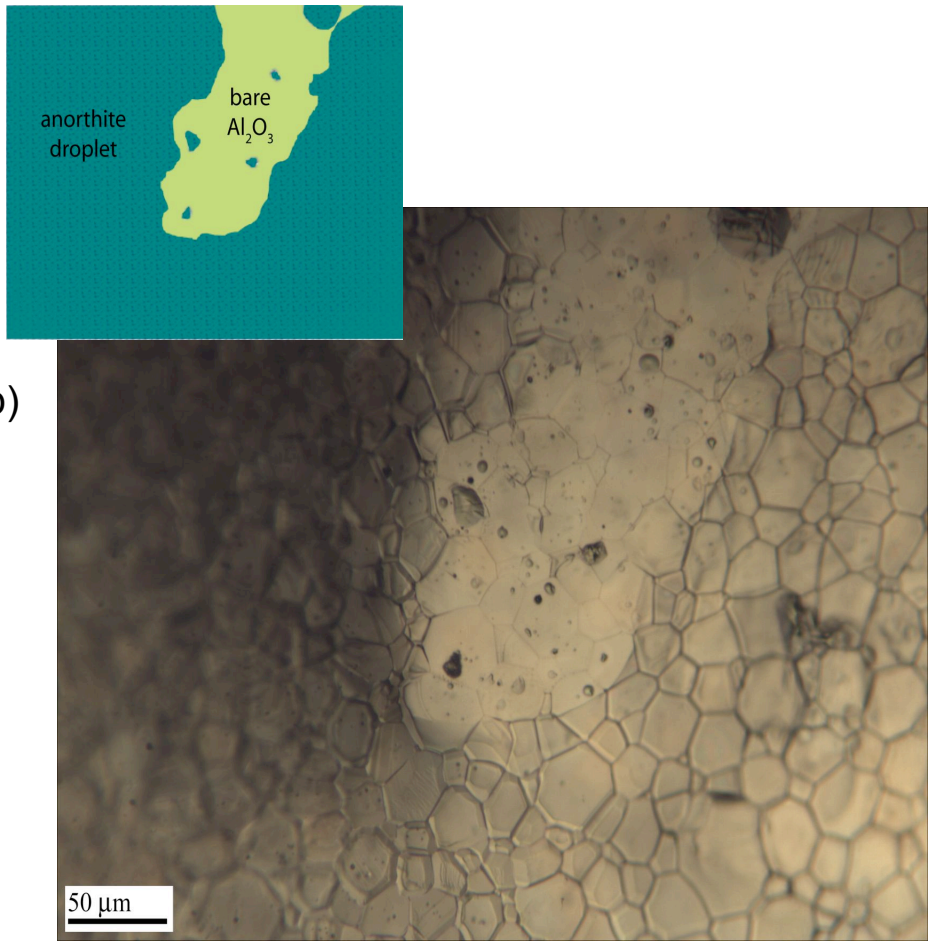

Figure 3.7: The presence of glass allows larger grain boundary grooves to form beneath the glass. The bare surface did not experience accelerated groove formation.

a)

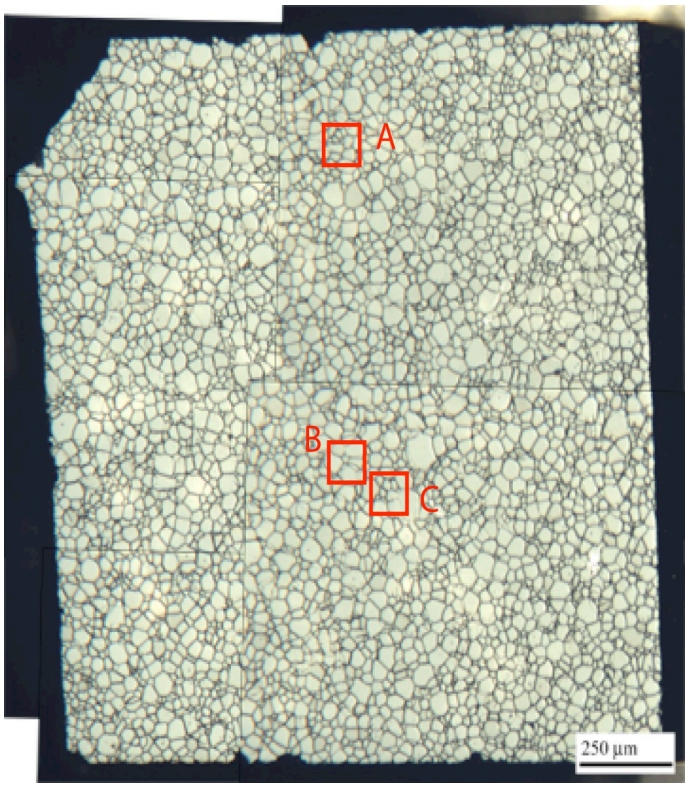

b)

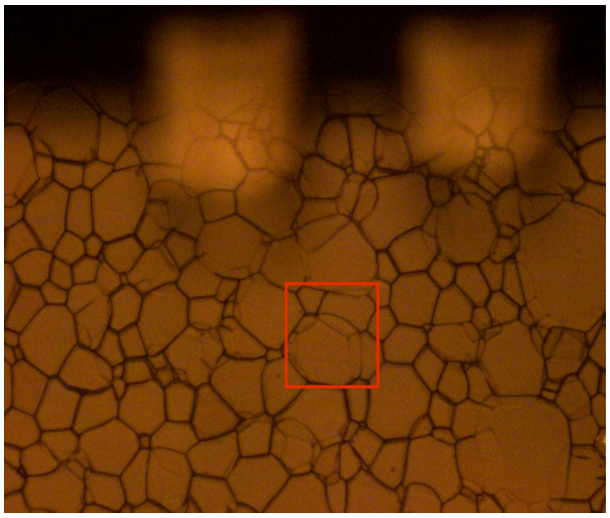

Figure 3.8: VLM mapping of the surface (a) allows the same grains to be found using the VLM optics of the AFM (b). The canitilvers can be seen above the region of interest (out of focus) in (b).

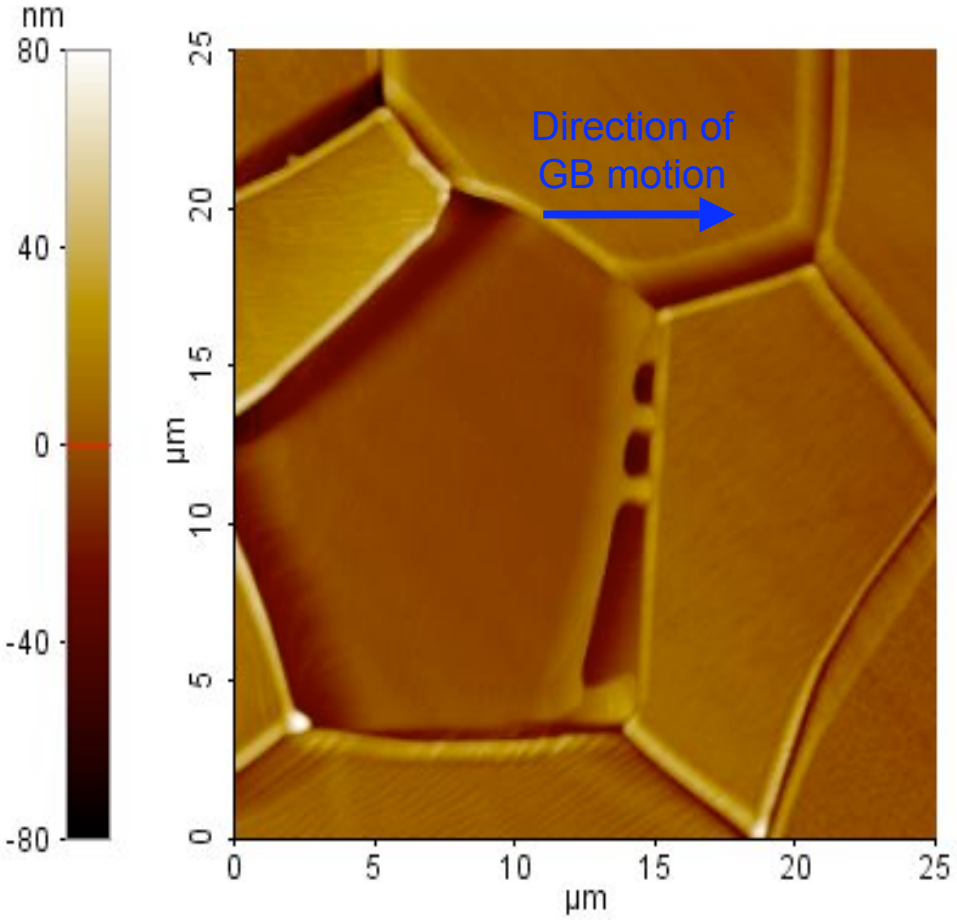

Figure 3.9: A grain boundary is in the middle of migrating and leaving its remnant groove behind.

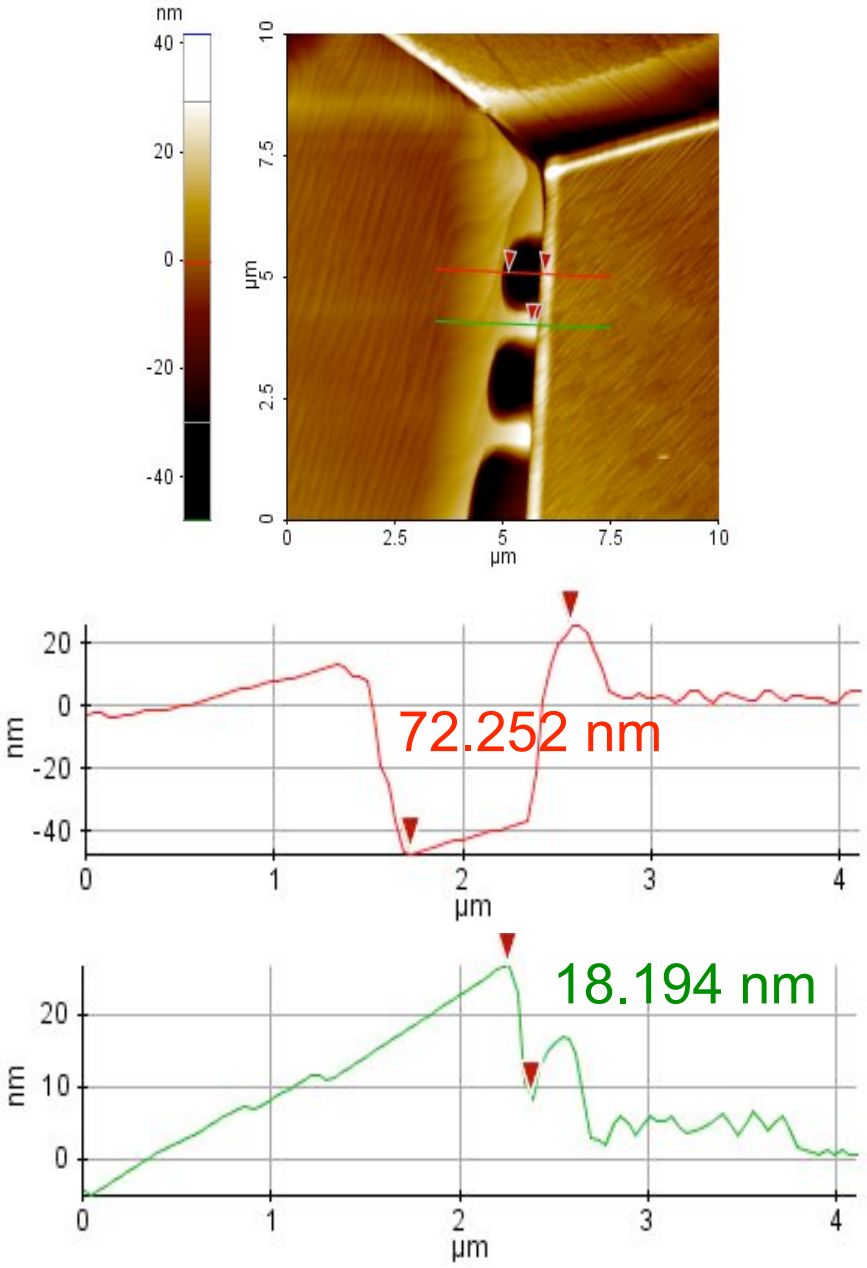

Figure 3.10: Section analysis perpendicular to the migrating grain boundary.

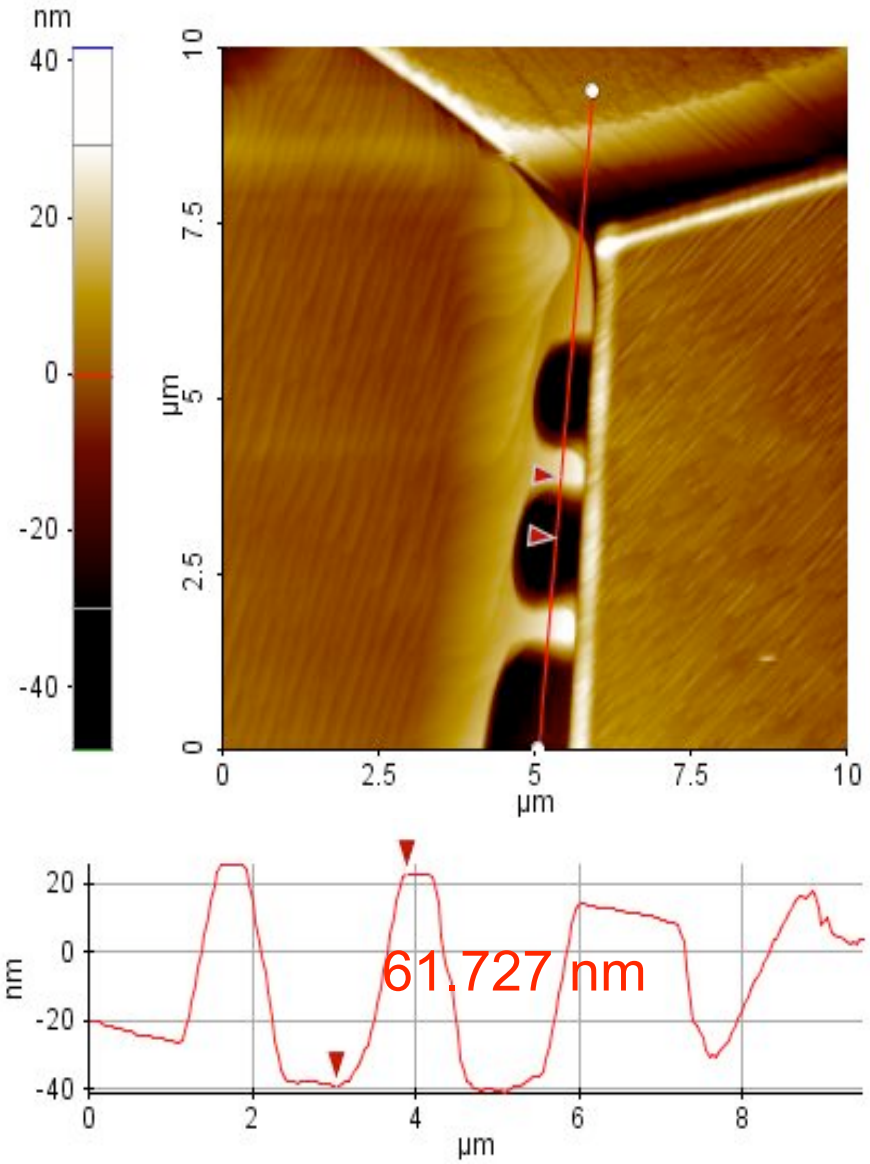

Figure 3.11: Section analysis parallel to the migrating grain boundary.

a)

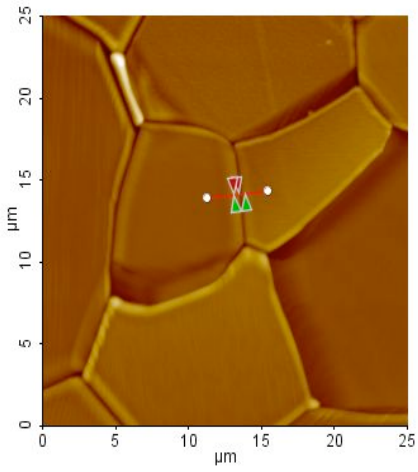

Annealed for 30 min at 1650˚C

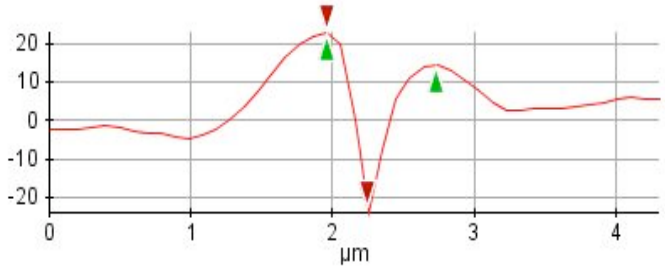

Depth = 45.851 nm

Width = 8.507 nm

b)

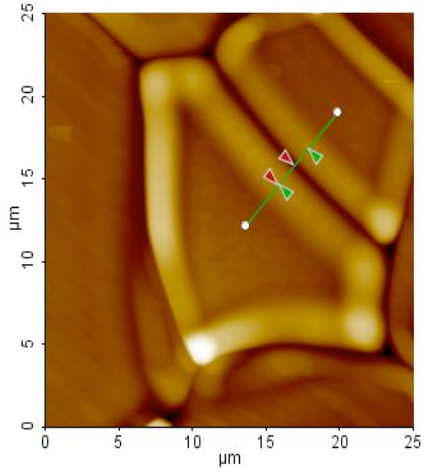

Annealed for 16 hr at 1650˚C

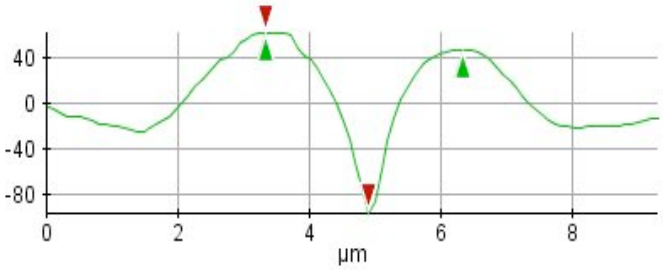

Depth = 157.923 nm

Width = 15.461 nm

Figure 3.12: Thermal groove depth and width is dependent on time at the anneal temperature.

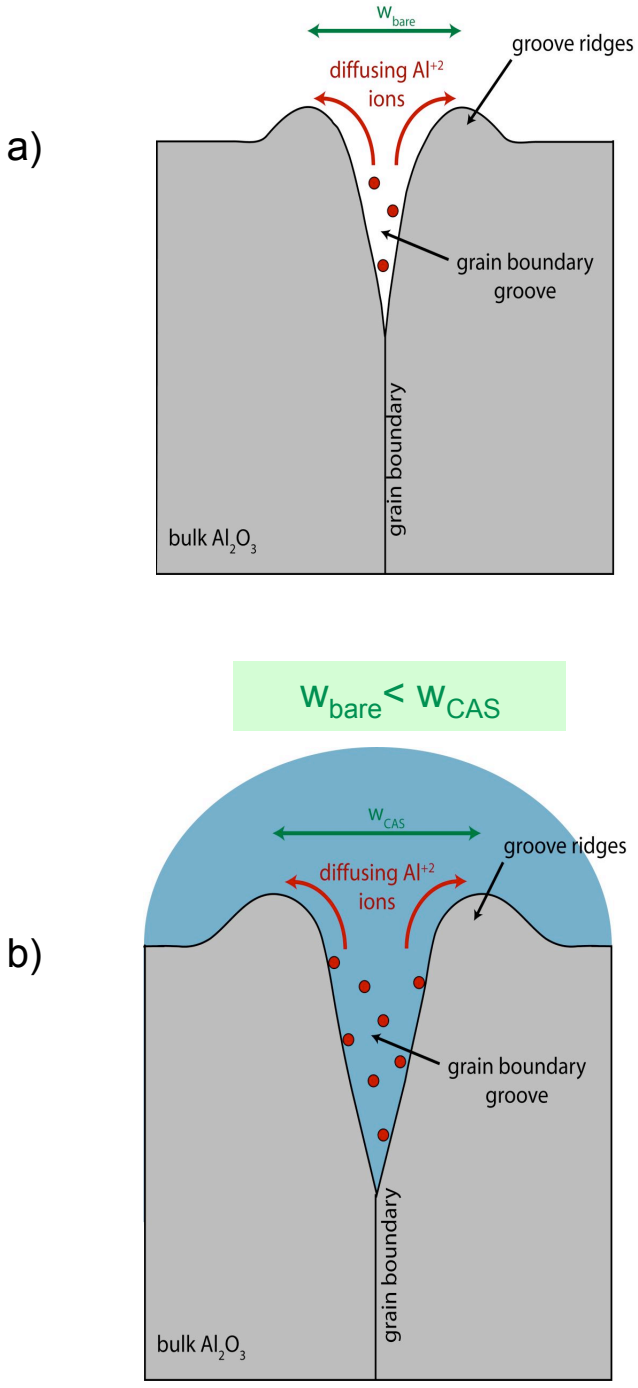

Figure 3.13: (a) Thermal grooves form by surface diffusion from where the grain boundary meets the free surface. (b) Glass at the free surface accelerates grooving since diffusion through the liquid may occur.

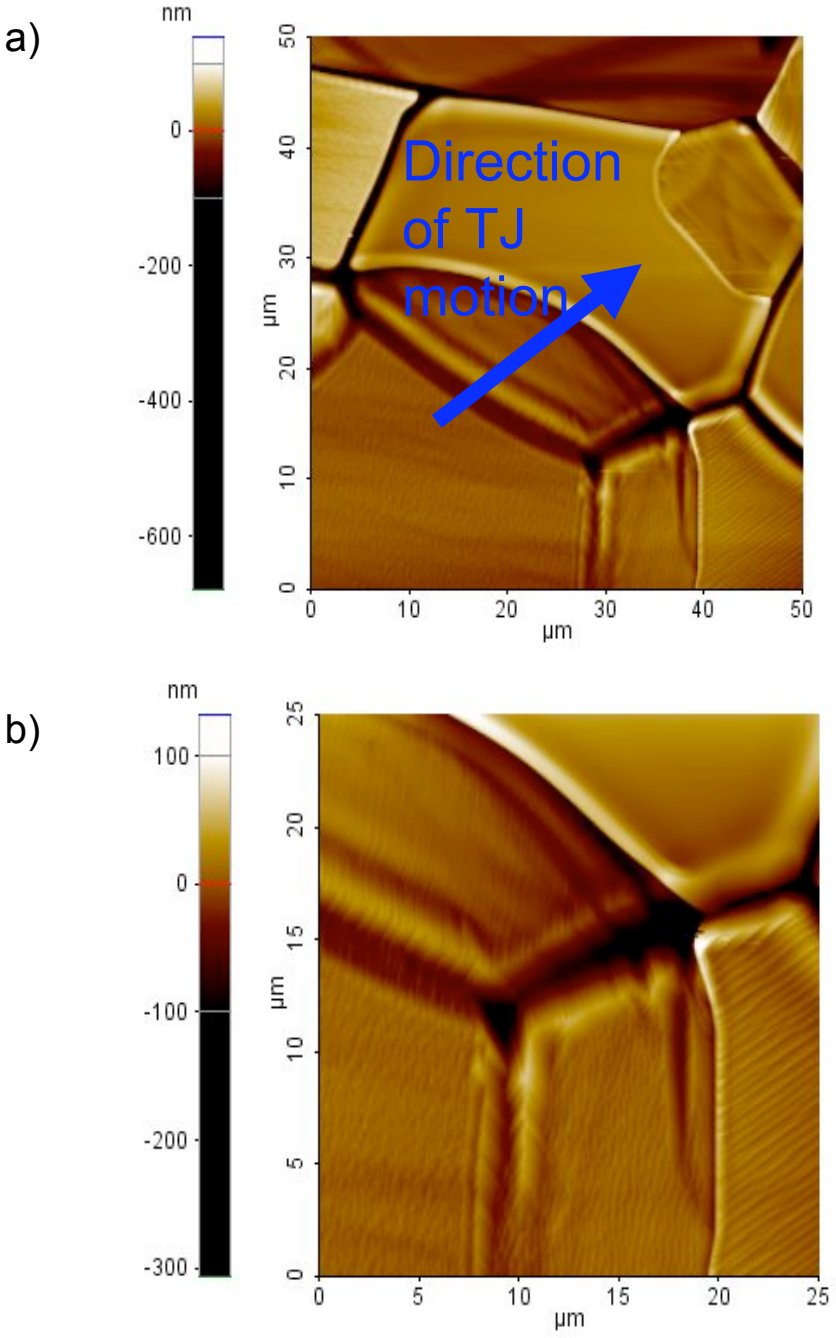

Figure 3.14: Triple junctions can move in conjunction with grain boundaries and leave behind a remnant triple junction at the original position.

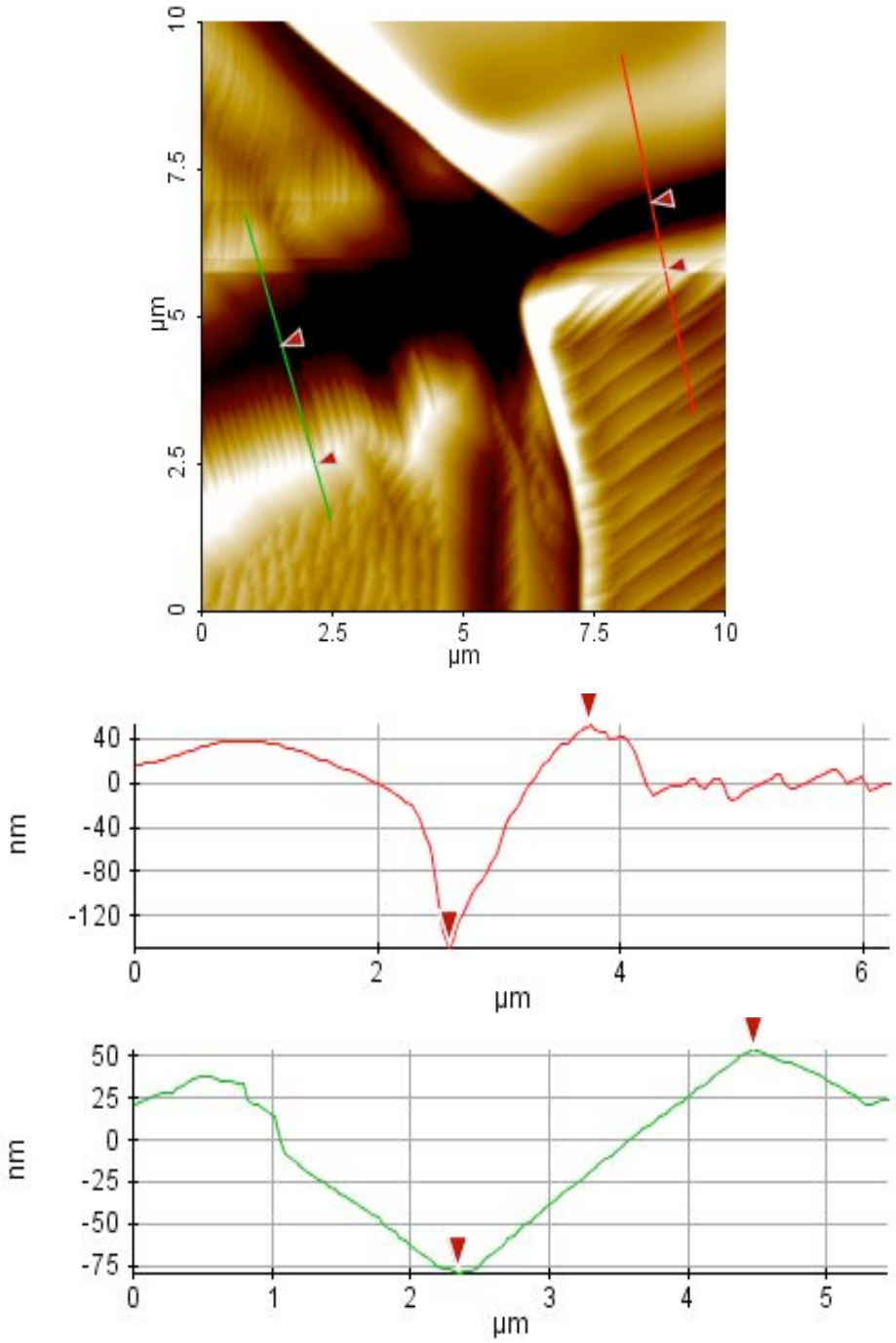

Figure 3.15: The remnant groove (green) section is much more shallow and wider than the actual grain boundary (red).

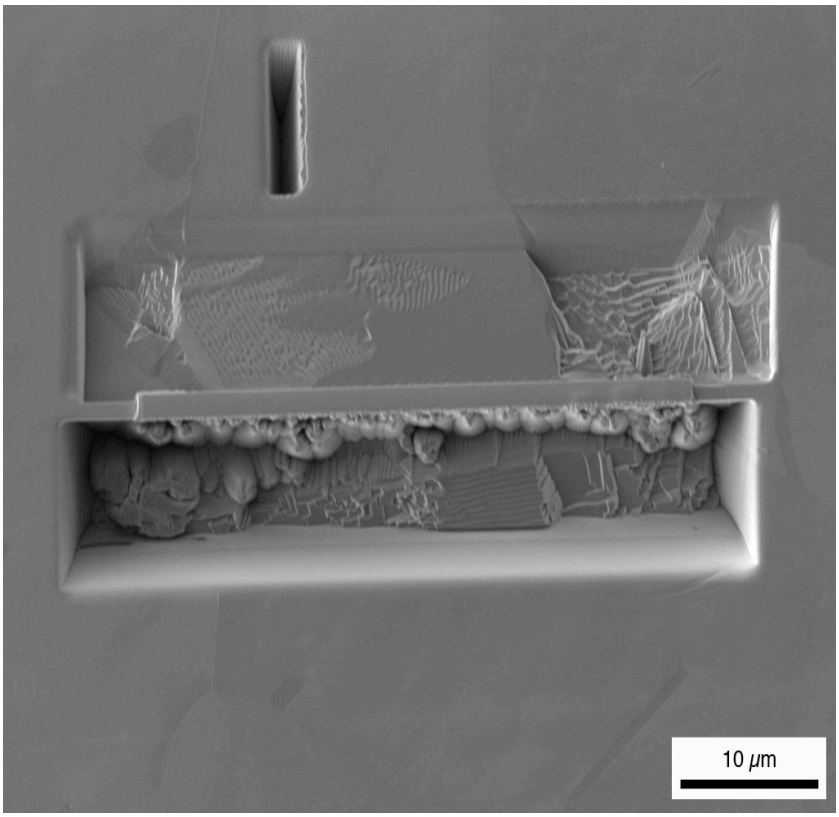

Figure 3.16: Grains of different orientation in Cu have been etched at different rates within the FIB tool.

Chapter 4: Dewetting of SiO_2 on TiO_2

4.1 Introduction

Dynamically active behavior, such as phase separation and dissolution of phases, are desirable in glazes and enameling.[1] Heat and mass transfer are important in crystal growth, coatings and biological applications.[2] Studying convection mechanisms can lead to the ability of tailoring alloy microstructures[3] and understanding flaws in welds. Capillary forces have been shown to heal cracks, form pores and aid in sintering.[4]

Traditional lithography is expensive. However, understanding dewet patterns of thin films would lead to a much less expensive assembly method for various applications. In addition, fewer processing steps would be needed saving production time. Dewet patterns could also be of use in controlling cell growth in cancer research.[5] Wetting and dewetting phenomena are important in another alternative lithography technique; self-assembled monolayers (SAMs) of polymer chains depend on the interfacial energy between the polymer and the metal or semiconductor substrate in microelectronics.[6]

TiO_2 and SiO_2 have several valuable applications. Multilayers of these materials serve as antireflection coatings for solar cells.[7] TiO_2 is a good photocatalyst,[8] has high chemical stability, is nontoxic and is biocompatible[5]. Gas and humidity sensors and air purification also uses TiO_2. TiO_2 has also been shown to be a promising material for water splitting and energy production using the sun.[9] Silica has good mechanical strength and high thermal stability. The SiO_2-TiO_2 system has shown to be hydrophilic and be useful for antifogging coatings.[10] The appendices at the end of this chapter discuss applications in greater detail.

4.1.1 TiO_2 crystallography

TiO_2, also known as titania, can be found in three different phases: rutile, anatase and brookite. Figure 4.1 compares the three possible TiO_2 crystal structures.

Rutile has a tetragonal crystal structure with linked octahedrons.[11] Rutile belongs to the $P4_2/mnm$ space group; lattice parameters of rutile are a = 0.459 nm and c = 0.296 nm. The rutile TiO_2 surface reconstruction has been well characterized for all of the low-index planes of (001), (100) and (110) by several researchers.[12-15] These surfaces are difficult to cleave.[9] As illustrated in figure 4.2, the {001}, {110} and {100} planes are very different. The four-fold symmetry of the {001} plane makes the structure resemble a checkerboard and the Ti-O atoms are seen to form octahedrons. The (100) plane of rutile clearly shows the Ti^{+4} ions are bonded to six O^{-2} atoms. The [001]- and [100]-projections show that rutile is body-centered tetragonal, with Ti^{+4} ions sitting at the lattice points. The formation of symmetric surface facets can be recognized in the (110) projection. The (110) surface is completely oxygen-terminated.

Rutile has a refractive index between 2.065-2.616[16], depending on impurity level, and a high dielectric constant of ~100.[11] When found as a mineral, rutile has a reddish-brown to rusty yellow color.[16] The anisotropy leads to strong internal reflection of white and yellowish-brown.[17] Rutile is also used as a pigment and with insulating second phases, such as Al_2O_3, in gas sensors of CO, CO_2, H_2 and H_2O.[18]

Anatase TiO_2 is also tetragonal, but distorted and much more complicated compared to rutile.[11] From the [100] projection in figure 4.1, the anatase crystal structure appears to be layered. The Ti +4 ions can be seen to sit in the center of the oxygen octahedrons, similar to rutile, the octahedrons are rotated in different directions. The anatase phase has a refractive index of 2.4[7] and a band gap of 3.2-3.25 eV.[10] The (112) plane is the growth and twinning plane in anatase.[10] Anatase TiO_2 is the low-temperature phase, while brookite TiO_2 is stable usually under high pressure. Brookite TiO_2 has the lowest symmetry and is the least stable of the phases. Figure 4.1 shows that orthorhombic brookite is also the most densely-packed phase of TiO_2.

The density of TiO_2 liquid was found to be 3.7611-0.00028T˚C between the temperature range of 1600—1925˚C.[19] Titania is known to have good photocatalytic

properties and experiences a blue-shift in the absorption band when titania particles are quantum dots.[10] Appendix 4.3 gives a description of the phase diagram.

4.1.2 SiO_2 Crystallography

Silica, (SiO_2), has many different forms, as seen in the phase diagram in figure 4.3.[11] Since silica glass was used in this study, the reader is referred elsewhere for a detailed description of the crystalline SiO_2 phases.[11] Because silica has 60% covalent bonding, the Si-O-Si bonds are highly directional and tend to form tetrahedrons. Short range structure of silica glass can exist; small crystallites have been found within a random network of Si-O atoms.[20] The melting point for silica has been measured to be 1723^{o}C.[21] Appendix 4.3 gives a description of the phase diagram.

Silica has several uses. Doped silica glass is commonly found as bottles and windows. Quartz is the preferred measurement standard for X-ray diffraction and indentation studies. Silica is often used in refractory applications and old silica furnace bricks can be recycled into new bricks and insulation for high temperature applications.[22] Silica has a refractive index of 1.4.[7] Integrated circuits utilize thin silica films as an insulating material between device layers.[23]

Silica is the most common mineral on the earth. Gem-quality silica is referred to as quartz when it is clear or yellowish. When the mineral is brownish-grey colored, it is called smoky quartz while rose quartz is pink. Amethyst is created when quartz is properly doped to give it a purple or lavender color. Amethyst and quartz crystals can be seen in figure 4.4. Rutilated quartz forms when gold or reddish-brown rutile needles grow within clear or yellowish quartz. Striking crystallographic patterns form within the stone.

4.2 Background

Wetting phenomena can be related to water on a car windshield. When the water is evenly spread across the glass, the water is said to “wet” the surface. When the water

balls up on the windshield into droplets, the water film has "dewet" the windshield. Films dewet to minimize the liquid/vapor interface area.[24] Surfactants are substances that control the degree of wettability of a film on a substrate. Often when the film is a liquid at higher temperatures, the liquid is more reactive than the solid and reactive wetting may be used to alter the chemistry or surface properties of the system.

In 1804, Young[25] was the first to describe a dewet film or liquid on a substrate in air and recognize that a unique contact angle exists between the three phases. He applied the same theory to any system of curved surfaces. Equilibrium must exist between the surfaces and interfaces that are described by specific angles, as given in equation 4.1 and illustrated in Figure 4.5. The surface energies between the solid-vapor, γ_{SV}, solid-liquid, γ_{SL}, and liquid-vapor, γ_{LV}, interphases must balance using the unique critical angle, θ_c. The critical angle can vary between 0 and 180˚. When this angle is low, the liquid spreads or wets the surface. When the critical angle is high, the liquid balls-up and dewets the solid. The following criterion define the degree of wetting on the surface.[9]

- Non-wetting: $\gamma_{SV} - \gamma_{SL} = \gamma_{LV}$
- Partial wetting: $0 < \gamma_{SV} - \gamma_{SL} < \gamma_{LV}$; $-\gamma_{LV} < \gamma_{SV} - \gamma_{SL} < 0$
- Total wetting: $\gamma_{SV} - \gamma_{SL} < -\gamma_{LV}$

The equilibrium is related to capillary forces and hydrostatic pressure. Capillary forces and hydrostatic pressure (ΔP) also drives sintering of particles, with or without a liquid phase present, as described in equations 4.2 and 4.3, and further explained in chapter 5.[11] Impurities and asperities on the solid surface would be able to change the behavior of the liquid.

$$\gamma_{SV} - \gamma_{SL} = \gamma_{LV} \cos\theta_c \qquad [4.1]$$

$$\Delta P = \frac{2\gamma}{r} \qquad [4.2]$$

$$\gamma = \frac{r\rho g h}{2\cos\theta} \qquad [4.3]$$

Young[25] also noted after studying mercury that a thickness limit existed. Liquid films thinner than the critical thickness were able to dewet, while larger thicknesses were only capable of wetting the surface.

Dewetting of thin films has a similar geometry to that of thermal grooves, as compared in figure 4.6. Both are dictated by Young's equation, which balances the surface tensions of the phases present. Gibbs defined a force similar to a surface tension, ζ_{SL}, describing the solid-liquid interface.[26] This force is exactly balanced by the surface tension between the solid-vapor and liquid-vapor interfaces of a droplet. (equation 4.4)

$$\zeta_{SL} = \gamma_{SL} - \gamma_{SV} \qquad [4.4]$$

An equation of state describing interfacial tensions of a solid-liquid-vapor (SLV) triple junction has been described.[27] Three assumptions were made: 1) The solid surface is smooth and homogeneous, 2) there is no dissolution of the solid, or absorption by the solid of the liquid or vapor and 3) the solid is rigid such that movement of the triple-phase line has no affect on the solid surface. Obviously, these conditions assume an ideal system at equilibrium and do note accurately describe real materials.

Length scales are important in wetting studies.[28] The apparent contact angle of a solid-liquid-vapor (SLV) contact interface may be quite different when studied at low magnification of the bulk than at higher magnification of at the atomic or molecule scale. For instance, if the solid surface has facets only a few unit cell heights in size, the contact angle can be measured incorrectly if the facets are not noticed in a bulk observation. (Figure 4.7) While measuring at low magnifications has been proven to still be valid for Young's equation,[28] it is important to not that this may be a source of measurement error.

4.2.1 Marangoni Convection

Dewetting behavior and pattern formation is determined by film thickness, film curvature, composition and temperature.[29] Liquid films need to balance three forces: 1) capillary forces, 2) buoyancy and 3) hydrodynamic forces (i.e. drag).[2] Large capillary forces are responsible for creating holes in the film.[30]

Surface tension at an interface varies with temperature and composition.[2] Marangoni convection occurs when heat and mass begin to flow due to temperature and composition gradients.[31] When surfaces with films are heated, material diffuses into the film to balance the composition gradient. Even a small temperature difference between the atmosphere and the substrate will prevent the liquid from wetting the surface.[3] The liquid will move towards the hot region of the system,[3] and the solute diffuses far from the substrate, creating another composition gradient. If the Marangoni effect is strong enough relative to time and film viscosity, the heat and material flow can be sustained.[2] Figure 4.8 illustrates Marangoni convection. The warm substrate creates the less pressure within the liquid. The liquid at the liquid-vapor interface is more viscous, creating a larger Marangoni force, and drives material in the direction of the temperature gradient. When two immiscible liquids are mixed and the temperature gradient is large enough, a liquid drop of one fluid may be completely suspended within the other fluid.[3]

When films on a substrate are heated from above, the film remains in hydrostatic equilibrium. But when the temperature difference is between the cool atmosphere and the warmer substrate, the heat flow can create Bénard cells to form in the film.[32] The cells form from the circular motion of material in the film moving from the warm substrate towards the cold surface. A stable hexagonal pattern of Bénard cells in the surface film forms. The fluid moves from near the solid-liquid interface through the center of the cell towards the liquid-vapor interface. Once cooled, the material flows down the edge of the cell back to the solid-liquid interface. A dimple forms in the center of the cell from this convection and surface tension,[32] shown in figure 4.9. A perfect

array of hexagonal cells will form if the system is in steady-state, heating is uniform and no impurities exist. Convection can be treated in two-dimensions in the horizontal plane with the *z*-direction being fixed by the film thickness. Bénard characterized the cell size by defining λ as the wavelength, measured from center-to-center of the cell depressions, and normalizing this value on the fluid layer's thickness. This ratio was found to depend on the fluid layer's composition, decrease as the temperature difference decreased and increase as the fluid layer became deeper.[32] A critical temperature difference exists when a unique λ becomes independent of the fluid's thickness. This type of heat diffusion and convection is often seen in cloud formations in the atmosphere,[33] heating systems of buildings and nuclear power plants.[31] When the heat flow leads to a phase transition the instability is referred to as the Mullins-Sekerka instability.[34, 35]

Prior to Marangoni, Thomson[30] did work on the dewetting of wine on glass surfaces. Dewet cells with radial flow patterns beginning at the center of the droplets were found in the wine and other alcohols. These patterns resembled Bérnard cells. He recognized that the tensile forces of different liquids would be different. He also realized that impurities on a substrate would alter the dewetting patterns of the liquid.

However, Vogel[1] proposed that the differences in density may create turbulent flow within the glass or liquid film. The substrate would dissolve into the film to create a more dense liquid or glass. The surface energy of the film would then change and the film would break apart into droplets. Even Young[25] believed that the force in common between two phases is proportional to the difference of their densities.

Supercooling of the system will create complex patterns to form on the substrate surface. Patterns in different materials systems have been observed experimentally and theoretically.[29, 34, 36, 37] Pattern formation requires a seed for nucleation and a homogeneous environment.[34] The presence of other nearby droplets can alter the droplet's shape.[2] Growth rate of patterns depends on the rate of heat transfer.[34 29] Length-scales develop from the viscosity and surface tension of the film, and dictate the droplet shape and density.[29] When a Marangoni instability is present, temperature and

compositional gradients lead to fingers developing from a dewet droplet. Branching and fingers usually develop in films which exhibit secondary dewetting between the large droplets, where the droplet fingers are on the same order of magnitude as the secondary droplet height.[29, 36, 37] Morphology diagrams are currently being compiled to describe transitions between complex patterns as a function of changes in variables, such as degree of undercooling and composition.[34]

4.2.2 The Rayleigh Instability

Capillary forces are surface-tension driven and can depend on composition.[25] When a critical composition exists, surface tensions and interfacial energies will be specific values describing an equilibrium condition.[1]

The Rayleigh instability occurs when the film or liquid is heated from below.[38] At a critical temperature, the warm material at the bottom begins to move to the top of the film and the cold material moves towards the bottom. The warm material is lighter/less dense than the cold material, and thus, sets up a viscosity gradient to begin convection. Surface tension does not initially play a roll in this form of convection.[38] Questions still exist as to why the films/liquid break apart into droplets, hexagons and cylinders, but surface perturbations are believed to contribute, as shown in figure 4.10.

Mullins and Sekerka[35] derived expressions for capillary effects on an interface perturbation when exposed to a thermal gradient. They proposed that cell formation during solidification at a solid-liquid interface was driven by both heat and mass transport. One possible perturbation able to induce the Rayleigh stability[39] is the degree of miscut of the substrate.[40] If the substrate is not cut exactly on zone, a large degree of anisotropy may be introduced, altering the film's wettability.

The Rayleigh instability is more susceptible to film thickness variations and buoyancy forces play a greater role than in Marangoni convection.[31] While the Rayleigh instability can initiate Bénard cell formation, the cells have little to do with bounyancy.[32] The Rayleigh instability will be responsible for wetting behavior in

intermediate film thicknesses. For films that are very thin, van der Waals forces will control dewetting, while Bénard-Marangoni convection will control very thick films.[24] The Rayleigh instability concerns flow internal to the film, while the Marangoni effect involves the films surfaces.[2]

Pores form during sintering due to capillary forces between the particles and during crack healing. These capillary forces are the same forces involved in the Rayleigh instability. In crack healing, evenly spaced pores with regular shapes form from the nucleation point at the crack tip. Santala and Glaesar[4] showed that surface tension anisotropy is key in pore formation rates. The more stable the crystal face, the slower pores will become isolated from cylindrical cracks. Pores form quickly and easily in unstable crystallographic directions. In addition, the surface tension anisotropy causes the pores to form farther apart than pores forming on isotropic surfaces.

By combining the Rayleigh instability with substrate surface morphologies, dewet droplets can be tuned to produce self-assembled structures.[41-43] Droplet size and surface coverage can be adjusted depending on the substrate orientation and chemical composition. Steps and hills are preferred sites for droplets, rather than terraces and valleys.

4.2.3 Previous Dewetting Studies

Ravishankar, Gilliss and Carter[44] looked at dewetting behavior of anorthite on Al_2O_3. They related the dewetting behavior to the surface reconstruction and how liquid-phase sintering (LPS) would be affected by dewetting at grain boundaries. In another paper,[37] they looked at silica dewetting the (110) and (001) rutile planes. They determined that Marangoni convection and the Rayleigh instability were responsible for the different patterns on the surface. However, a detailed study of the dewetting mechanisms was not presented.

In a study continuing their work,[45] contamination was found to dramatically alter the droplet patterns on the (001) rutile surface. The addition of alumina was found at the

silica-rutile interface. The contamination was attributed to using plasma-enhanced chemical vapor deposition (PECVD), which is known to be a "dirty" deposition technique, rather than pulsed-laser deposition (PLD). However, the work presented here proves that the deposition method does not necessarily introduce contaminates, but rather, sublimation of the crucible during heat treatment changes the film composition.

Monti, et al.[3] have done extensive work monitoring the Marangoni forces using two immiscible liquids and microgravity. By using these conditions, the buoyancy and composition effects during convection can be neglected and effects due to only temperature gradients can be isolated for study. The group has been able to confirm that liquid drops will migrate toward the hotter portions of the surrounding matrix due to the Marangoni effect.

Measuring pore spacing and size can lead to determination of which transport mechanism for diffusion is active in systems during pore formation via the Rayleigh instability.[4] The relative diffusivity can also be measured.

4.3 Experimental

4.3.2 TiO_2 Surface Preparation

As-received single-crystal rutile TiO_2, purchased from Crystal Systems, Inc., was cut into 2 x 2 mm^2 pieces. The (001)-surface orientation was used. Surfaces were cleaned with acetone and methanol using an ultrasonic cleaner for 10 minutes, respectively.

4.3.2 SiO_2 Film Deposition

Two methods were used for film deposition: pulsed-laser deposition (PLD) and plasma-enhanced chemical vapor deposition (PECVD). Films were deposited to be 50 nm, 100 nm or 200 nm thick. PLD films were deposited using a KrF excimer laser operating at 248 nm wavelength and 10 Hz pulse frequency. The substrate heater was kept at 200˚C and the chamber was under 20 mTorr of O_2. Substrates were kept at 200˚C during PECVD, as well. PECVD was used only when the PLD system was not operational.

4.3.3 Thermal Treatment

After film deposition, the surfaces were carefully cleaned in the same manner as above. Using a high-temperature box furnace in air atmosphere, samples were heated to 1600˚C at 20˚/min. Samples were kept at temperature for 1 hr, and air quenched to freeze the high-temperature behavior into the films. Films held for 1 hour or 2 hours were allowed to cool naturally in the furnace.

Two types of crucibles were used during heat treatment. A Pt boat and lid was made by folding Pt foil. The Pt crucible was cleaned using phosphoric acid at 170˚C for 2 hours and rinsed with distilled water before each thermal treatment. Identical heat treatments were also performed using alumina crucibles. Alumina crucibles were cleaned in aqua regia (1 part hydrochloric acid: 1 part nitric acid) at room temperature until the acid stopped bubbling. The crucibles were rinsed in distilled water after acid cleaning.

4.3.3 Atomic Force Microscopy

Atomic force microscopy (AFM) was used to characterize the films after deposition and after thermal treatment. A Park Systems XE-70 and a Digital Instruments Nanoscope III were used in contact mode with Si or Si_3N_4 cantilevers. All cantilevers used had an approximate 10 nm radius of curvature and force constant of roughly 0.95 N/m. The Si cantilevers were Al backside-coated to allow greater signal to be reflected into the piezodetector.

4.3.4 Cross-Section Characterization

Site-specific cross-section samples were made using the FEI Strata Dualbeam focused ion-beam (FIB) tool operated at 30kV. Bulk samples were coated prior to FIB milling with 50 nm of Pt to protect the surface features. An additional 10 nm Pt was deposited using the electron beam in the FIB. Using the electron beam causes less surface amorphization than the ion beam. Samples were milled at 52˚ to the electron beam. An

Omniprobe *in situ* micromanipulator was used to pluck the membrane from the bulk and place onto a Mo transmission electron microscope (TEM) grid cut into half.

TEM imaging was done in an FEI F30 G^2 ultratwin lens operated at 300kV. High-resolution images were taken of the films to determine what was happening at the film-substrate interface. The TEM was also equipped with energy-dispersive spectroscopy (EDS), which was used to determine the film composition. Crystalline films observed in samples heated in alumina crucibles were too thin to do selected-area diffraction (SAD) work to determine the crystalline phase.

4.4 Results

Different dewet patterns were observed depending on the films' processing conditions. Samples with a (001)-surface orientation and thermally treated in a Pt crucible resembled flowers and were somewhat randomly distributed, as shown in figures 4.11 and 4.12. The droplets are arranged on the surface with respect to the underlying crystal orientation. Section analysis of a flower-shaped droplet in figure 4.13 shows that at the center of the droplet's "petals" there is a dimple. In addition, the droplet is surrounded by a skirt or ridge of material.

When the enhanced image feature of the Park Systems XEI analysis software is used in figure 4.14, small features are found to lie between the large droplets. Section analysis shows that these features are small pits in the surface. The droplets were on average 3.5 nm deep, corresponding to 12 unit cells in the rutile TiO_2 *c*-direction.

In some areas of the dewet film, the droplets form tracks of droplets. Several droplets are adjacent to each other and line up to be nearly identical in size and shape, as seen in figures 4.11a and 4.15. When section analysis is used in figure 4.15 to look at the droplets closer, four droplets can be clearly made out to be lying left of a long droplet. This long droplet appears to have undulations on the surface. However, using the enhanced image feature again, these features are found to be scanning artifacts.

The samples with a (001)-surface orientation and annealed in the Al_2O_3 crucibles had etched surfaces or formed droplets and cylinders on top of the substrate facets, depending on the film thickness. Surface etching along crystallographic directions was observed when the initially continuous film was 50 nm thick and deposited via PLD. The dark regions in figure 4.16 are regions were etching has occurred. Surface facets have also formed. Figure 4.17 uses section analysis to prove that classic facets have formed and that depressions in the surface have formed where material has been lost. Similarly to the sample exposed to Pt, the surface exposed to Al_2O_3 had small etch pits. The surface facets appeared to be in the middle of forming when quenched, since they have a wrinkle-like appearance. Both features can be seen in figure 4.18.

When the film thickness is increased, the behavior of the samples annealed in the Al_2O_3 crucibles dramatically changes. When the initially continuous film was 100 nm thick and underwent the same heat treatment as the 50 nm film, the film broke-up into an array of droplets and cylinders residing on top of small surface facets, as seen in figure 4.19. When the film thickness was increased to 200 nm, a dewetting front was observed. The continuous film can be seen to be in the middle of breaking apart into droplets in figure 4.20. The continuous film is still intact at the bottom of both the VLM and AFM images. A TEM cross-section was prepared from the 200 nm sample using the FIB tool. The high-resolution image in figure 4.21 shows an amorphous SiO_2 droplet resting on top of a surface facet. A crystalline layer of β-$Al_2O_3 \bullet TiO_2$ can be seen between the SiO_2 and rutile TiO_2. EDS was used to determine composition of the layers.

4.5 Discussion

4.5.1 Patterns from Pt Crucibles

Instead of a regular pattern of droplets, the films heated in the Pt crucible broke apart into random patterns. However, the droplets were crystallographically aligned. Cooling in ambient atmosphere is not uniform, since the heat from the film warms the local atmosphere and creates convection at the film-vapor interface.[32] The uneven cooling could explain the irregular patterns. The nearly square droplets are aligned with the

(001) rutile TiO_2 surface below. Surface tension is lower in low-index directions, and therefore, is able to influence droplet shape.

The droplets shown at higher magnification in figure 4.12 are clear examples of Bénard-Marangoni convection. Comparing figure 4.12 with figure 4.9, the droplets have formed square Bénard cells by moving dissolving the substrate into the SiO_2 film at temperature. The change in density and composition forms a gradient and drives convection. A change in density would drive the dissolution of TiO_2 into the SiO_2 while at temperature. Upon cooling, the glass becomes supersaturated and the TiO_2 must crash back out of solution, forming the epitactic humps at the interface. The density of SiO_2 changes with the addition of TiO_2 by $\rho_{TiO2} = 3.7611\text{-}0.00028T^{\circ}C$ between the temperature range of 1600 and 1925˚C.[19] The TiO_2 coming out of solution forms the skirt seen in the section analysis of the droplet in figure 4.13. FIB sections have shown that TiO_2 humps have formed near the edge of droplets[37], supporting Vogel's theory[1] and this work.

Contact angles in sessile drop experiments have been shown to depend on the size of the droplet.[27] Since all of the droplets have the same length scale in this study, obviously droplet size is an important factor in overall pattern formation. More regular hexagon patterns in the same materials system has been previously observed in thicker films.[37] It is proposed here that with a thinner glass film, substrate space charge has a greater effect in droplet formation than when the film is thick.

The droplet formation mechanism in figure 4.15 is unclear. Scratches in the film from cleaning or mishandling may lead to local surface tension configuration allowing droplets to align very close to one another. More is needed to understand these formations.

However, figure 4.15 makes and important point regarding scan artifacts in the AFM. When the AFM height image is compared with the enhanced image, one can clearly see the horizontal scan lines in the enhanced image. The noise in scan lines is systematic, i.e. temperature change or vibrations in the room during imaging. When a section

analysis is taken at slight angle to the horizontal, these scan lines produce features that look like ripples on a surface that is actually smooth. Care should be taken in further analysis.

4.5.2 Patterns from Al_2O_3 Crucibles

Using an Al_2O_3 crucible rather than a Pt one for the exact same heat treatment on a film of the same thickness gives a dramatically different result. No evidence of the SiO_2 film could be found. Rather, the surface has large facets that are not in a regular array like in the faceting of alumina described in chapter 2 of this dissertation. Figure 4.17 shows the cross-section of a representative area of the sample. Along with facets, depressions have formed. Bench, et al.[46] grew TiO_2 on Al_2O_3 using PLD. The epitactic film gave diffraction patterns that were not identifiable. Phases were thought to be nonstoichiometric TiO_{2-x} or a reaction layer between TiO_2 and Al_2O_3. Also, Sata and Sasamoto[47] have found that Al_2O_3 will vaporize when heated to high temperatures ($\geq$1800˚C) and/or under vacuum (10^{-2}-10^{-3} Pa). The presence of other phases is thought to decrease the temperature and vapor pressure needed for Al_2O_3 to sublime. Al_2O_3 found between the SiO_2 and TiO_2 layers comes from sublimation of the high-purity crucible during heat treatment (see section 4.5.3). Effects of atmosphere altering the surface tension of the upper layer of a glass film have been reported.[1] The glass film may have been too thin and TiO_2, SiO_2 and Al_2O_3 would be allowed to sublime. The combination of atmosphere, impurities and sublimation of the film and surface may be the reasons for this unexpected surface.

The observations in figure 4.18 confirm this hypothesis. The small dark features in 4.18a are etch pits in the surface. The facets in 4.18b are unexpected irregular due to surface energy considerations. Small etch pits were also observed in the films heated in a Pt crucible, but to a much smaller extent, seen in figure 4.14. While no Al_2O_3 was intentionally placed near the samples during heat treatment, the furnace itself may have contributed enough impurities to allow sublimation of the surface. More work is needed to exactly understand the effect of Al_2O_3 on the TiO_2 surface.

4.5.3 Film thickness variations

When the thickness of the film increases, the film remains but is markedly different from when a Pt crucible is used. Small additions of impurities to a glass film can significantly alter the surface tension of the film.[1] These results have previously been reported elsewhere,[45] but are presented here in order to show a more complete story.

When the film was 100 nm thick, the Rayleigh instability caused the film to break apart. The underlying substrate began to reconstruct. When the substrate is warmer than the film and the surface facets change the local thickness of the film, the film breaks apart into cylinders, and later, droplets of nearly the same size. The cylinders and droplets of glass all sit on the tops of the facets, as seen in figure 4.19.

When the film was 200 nm thick, dewetting occurred more slowly than in the 100 nm thick film. The continuous film at the bottom of both of the images in figure 4.20 breaks apart into droplets. These droplets form a regular array of nearly uniform droplets. Dewetting fronts of thin liquid films may be thought of as having a two-phase region (solid and liquid) growing into a single-phase (liquid only) region on an initially smooth interface, as described by the Mullins-Sekerka instability.[34, 35] Marangoni forces play a roll in solidification fronts by causing the droplets to repel each other.[3] Therefore, thickness is an important factor which helps to determine the dewetting behavior of glass films.

Al_2O_3 was previously confirmed[45] to be present in the samples heat treated in an Al_2O_3 crucible and shown in figure 4.21. The composition was determined using EDS during high-resolution TEM in scanning transmission (STEM) mode. In the previous work, the use of PECVD rather than PLD for the deposition method was thought to introduce impurities. The work presented here proves that this was not the case, and rather, impurities are introduced from the sublimation of crucibles. The formation mechanism of the reaction layer is still unknown.

4.6 Summary and Future Work

In this work, dewetting patterns of SiO_2 glass on rutile TiO_2 substrates were found to depend on the type of crucible used during heat treatment and the thickness of the continuous film. Marangoni and Rayleigh convection are responsible for the type of patterns. Both types of convection are driven by thermal, composition and viscosity gradients. Marangoni convection is also driven by surface tension. Films brought to temperature in Pt crucibles showed Marangoni convection and the formation of Bénard cells. Rayleigh convection was observed when films were heated in the presence of Al_2O_3. The surface in both cases was observed to sublime when the glass film was very thin, but to a lesser extent in films exposed to Pt. The thickness of the film determined whether the film would sublime to leave irregular surface facets, form a uniform array of droplets or be caught in the initial dewetting of the continuous film.

The equilibrium structure of the dewet film should be determined. By heating the films continuously for 24 h at 1600˚C, the dewetting pattern should be at or closer to the equilibrium morphology and concentration. Slow-cooled and quenched samples should be compared after long heat treatments to determine the glass composition at temperature and upon cooling. The experiment should be repeated for a heat treatment of 96 h to determine how long the system needs to achieve equilibrium.

In situ TEM would be an ideal method for watching films dewet on surfaces. However, the small sample size may alter the surface energy of the system. In addition, TEM heating holders are only capable of reaching 1300˚C, which is too low for most ceramic studies. Electron-energy loss spectroscopy (EELS) would be able to determine the Ti oxidation state and give insight into whether the valence plays a roll in pattern formation, sublimation and reaction layer formation.

Appendix 4.1 TiO_2 is Hot

Solar cells are becoming an increasingly more important topic of research. One of the limitations solar cells have is the loss in efficiency due to reflection instead of absorption of the sun's energy. Antireflection coatings (ARCs) have been fabricated in order to allow more wavelengths to be absorbed. ARCs are usually thin films of a dielectric material that has a refractive index equal to the square root of the substrate's refractive index, film thickness equal to one quarter of the wavelength desired for absorption. By layering films of different materials, minimum reflection of multiple layers may be achieved.[7] Recently, work has been done on sol-gel deposited TiO_2, TiO_2-SiO_2, and SiO_2 films onto Si substrates.[7] The overall absorption efficiency was found to improve by 39% and increased absorbance of wavelengths between 400 nm and 1000 nm with a triple-layer system of the three materials. Also, by varying the concentrations of the TiO_2-SiO_2 layer, the refractive index may be tuned to a desired value.

In addition to solar cells, TiO_2 and SiO_2 have desirable photocatalytic properties.[8] Using a liquid-phase deposition method to mix anatase TiO_2 nanoparticles into amorphous SiO_2 films, the photocatalytic behavior was found to increase by a factor of two compared to TiO_2 alone. The SiO_2 retards the crystallite growth of TiO_2, creating a larger quantum confinement effect and more absorption sites on the crystallite surfaces. A higher photocatalytic behavior results.

The photocatalytic properties of TiO_2 films on SiO_2 slides have been used for controlling cell growth in cancer research and biosensing applications.[5] Chinese hamster lung fibroblast V79 cells have been shown to have retarded growth under LED light of 370 nm wavelength. However, when the cells are grown on the TiO_2 films and exposed to the same wavelength, the cell growth rate increases. The UV light is reflected off of the TiO_2 instead of absorbed in the SiO_2. The growth rate can be tuned depending on the power density of UV light the cells are exposed to. Using dielectric stacks of TiO_2-SiO_2 multilayers allows further control of cell growth.

Appendix 4.2 TiO_2/SiO_2 mirrors & the interface

Microcavity structures can be used to amplify internal electric fields and are usually made of several multilayers of different materials.[48] Optical anisotropy can be exploited to get differently polarized modes of varied energies when the microcavities are dielectric mirrors. One common mirror geometry is a distributed Bragg reflector (DBR) and can be used in biological monitoring devices.[48] This geometry is good for external reflectivity of light and provides high contrast.[49] Obliquely-orientated TiO_2-SiO_2 multilayers have shown to create birefringence in mirrors when polarized light is used.[48]

When internal reflection is needed, omni-directional reflectors (ODR) are the better choice, since DBR mirrors will create destructive interference within the cavity from the reflected wave.[49] Internal ODR mirrors are needed to reflect electric and magnetic polarization at any incident angle while limiting optical losses in semiconductor light-emitting diodes (LEDs). Metals do not have high enough reflectivity, but TiO_2-SiO_2 multilayers have been shown to be suitable between high refraction index media (i.e. the air) and the LED.[49] When nanoporous SiO_2 is electron-beam evaporated onto GaP, with a continous TiO_2 film on top of the SiO_2, the mirror loss is reported to be two orders of magnitude better than metal mirrors.

However, a temperature dependence on the refractive index of TiO_2 and SiO_2 exists.[50] The temperature dependence can lead to a shift in wavelengths that are filtered or absorbed. Differing TiO_2 concentrations will change the dependence in TiO_2-SiO_2 films. The difference in thermal expansion between the two components is thought to contribute to the dependence.[50] The refractive index will increase with higher TiO_2 concentrations and lower temperatures.

The sol-gel technique is most commonly used for depositing multilayers or creating varying concentrations of TiO_2-SiO_2 thin-films.[48, 49, 51] Feng, et al.[51] give a detailed recipe for preparing sol-gel films of varying TiO_2-SiO_2 compositons and dopants. Recently, anatase quantum dots were grown on amorphous SiO_2 nanoparticles via sol-gel.[10]

The amorphous layer between anatase TiO_2 and SiO_2, along with the mutual diffusion between multilayers, have been thought to contribute to the blue-shift in the absorbance band of TiO_2-SiO_2 thin films.[10]

Appendix 4.3 TiO_2-SiO_2 phase diagram

The TiO_2-SiO_2 phase diagram was determined in detail by DeVries, Roy and Osborn in 1954.[52] (Figure 4.22) Cristobalite SiO_2 and rutile TiO_2 have a eutectic point at 10.5 wt% TiO_2 and 1550˚C. The temperature used for thermal treatments in this study was 1600˚C, which lies in the single-liquid phase that is associated with the eutectic point. At the beginning of heating, the film is silica rich. With liquid phase transformation, the rutile will dissolve into the silica film. As the temperature increases and is held at 1600˚C, the TiO_2 concentration increases and the composition of the film will approach the liquidus lines at 1600˚C. On rapid cooling, the TiO_2 concentration that remains in the glass will be equal to the concentration of the liquidus at temperature. The glass becomes supercooled and the titania will come out solution, as illustrated in Ravishankar and Gilliss[37] If the liquid is cooled in a slow, controlled manner, the final composition of the glass will equal the eutectic composition of 10.5 wt% TiO_2. However, the system is not at equilibrium unless the material is held at temperature for a long time. Even DeVries, Roy and Osborn[52] noted, "the liquid co-existing with either cristobalite or rutile in the temperature range 1550-1600˚C is of such a nature that equilibrium is not readily attained. Reactions either to dissolve or form crystals are very sluggish."

β-Al_2O_3 and TiO_2 have a eutectic point at 1705˚C, as given in figure 4.23. Below this, a mixture of TiO_2 and β-Al_2O_3• TiO_2 exists. The structure of β-Al_2O_3• TiO_2 is not clear.[46]

References

[1] W. Vogel, in, Leipzig, Germany, (1965), pp. 134-202.

[2] M. G. Velarde, in: E. D. Hondros *et al.* (Eds.), Marangoni and Interfacial Phenomena in Materials Processing, London, (1998), pp. 15-30.

[3] R. Monti, R. Savino, G. Alterio, "Pushing of liquid drops by Marangoni force" Acta Astro., **51** [11] 789-796 (2002).

[4] M. K. Santala, A. M. Glaesar, "Surface-energy-anisotropy-induced orientation effects on Rayleigh instabilities in sapphire" Surf. Sci., **600** 782-792 (2006).

[5] B. S. Kang, F. Ren, B. S. Jeong, Y. W. Kwon, K. H. Baik, D. P. Norton, S. J. Pearton, "Use of 370 nm UV light for selective-area fibroblast cell growth" J. Vac. Sci. Technol. B, **23** [1] 57-60 (2005).

[6] G. S. Ferguson, G. M. Whitesides, in: M. E. Schrader, G. Loeb (Eds.), Modern Approach to Wettability: Theory and Applications, New York, (1991), pp. 143-177.

[7] S.-Y. Lien, D.-S. Wuu, W.-C. Yeh, J.-C. Liu, "Tri-layer antireflection coatings (SiO_2/SiO_2-TiO_2/TiO_2) for silicon solar cells using a sol-gel technique" Sol. Energ. Mater. Sol. C., **90** 2710-2719 (2006).

[8] F. Mei, C. Liu, L. Zhang, F. Ren, L. Zhou, W. K. Zhao, Y. L. Fang, "Microstructural study of binary TiO2:SiO2 nanocrystalline thin films" J. Cryst. Growth, **292** 87-91 (2006).

[9] C. Noguera, Physics and Chemistry at Oxide Surfaces, Cambridge University Press Cambridge, UK, (1996).

[10] M. Fujimoto, T. Ohno, H. Suzuki, H. Koyama, J. Tanaka, "Nanostructure of TiO_2 nano-coated SiO_2 particles" J. Am. Ceram. Soc., **88** [11] 3264-3266 (2005).

[11] C. B. Carter, M. G. Norton, Ceramic Materials: Science and Engineering, Springer New York, NY, (2007).

[12] M. D. Antonik, R. J. Lad, "Faceting, reconstruction, and defect microstructure at ceramic surfaces revealed by atomic force microscopy" J. Vac. Sci. Technol. A, **10** [4] 669-673 (1992).

[13] M. Hu, S. Noda, H. Komiyama, "A new insight into the growth mode of metals on TiO_2(110)" Surf. Sci., **513** 530-538 (2002).

[14] M. J. J. Jak, A. van Kreuningen, J. Verhoeven, J. W. M. Frenken, "The effect of stoichiometry on the stability of stes on TiO_2 (110)" Appl. Surf. Sci., **201** 161-170 (2002).

[15] M. Li, W. Hebenstreit, U. Diebold, "Oxygen-induced restructuring of the rutile TiO_2 (110)(1x1) surface" Surf. Sci., **414** L951-L956 (1998).

[16] W. W. Mullins, "Theory of Linear Facet Growth During Thermal Etching" Phil. Mag., **6** [71] 1313-1341 (1961).

[17] W. Uytenbogaardt, E. A. J. Burke, Tables for Microscopic Indentification of Ore Minerals, Dover Publications, Inc. New York, (1985).

[18] J. Muscat, N. M. Harrison, "The physical and electronic structure of the rutile (001) surface" Surf. Sci., **446** 119-127 (2000).

[19] D. B. Dingwell, "The density of titanium (IV) oxide liquid" J. Am. Ceram. Soc., **74** [10] 2718-2719 (1991).

[20] R. Hosemann, A. M. Hindeleh, R. Brueckner, "Paracrystalline lattice structure of silica glass, α- and β-crystobalite" Phys. Status Solidi A, **126** [2] 313-324 (1991).

[21] E. M. Levin, C. R. Robbins, H. F. McMurdie (Eds.), Phase Diagrams for Ceramists, The American Ceramic Society, Inc., Columbus, Ohio, p. 601, (1964).

[22] X. Buttol, R. Dramais, G. Richez, J. Ruelle, "Silica refractories get a second life" Glass Ind., **82** [3] 12-14 (2001).

[23] S. A. Campbell, The Science and Engineering of Microelectronic Fabrication, Oxford University Press New York, (2001).

[24] G. Callegari, A. Calvo, J.-P. Hulin, F. Brochard-Wyart, "Dewetting versus Rayleigh Instability inside Capillaries" Langmuir, **18** 4795-4798 (2002).

[25] T. Young, "An Essay on the Cohesion of Fluids" Phil. Trans. R. Soc. Lon. 65-87 (1805).

[26] R. E. Johnson Jr., "Conflicts between Gibbsian Thermodynamics and Recent Treatments of Interfacial Energies in Solid-Liquid-Vapor Systems" J. Phys. Chem., **63** [10] 1655-1658 (1959).

[27] j. K. Spelt, D. Li, A. W. Neumann, in: M. E. Schrader, G. Loeb (Eds.), Modern Approach to Wettability: Theory and Applications, New York, (1991), pp. 101-142.

[28] A. Marmur, in: M. E. Schrader, G. Loeb (Eds.), Modern Approach to Wettability: Theory and Applications, New York, (1991), pp. 327-358.

[29] B. M. Besancon, P. F. Green, "Moving fronts in entangled polymeric films" Phys. Rev. E, **70** (2004).

[30] J. Thomson, "On certain curious Motions observable at the Surfaces of Wine and other Alcoholic Liquors" Phil. Mag., **10** 330-333 (1855).

[31] M. A. O'Keeffe, "News and Views: Edge effects" Nat. Mater., **419** 28-29 (2002).

[32] E. L. Koschmieder, in, Bénard Cells and Taylor Vortices, Cambridge, (1993), pp. 4-10.

[33] K. Horrocks, E. Masuoka, Cloud vortex streets off the Cape Verde Islands, website, http://images.google.com/imgres?imgurl=http://rapidfire.sci.gsfc.nasa.gov/gallery/2005005-0105/CapeVerde.A2005005.1225.150x115.jpg&imgrefurl=http://rapidfire.sci.gsfc.nasa.gov/gallery/%3F2005005-0105&h=115&w=150&sz=3&tbnid=jfe0dPQ1L2oJ:&tbnh=69&tbnw=90&hl=en&start=33&prev=/images%3Fq%3DNASA%2Bcloud%2Bstreets%26start%3D20%26svnum%3D10%26hl%3Den%26lr%3D%26client%3Dfirefox-a%26rls%3Dorg.mozilla:en-US:official%26sa%3DN
, (4 October 2005).

[34] E. Brener, H. Müller-Krumbhaar, D. Temkin, T. Abel, "Structure formation in diffusional growth and dewetting" Solid State Ionics, **131** 23-33 (2000).

[35] W. W. Mullins, R. F. Sekerka, "Morphological stability of a particle growing by diffusion or heat flow" J. Appl. Phys., **34** [2] 323-329 (1963).

[36] S. R. Gilliss, Ceramic Oxides: Surfaces and Amorphous/Crystalline Interfaces, Minneapolis, MN, University of Minnesota, 261 (2004).

[37] N. Ravishankar, S. R. Gilliss, C. B. Carter, "Glass and metals on crystalline oxides" J. Euro. Ceram. Soc., **23** 2777-2785 (2003).

[38] E. L. Koschmieder, Bénard Cells and Taylor Vortices, University of Cambridge Cambridge, UK, (1993).

[39] L. Rayleigh, "On the Instability of Jets" Proc. Lon. Math. Soc., **10** 4-13 (1878).

[40] P. G. de Gennes, "Wetting: statics and dynamics" Rev. Mod. Phys., **57** [3] 827-863 (1985).

[41] Z. Gai, J. Y. Howe, D. A. Blom, E. W. Plummer, J. Shen, "Self-assembled FePt nanodot arrays with mono-dispersion and -orientation" Appl. Phys. Lett., **86** 1-3 (2005).

[42] Z. Lødziana, J. K. Norskov, "Interaction of Pd with steps on a-Al_2O_3 (0001)" Surface Science Letters, **518** L577-L582 (2002).

[43] N. Ravishankar, V. B. Shenoy, C. B. Carter, "Electric Field Singularity Assisted Nanopatterning" Adv. Mater., **16** [1] 76-80 (2004).

[44] N. Ravishankar, S. R. Gilliss, C. B. Carter, "Dewetting of liquids on ceramic surfaces at high temperature" Microsc. Microanal., **8** 257-267 (2002).

[45] J. L. Riesterer, Combining FIB, AFM and EBSD for Analysis of Dynamic Processes on Ceramic Surfaces, Minneapolis, MN, University of Minnesota (2005).

[46] M. W. Bench, P. G. Kotula, C. B. Carter, "Influence of the nature of the (0001) alumina surface on thin film growth" Surf. Sci., **391** 183-195 (1997).

[47] T. Sata, T. Sasamoto, in: W. D. Kingery (Ed.), Structure and Properties of MgO and Al_2O_3 Ceramics, Columbus, OH, (1984), pp. 541-552.

[48] R. Gehlhaar, M. Swoboda, M. Sudzius, M. Hoffmann, h. Fröb, H. Wendrock, "Polarization splitting and terahertz oscillations from a single planar Fabry-Pérot microcavity" Appl. Phys. Lett., **88** (2006).

[49] J.-Q. Xi, M. Ojha, J. L. Plawsky, W. N. Gill, J. K. Kim, E. F. Schubert, "Internal high-reflectivity omni-directional reflectors" Appl. Phys. Lett., **87** (2005).

[50] H. Hirota, M. Itoh, M. Oguma, Y. Hibino, "Temperature coefficients of refractive indices of TiO_2-SiO_2 films" Jap. J. Appl. Phys., **44** [2] 1009-1010 (2005).

[51] Z. Feng, L. Kaiming, W. Guoliang, S. Hua, H. Anmin, "Crystallizaton behavior of Li^+-doped SiO_2-TiO_2 films prepared by sol-gel dip coating" J. Cryst. Growth, **264** 297-301 (2004).

[52] R. C. DeVries, R. Roy, E. F. Osborn, "The system TiO_2-SiO_2" Trans. Brit. Ceram. Soc., **53** [9] 525-540 (1954).

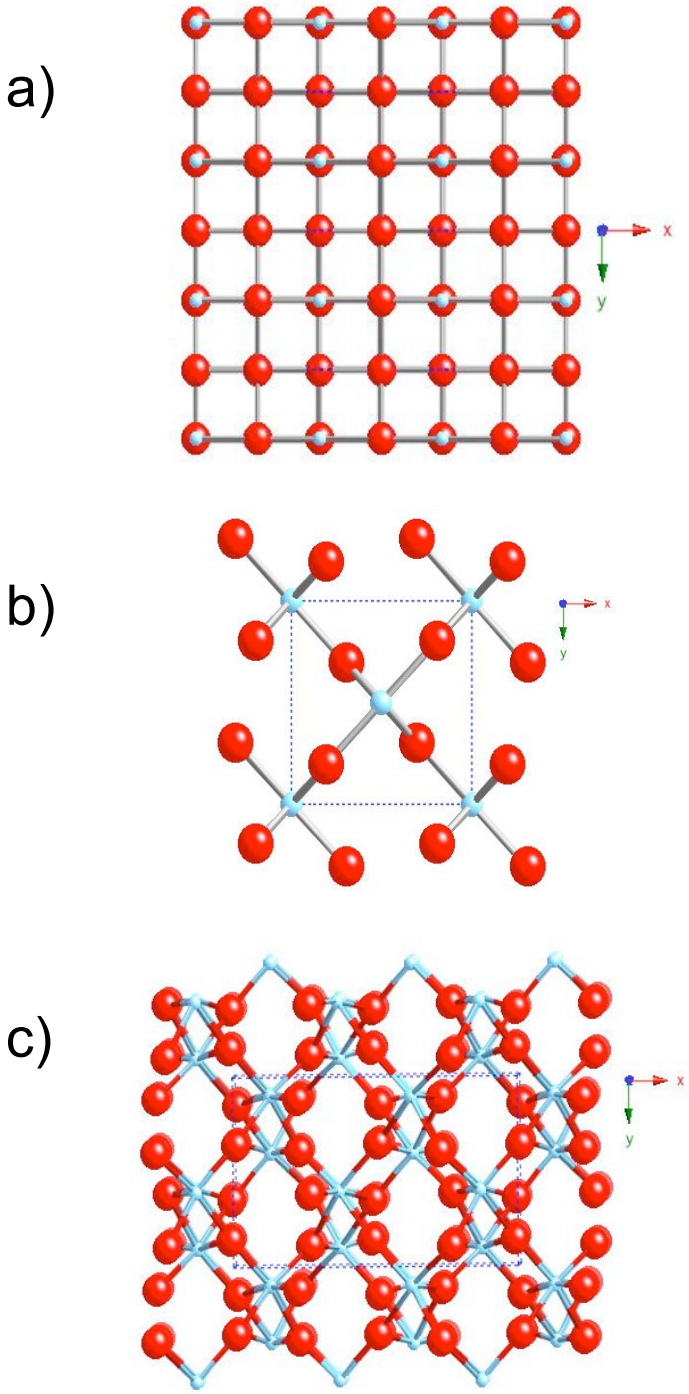

Figure 4.1: The (001) planes of a) anatase, b) rutile and c) brookite TiO_2.

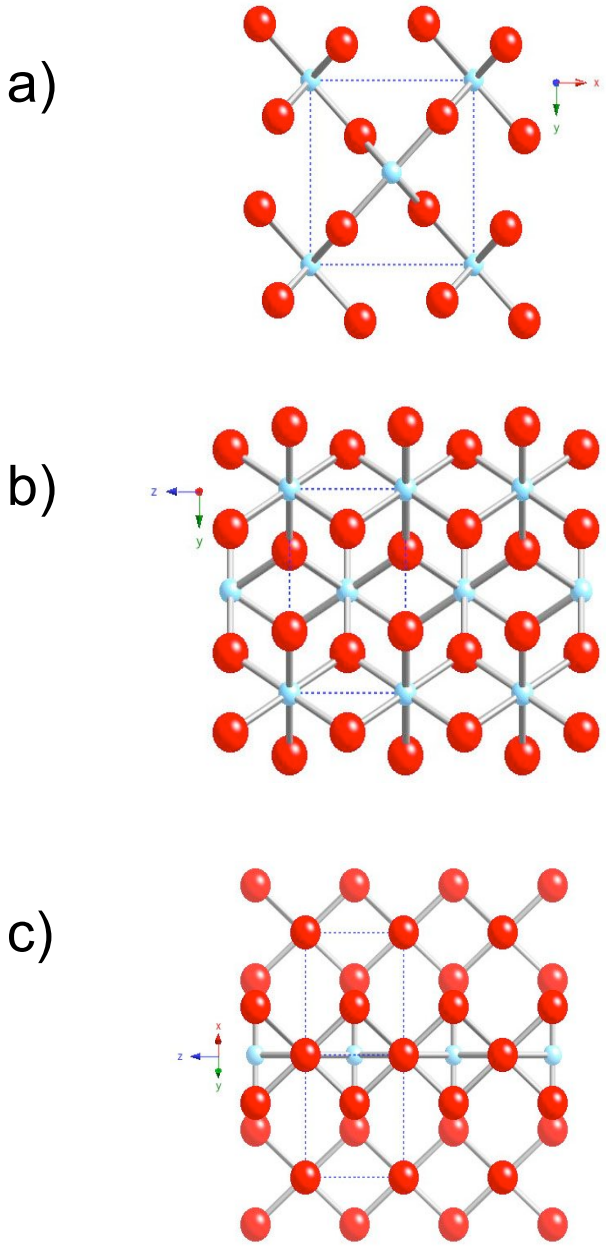

Figure 4.2: Rutile TiO_2 surface projections in the a) [001]- b) [100]- and c) [110]-directions.

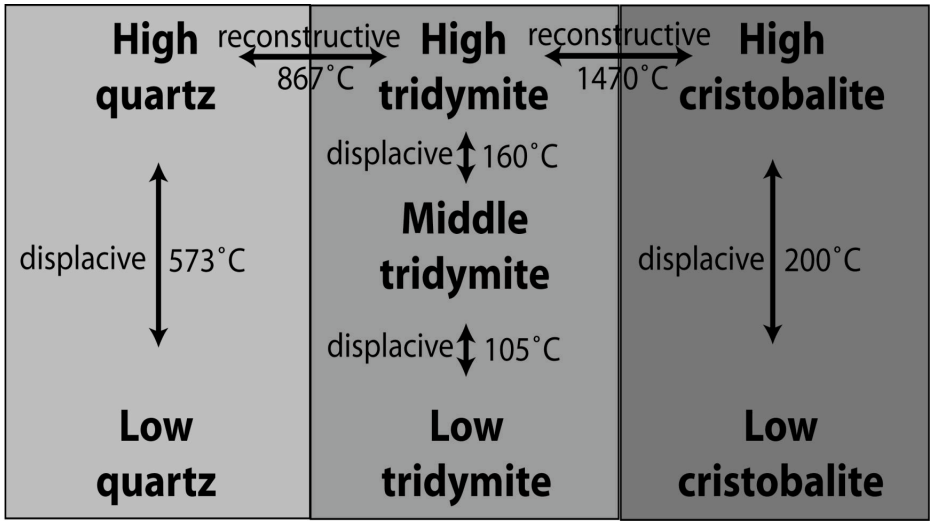

Figure 4.3: Diagram displaying the different polymorphs of SiO_2.

Figure 4.4: Amethyst (purple) and quartz (clear) crystals are forms of SiO_2.

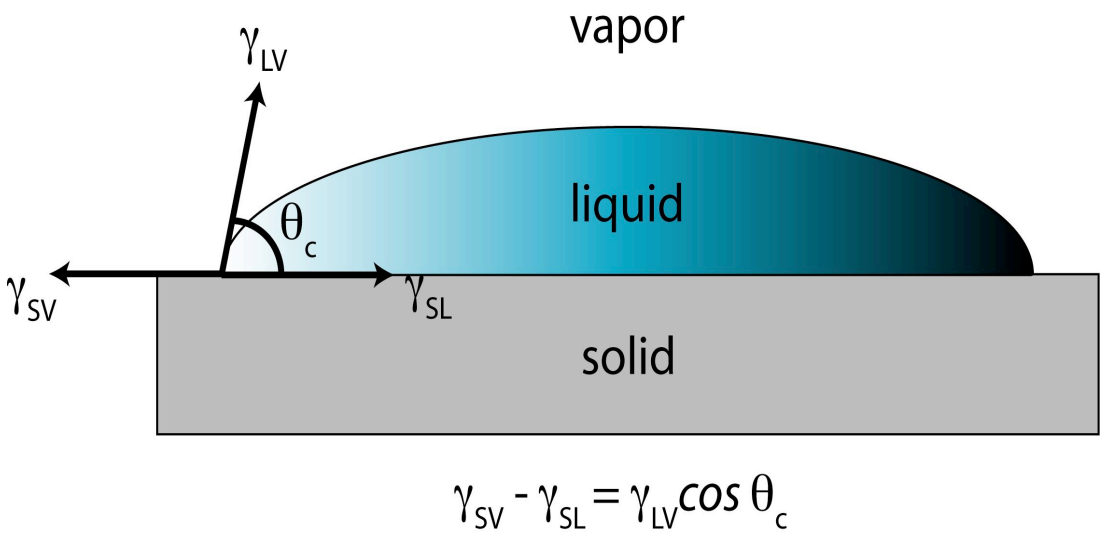

Figure 4.5: Young's equation describes the SLV triple junction and the balance of forces.

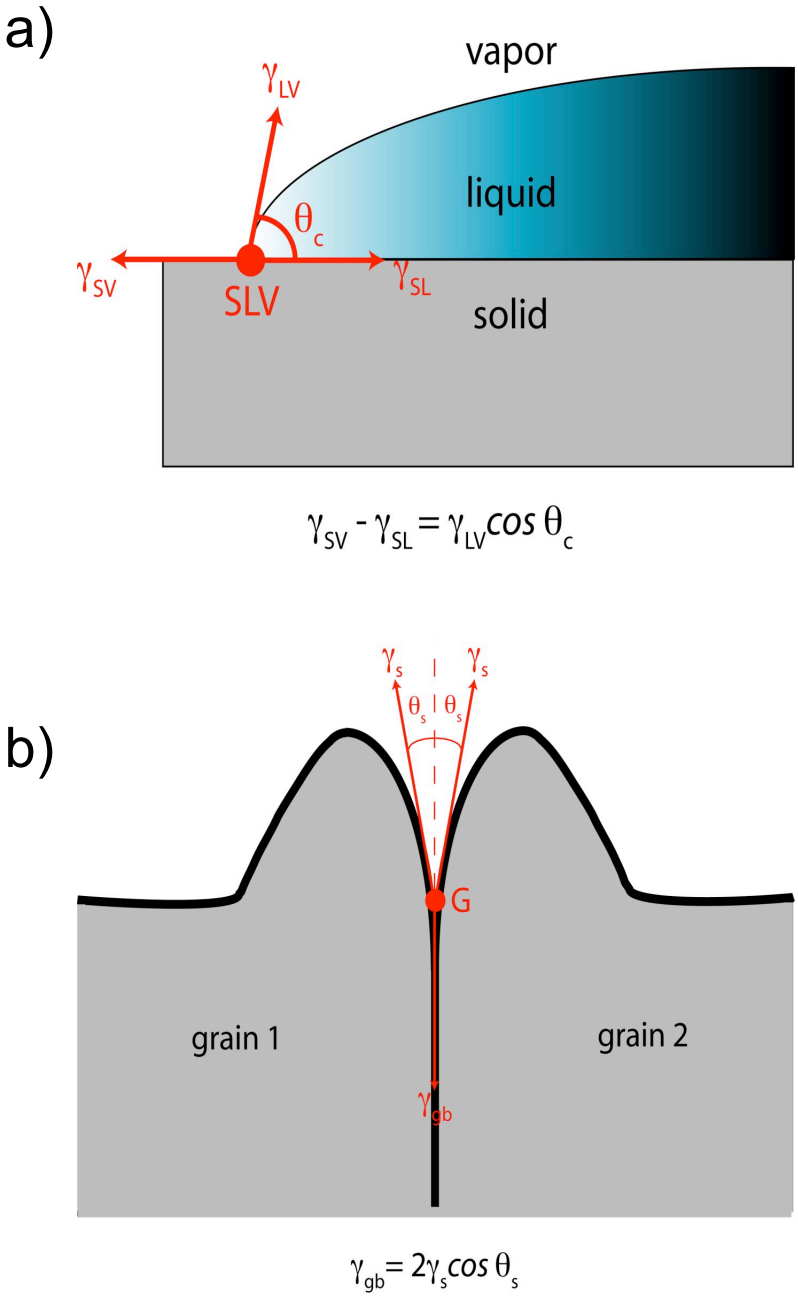

Figure 4.6: A triple phase point (a) has similar geometry and force balances as a grain boundary thermal groove (b).

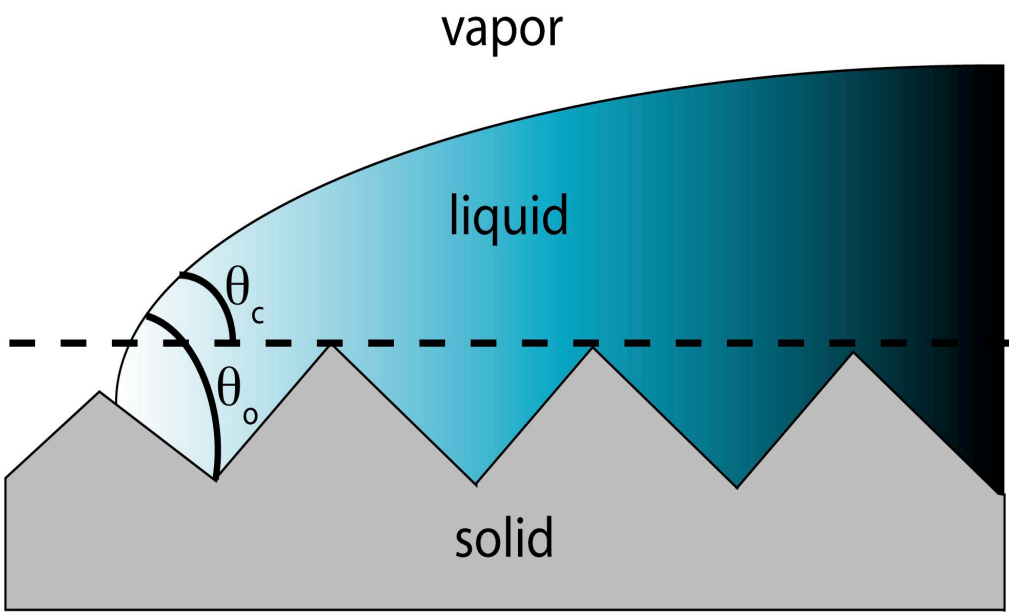

Figure 4.7: Contact angle measurements need to be carefully made. When the surface is assumed to be flat, an apparent contact angle is measured. However, the actual angle may be very different if small surface features exist.

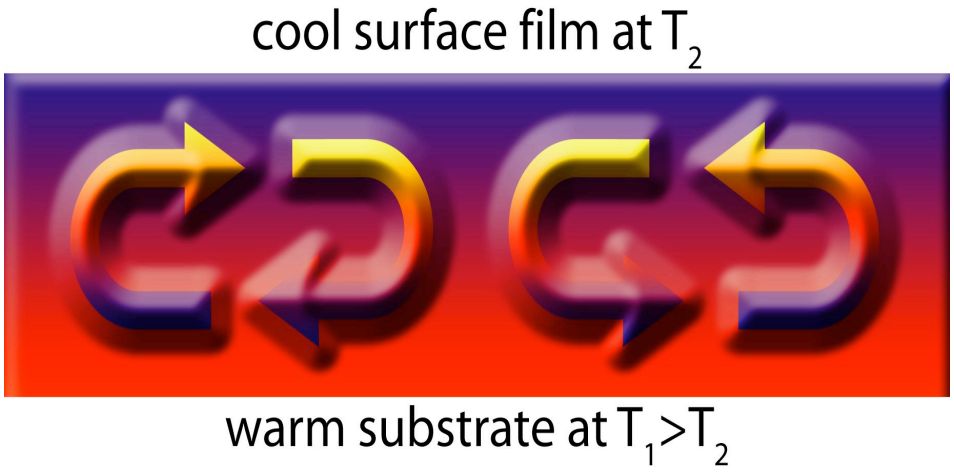

Figure 4.8: Marangoni convection involves the motion of material from the bottom of the material to the top due to a temperature, composition or viscosity gradient.

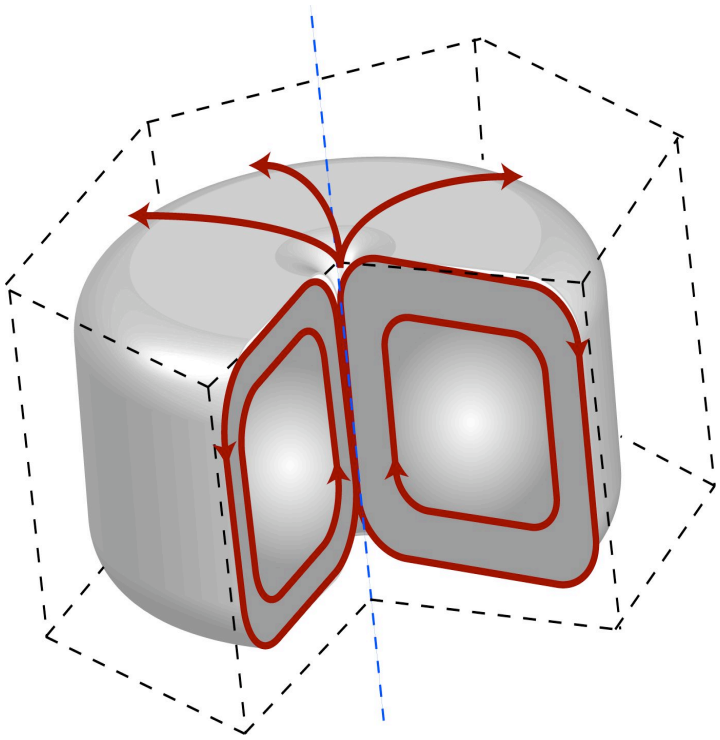

Figure 4.9: Hexagonal Bénard cells form from motion of material from the center of the cell outwards. A dimple forms in the center of the cell.

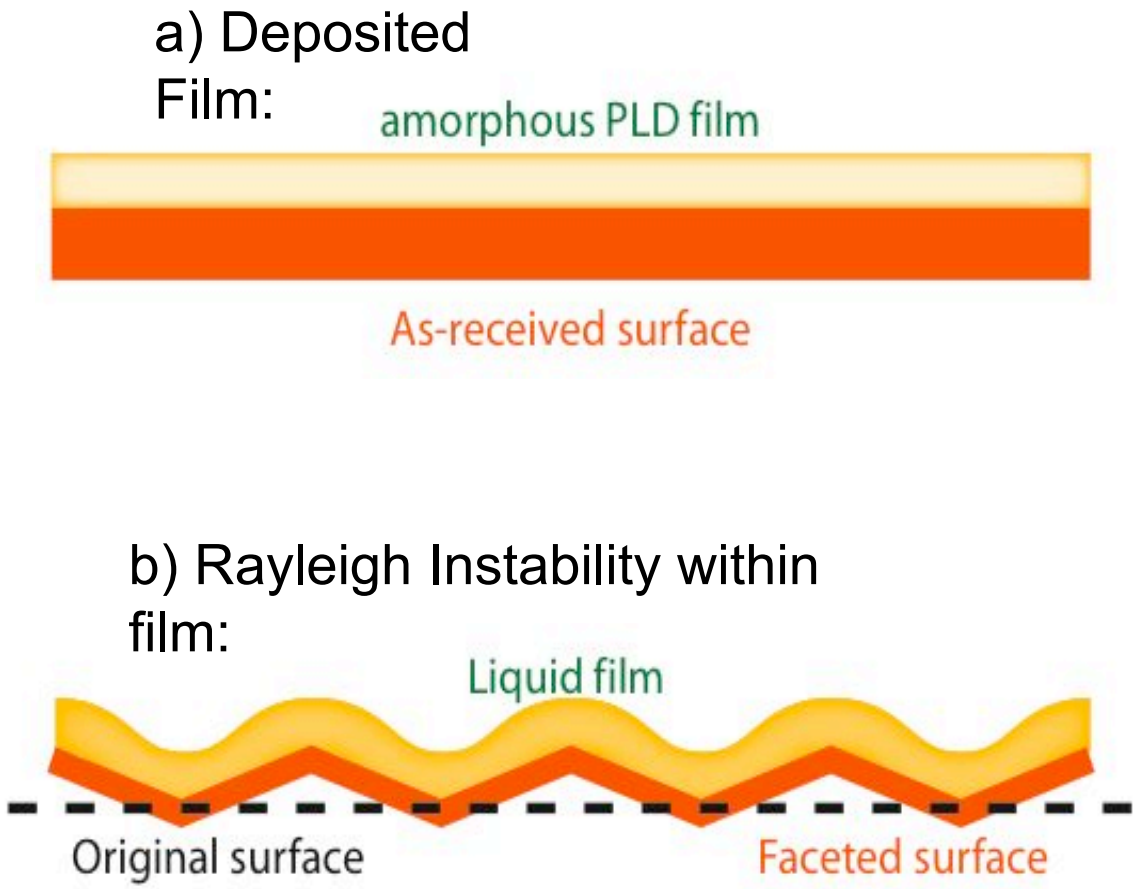

Figure 4.10: Rayleigh Instability forms after an initially flat,, continuous film breaks apart and forms droplets on top of surface features.

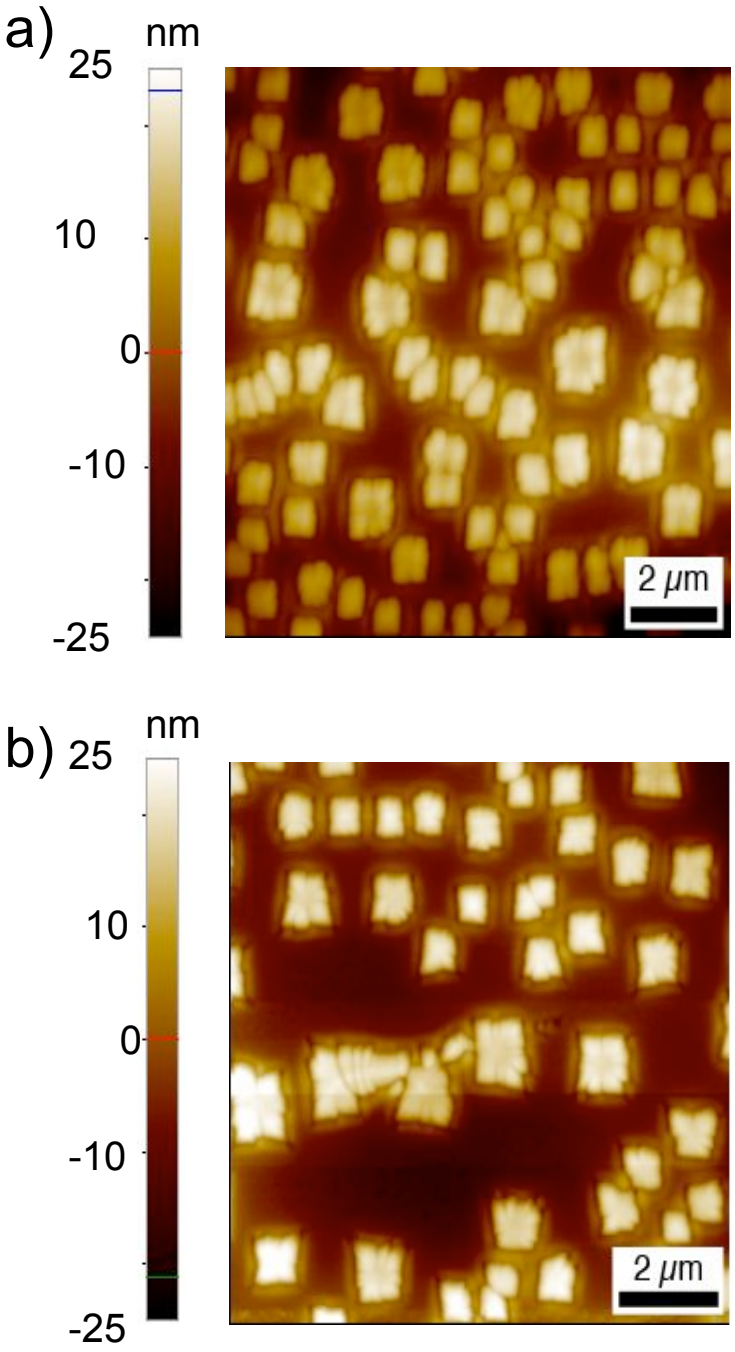

Figure 4.11: Films heated in a Pt crucible form Bénard cells of uniform size.

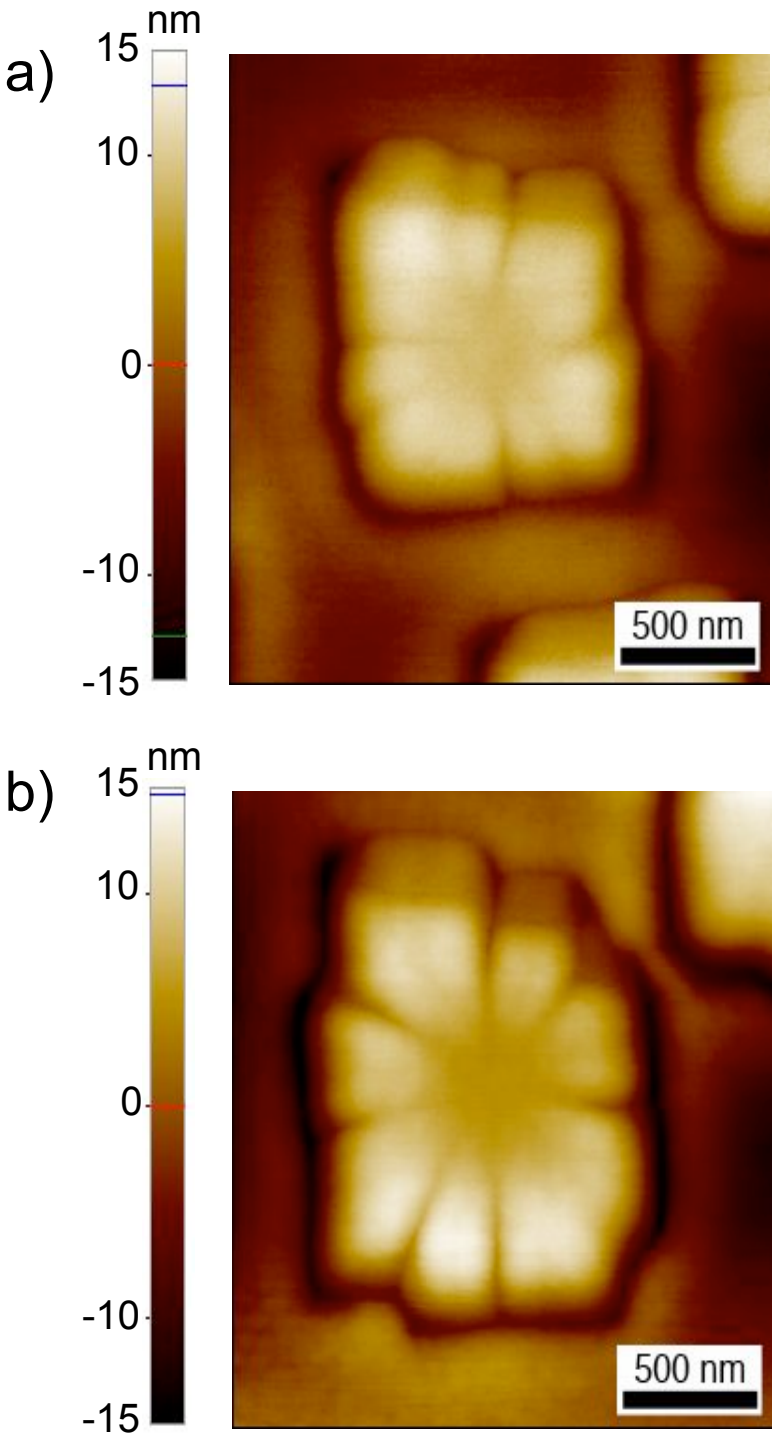

Figures 4.12: High magnification images of the Bénard cells.

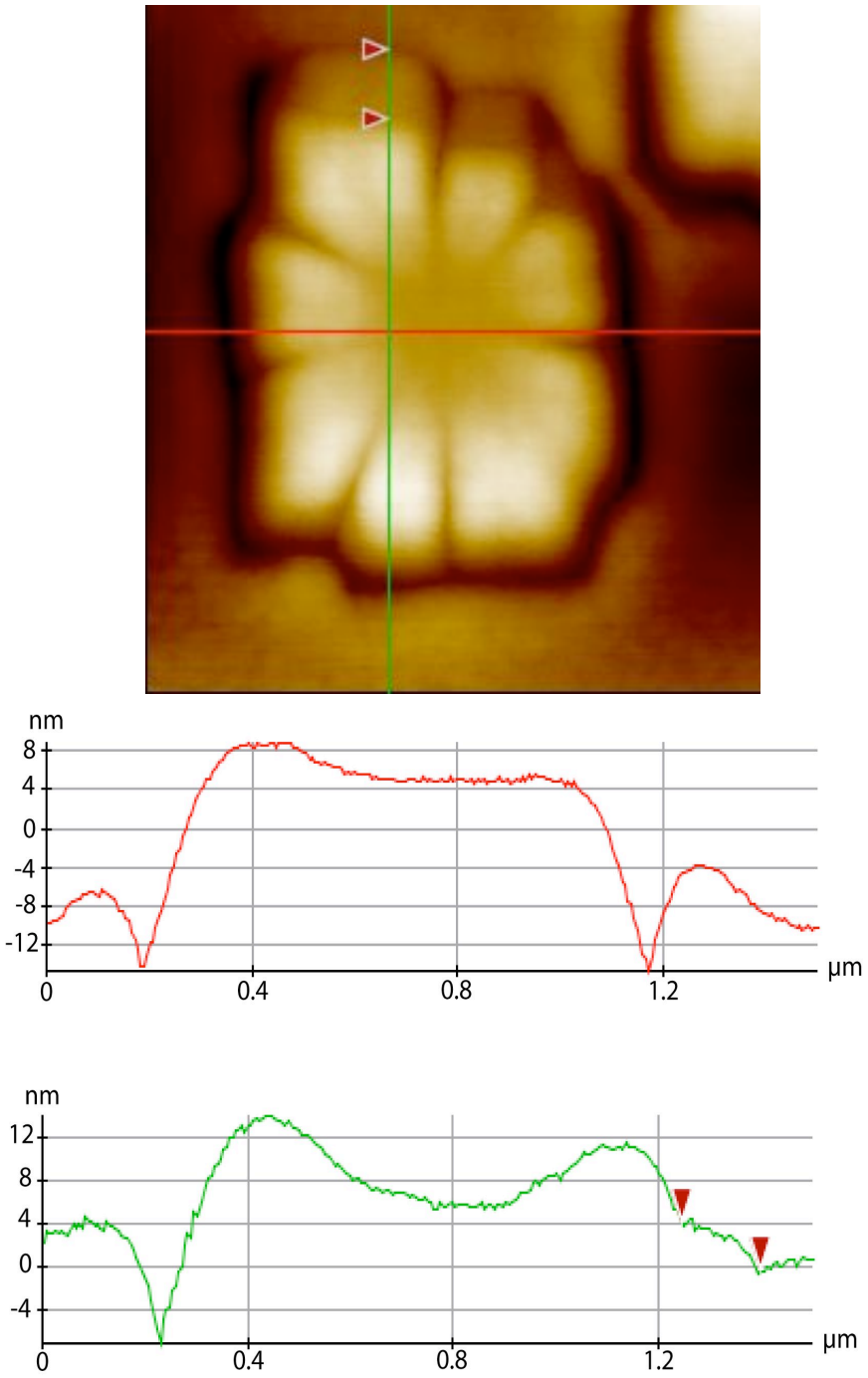

Figure 4.13: Sections of the Bénard cells show that there is dimple in the center and a skirt surrounds the cells.

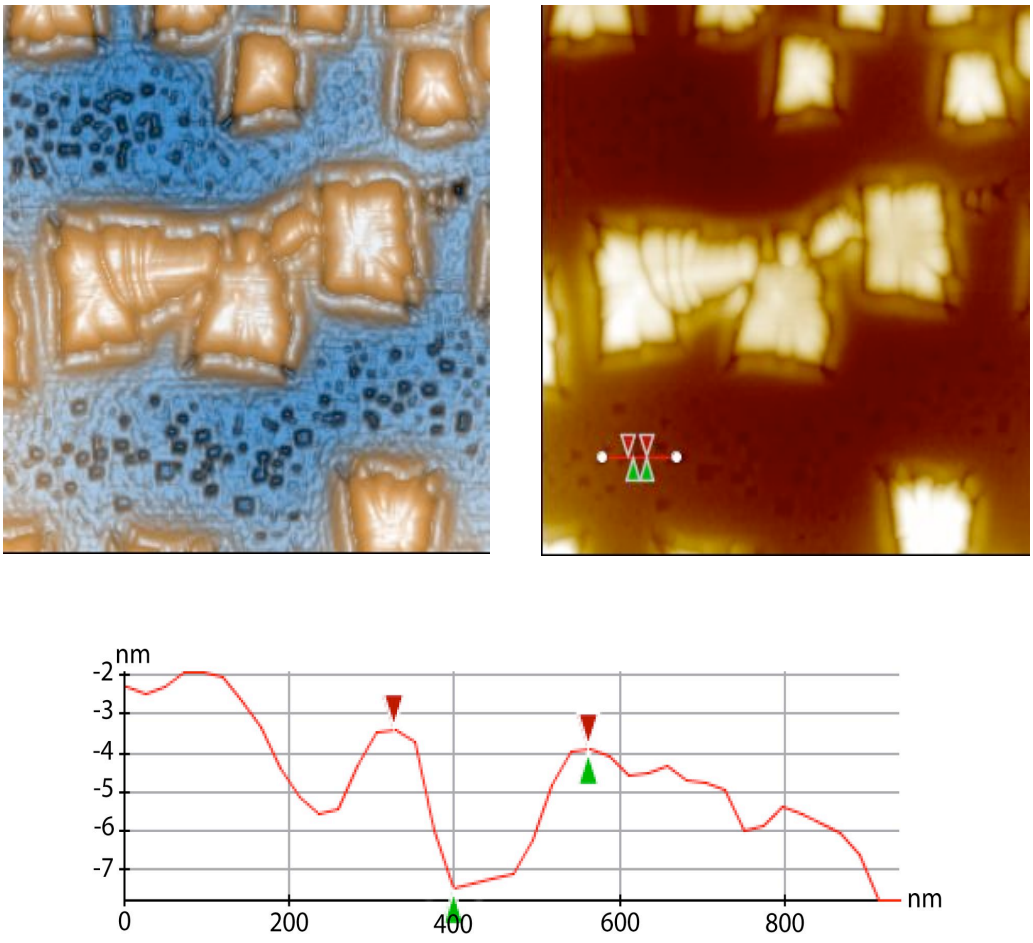

Figure 4.14: Pt Surface pits in surfaces annealed in a Pt crucible are seen in an enhanced AFM height image.

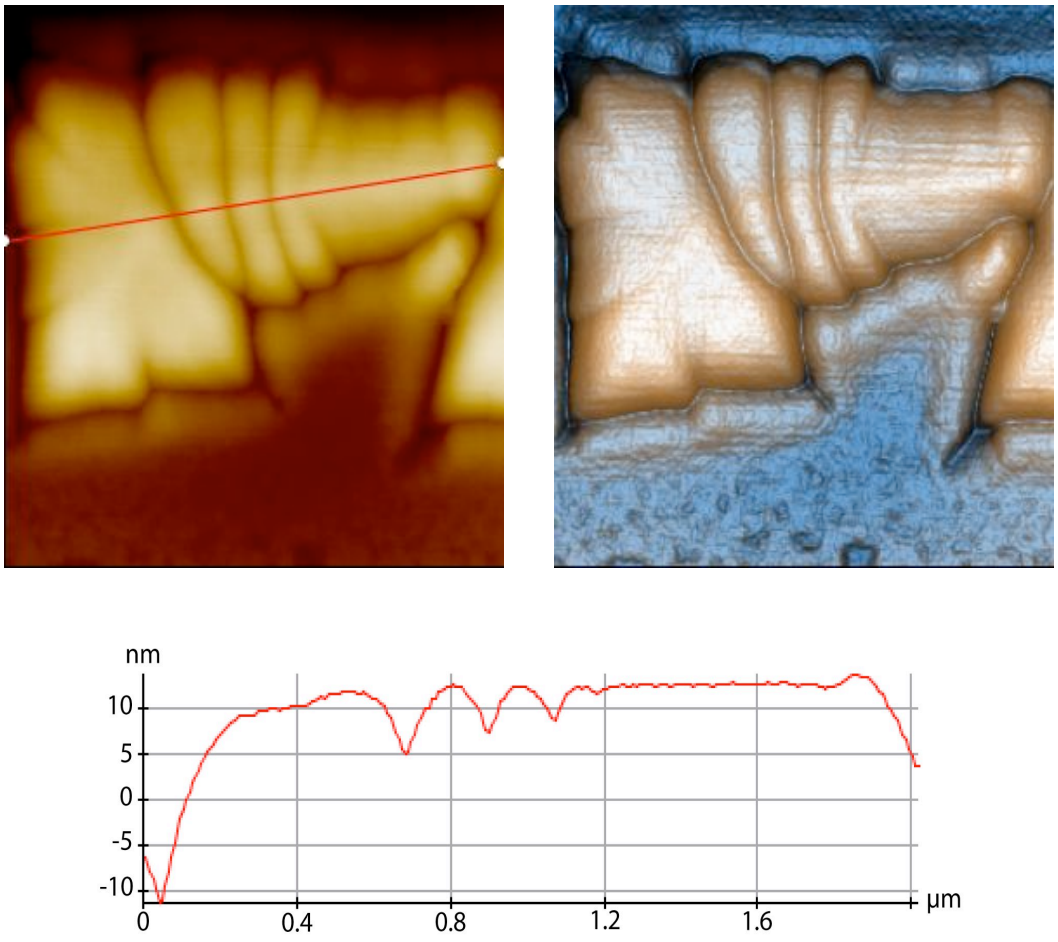

Figure 4.15: Scanning artifacts produce tiny undulations in the section analysis that may be mistaken as real features. The enhanced AFM height image shows that noise in the scan lines are creating the undulations.

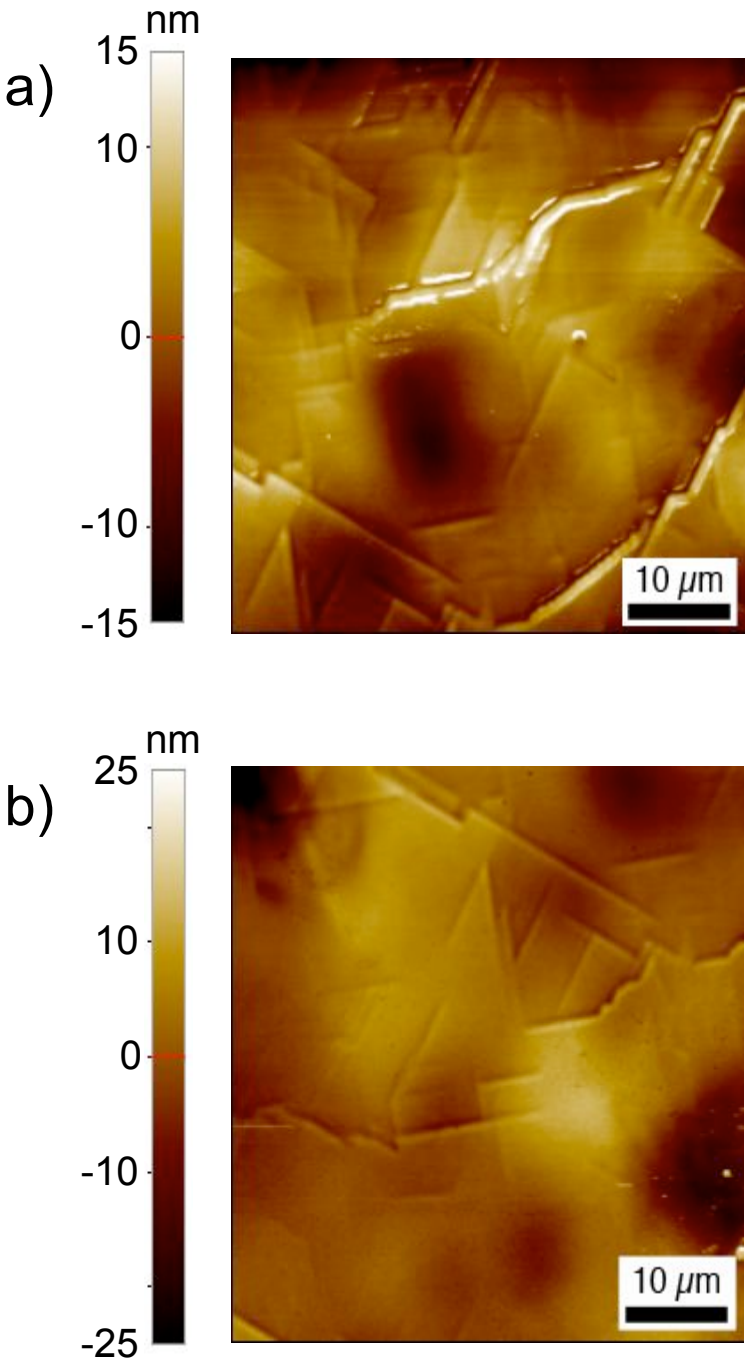

Figure 4.16: Films heated in an Al_2O_3 crucible had the SiO_2 film disappear and irregular surface facets form.

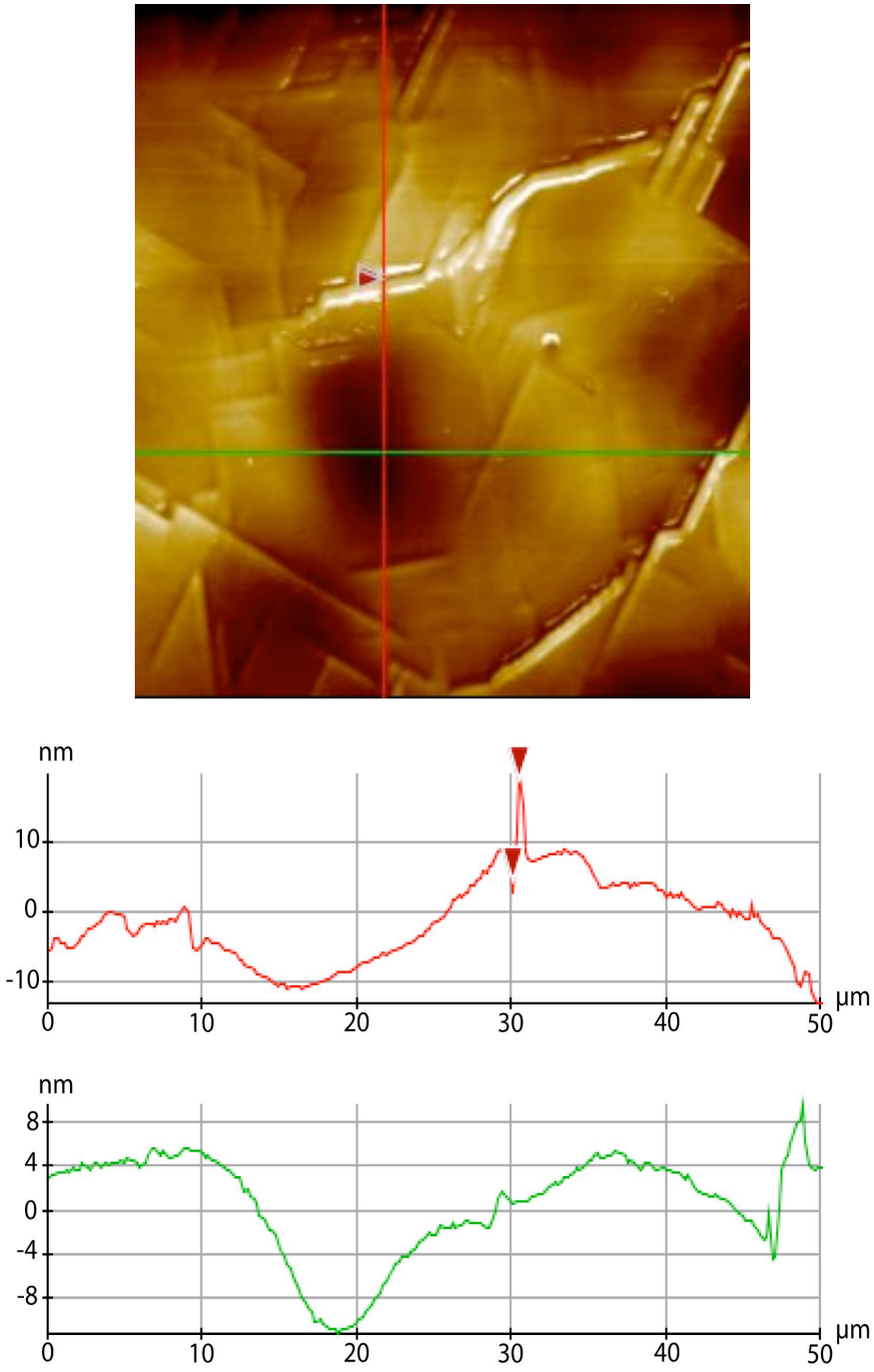

Figure 4.17: Section analysis of samples heated in an Al_2O_3 crucible shows surface facets and large depressions on the surface.

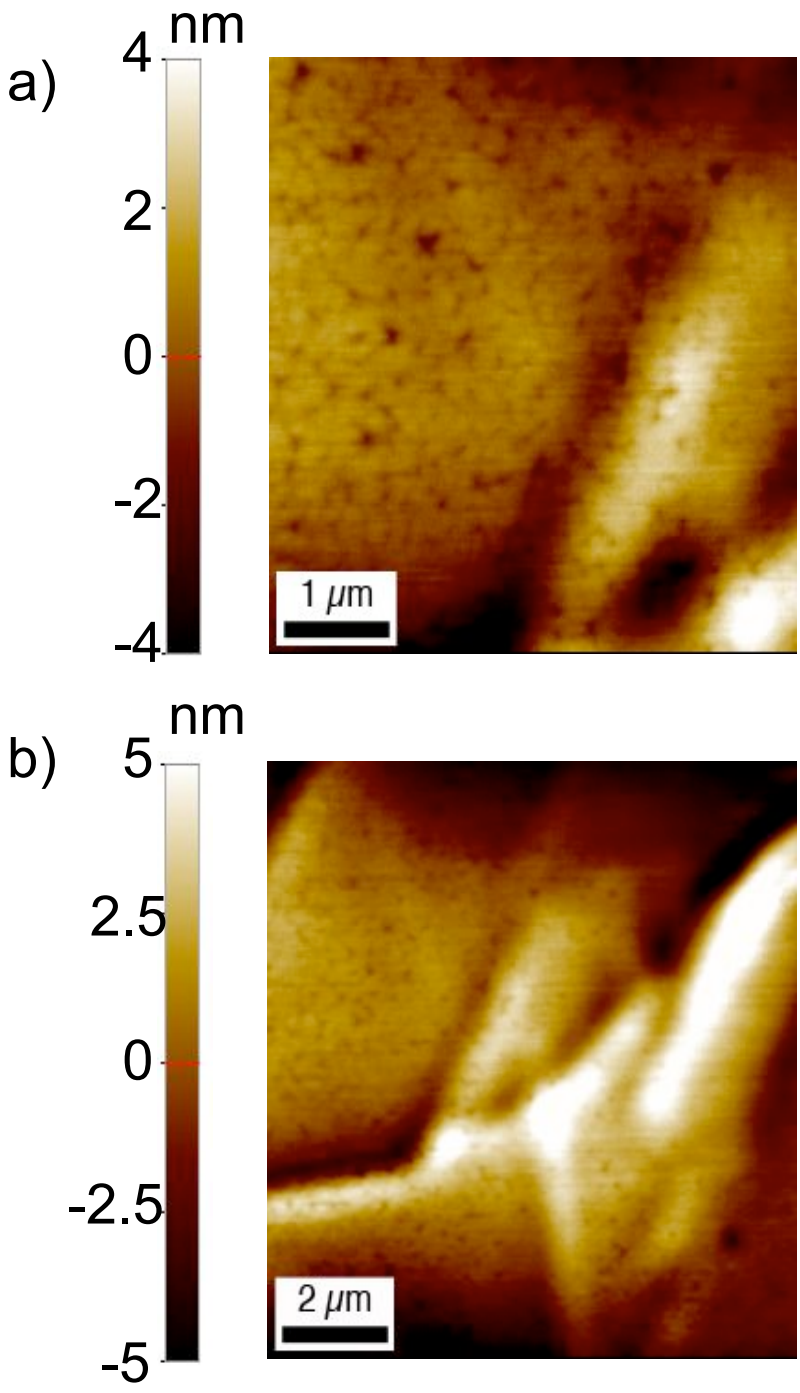

Figure 4.18: Small surface pits covered the surface of those samples exposed to Al_2O_3.

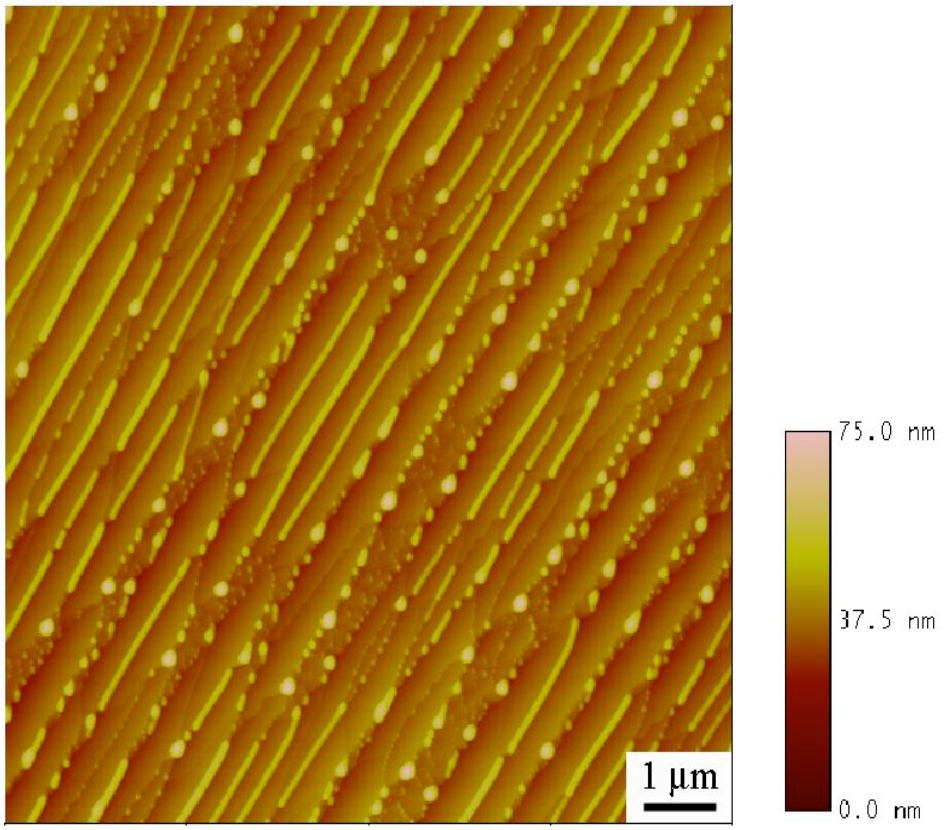

Figure 4.19: When film thickess is increased to 100 nm ,contaminated droplets undergo the Rayleigh instability.

a)

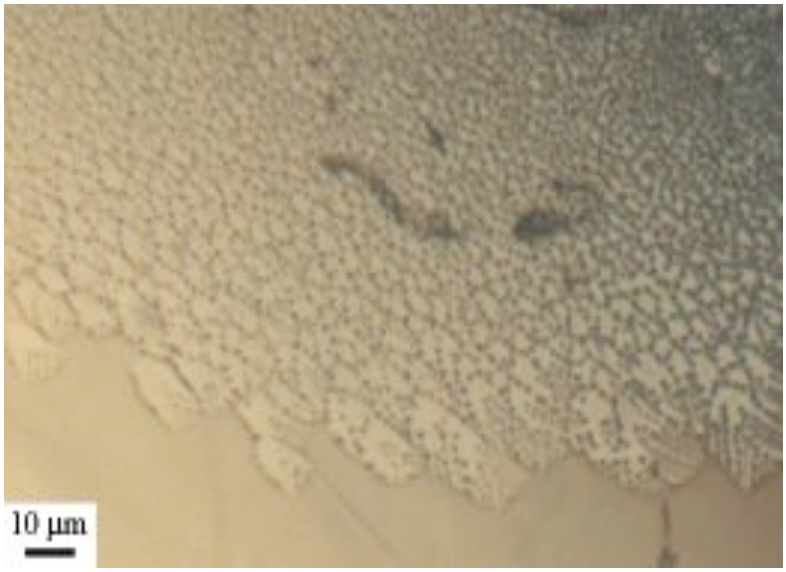

b)

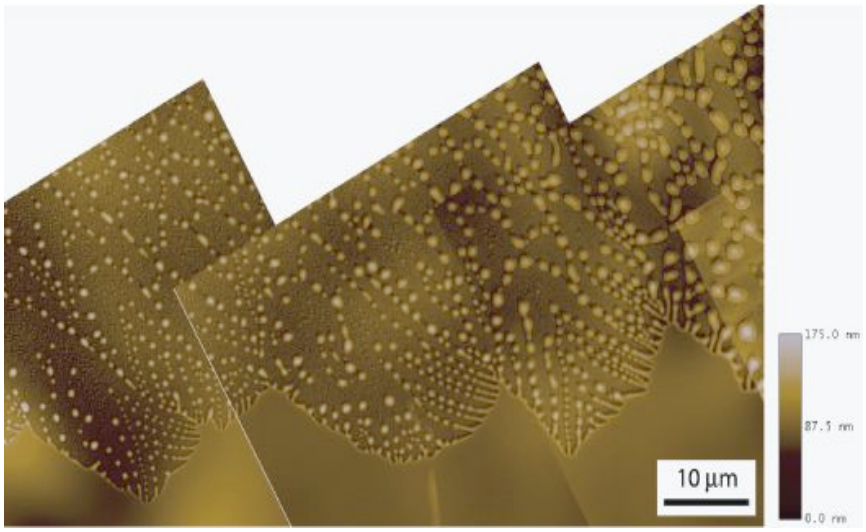

Figure 4.20: A dewetting front was observed via (a) VLM and (b) AFM of a 200 nm thick film that underwent the identical anneal as thinner films.

a)

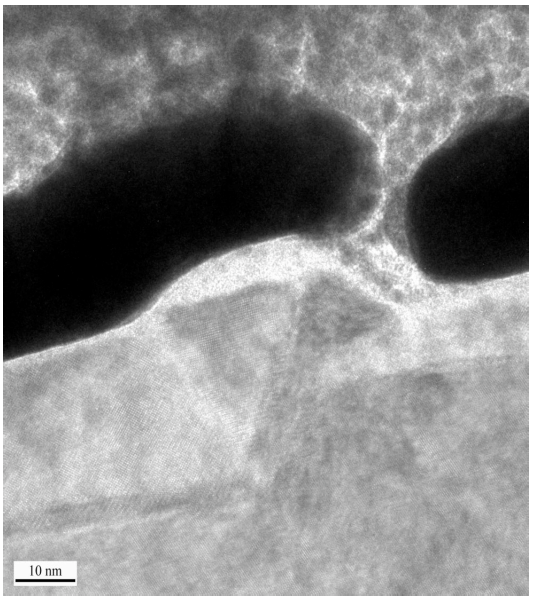

b)

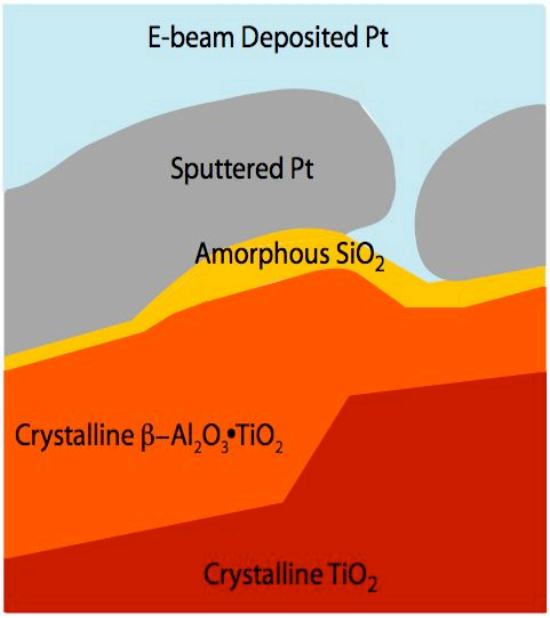

Figure 4.21: (a) HRTEM and (b) schematic of a FIB cross-section showing the reaction layer of Al_2O_3 contaminates.

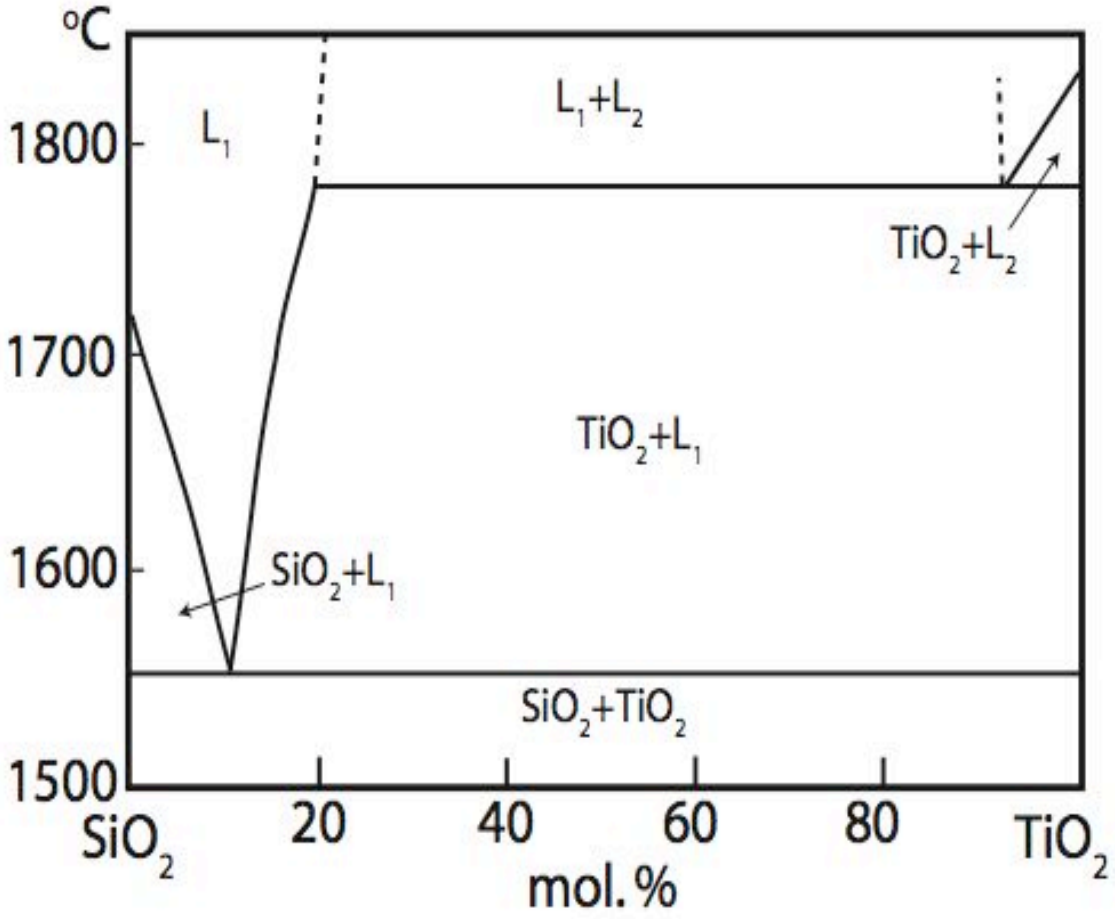

Figure 4.22: SiO_2-TiO_2 phase diagram

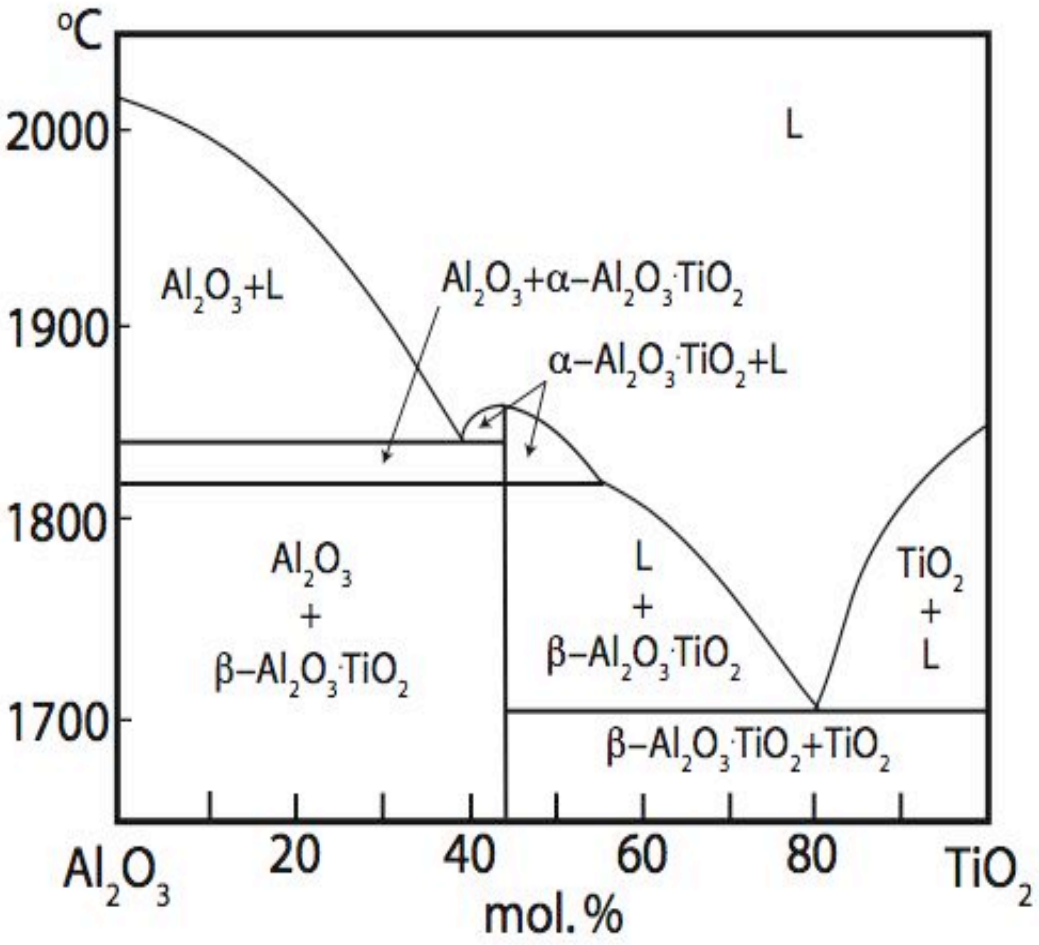

Figure 4.23: Al_2O_3-TiO_2 phase diagram

Chapter 5: Exudation and Penetration of Glass

5.1 Introduction

Glass at grain boundaries is an important topic in ceramic processing. Glass is one of the oldest materials used in history[1] and is currently important in technological applications, such as electrical insulating, chemically inert applications and varistors. Often it is difficult to have a completely glass-free polycrystalline compact due to impurities during processing. Glass will form intergranular films (IGF); the grain boundaries are able to accommodate the addition of larger atoms or a structure change. Whether glass is intentionally placed within a component or not, a dramatic change in the component's properties will result.

Liquid-phase sintering (LPS) relies on the presence of glass.[2] Glass can make up nearly 20% of the total volume during LPS.[3] LPS depends on capillary forces to draw the liquid in and out of the boundaries. Leonardo Da Vinci is reported to be the first to study capillary rise within a tube.[4] Because of the high porosity at the beginning of LPS, capillary forces are 3D in nature.[5] As sintering proceeds, grain boundaries and triple lines act more like tubes. While much has been done on the 2D problem of capillarity, little is known when the matrix becomes more porous.

Glass lacks long-range order and is sometimes thought of as a liquid that has solidified too quickly to nucleate crystallographic structure, i.e., a super-cooled liquid. The presence of glass at a grain boundary disrupts the properties of the bulk. Glass is usually a good insulator and has a high dielectric constant,[6] making it an important packaging material for microelectronics. The electrical and thermal conductivities of glass make it a good candidate for seals and joining metal to ceramics. Glass can be recycled by melting and reforming.[6] Combining two immiscible glasses can result in glass-ceramic production. Glass is only metastable; local phase separation can occur depending on the

local chemistry.[7] Borosilicates commonly phase separate, even when the equilibrium phase diagram says separation is not possible. Glass is inheritantly not at equilibrium. One example of this is in float-glass preparation.[6] The glass phase separates into two liquids in order to "float" the glass plate and solidify it. The phase separation and floating rely on capillary forces and wetting behavior.[8]

Glass is not unique to ceramics. Metals and polymers can have glassy phases. Amorphous polymers are ones that do not have any alignment or periodic structure of the polymer chains.[9] The degree of crystallinity within a polymer will change the glass transition temperature. Similar to inorganic materials, polymers can be quenched into an amorphous state and annealed to become crystalline.

5. 2 Background

Films at grain boundaries have received a lot of attention. IGFs have been found to both hinder and promote grain growth. The films can collect impurities and sweep pores from the bulk. IGF properties and behavior will be summarized here. Previous results will also be reviewed and characterization methods for observing IGFs will be given.

5.2.1 Glass in Art

Glass blowers rely on the same properties of glass as scientists do. The glass must be the correct viscosity when heated to easily form the desired shape on the blowpipe.[1] Glass gobs can be blown into molds just like bubbles are blown; both rely on surface tension of the glass. The glass viscosity is important for blow molding. By understanding the actual change in surface tension with partial pressure, glass blowing can be mechanized for bottle and jar production.[6]

Potters use glass for glazing their creations. By doping the glass with impurities, glass can take on brilliant colors. Metal and rare-earth ions are the most common colorizing dopants. Table 5.1 lists some dopants and their resulting colors. Crackle glazes take advantage of differences in thermal expansion coefficient to produce decorative cracks

at the surface.[10] Spherulites within a glass matrix form on the surface, usually of a different color. The formation of the spherulites is similar to plate and needle formation.[10] Growth in the *x*- and *y*- directions is unrestricted, but growth in the *z*-direction is limited due to the glaze thickness. Raku glazes use trapped metal ions and keep them from oxidizing.[10] The result is a brilliant variation of color. Examples of these three glaze techniques can be seen in Figure 5.1. Glassy glazes can be a source of material for the necessary phase transformations during sintering of the pre-processed bodies (i.e., "green" bodies).

5.2.2 Capillary forces and Grain Boundaries

As in wetting of surfaces, capillarity at grain boundaries is important. However, in the case of grain boundaries, the capillary forces resemble the classic geometry that controls thermometers and liquids in tubes, i.e., spontaneous penetration.[7] In particular, triple lines can act like a pipe. Capillary forces act on IGFs within the triple lines, as illustrated in figure 5.2. These capillary forces and IGFs can cause the grain boundaries to be pinned. Penetration is defined as liquid or gas filling a void by moving from the surface.[4] Liquid films can penetrate grain boundaries or exude from them and wet the surface.[11] The liquid is trying to find pressure equilibrium by penetrating an otherwise empty capillary tube. The liquid will wet the capillary walls and form a distinct contact angle with the wall resulting in the liquid's meniscus. If the pressure/tension equilibrium is disturbed, the liquid level within the capillary will rise or fall to balance the change. The pressure acting counter to the liquid is the hydrostatic pressure.[4] Penetration will occur only if the pressure within the liquid is greater than the hydrostatic pressure if an infinite reservoir of liquid is present.

The surface tension of curved surfaces will be affected by the vapor pressure on either side of the liquid film. Equations 5.1 and 5.2 describe capillarity at an interface with respect to surface energy. Equation 5.1 is particularly important in sintering kinetics, while equation 5.2 describes the contact angle at a symmetric grain boundary groove. The contact angle, θ, is a key component of the driving force for penetration across the

interface.[4] Penetration velocity has been shown to be linearly dependent on the inverse of the length of grain boundary penetrated for Newtonian liquids in cylindrical capillaries.[4]

$$\Delta P = \frac{2\gamma_S}{r} \qquad [5.1]$$

$$\gamma_{GB} = 2\gamma_S \cos\theta_S \qquad [5.2]$$

The same capillary forces are what act on particles being sintered. From these equations one can deduce that the smaller the radius of curvature, r, of a particle or meniscus, the greater the vapor pressure, ΔP, at the surface and larger surface energies, γ_S. In addition, smaller particles will have lower melting temperatures and be more subject to Ostwald ripening. Of course, a change in temperature will change the vapor pressure. Chapter 3 of this dissertation goes discusses equation 5.2 in greater detail.

The interface curvature initially drives material to move and join the particles. Figure 5.3 illustrates traditional particle sintering that is curvature-driven. When an IGF is present, the material is able to dissolve into the liquid and reprecipitate at a preferred site. Diffusion through the IGF is much easier than through the bulk or at the surface. Curvature depends on pressure.

A balance between capillary forces and interfacial tensions determines whether liquid films penetrate or exude from grain boundaries. Brada and Clarke[11] derived equations governing these behaviors, assuming the volume of liquid present remains constant (i.e. nothing lost to evaporation or diffusion). The thickness of the IGF is assumed to remain constant, also, which agrees with experimental findings.[11] Figure 5.4 shows the geometry of liquid at a grain boundary that intersects the free surface. The force balance of the geometry becomes complicated since three angles (χ, ϕ, θ) and five interfacial tensions (γ_{LV}, γ_{SV}, γ_{SL}, γ_{LB}, γ_{GB}) describe the system. Van der Waal's forces will also contribute to the grain boundary equilibrium. If a change in just one of the interfacial tensions occurs, the equilibrium configuration must change and the liquid will move to

balance the forces. In order to simplify the system, wetting parameters for the surface and boundary were defined as k_s and k_b, respectively, and given in equations 5.3 and 5.4.

$$k_s \equiv \cos\theta = \frac{\gamma_{SV} - \gamma_{SL}}{\gamma_{LV}} \quad [5.3]$$

$$k_b \equiv \cos\chi = \frac{\gamma_{GB}/2 - \gamma_{LB}}{\gamma_{LV}} \quad [5.4]$$

If k_s is positive, then the contact angle with the surface is less than $\pi/2$ and the liquid will wet the surface. But if k_s is negative, the contact angle will be greater than $\pi/2$ and the liquid at the surface will tend to dewet or ball-up. The same is true for k_b, except instead of wetting or dewetting the surface, the grain boundary is the interface of interest. Negative wetting parameters were found to increase the energy, while positive wetting parameters were found to lower excess energy.[11]

Brada and Clarke's[11] calculations showed that either the grain boundaries will be wet or the surface will be wet, and a wetting transition is present. Only at a unique condition ($\phi < \pi$) will the liquid wet the boundary and the free surface at the same time. The wetting transition describes necessary conditions for the exudation of the IGF from the grain boundary to the surface. The wetting transition can be made sharper if more liquid is added to the system. The observation of one unique set of processing conditions to draw liquid from the grain boundary to the surface in a continuous manner explains why removal of the second phase in LPS materials is so difficult.

Penetration of grain boundaries by liquid could occur by either dissolution and reprecipitation or a wedging process similar to crack growth.[11] In either situation, a "core" region exists at the point where the glass is trying to infiltrate the grain boundary. The core within the grain boundary and the solid-liquid-vapor (SLV) triple point on the surface are where all of the forces are balanced. In general, the curvature of the liquid on the free surface equals the curvature of the liquid within the boundary, no

matter if the grain boundary is wet, the surface is wet, or both are continuously wet. Therefore, the pressure within the liquid phase always tries to remain constant everywhere.[11] When there is an absence of externally-applied stress, the driving force, ΔF, for interfacial energy reduction at wet grain boundary can be described by equation 5.5.[12]

$$F_D = \gamma_{GB} - 2\gamma_{SL} \qquad [5.5]$$

Of course, changes in processing temperature and liquid viscosity affect the capillary forces and can change the resulting behavior. In addition, crystal orientation at the grain boundary and free surface will change the magnitude of the capillary forces.[13] Ultimately, the grain-boundary and liquid-film mobilities will change if any of these conditions are altered. On heating, IGFs will expand and exude from the grain boundary. Likewise, a small change in cooling rate can change the liquid film's mobility and allow the film to rapidly penetrate the grain boundary.

Besides having curvature within a liquid film, grain boundaries can be curved, adding another curvature term to the capillarity effects. Curved grain boundaries promote Ostwald ripening due to the difference of pressure across the boundary.[14] The grain boundary velocity will depend on this curvature and the extrinsic grain boundary mobility.[15] Spherical grains may not migrate since the driving force may not be able to overcome the local pressure equilibrium. Correct reaction kinetics and driving force magnification can be determined numerically when grain boundaries are assumed to have a hyperbola curvature. Grain boundary mobilities depend on many extrinsic factors, including curvature in 3D, which can not be easily isolated. Therefore, mobilities determined experimentally should only be used as a rough estimate and to determine grain growth trends.[15]

Penetration of a grain boundary with a liquid occurs in three stages.[12] An incubation period is needed to allow the infiltrating material to reach its melting temperature and transform to the liquid state. Once the liquid forms, the liquid can penetrate grain boundaries. Liquid motion stops when the saturation condition is reached. The IGF is

the equilibrium thickness, all possible grain boundaries are wet and the glass has exuded onto the other side of the sample. In addition, wetting of the free surface occurs.

Processing atmosphere can change the capillary effects on the grain boundaries.[16] Liquid films have been found to exude from grain boundaries in reducing atmospheres, but wet only the grain boundaries in oxidizing atmospheres. In addition, if a void, pocket of vapor, or pore exists within the compact, the pressure in any grain boundaries meeting the void will change. The presence of the void can change the liquid film wettability at that particular grain boundary.[11]

As is the case in geologic ceramics, water can change the IGF behavior and composition. Humid processing conditions, or the lack there of, would change the IGFs in processed ceramics. The spreading behavior of methylene iodide on soda-lime silicate glass was monitored with changing relative humidity.[17] As the relative humidity was lowered, the contact angle of the droplets lowered, indicating more of a tendency to spread on the surface. The presence of a water monolayer on the surface at high relative humidity is thought to mask the forces from the glass substrate.

5.2.3 Glass and the Grain Boundary Groove

Even when great care is taken during processing, glass may form at the grain boundaries during sintering or mechanical processing. Glass at the grain boundaries of alumina has been found to aid in coalescence and annihilation of pores during sintering of green compacts.[11]

Films at grain boundaries are subject to the same thermodynamics and kinetics as bulk material. The phase diagram for the bulk/glass system will indicate when the glass becomes a liquid. At this point, the bulk material will be able to dissolve within the liquid. At a grain boundary, dissolution of one of the interface planes may occur with subsequent reprecipitation of the material on the other interface plane. If one plane is able to dissolve faster than another, a concentration gradient across the boundary is established and grain boundary migration occurs. Figure 5.5a illustrates this process.

Thermal grain boundary grooving occurs when a grain boundary meets the surface and is subjected to an anneal. When a liquid film is present at the grain boundary, the groove geometry changes. Grooves with IGFs are more acute than grooves with out a liquid film present.[18] In addition, the groove formation occurs much faster. Groove formation in the presence of an IGF is controlled by dissolution and diffusion, rather than diffusion alone. Mullins'[19] theory on thermal grooving may not apply in all cases when a liquid is present since dissolution of material is not accounted for.[18] The formation rate for the groove is faster at the groove tip than near the surface. The liquid can be thought of as corroding or etching the groove. Chapter 3 of this dissertation goes into greater detail on groove formation.

When an IGF is present, the glass is thought to exude when the sample is brought to temperature and wet the surface. Grain boundary migration occurs underneath the wet film. As the boundary moves in a spasmodic motion, the film is left behind. The ridge formed at the grain boundary can cause enough instability with in the film so that the film can begin to break apart and form droplets. The droplets become markers for where the grain boundary has been,[20] as shown in Figure 5.5b. Of course, orientation of the interface planes and the free surface plays an important role in this process.

5.2.5 Mechanical Properties of IGFs

Thermal expansion is the primary mechanical parameter of interest with IGFs. Solids expand or contract depending on temperature fluctuations, and this behavior is described by the coefficient of thermal expansion (α) in equation 5.6. The change in length (Δl) and change in temperature (ΔT) are compared to the original length (l_o) of solid. Thermal expansion depends on the bond character of the solid. Ionically bonded materials will generally expand more on heating than covalently bonded materials.[7] When an IGF is present in a polycrystalline solid, the α are usually not the same for the IGF and the bulk. The difference can cause stresses to form at the interface when a component is heated or cooled. Bowing, cracking or delamination may occur. When put

into service, the difference in thermal expansion can cause the component to fail. Table 5.2 lists mean α of a variety of ceramics for comparison.

$$\alpha = \frac{\Delta l}{\Delta T l_o} \qquad [5.6]$$

Of course, thermal expansion is subject to anisotropy. Cubic materials are usually isotropic in the three major crystal directions. However, non-cubic crystal structures can have different thermal expansion behavior along different crystal directions. In some cases, the difference can be quite dramatic. For example, TiO_2 has a α equal to 8.3 ppm/°C parallel to the *c*-axis, but only 6.8 ppm/°C normal to the *c*-axis.[7] In the case of glass, the thermal history the glass experienced may also change the degree of thermal expansion.

Thermal expansion isn't the only mechanical property that will change because of the presence of IGFs. Viscosity of the IGF will change depending on the temperature of the system. At higher temperatures, a less viscous film will decrease creep resistance of the material. When cooled or heated, the IGFs may change composition. The change in composition can also result in a viscosity change. Most glasses behave as Newtonian liquids at high temperature, allowing glass to be drawn without necking.[21]

These differences in mechanical properties can change the performance quality and lifetime of components. Glazes and enamels may unintentionally crack, allowing corrosion of the material below. Metal-to-ceramic bonding and seals will delaminate. The seals may allow leakage if the assemblage is subjected to thermal cycling. Thin films may also delaminate from substrates. Large stresses at the interface may cause the formation of dislocations in thin films. A component's thermal shock resistance may be degraded if the crystalline and IGF mechanical properties do not match. Crystallization of the IGF after processing may improve the component's mechanical properties.

5.2.5 Observations of Capillary Forces in Alumina

Cross-section analysis of grain boundaries shows that when a liquid film is present, one interface plane may be faceted while the other can remain flat. The IGF can easily accommodate the difference in orientation and morphology. Faceting under a glass droplet[22] has been shown to be different than faceting of the free surface.[23] Presumably, faceting of the grain boundary will also change when a liquid is present.[18] Therefore, glass can accommodate, and even alter, differences in surface tension.

Previous work on the alumina/anorthite system has shown that the IGF can wet preferentially at the grain boundary.[24] The orientation at the interface plays an important role in the IGF's behavior. When a grain boundary facets, one facet plane may be wet, while the other plane has no film at all. The orientation of the interface planes will create a surface-tension dependence. The facets form to lower the surface tension by creating more surface area of a low-energy plane. Likewise, the glass will wet the most energetically-favorable planes.[25] In some cases, the glass will prefer to exude from the boundary and wet the free surface.[26] As described earlier in this dissertation, wetting of glass on free surfaces is also orientation dependent.

Crystallization of the IGF or exuded glass may occur.[25] A second phase will then be present. In the case of an IGF, the crystalline film may not be the lowest possible energy state, but is lower than the original configuration. The phase diagram plays an important role in determining whether an IGF will crystallize or not.

At what point does the IGF become a phase boundary? The width of the IGF will change the solid-liquid interactions and will change the capillary forces in the grain boundary.[25] Little has been done on this dependence.

Ravishankar[25] determined that the cooling rate is the most important stage of thermally treating glass films at interfaces. By altering the cooling rate of anorthite films on *m*-plane sapphire, the droplet shape was shown to change. Water-quenched droplets had an elongated shape, while naturally cooled droplets were spherical. Glass that has exuded

from grain boundaries to form droplets on the free surface will also form in different patterns depending on the free surface orientation. Using bicrystals with known interface and surface orientation, a comparison of the glass behavior on different orientations of sapphire was made.[25]

Glass is most often forced to be at the grain boundaries. But when the temperature is raised, the glass is able to move to a lower energy configuration. The glass will move to a new position where capillary forces, surface tension and concentration gradients are all balanced.[25] In order to achieve this equilibrium, the IGF may dewet the grain boundary, move to a different grain boundary, crystallize or exude onto the free surface.

Similar experiments watching monticellite- ($CaMgSiO_4$) infiltrated MgO showed similar behavior to the alumina/anorthite system.[26] The monticellite-glass formed an IGF, exuded from the grain boundaries and dewet the free surface. A unique geometry was used to study these effects. A dimpled sample of polycrystalline MgO was prepared and monticellite powder was allowed to reside within the dimple during heat treatment. The powder turned to liquid during annealing and the liquid infiltrated the grain boundaries. The sample was held at temperature long enough to let the glass penetrate completely through the sample and exude on the other side. Observations using SEM showed that the glass droplet at a triple junction had a depression, indicating that the glass is pulled back into the grain boundary after exuding. The behavior was proposed to occur during cooling to balance the capillary forces.

Santala and Glaesar[13] showed that capillary forces along different crystallographic directions have different behaviors. By using lithography and diffusion bonding, void channels were created along low-index directions in alumina. The higher energy directions were found to close the channels through diffusion at high temperature much faster than lower energy directions.

5.2.6 Studies on Other Materials Systems

IGFs are not found just in traditional ceramics. Much work has been done to understand IGFs and dopants at grain boundaries in metals, semiconductors and electronically-active ceramics. In these materials, creep, fracture, conductivity, and crystallization are just a few properties that are altered by the presence of an IGF. Subramaniam, et al.[27] presents a brief review paper explaining important terms when dealing with IGFs and classic materials systems that have been studied. Some of these systems will be briefly mentioned here.

A lot of research has been done on understanding varistors, which act as surge protectors for microelectronics. ZnO varistors use Bi_2O_3 IGFs to create an electrical depletion region on either side of the grain boundary.[7] The varistor behavior more readily occurs in this case. The Bi_2O_3-ZnO system is unique in that an equilibrium film thickness has been found.[27] When the ZnO is co-doped with Bi_2O_3 and various rare-earth elements to form IGFs, the electrical conductivity was found to improve.[28]

Si_3N_4 and AlN are both electronically important ceramics, but are often doped with several different elements that create IGFs. Common dopants for Si_3N_4 are La_2O_3, MgO,[29] Yb, SiO_2, Al_2O_3,[30] Y_2O_3, Gd_2O_3, Nd_2O_3, [27] and CaO,[31] to name a few. The IGFs have been shown to create a space charge at the grain boundaries, which could possibly alter the performance of devices made from these materials.[29] Doping with rare-earth elements can improve the mechanical properties of Si_3N_4.[30] AlN is commonly doped with Y_2O_3 in order to produce a dense material during sintering. In addition, the Y_2O_3 acts as an oxygen getter to remove oxygen from the bulk AlN.[32] However, by doing this, the thermal conductivity properties of AlN are dramatically changed depending on the doping levels.[33] The thermal conductivity of AlN is most efficient at the grain boundary, but the presence of the Y_2O_3 glass changes this.

Liquid-metal embrittlement is a classic problem illustrating the importance of studying IGFs. Liquid metal forces itself between the grains of the bulk and causes intergranular

fracture.[12] Common systems for this to happen in are Ga in Al and Bi in Cu.[34] For more information on liquid-metal embrittlement, see appendix 5.2.

5.2.7 Characterization of Glass

The earliest methods used for characterizing glass included transmission electron microscopy (TEM), low-energy electron diffraction (LEED) and neutron scattering. Early work was done on characterizing glide planes in SiO_2 glass[35], metallic glasses[36] and porous sol-gel-prepared SiO_2-gels[37] using the TEM. The contrast mechanisms in TEM allow glass-phases to be easily identified from crystalline ones.[38] When TEM is used in selected-area diffraction (SAD) mode, glass can be immediately identified by the lack of a spot pattern.

LEED was the most popular tool to study surfaces until the invention of scanning probe microscopy (SPM).[39] A low-energy electron beam is allowed to glance the surface of interest and the resulting backscattered electrons are collected for analysis. The backscattered electrons are Bragg diffracted and give information on any surface and unit cell periodicity. LEED can also determine any surface relaxations.[40] Glass is used as a substrate for thin-films in order to not introduce any inaccurate periodicity into the collected data.[41]

Neutron scattering uses the deflection of neutrons off of an atoms or ions nucleus to gain information about the material. Neutrons are electrically neutral, and therefore, are able to probe much deeper within bulk material since the neutron will not be affected by an atom's electron cloud. Similar data to that collected during X-ray scattering can be collected. However, equipment is much more expensive and often difficult to have access to. The earliest use of neutron scattering in ceramics was to study the nucleation of glass-ceramics.[42] Most recently, various forms of neutron scattering were used to determine the ring structures in SiO_2 glass.[43]

5.3 Experimental

5.3.1 Dimple Sample Preparation

A useful sample geometry implemented here was a dimpled polycrystalline sample of Lucalox™, a commercially available alumina that has been doped with 0.5 wt% MgO to inhibit grain growth. The material comes in the form of a tube with a wall thickness of roughly 1 mm. Samples were cut from the tube in 2 x 3 mm rectangles. Both sides were polished using 30-μm grit diamond-embedded lapping film until flat. The originally convex side of the tube was polished to a 0.5-μm finish. The opposite side was ground using 30-μm grit until the specimen thickness was roughly 400 μm. The sample was then mounted to a stainless steel dimpling puck and ground in the same manner for making traditional TEM samples using diamond paste, ethylene glycol and cloth-padded dimpling wheels. A succession of finer diamond paste was used; the final polish used a 0.25 μm paste. The final thickness of the dimple center was approximately 10 μm. Figure 5.6a shows the flat sample surface prior to annealing.

5.3.2 Annealing for Glass Infiltration and Exudation

Anorthite ($CaAl_2Si_2O_8$ or CAS) powder was sprinkled inside the dimple. The dimple acts like a bowl holding enough powder so that an infinite source of anorthite was present. Figure 5.7a shows the prepared sample geometry. The dimpled sample and powder were then heat treated in a box furnace in air at 1650˚C. Anorthite melts at 1550˚C,[44] (see Figure 5.8), allowing the powder to melt before the anneal temperature was reached and infiltrate the grain boundaries. The dimpled samples were propped up on two pieces of single crystal alumina so that the flat surface of the sample would not sinter to the crucible. The behavior of glass that infiltrated the entire sample and exuded from the flat side would also not be interfered with by using this geometry, illustrated in figure 5.7b. When in this configuration, grain boundary infiltration was also assisted by gravity. Samples were heated to 1650˚C at 20˚C/min. The dwell temperature was held for 6 min. and the sample was allowed to cool naturally afterwards. Subsequent anneals were identical.

5.3.3 Characterization of Surface Features

Behaviors of the IGFs where the sample surface was met could be monitored using atomic force microscopy (AFM) and scanning electron microscopy (SEM). By using a dimpled sample, many characteristics of IGFs can be monitored at once. A dimpled surface automatically has a thickness variation, and therefore, diffusion rates and specimen-thickness dependence can be determined. The polycrystalline compact allows all possible orientations to be studied at once. The wetting behavior of the grain boundaries can be directly compared. With only a small amount of further thinning, the sample is TEM ready.

5.4 Results

5.4.1 Infiltration and Exudation of Glass

During the 6 min anneal, the glass formed a large droplet within the dimple and droplets were found on the reverse flat side of the sample. Figure 5.6b shows the droplets on the surface at low magnification, while figure 5.9a shows the surface at higher magnification. The sample is thin enough that the glass reservoir on the dimpled side may be viewed in transmission in figure 5.6b.

Figure 5.9a shows the surface after the first anneal. Droplets of different size, shape and pattern can be seen to decorate the surface. EBSD was used to show that surface orientation influenced the type of droplet patterns formed on the free surface. Grains from the same area shown in figure 5.9a are labeled in figure 5.10 with the EBSD point analysis surface normal. The AFM images in figure 5.11 clearly show an orientation dependence on droplet behavior.

5.4.2 Ostwald Ripening of Droplets

The images in figure 5.9 shows a comparison of the same area after 6 min and 12 min at temperature. Ostwald ripening of the droplets can be clearly seen, even at low

magnification, in the corresponding colored boxes. Large droplets consumed smaller droplets that were located near them.

5.4.3 Decoration of a Remnant Groove

During annealing, select grain boundaries were able to migrate and leave behind a remnant groove. Figure 5.12 is an example of a remnant groove that has been decorated with anorthite droplets. The droplets were left behind when the grain boundary migrated. When the same grain boundary/remnant groove is annealed again, the droplets coalesce, the remnant groove becomes shallower and the grain boundary looses some of its curvature. Figure 5.13 compares the same area before and after the second anneal. The grain boundaries of the grain in the center of the image become much straighter and the surrounding droplets also combine with surrounding grains. The droplet on the left side of the center grain has completely disappeared.

Figures 5.14 and 5.15 show the section analysis of the remnant groove (red) and grain boundary (green) after 6 min and 12 min at 1650˚C, respectively. Accurate measurement changes of the grain boundary can not be made, since droplets have formed along the boundary after 12 min. The large hump on the right side of the 12 min section analysis in figure 5.15 indicates a droplet. The remnant groove width has not changed with further anneal, but the depth has. The remnant groove has healed roughly 10 nm.

5.4.4 Completely Wet Grains

Completely wet grains were found at the edge (figure 5.16) and the interior (figure 5.17) of the flat sample surface. When comparing before and after the second anneal in figure 5.18, the completely wet grain in figure 5.17 appears to be pulling away from the grain boundaries and beginning to dewet the surface. In a higher magnification image, (figure 5.19b. grain on the right side) facets along the thermal groove where the droplet has receded after the second anneal can be seen.

Energy-dispersive spectroscopy (EDS) of the large droplet at the edge of the sample surface, shown in figure 5.16, confirmed qualitatively that the glass composition was anorthite.

5.4.5 Glass at Grain Boundaries

The AFM images in figure 5.19 show the same grain and triple junction after 6 min at 1650˚C and again after an additional 6 min at temperature (12 min total). Clearly, the grain boundaries have changed. Section analysis of the two images in figure 5.20 shows that after the first thermal treatment, a droplet was indeed residing over the triple junction (green line trace). When the same triple junction is returned to after an additional 6 min at temperature, a line trace shows a thermal groove has now formed at the triple junction. Since no large amounts of additional glass can be seen on the surface near the triple junction, the glass must have penetrated back into the grain boundary in order to satisfy force balances.

Glass can be seen at the grain boundaries in figure 5.19 after a 6 min anneal. This glass has disappeared after an additional 6 min. Section analysis (red line traces) in figure 5.20 shows that the grain boundary groove changes from being broad and flat-bottomed to thinner and sharp.

5.5 Discussion

5.5.1 Infiltration and Exudation of Glass

Mullins[45] proposed the "specimen thickness effect." When the sample thickness is on the order of the grain size, grain-boundary mobility was retarded. The lack of curvature needed to drive a grain boundary to move is no longer present in thin samples. While the samples in this study were in this regime at the center of the dimpled region, grain boundary migration was not the main focus. When a second-phase is present, specimen thickness has less of an effect on boundary inhibition than the second phase. Only the nature of the intergranular glass film was being considered. Therefore, this effect may

be ignored. The grain boundary migrating in figure 5.12 moved very quickly and agrees with this assumption.

The images shown (figures 5.10-11) clearly display that orientation is important in the dewetting process. Each orientation of a crystal has a different surface tension associated with it. Therefore, by equations 5.3 and 5.4 and figure 5.4, if surface orientation is given then the surface tension of the solid-liquid and solid-vapor interfaces (γ_{SL} and γ_{SV}, respectively) are defined. In order to balance the surface tensions only the contact angle (θ) and liquid-vapor surface tension (γ_{LV}) must be determined. By using Young's equation, given in equation 5.7 as essentially an expanded version of equation 5.2, one can see that that γ_{LV} will be different when the underlying surface orientation changes to maintain force balance, and thus, the droplet patterns will change.

$$\gamma_{SV} - \gamma_{SL} = \gamma_{LV} \cos\theta_c \qquad [5.7]$$

The EBSD data in figure 5.10 confirms that droplet pattern depends on the underlying orientation of the surface. Orientation mapping would be the ideal method for gaining statistical confirmation of this, but because of the technique's limitations, is not possible. EBSD is sensitive to only the first 100 nm of the surface. The electron beam is incapable of penetrating the droplets to reach the surface below. Therefore, EBSD point analysis is the most efficient way of sampling surfaces in this case.

Droplets sitting on the surface at the exit of a triple line act as a finite reservoir of liquid. When the liquid penetrates the grain boundary, the size of the droplet will decrease.[4] When the radius of curvature for the droplet equals the radius of the capillary meniscus, penetration will cease. (See figure 5.2) Therefore, a finite penetration depth must exist depending on the droplet size, and ultimately, the initially wet-film thickness. The finite size of the droplet feels an increased pressure, which assists penetration. An infinite reservoir of material (a wet film) will not rise within the capillary as far or as quickly as a drop with a finite size. In addition, contact angles within a capillary can exist when $\theta > 90^\circ$ with a finite liquid source, but can not if the source is infinite.[4]

Whether a film dewets to form a droplet or stays wet to be an infinite source is surface tension dependent. Therefore, the surface orientation of the grains bounding the internal interface will contribute to how deep the liquid penetrates the interface. The droplet in figure 5.19a residing over the triple junction resembles the situation illustrated in figure 5.2a. The droplet is not in equilibrium with the rest of the grain boundary below, and therefore, is drawn back into the grain boundary with further heat treatment. Figure 5.19b more closely resembles the equilibrium configuration illustrated in figure 5.2c. However, subsurface investigation using a FIB tool or TEM is needed to confirm this.

5.5.1 Ostwald Ripening of Droplets

As expected large droplets consumed smaller droplets when the droplets resided on the same grain surface. Ostwald ripening is driven by a reduction of surface energy. Two droplets will combine in order to reduce the total amount of surface area. Ostwald ripening can be clearly within the blue box in figure 5.9 and throughout figure 5.13. The height scales for both images in figure 5.13 are identical, so a direct comparison of the droplets may be made.

While most droplets combine with neighbors on the same grain surfaces, the droplets may migrate to other grains and ripen droplets on the surface of another grain. This appears to be the case for the large droplet in the left corner of the center grain in figure 5.13a. This droplet has disappeared in figure 5.13b. However, the droplets on the grain in the bottom-left corner of 5.13b are all larger than they were prior to the second anneal. All of the droplets present after the first anneal are present after the second anneal, so Ostwald ripening of droplets from the same grain has not occurred. The droplet that disappeared from the center grain migrated to the adjacent grain and combined with the other droplets.

5.5.2 Decoration of a Remnant Groove

The observation in figure 5.11 proves that the glass is infiltrating and exuding from the grain boundaries rather than migrating along the surface or evaporating and condensing

when the sample is at temperature. If the glass became present on the opposite surface due to surface diffusion, the droplets would have moved with the grain boundary when it migrated from its original position. If evaporation/condensation was the active mechanism, the remnant groove and the migrated grain boundary would both be decorated with droplets. Instead, only the remnant groove is decorated, indicating that the glass exuded from the grain boundary prior to grain boundary migration. The glass droplets were left behind when the grain boundary moved. In addition, figure 5.19a shows glass exuding from the grain boundaries.

The section analysis of the same grain boundary and remnant groove in figures 5.14 and 5.15 show that the remnant groove (red section line) has begun to heal as expected and described in chapter 3 of this dissertation. The grain boundary (green section line) can not be used to definitively say anything about the grain boundary. Droplets decorate one edge of the grain boundary in figure 5.15, indicated by the large hump in the section analysis and seen in the AFM image. Accurate measure of the thermal groove can not be done.

5.5.3 Completely Wet Grains

The completely wet grain shown in figure 5.16 can not be considered in this study since it is adjacent to the edge of the sample. There is no way of proving whether the glass arrived there by diffusion through the compact or along a "short-circuit path" along the external surface of the specimen. However, the droplet is quite large and thick in comparison to other droplets on the surface and can be used to determine the glass composition. The EDS spectrum in figure 5.16 shows qualitatively that the glass is anorthite. Because of the relatively poor resolution of EDS within the SEM, further quantitative measurements of composition should be made using EDS within the TEM or wavelength-dispersive spectroscopy (WDS).[46]

Figures 5.17-19 show a grain that was completely wet by anorthite glass that was in the interior of the sample. The glass at the grain boundaries adjacent to this grain indicates that the glass exuded from the grain boundary to wet the surface. This grain stands out

even in VLM images (figure 5.17a) where Newton's rings give the grain brilliant colors. The rings are a diffraction effect and indicate that the droplet's thickness is on the order of visible light's wavelength.

The section analyses in figure 5.18 show that the droplet is pulling away from the grain boundaries with additional time at temperature. In 5.18a, the droplet reaches all the way to the grain edges. But in 5.18b, small ledges can be seen on either side of the droplet. Figure 5.19 gives a higher magnification of the droplet (right-most grain). When the grain is compared before and after the second anneal, a thermal ridge has formed after the second anneal. The thermal ridge is faceted and is the ledge in the section analysis of figure 5.18b. The droplet is trying to lower its surface energy by balling up into a sphere and reducing its surface area.

5.5.4 Glass at Grain Boundaries

Figures 5.19 and 5.20 show glass at the grain boundaries of the center grain. After 12 min at 1650˚C, the glass has disappeared from the boundaries and the large triple junction. Since no large amounts of additional glass can be seen on the surface near the triple junction, the glass must have penetrated back into the grain boundary in order to satisfy force balances, as previously discussed in section 5.5.1.

Section analyses in figure 5.20 show that the grain boundary adjacent to the triple junction (red section line) has become thinner and sharper. After the first 6 min at temperature, the grain boundary is wide, shallow and contains an IGF. After an additional 6 min at 1650˚C, the glass has drawn back into the grain boundary and the boundary has begun to close up. A non-equilibrium condition similar to figure 5.2b is in place. In addition, once the IGF has left a portion of the grain boundary, the respective boundary planes will be driven closer to one another in order to satisfy dangling bonds.

5.5.5 Other Considerations

The analysis given here assumes that no pores exist at the grain boundary subsurface. The pores will change the pressure conditions needed for penetration and exudation of the liquid.[4] Of course, this assumption is not entirely realistic unless the material is 100% dense. Pores are swept from the bulk when a grain boundary migrates through them. The pores move along with the grain boundaries.[5] However, the assumption simplifies the analysis, and by monitoring behavior at many grain boundaries, can be justified.

Droplets during the process of being pulled back into triple junctions on cooling were not observed here as in Ramamurthy's experiment[26] with MgO and monticellite. However, this observation could only be a matter of adjusting the processing parameters and timing. By lowering the processing temperature, shortening the dwell time, or altering the cooling rate, this behavior may possibly be seen.

One unexpected consequence of using this sample geometry is sample warping. The sample is so thin that the grains are able to shift or rotate in order to relieve stresses from the preparation process. In addition, glass infiltration creates stresses in the grain boundaries that were not previously there. The sample warps locally, making measurements of diffusion rate difficult since the total thickness can not be accurately measured.

5.6 Summary and Future Work

Glass can easily penetrate and exude from grain boundaries in an effort to balance surface tensions when an IGF is present. The same forces act to try to balance glass and liquid films on the free surface of materials. In order to balance these forces, several behaviors may occur. The glass can completely wet or dewet the surface of the grains. The behavior depends on the surface orientation of the grain.

Despite the presence of IGFs, grain boundary migration can still occur. The IGF may allow glass to exude and decorate the grain boundary where it intersects the free surface. Boundaries that have had glass exude from them will migrate and leave the decorated remnant groove behind. The remnant groove continues to heal in the same manner as if the droplets were not present.

Once glass has exuded from the grain boundaries, the dewet droplets can move around on the surface. Ostwald ripening may occur in order to lower the total surface energy of the droplets.

While VLM, SEM, EDS, EBSD and AFM were all used to study the behavior of IGFs here, more characterization techniques should be used to fully understand the behaviors. TEM would give more information about the subsurface structure of the grain boundaries and would be able to confirm orientations at interfaces. *In situ* TEM, if a high enough temperature could be reached, would allow the IGF to move in and out of the grain boundary to gain a direct understanding of the behaviors. Specific grain boundaries could be characterized if cross-section samples were made using the FIB tool. By combining the surface analysis performed in this study with the cross-section analysis, a complete pictures could be gained.

Using multilayers and bicrystals would allow IGFs at specific grain boundaries of known orientation to be monitored. Pulsed-laser deposition (PLD) would deposit a thin anorthite film onto single-crystal alumina of known surface orientation. The film/substrate assemblage could be hot pressed to another single crystal alumina piece. The orientation at the boundary of the second piece would also be known. Several pieces could be hot-pressed at once to make a multilayered structure. The PLD could be used again to deposit additional layers after the first glass layer, rather than hot-pressing a substrate onto the assemblage. A series of multilayers of tailored thicknesses and composition could easily be constructed. Figure 5.21 shows the finished sample geometries. By polishing multilayers into a wedge, the effect of grain boundary depth could be determined.

In summary, surface-tension balances are constantly trying to be achieved by the materials system when glass and IGFs are present. The most interesting behaviors occur in non-equilibrium conditions, while these balances are trying to be reached.

Appendix 5.1: Surface Energy vs. Surface Tension

Some researchers use surface energy and surface tension interchangeably. However, care should be taken when using these terms, as they may not be equivalent. Surface energy has units of energy/area, while surface tension has units of force/length. The units for both are equivalent, but they have different physical meanings.[47] Energy implies a flow and tension implies a displacement. The motions are very different. Liquids do not have shear strength, and therefore, can not experience a force. However, liquids flow, so they have surface energy. Solids, on the other hand, have shear strength. Unless close to their melting point, solids do not readily flow. Rather, atoms within a solid move by displacements or diffusion. In both, strain is introduced into the crystal. A force is exerted on the surrounding atoms, and thus, surface tension has more physical meaning to solids than surface energy.

However, solid surfaces do have a surface energy, but it is not of the same kind as liquids.[47] The surface energy comes from the force exerted at a free surface by the atoms and molecules normal to the surface. This unbalanced force is usually described as the Hamaker coefficient (A).[17]

Appendix 5.2: Liquid-Metal Embrittlement

Liquid-metal embrittlement (LME) occurs in several materials systems and is a long-studied problem. The penetration of grain boundaries with liquid or glass causes the grains to break apart from one another, resembling a reverse sintering process. The difference between LME and grain boundary wetting is that an external stress is applied during LME.[12] When the grains break apart, a component loses ductility and will experience brittle fracture. The most commonly studied systems are Ga in Al and Bi in Cu. Bi in Ni and Ga in Zn are other examples of systems that experience LME.[12] The

length scale of grain boundary thickness and penetration can range from several nanometers to several microns.[34]

The glass is believed to force the grain boundary open similar to crack-tip growth. The strain at the penetration front within the grain boundary is thought to drive further penetration. Grain boundaries are thicker near the liquid reservoir and get thinner farther away.[34] Unfortunately, in situ studies to monitor the kinetics are not possible. Because of the embrittlement, TEM samples are nearly impossible to make. Even if a sample can be prepared, measurements are limited by the camera speed. The kinetics occur so quickly that current CCD cameras are unable to capture the process.[34]

The Ga-Al system has found to lose cohesion between the grains due to a monolayer of Ga bonding tightly to the Al lattice. Ga-Ga bonds are weaker than some Ga-Al bonds. Therefore, if the Ga bonds to the Al lattice at the grain boundary walls, grain boundary sliding and infiltration can occur at the Ga-Ga bonds within the grain boundary.[34] Synchrotron radiography was used to watch the Ga liquid penetration *in situ*.[12] Penetration depth was found to have linear time dependence. Grain boundaries with misorientations that normally do not wet are capable of wetting when a stress is applied.

While most of the research on penetration of second phases into the grain boundaries to cause LME has focused on understanding the stress state near the penetration front, little has been done to understand the pressure effects due to capillary forces. The belief that a tensile stress is necessary in all LME penetration creates the notion that thermodynamics are not important.[12] In addition, only qualitative theories have been developed to describe the behavior. Materials systems are usually treated individually in quantitative studies. Most work has been done on bicrystals, since the stress state and grain boundary energy can not be easily controlled in polycrystalline materials.[12]

References

[1] J. Burton, Glass: Philosophy and Method, Bonanza Books New York, (1967).

[2] R. M. German, P. Suri, S. J. Park, "Review: liquid phase sintering" J. Mater. Sci., **44** [1] 1-39 (2009).

[3] D. W. Susnitzky, Y. Kouh Simpson, B. C. DeCooman, C. B. Carter, "The structure of surface steps on low-index planes of oxides" Journal, **60** [Issue] 219-226 (Year).

[4] A. Marmur, in: M. E. Schrader, G. Loeb (Eds.), Modern Approach to Wettability: Theory and Applications, New York, (1991), pp. 327-358.

[5] J. E. Burke, "Role of grain boundaries in sintering" J. Am. Ceram. Soc., **40** [3] 80-85 (1957).

[6] M. N. Rahaman, Ceramic Processing, Taylor & Francis Boca Raton, (2007).

[7] C. B. Carter, M. G. Norton, Ceramic Materials: Science and Engineering, Springer New York, NY, (2007).

[8] J. Schultz, M. Nardin, in: M. E. Schrader, G. Loeb (Eds.), Modern Approach to Wettability: Theory and Applications, New York, (1991), pp. 73-100.

[9] R. J. Young, P. A. Lovell, Introduction to Polymers, Stanley Thornes (Publishers) Ltd. Cheltenham, UK, (1981).

[10] J. Britt, The Complete Guide to High-Fire Glazes, Lark Books New York, (2004).

[11] G. Rossi, J. E. Burke, "Influence of additives on the microstructure of sintered Al_2O_3" J. Am. Ceram. Soc., **56** [12] 654-659 (1973).

[12] W. Ludwig, E. Pereiro-López, D. Bellet, "In situ investigation of liquid Ga penetration in Al bicrystal grain boundaries: grain boundary wetting or liquid metal embrittlement?" Acta Mater., **53** 151-162 (2005).

[13] M. K. Santala, A. M. Glaesar, "Surface-energy-anisotropy-induced orientation effects on Rayleigh instabilities in sapphire" Surf. Sci., **600** 782-792 (2006).

[14] W. D. Kingery, H. K. Bowen, D. R. Uhlmann, Introduction to Ceramics, John Wiley & Sons New York, (1960).

[15] R. C. Sun, C. L. Bauer, "Measurement of grain boundary mobilities through magnification of capillary forces" Acta metall., **18** 635-638 (1970).

[16] M. P. Brada, D. R. Clarke, "A thermodynamic approach to the wetting and dewetting of grain boundaries" Acta Mater., **45** [6] 2501-2508 (1997).

[17] M. E. Schrader, in: M. E. Schrader, G. Loeb (Eds.), Modern Approach to Wettability: Theory and Applications, New York, (1991), pp. 53-71.

[18] B. S. Bokstein, L. M. Klinger, I. V. Apikhtina, "Liquid grooving at grain boundaries" Mater. Sci. Eng. A, **203** 373-376 (1995).

[19] W. W. Mullins, "Theory of thermal grooving" J. Appl. Phys., **28** [3] 333-339 (1957).

[20] N. Ravishankar, C. B. Carter, "Migration of alumina grain boundaries containing a thin glass film" Acta Mater., **49** 1963-1969 (2001).

[21] C. B. Carter, "S=99 and S=41 Grain Boundaries" Acta Metall., **36** [10] 2753-2760 (1988).

[22] S. Ramamurthy, H. Schmalzried, C. B. Carter, "Interaction of Silicate Liquid with a Sapphire Surface" Philos. Mag. A, **80** [11] 2651-2674 (2000).

[23] J. R. Heffelfinger, M. W. Bench, C. B. Carter, "On the faceting of ceramic surfaces" Surf. Sci. Let., **343** L1161-L1166 (1995).

[24] D. W. Susnitzky, C. B. Carter, "Surface Morphology of Heat-Treated Ceramic Thin Films" J. Am. Ceram. Soc., **75** [9] 2463-2478 (1992).

[25] N. Ravishankar, C. B. Carter, "Glass/Crystal Interfaces in Liquid-Phase Sintered Materials" Inter. Sci., **8** 295-304 (2000).

[26] S. Ramamurthy, M. P. Mallamaci, C. B. Carter, "Initial stages of solid-liquid interactions in the MgO-$CaMgSiO_4$ system" Scripta Mater., **34** [11] 1779-1783 (1996).

[27] A. Subramaniam, C. T. Koch, R. M. Cannon, M. Rühle, "Intergranular glassy films: An overview" Mater. Sci. Eng. A, **422** 3-18 (2006).

[28] Y. Huang, M. Liu, Y. Zeng, C. Li, "The effect of secondary phases on electrical properties of ZnO-based ceramic films prepared by a sol-gel method" J. Mater. Sci., **15** 549-553 (2004).

[29] S. Bhattacharyya, C. T. Koch, M. Rühle, "Projected potential profiles across intergranular glassy films" J. Ceram. Soc. Japan, **114** [11] 1005-1012 (2006).

[30] A. Ziegler, M. K. Cinibulk, C. Kisieloski, R. O. Ritchie, "Atomic-scale observation of the grain-boundary structure of Yb-doped and heat-treate silicon nitride ceramics" Appl. Phys. Lett., **91** [14] 141906 (2007).

[31] H. Gu, R. M. Cannon, I. Tanaka, M. Rühle, "Calcia partition in phase-separated intergranular glass and interfaces in doped silicon nitride produced by hot isostatic pressing" Mater. Sci. Eng. A, **422** 51-65 (2006).

[32] H. Nakano, K. Watari, K. Urabe, "Grain boundary phase in AlN ceramics fired under reducing N_2 atomosphere with carbon" J. Euro. Ceram. Soc., **23** 1761-1768 (2003).

[33] G. Pezzotti, A. Nakahira, M. Tajika, "Effect of extended annealing cycles on the thermal conductivity of AlN/Y_2O_3 ceramics" J. Euro. Ceram. Soc., **20** 1319-1325 (2000).

[34] W. Sigle, G. Richter, M. Rühle, S. Schmidt, "Insight into the atomic-scale mechanism of liquid metal embrittlement" Appl. Phys. Lett., **89** (2006).

[35] P. Donnadieu, "TEM investigations of glide lines in amorphous silica below the glass transition" J. Non-Cryst. Solids, **111** 7-15 (1989).

[36] K. Müller, M. von Heimendahl, "TEM investigation of crystallization phenomena in the metallic glass Vitrovac® 0040 ($Fe_{40}Ni_{40}B_{20}$)" J. Mater. Sci., **17** 2525-2532 (1982).

[37] C. A. M. Mulder, G. van Leeuwen-Stienstra, J. G. van Lierop, J. P. Woerdman, "Chain-like structure of ultra-low density SiO_2 sol-gel glass observed by TEM" J. Non-Cryst. Solids, **82** 148-153 (1986).

[38] D. B. Williams, C. B. Carter, Transmission Electron Microscopy: A Textbook for Materials Science, Plenum New York, (1996).

[39] D. J. Vaughan, R. A. D. Pattrick (Eds.), Mineral Surfaces, Chapman & Hall, London, p. 370, (1995).

[40] M. F. Hocella Jr, C. M. Eggleston, V. B. Elings, M. S. Thompson, "Atomic structure and morphology of the albite {010} surface: An atomic-force microscope and electron diffraction study" Amer. Miner., **75** 723-730 (1990).

[41] M. S. Zei, Y. Nakai, G. Lehmpfuhl, D. Kolb, "The structure of gold and silver films evaporate on glass" J. Electroanal. Chem., **150** 201-206 (1983).

[42] A. F. Wright, J. Talbot, B. E. F. Fender, "Nucleation and growth studies by small angle neutron scattering and results for a glass ceramic" Nature, **277** 366-368 (1979).

[43] T. T. To, D. Bougeard, K. S. Smirnov, "Molecular dynamics study of the vibrational pattern of ring structures in the Raman spectra of vitreous silica" J. Raman Spectrosc., **39** 1869-1877 (2008).

[44] E. M. Levin, C. R. Robbins, H. F. McMurdie (Eds.), Phase Diagrams for Ceramists, The American Ceramic Society, Inc., Columbus, Ohio, p. 601, (1964).

[45] W. W. Mullins, "Effect of thermal grooving on grain boundary motion" Acta Metall., **6** [6] 414-424 (1958).

[46] J. Goldstein, D. Newbury, D. Joy, C. Lyman, P. Echlin, E. Lifshin, L. Sawyer, J. Michael, Scanning Electron Microscopy and X-ray Microanalysis, Kluwer Academic/Plenum Publishers New York, (2003).

[47] R. J. Good, C. J. van Oss, in: M. E. Schrader, G. Loeb (Eds.), Modern Approach to Wettability: Theory and Applications, New York, (1991), pp. 1-27.

Table 5.1: Colors produced by Glass Dopants[6]

Ion	*Color*
Copper	Light blue, blue, green, red ruby
Chromium	Green, yellow
Manganese	Violet, weak yellow, brown
Iron	Yellowish-brown, yellow-green, bluish-green, dark amber
Cobalt	Intense blue, pink, green
Nickel	Grayish-brown, yellow, green, blue, violet
Vanadium	Green, brown
Titanium	Violet
Neodymium	Reddish-violet
Praseodymium	Light green
Cerium	Green, yellow
Uranium	Yellow
Gold	Ruby

Table 5.2: Mean Thermal Expansion Coefficients of Selected Ceramics[7]

Ceramic	*α (ppm/˚C)*
α–Al_2O_3	7.2-8.8
$MgSiO_3$	10.8 (25-1000˚C)
$Al_6Si_2O_{13}$ (Mullite)	5.1 (25-1000˚C)
Fused silica	0.55
β–$CaSiO_3$	5.9 (25-700˚C)

a)

b)

c)

Figure 5.1: Materials Science in pottery includes topics like (a) crazing, (b) spherulites and (c) oxidation in Raku glazes and other glazes.

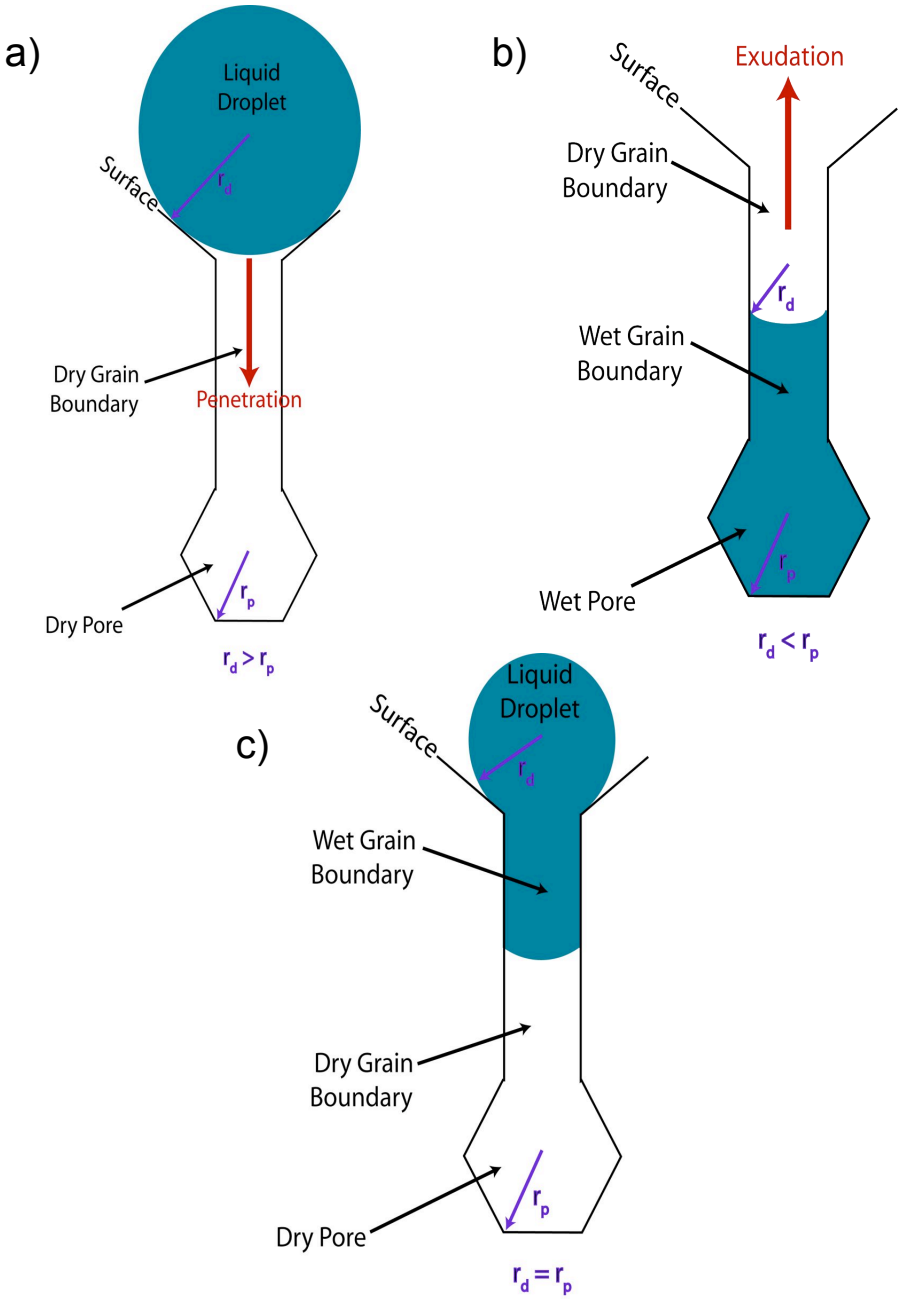

Figure 5.2: (a) If the liquid droplet at the surface is large compared to a pore within the GB, the liquid will penetrate the GB. (b) If there is more liquid in the pore, the liquid will exude from the GB in an effort to balance partial pressures. (c) An equilibrium GB wetting condition will exist when the pressures balance between the external surface droplet and the internal pore. Note the resemblance to an inverted thermometer.

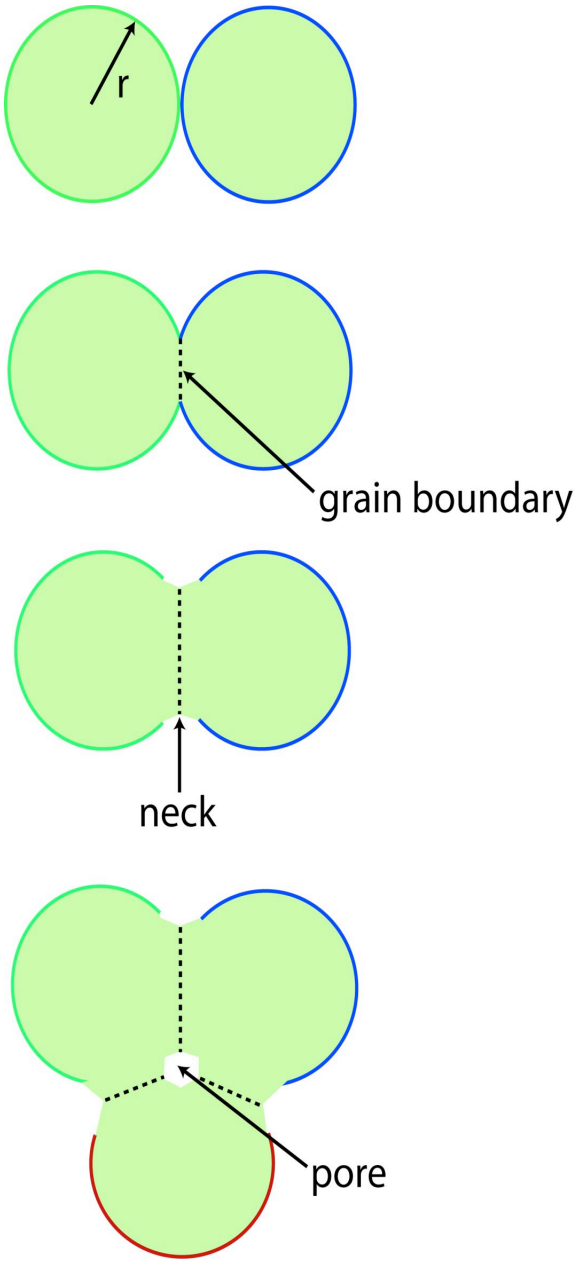

Figure 5.3: Curvature of the particles' surfaces drives the initial sintering of particles. Once a grain boundary forms between two particles, a neck forms via surface diffusion. Pores forms from a gap between particles.

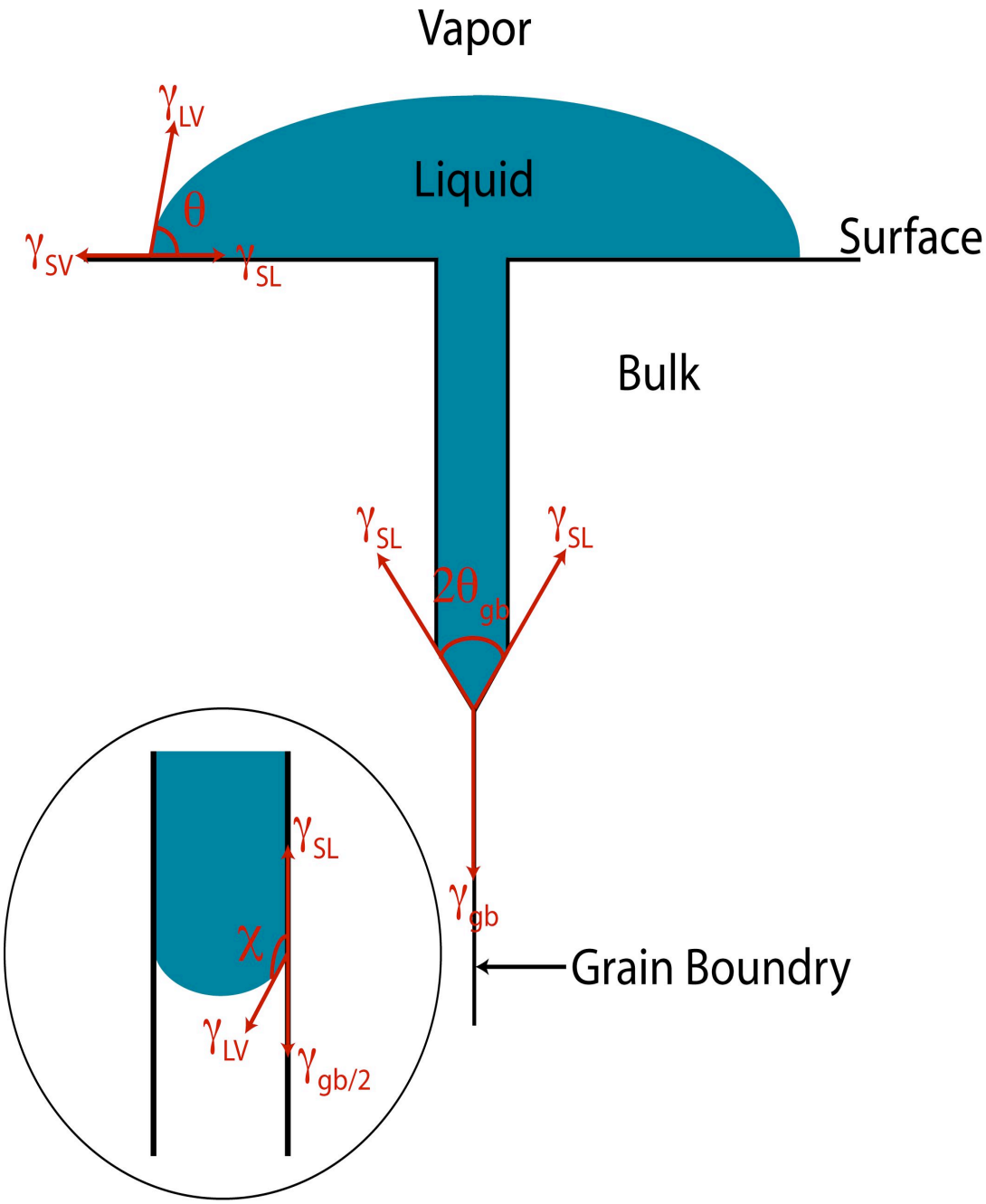

Figure 5.4: Interfacial tension geometry for the triple-phase boundary has similar geometry to the phase boundary within the grain boundary. The force balance of the internal phase boundary can be approximated by a meniscus (inset).

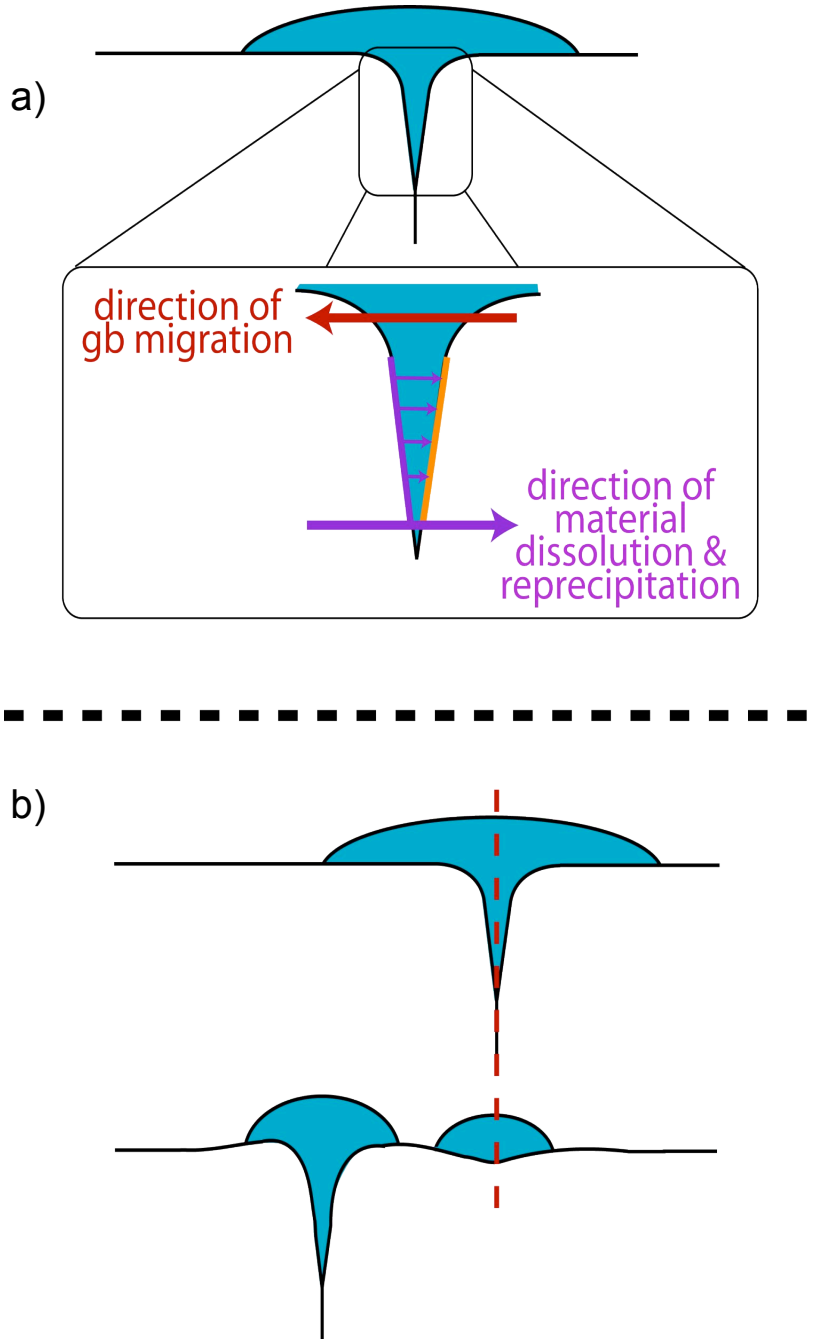

Figure 5.5: (a) During migration material from the purple interface dissolves in the liquid and reprecipitates at the orange interface. (b) A droplet is left on the left side of the original grain boundary position from the formation of the thermal ridge. The droplet marks where the grain boundary had been.

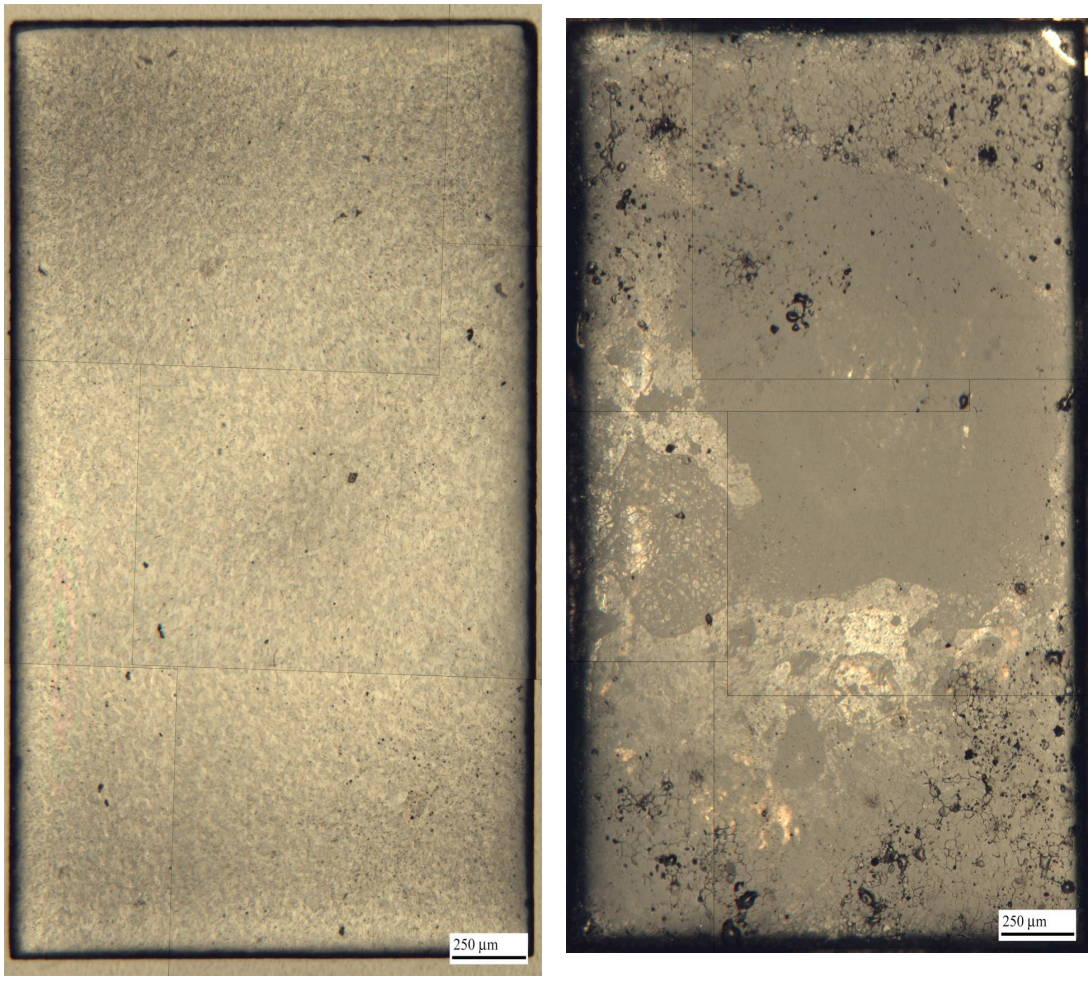

Figure 5.6: The sample surface (a) After polishing, but before annealing in the presence of anorthite powder. (b) After first anneal showing the glass droplet reservoir and the exuded droplets.

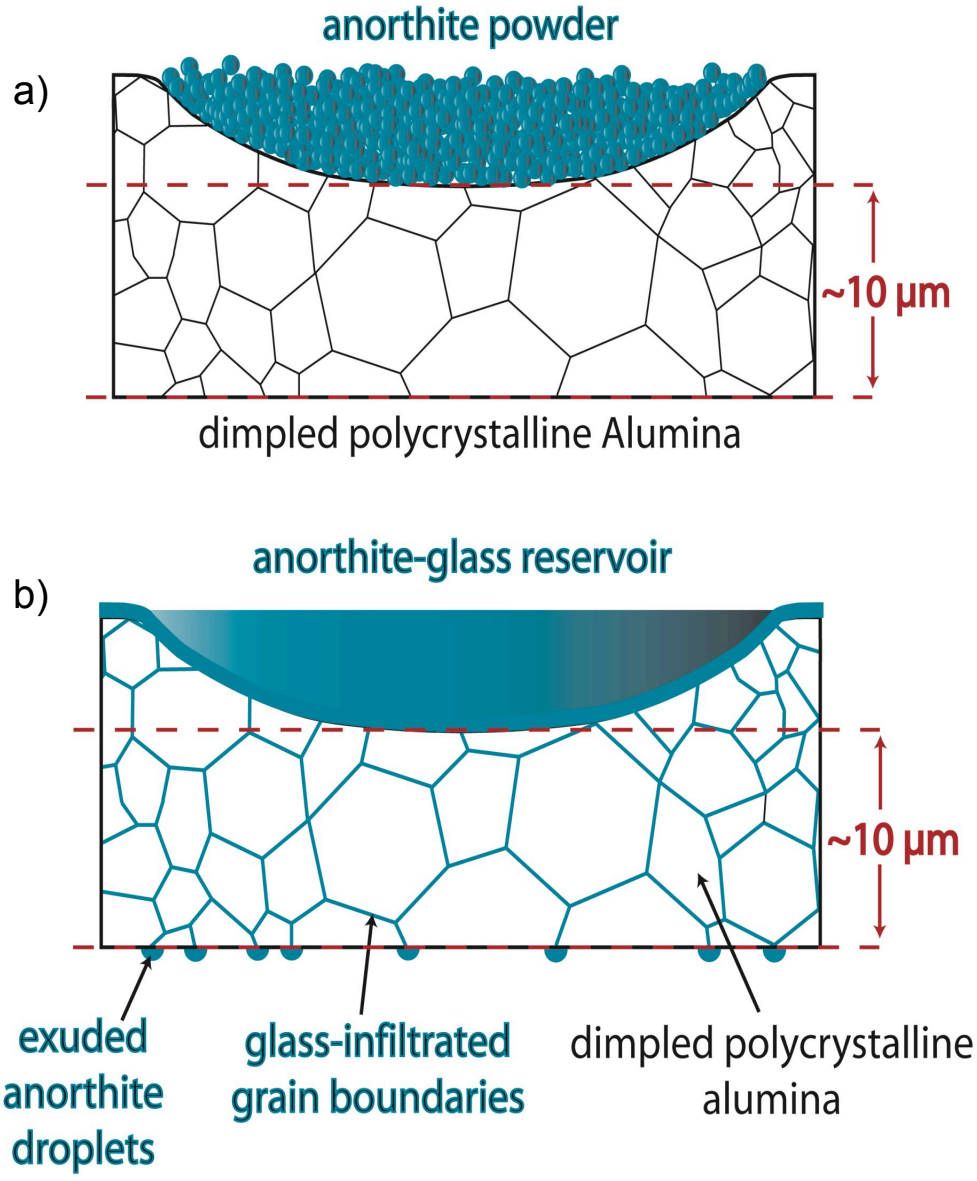

Figure 5.7: Prior to annealing (a) anorthite powder was sprinkled into the dimple. On heating (b) the glass melted and infiltrated the grain boundaries.

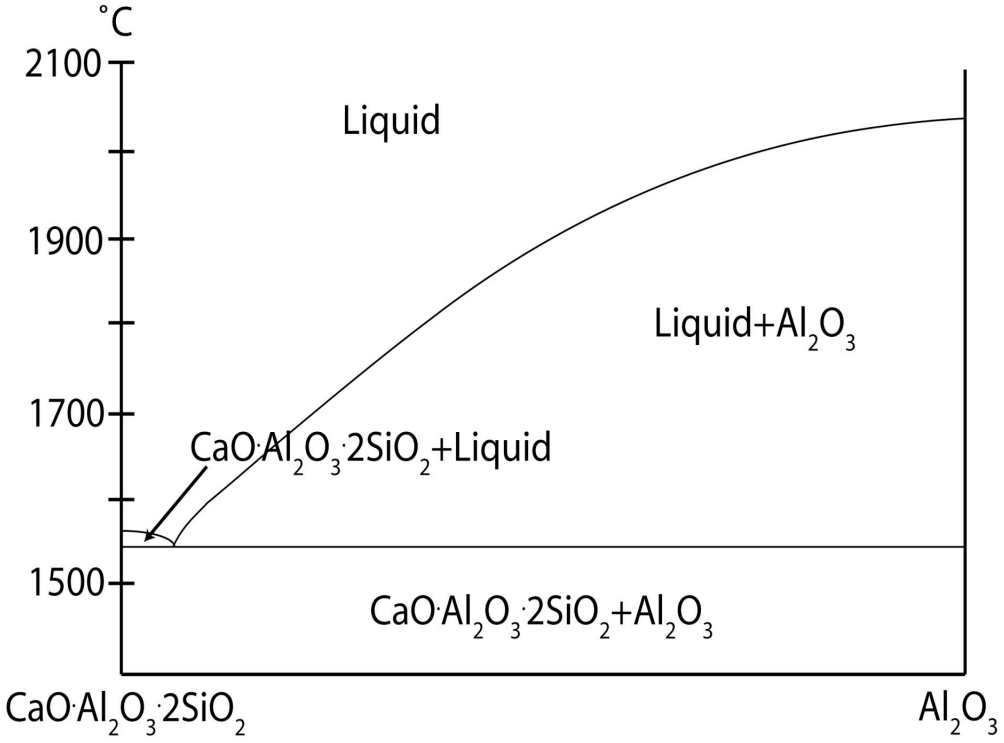

Figure 5.8: CAS-Al_2O_3 phase diagram

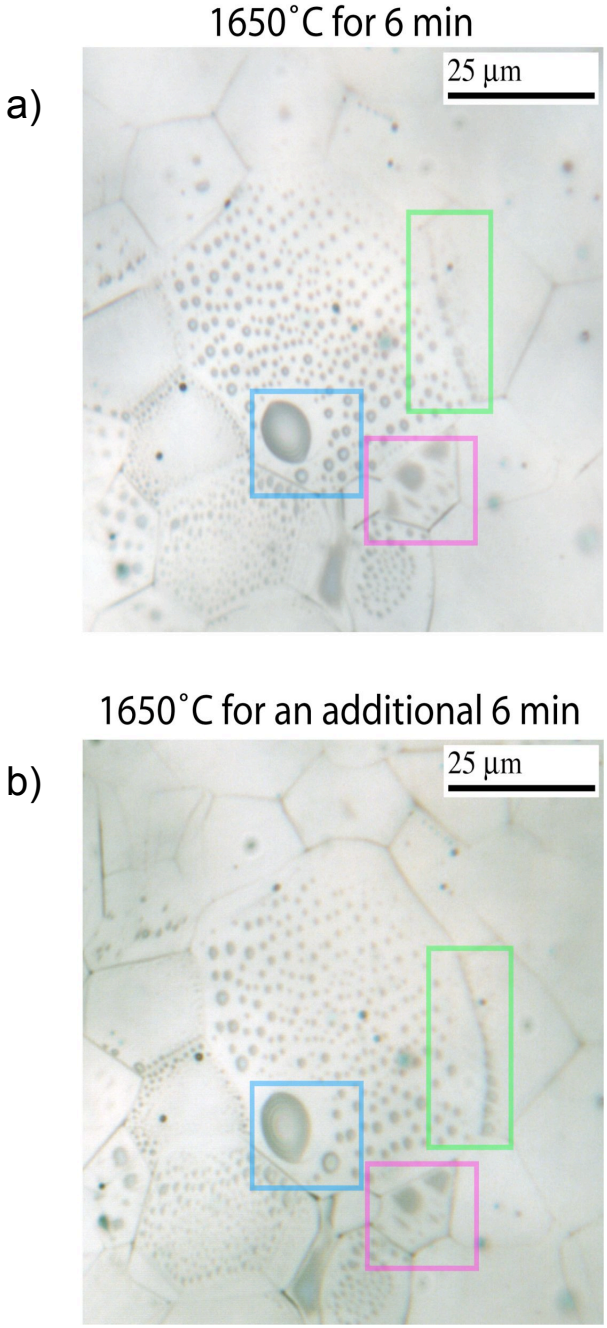

Figure 5.9: Highlighted areas are those where changes can be clearly seen with the VLM. In particular, Ostwald ripening and grain boundary migration has occurred.

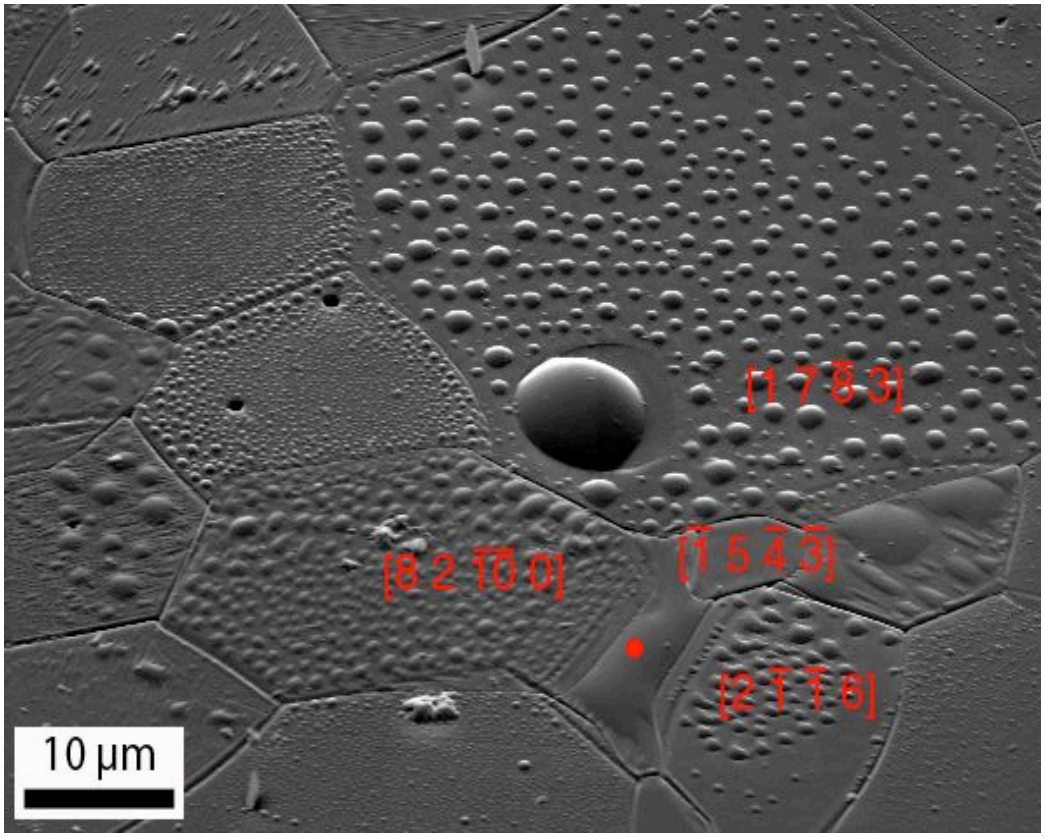

Figure 5.10: EBSD point analysis showing that droplet patterns are dependent on surface orientation. The spot was not able to be indexed because the film was too thick.

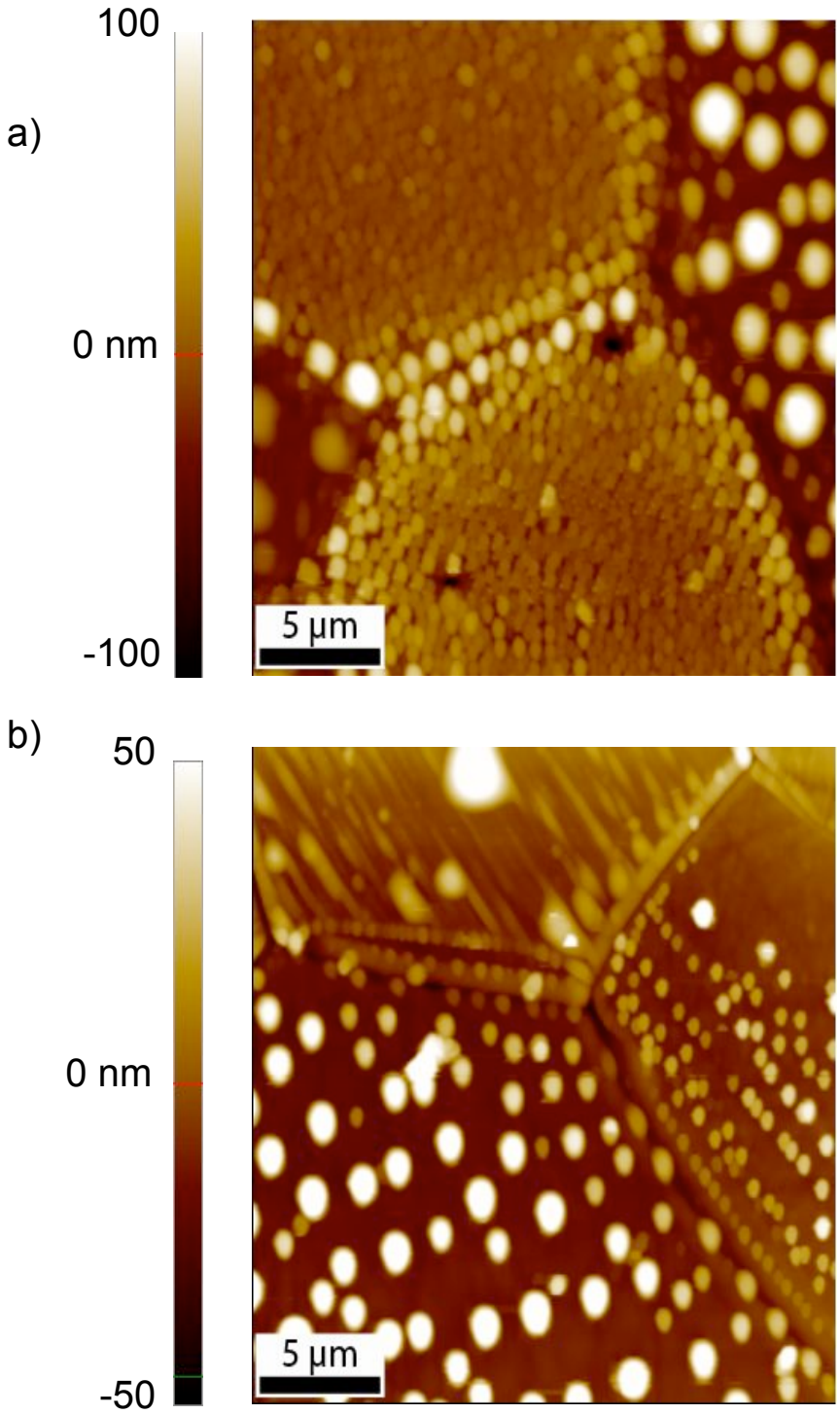

Figure 5.11: Droplet patterns depend on the underlying grain surface orientation. In addition, droplets align themselves along grain boundaries.

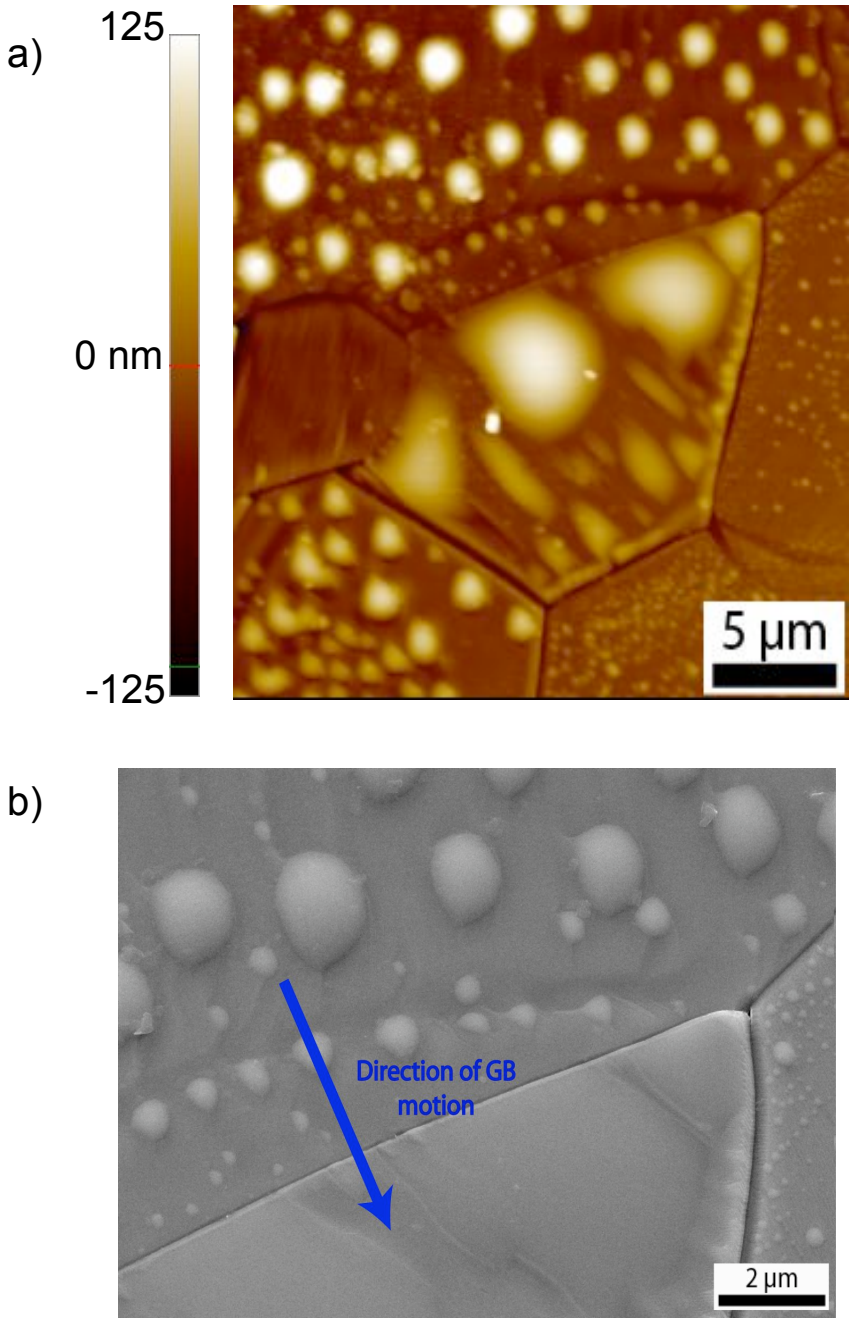

Figure 5.12: (a) AFM and (b) SEM showing the decoration of a remnant groove.

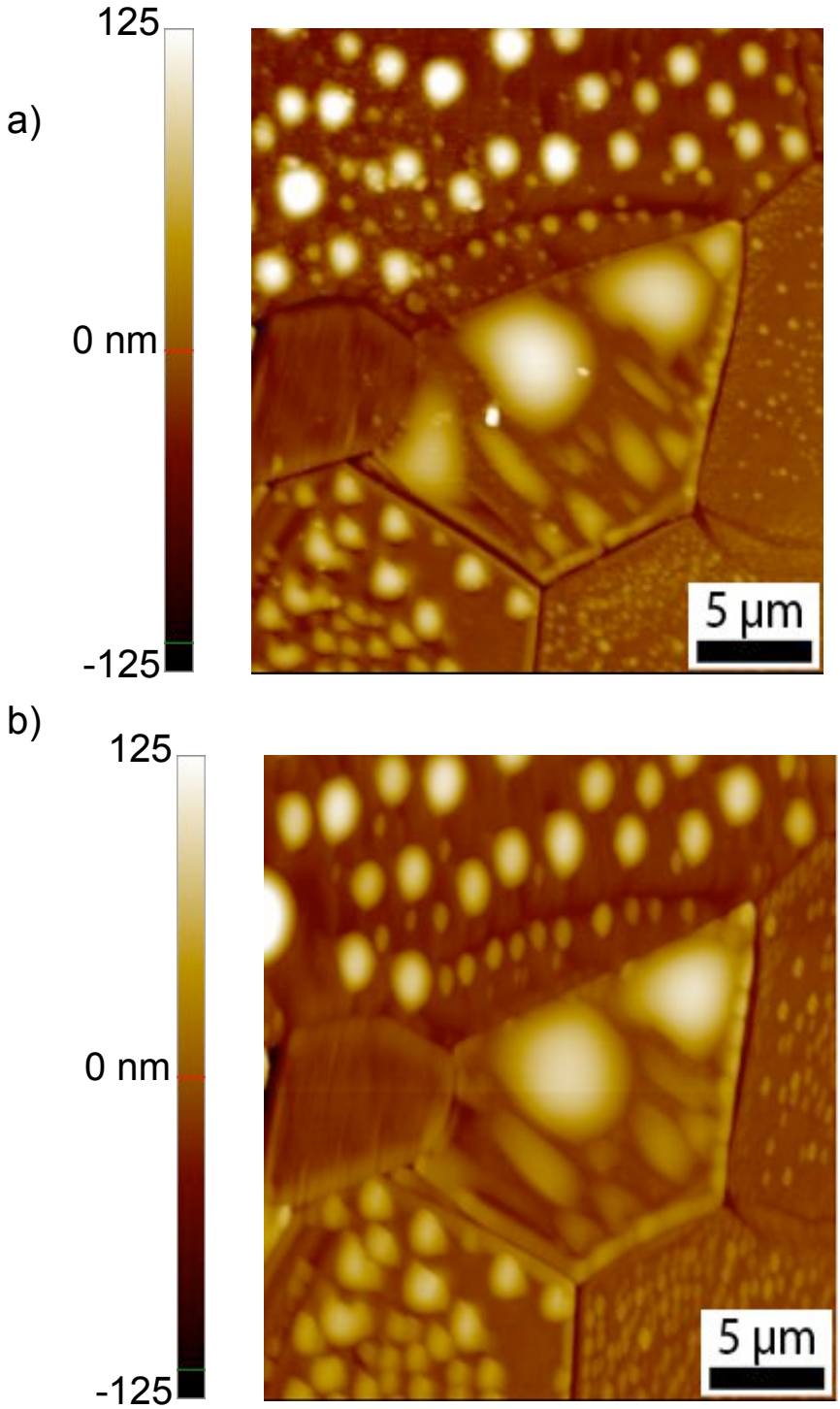

Figure 5.13: Comparison of a decorated remnant groove after (a) 6 min and (b) 12 min at 1650˚C.

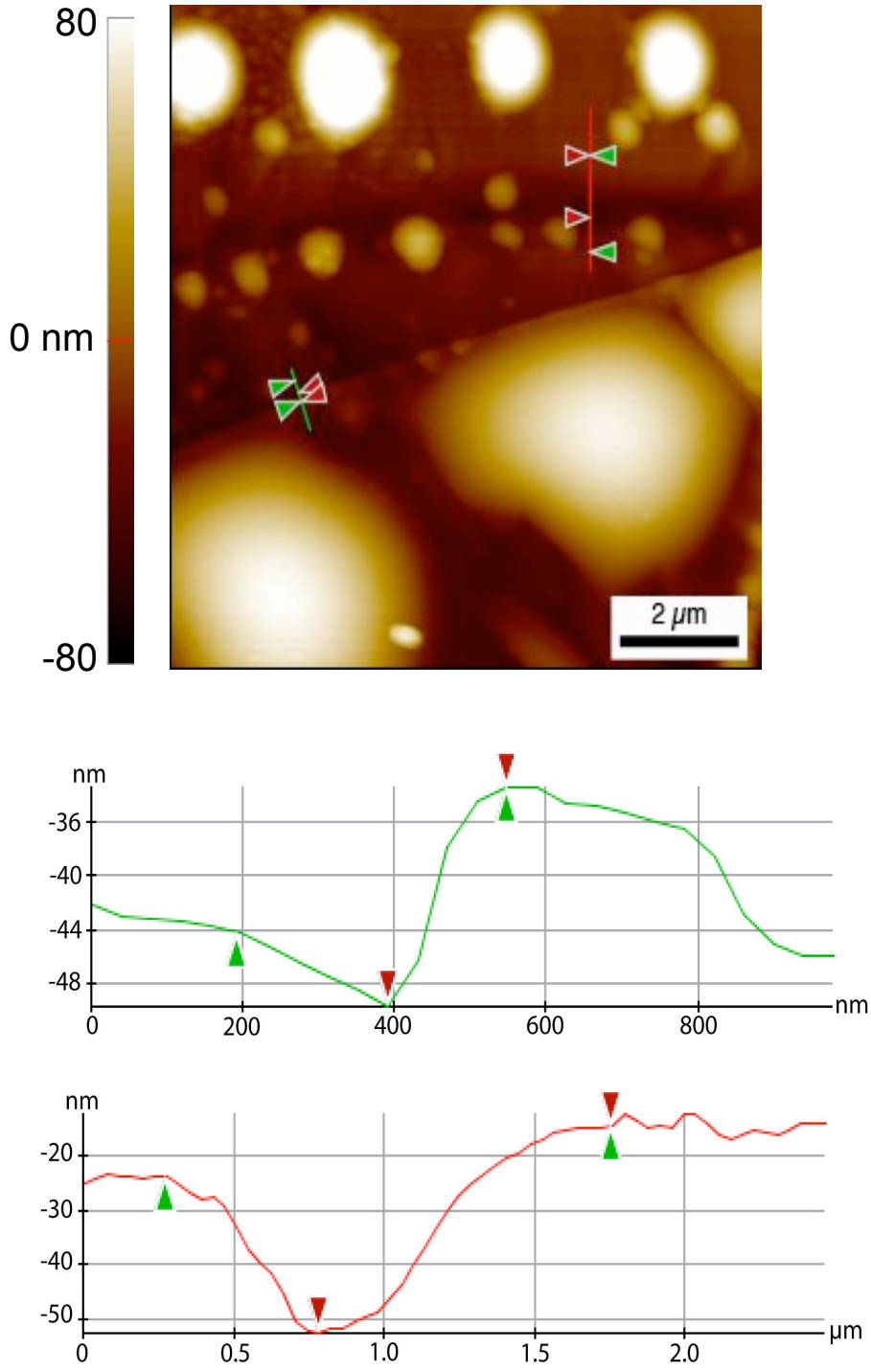

Figure 5.14: Section analysis of remnant groove after 6 min at 1650˚C.

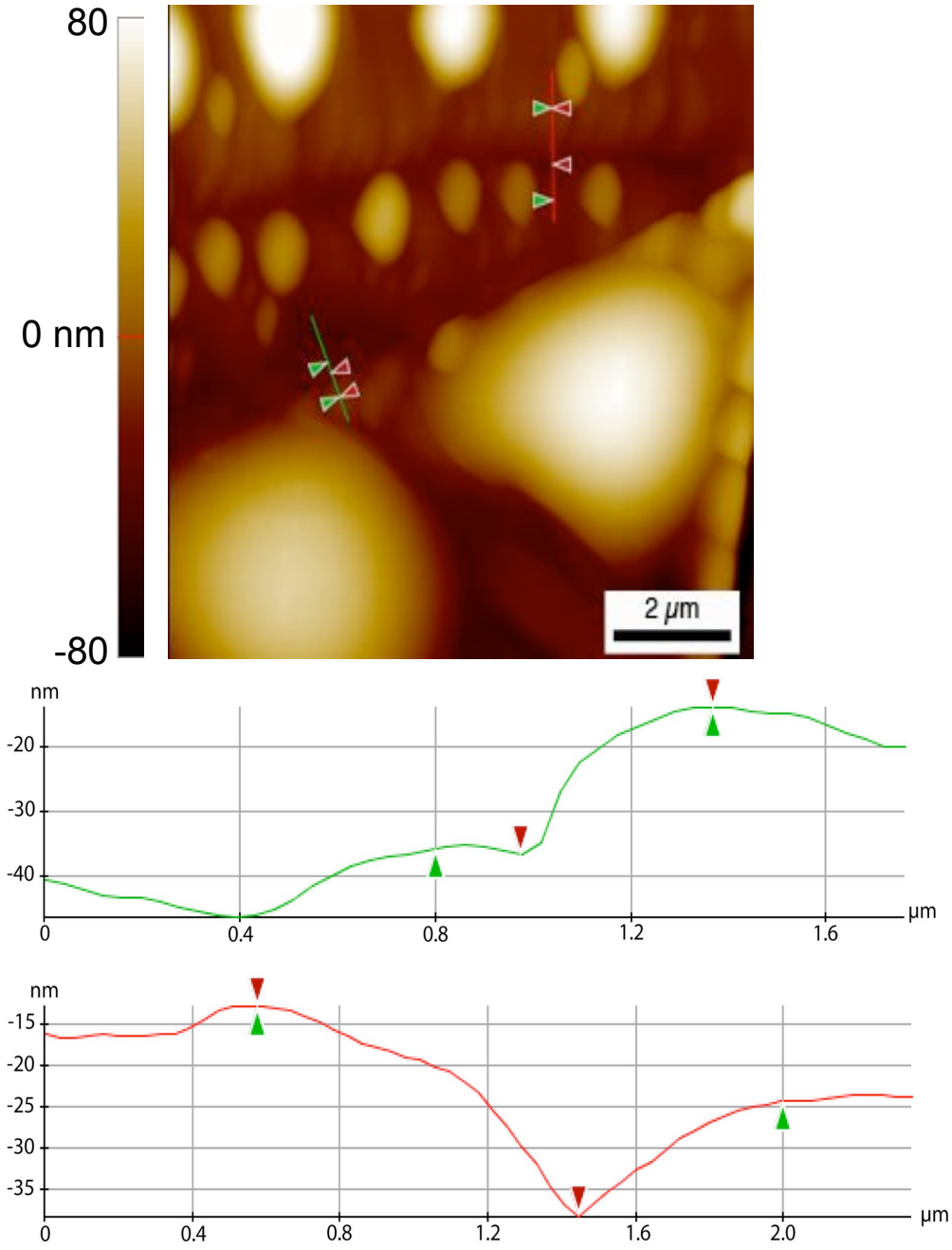

Figure 5.15: Section analysis of remnant groove after 12 min at 1650˚C.

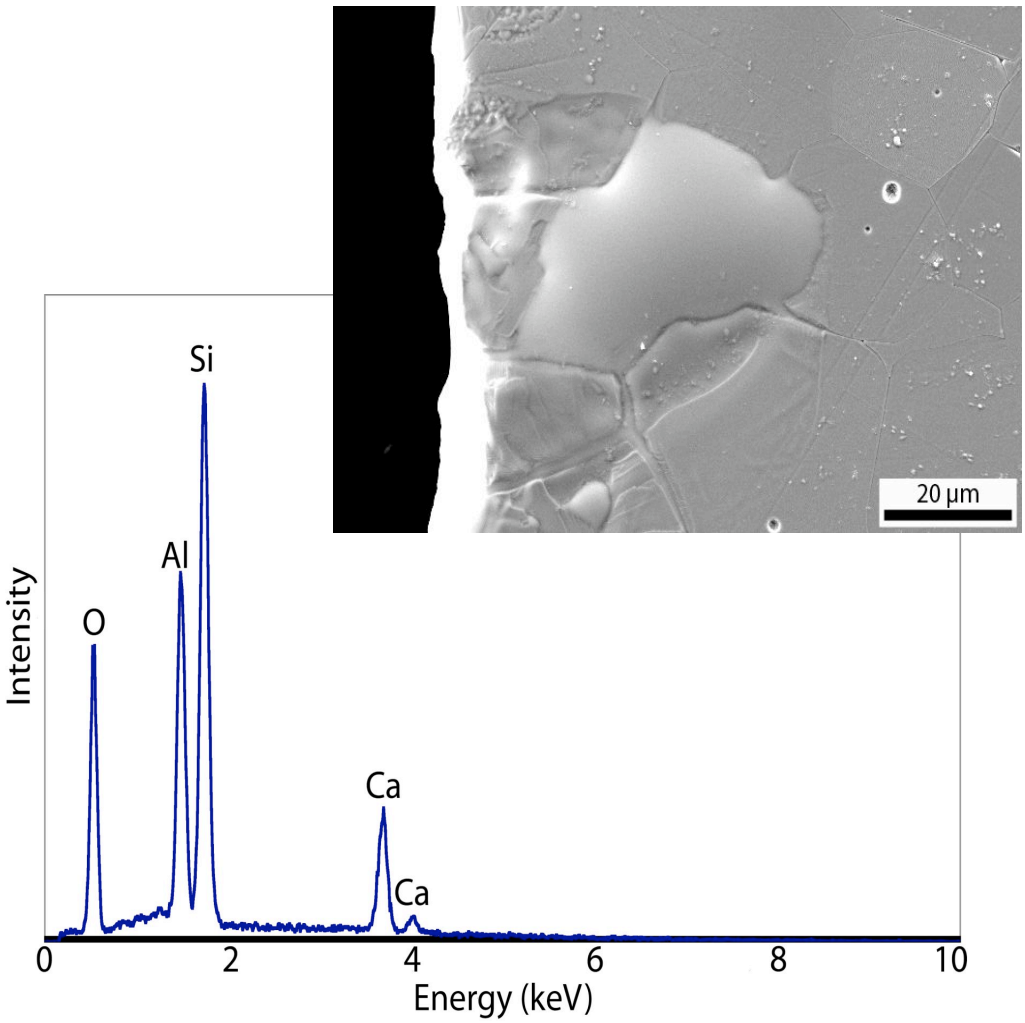

Figure 5.16: EDS of droplets confirmed qualitatively that the glass is anorthite. The large droplet at the edge of the specimen was used to get composition data.

a)

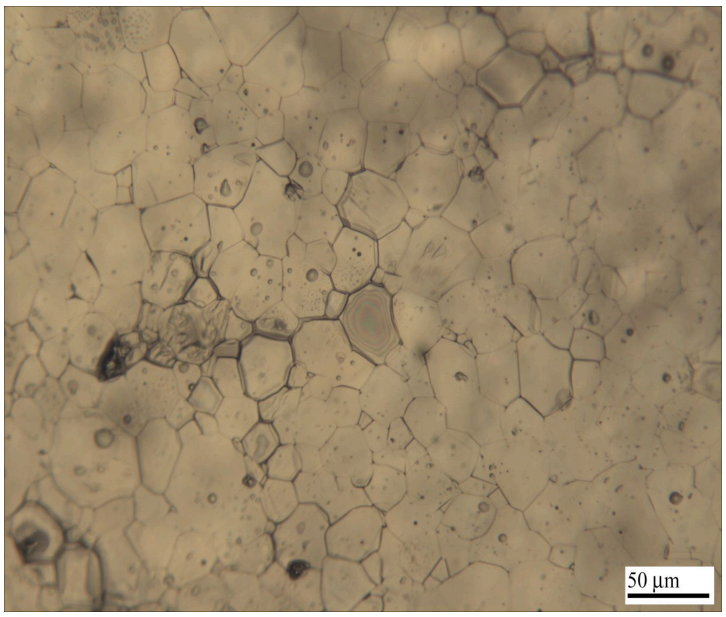

b)

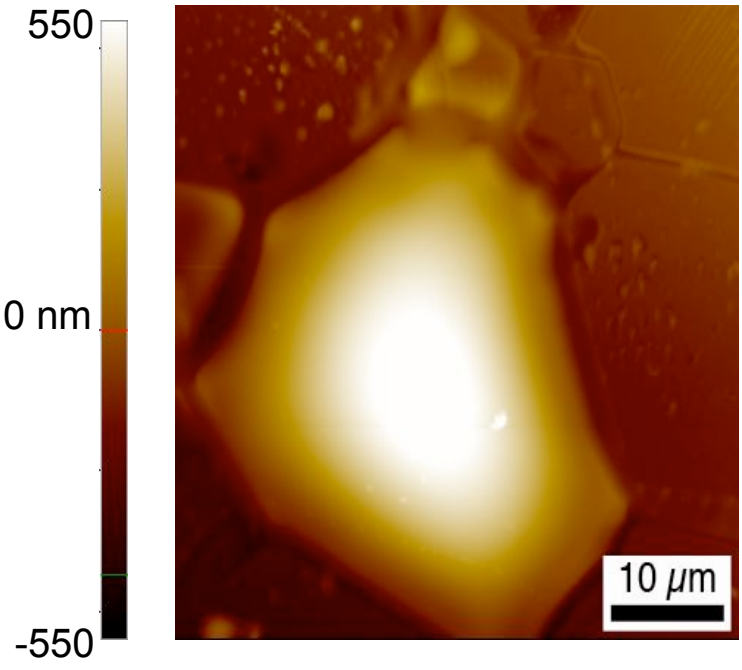

Figure 5.17: Completely wet grain away from any sample edges. In (a) the grain of interest is in the center of the VLM image and Newton's rings can be used to see the thickness difference of the droplet. The AFM image in (b) shows the finer detail of the droplet at the grain boundaries.

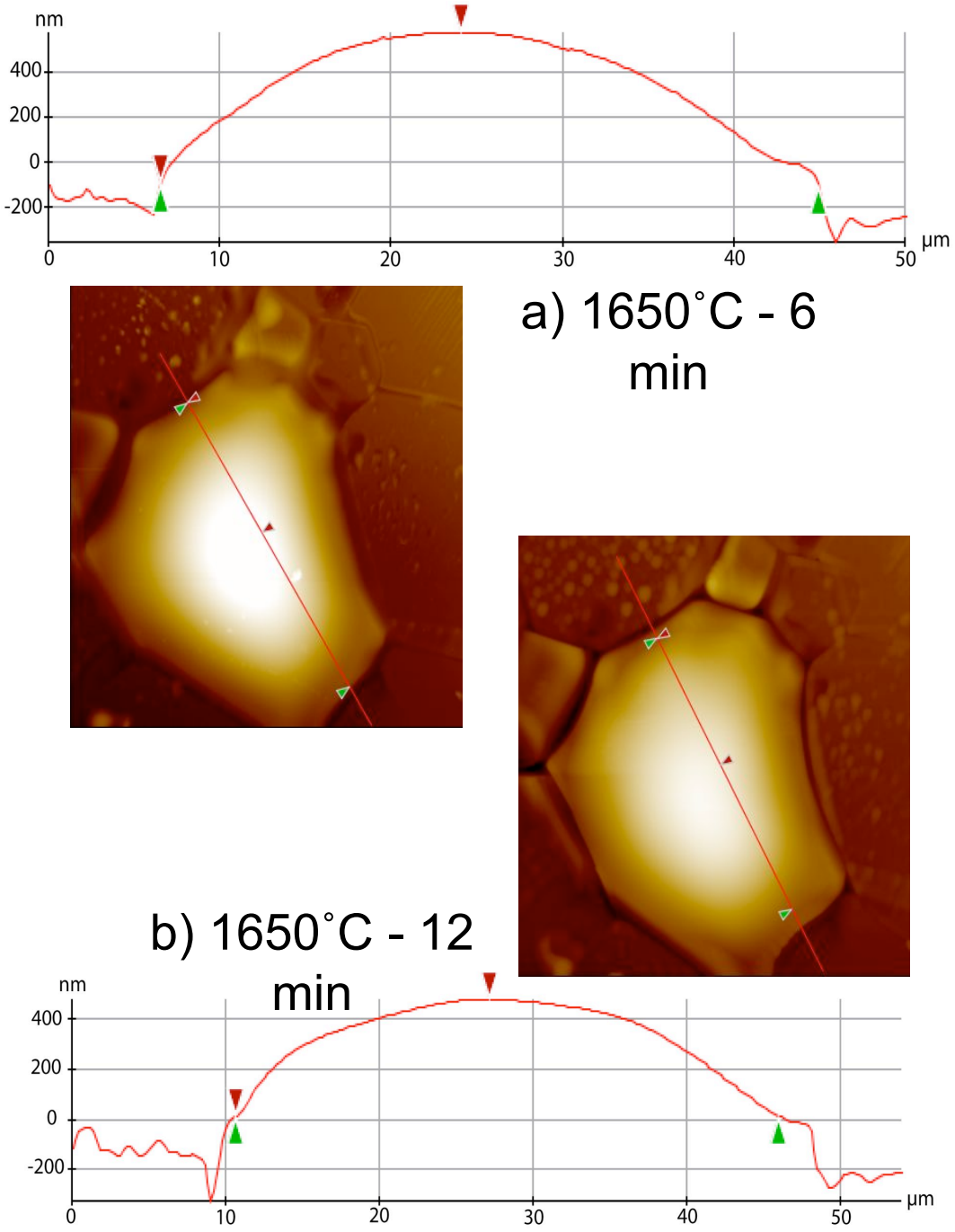

Figures 5.18: The grain is originally wet all the way to the grain boundaries. (b) After more time at temperature, the glass is pulling away, i.e. dewetting, from the thermal grooves.

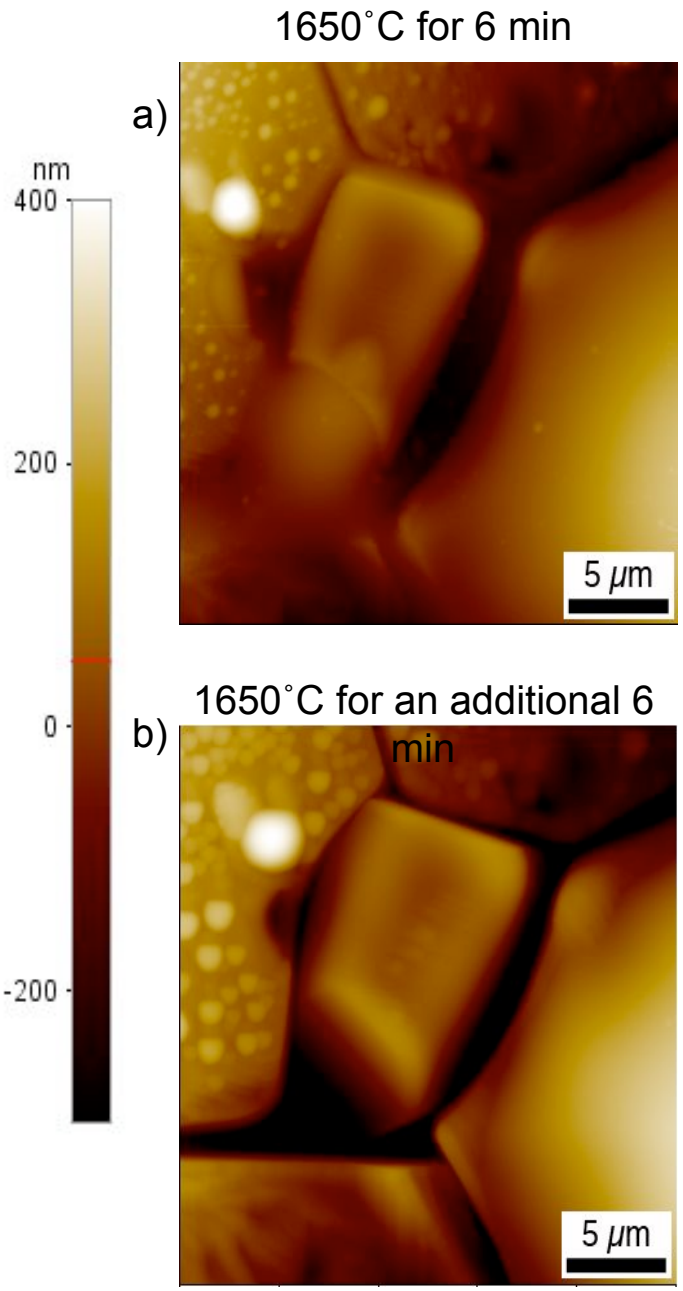

Figure 5.19: The droplet over the TJ has gone back into the GB. The large droplet on the grain to right is starting to pull away from the GB, exposing facets at the thermal grooves. The GBs initially had glass at at them, but now they are widely etched and dry. In (b) the right-hand grain shows the fine detail of the thermal grooves where a droplet has pulled away from the grain boundary.

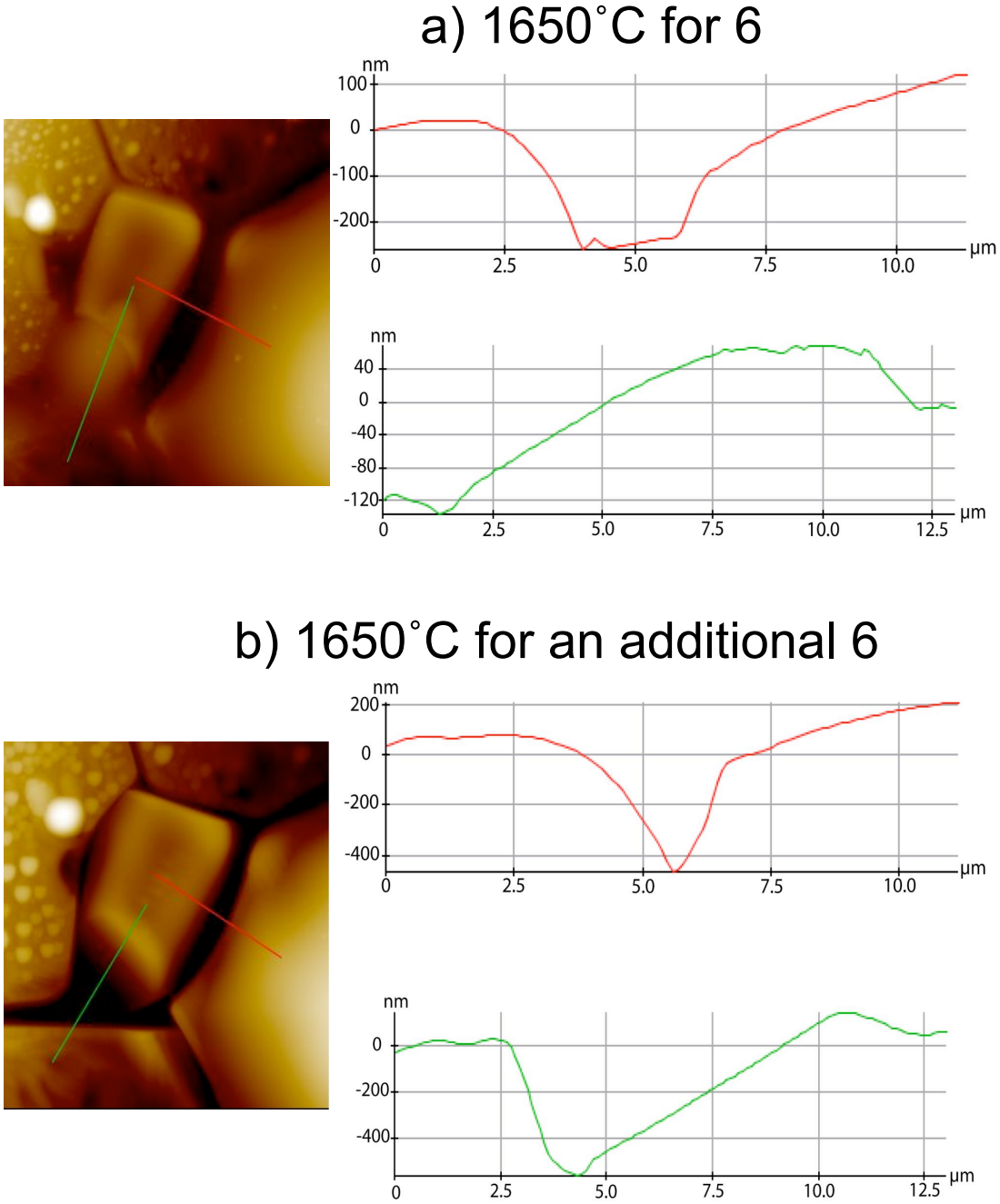

Figure 5.20: Clearly a droplet is at the GB initially and disappears after the second anneal to form a groove at the TJ. The other GB initially has glass at the GB, but forms a wide groove with further heat treatment.

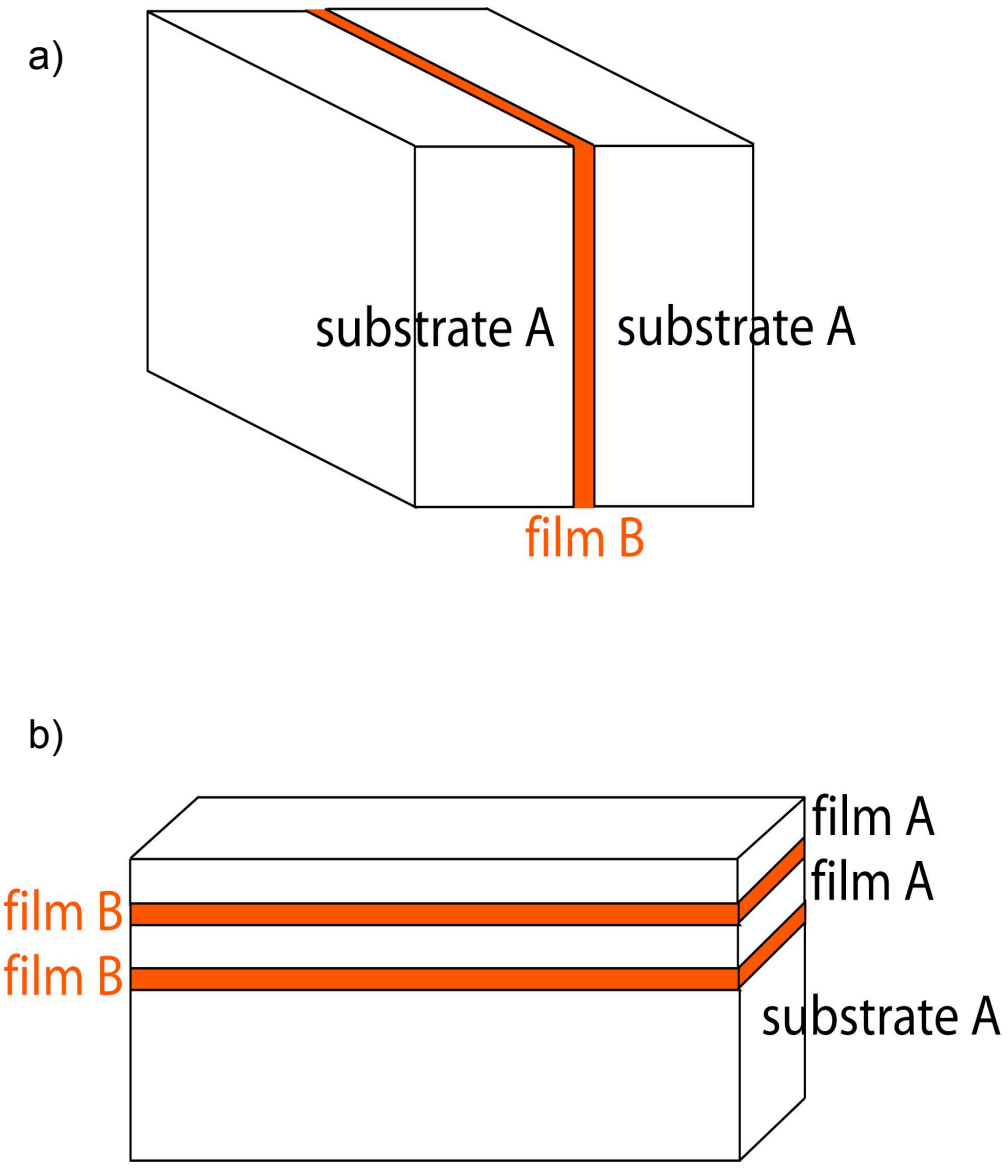

Figure 5.21: Two other possible sample geometries to further this would be a) bicrystals made from substrates of material with a glass film of material B at the interface and b) multilayers materials A and B deposited via pulsed-laser deposition (PLD) onto a substrate of material A. The interface would have known orientations, simplifying analysis.

Chapter 6: EBSD Study of GBM and AGG in Alumina in the presence of a liquid phase

6.1 Introduction

Kingery, et al[1] describes a grain boundary as being "one of the simplest kinds of interfaces between two crystals when the two crystals are slightly tilted and brought back together." When one begins to look at grain boundaries and their behavior, the realization that grain boundaries are not at all simple is quickly made. Grain boundaries in polycrystalline materials play an important role in every material property. The migration of grain boundaries due to some driving force acting perpendicular to the grain boundaries can affect recrystallization, precipitation, creep and phase transformations, for example. The ability to understand and modify grain boundary properties would enhance structural materials and provide a low-cost single crystal production method.

Grain boundary mobility defines how quickly grain growth can occur and can be controlled by orientation, chemistry and growth conditions. Impurity-drag effects are attributed to the growth-inhibiting effect.[2] Changes in point defect chemistry due to doping and impurities may also inhibit or enhance grain growth. Pore mobility has been long proposed to increase via sample doping, affecting grain boundary migration rates due to pore-boundary attachment.[3] Doping at the interface changes the interfacial energy, inevitably changing the growth kinetics. The chemistry at the interface determines whether or not grain growth will be enhanced or impeded. The mobility will determine sintering conditions and dictate whether the grains will grow normally or abnormally. Crystal anisotropy will create preferred diffusion paths, allowing for grain boundaries with a particular misorientation across the boundary to have different mobilities.

In liquid-phase sintering (LPS), the boundary chemistry is purposefully changed such that an intergranular film (IGF) is present. The film has a lower melting point than the

bulk and allows diffusion across the interface to occur much faster at a lower temperature. The liquid film may also pin grain boundary migration. Chemistry and orientation at the interface determine what behavior will occur.

Exaggerated grain growth has several uses. Single-crystal conversion (SCC) is a hot topic for industrial applications.[4] The ability to convert polycrystalline material into single-crystal substrate material at lower cost than growing single crystal from a melt has major financial implications in the technology sector.

Lucalox™ is a commercially available alumina that is doped with up to 0.5 wt% MgO. The MgO inhibits exaggerated grain growth. This material is most frequently used in sodium-vapor lamps, but is an excellent choice for studying grain boundary migration (GBM) in ceramic materials. Lucalox is translucent and has a large average grain size of 10 μm. The grains are also very uniform in size and shape.

The development of electron backscatter diffraction (EBSD), and the growing accessibility, has allowed more studies on grain growth. Chemistry and orientation can be probed simultaneously to see if the two possible driving forces are coupled or separate.

6.2 Background

Grain boundary migration can be studied using a variety of methods, including soap bubble rafts. Visible-light, scanning electron, atomic-force and transmission electron microscopies, (VLM, SEM, AFM, TEM, respectively), have all been used to monitor grain growth. Each technique has advantages and limitations. No matter the chosen technique, crystallography and chemistry must be considered. The increased accessibility to EBSD in recent years has allowed orientation and chemistry to be analyzed much quicker and with better resolution than ever before. The development of *in situ* techniques has allowed real-time measurements of diffusion coefficients and kinetic behavior. Just by changing processing conditions or dopant concentrations, grain

boundary migration may be drastically changed. The ultimate driving force for grain boundary migration is the reduction of interfacial energy.

6.2.1 Normal vs. Abnormal Grain Growth

Hillert[5] derived equations that describe normal (NGG) and abnormal grain growth (AGG) and enable the prediction of which regime will dominate. He proposed a model explaining the two regimes and how second-phase particles may hinder AGG. NGG is driven by interfacial free energy and is considered steady-state growth, while a critical grain size radius is necessary for AGG. If the initial grain size distribution is too wide, AGG will occur until all of the grains have been consumed and a more narrow grain size distribution has been reached. Hillert[5] stated "abnormal grain growth may thus sometimes be a necessary initial stage during the development toward NGG." Hillert's[5] model predicts that AGG can develop if all of the following are fulfilled:

1) NGG cannot happen due to the presence of second phase particles.

2) The average grain size is below 0.5z.

3) There is at least one grain much larger than the average.

The number of sides a grain has determines if the grains will grow or be consumed and is driven by the number of defects/grain. In studies on nickel[6], NGG was found to be expected if the migration rate of rough grain boundaries increased with the driving force arising from the grain size difference and was found to be limited by second-phase precipitates. Using TEM and EBSD, Randle and Brown[7] propose that AGG has a strain-related driving force, while NGG is boundary-curvature driven. Others have found during modeling that step-producing defects, which nucleate faceting, are responsible for the bimodal distribution leading to AGG.[8] Monitoring the thermal grooving may be a good way of determining whether AGG is occurring.[9]

During AGG, pores, second phases and grains with low-angle grain boundaries may be trapped within the large grains or crystals.[4, 10, 11] Pores act as a second phase and may

inhibit grain boundary migration. In addition, AGG in the presence of pores will never reach theoretical density, while the same material with pores under normal growth conditions can.[12]

Rollett and Mullins[13] present a modeling theory of AGG and introduce the turning angle and curvature equations. Mobility must be sufficiently high and boundary energy must be sufficiently low in order for AGG to be promoted. Gottstein and Shvindlerman[14] proposed that grain size increases the grain growth rate and that the presence of triple junctions will slow the grain boundary migration, but have not applied their theories to AGG.

6.2.2 The Role of Impurities on Grain Boundary Motion

Grain boundary drag depends on the grain boundary velocity, a function of temperature and composition, and the diffusivity of the impurity. Impurity atoms absorbed within the grain boundary are pulled along by the migrating grain boundary, while impurities that cannot be absorbed move in front of the boundary. Cahn[2] called this behavior "the impurity-drag effect," which allows prediction of whether the driving force or velocity will dominate, assuming the sample is a dilute solution of the impurity. The theory is summarized as:

1) "At low driving forces the relative decrease in velocity produced by an impurity is insensitive to driving force. At high driving forces it is inversely proportional to the square of the driving force.

2) At low driving force a slowly diffusing species has a greater composition effect. At high driving forces just the reverse is true, and the fast diffusing solute has the larger composition effect."

Hay and Evans[15] give a good comparison and description of chemically-induced grain boundary migration (CIGM) and liquid-film migration (LFM), along with diagrams illustrating the differences. Time, temperature and dopant type and level all affect grain

boundary migration. Instability of the solid-liquid interface (ISLI) occurs when the solutes corrugate the solid grains and increase the solid-liquid interfacial energy. The ISLI driving force is the same as that for CIGM and diffusion-induced grain boundary migration (DIGM), which is described as coherency strain energy stored in a thin solute diffusion zone. Chromia[16] has been found to induce ISLI and form a "finger-like" or lath-shaped microstructure in the alumina/$CaAl_2Si_2O_8$ (CAS) system.

6.2.3 Liquid-Phase Sintering

Additives have been shown to promote lattice diffusion.[12] Lattice diffusion is preferred at higher temperatures than surface and interface diffusion, but additives can lower the temperature needed for lattice diffusion to take place. During liquid-phase sintering (LPS), additives are introduced into the green ceramic compact. By purposely introducing impurities, a liquid phase can form in the ceramic compact. The liquid phase will melt at a lower temperature than the pure material, allowing diffusion through the liquid, rather than the solid to take place. As stated earlier, a lower sintering temperature can be used and a higher density compact may result. The remaining liquid phase becomes an intergranular film (IGF) between what were the pre-sintered particles that have now formed grains.

LPS of green compacts occurs in three steps.[17] First, solid particles rearrange when the liquid forms. Next, the solid will dissolve into the liquid and reprecipitate onto another solid particle. Finally, solid-state coarsening of the particles can begin to form traditional grains. Solid-state sintering is much slower than the first two LPS steps.

To be a suitable liquid-phase, the melting temperature must be lower than the bulk crystalline material and the crystalline material must be soluble in the liquid.[17] In addition, the liquid must be able to wet the bulk material at the surface and at the grain boundaries.

The liquid phase is not stationary while being heated and cooled. During sintering and continued grain growth, material from the shrinking grains will dissolve into the liquid

IGF and reprecipitate onto the other grain bounding the IGF. The IGF is subject to capillary forces and can preferentially wet grain boundaries and surfaces. As described in chapters 4 and 5 of this dissertation, preferential wetting depends on surface tension, interfacial energy, temperature and composition gradients and various convection methods. Upon cooling, crystalline second phases may precipitate out of the liquid. The viscosity of the liquid also changes, altering the IGFs ability to wet interfaces. German recently published an excellent review article that explains LPS in greater detail.

While the introduction of additives may lower sintering time and temperature, LPS has drawbacks. Uniform composition of the liquid can be difficult to achieve, and depends on premixing of the additives with the particles and the equilibrium composition with temperature. The IGFs are typically amorphous rather than epitactic with the surrounding grains, which can alter transport properties. Liquid phases at grain boundaries may degrade ionic conductivity.[18] This is less than desirable in materials like zirconia that are used as electrolytes in fuel cells. In this case, solid-solution additives such as Y_2O_3 are much more desirable, since no second-phases are present to degrade properties. The liquid phase can hinder future NGG or induce AGG. Material properties between the two phases may not match-up well. For example, the IGF may have a different coefficient of thermal expansion or mechanical behavior than the bulk material. The mismatch may cause early component failure when in service.

LPS has been utilized successfully in several applications.[17] Applications currently using LPS include ZnO/Bi_2O_3 varistors, $BaTiO_3/SiO_2$ capacitors, AlN/Y_2O_3 substrates and $Al_2O_3/MgO/SiO_2$ refractories.

6.2.4 Texture in Ceramics

Most ceramics are anisotropic in surface and interfacial energies, making orientation-dependence of material properties important. Thus, grain growth can occur in only preferred directions, and IGFs will exist only at preferred boundaries. Grain boundary structure can be dramatically different depending on the bounding planes.

Tape casting takes advantage of the anisotropy by using it to form templated films. A seed grain will induce a preferred texture for all of the rest of the cast grains.

6.2.5 EBSD and Previous Studies

The development of EBSD has allowed orientation data of surfaces to be obtained much easier than by TEM and more site-specific than X-ray diffraction (XRD). EBSD detectors are mounted to SEM and collect the electrons that are backscattered from the top 100 nm of the sample surface. The electrons are scattered from the surface in the form of Kossel cones.[19] The direction and angle of the pair of cones depends on the crystal planes the electrons are scattered from. When the plane of the detector intersects the cones, Kikuchi patterns result and an orientation map is created. Figure 6.1 illustrates a typical SEM/EBSD system. The computer fits a Hough transform to the Kikuchi bands and determines the surface orientation using a $y = mx+b$ fit. Entire crystal surfaces can be mapped by collecting Kikuchi maps at every point the electron beam is stepped to. EBSD can be used to measure strain in crystals, misorientation across grain boundaries and identify different phases at the surface.

EBSD does have limitations. The samples need to be tilted 70˚, with respect to the electon beam, in order for sufficient signal to be collected. The high tilt angle limits the ability to collect other signals simultaneously. A tilt of 70˚ is not a magic number, either; sometimes tilting to just under or over 70˚ can give a strong signal. Determining the optimal detector distance from the sample is also not straight forward. Surfaces need to be highly polished in order to minimize interference of surface features, i.e. shadowing, with the electrons. However, polishing must be carefully done in order to not produce enough damage to alter the surface. Often, the rough surface features are what are of interest. By polishing the features away, the crystallographic data is destroyed. Finally, as with any electron microscopy technique, charging of nonconductive materials is always an issue. Carbon or metal coatings may be needed on the sample surface to prevent charging during long mapping sessions. As pointed out earlier, EBSD is sensitive to the first 100 nm of material at the surface. Thick coatings

would not allow the electron beam to penetrate into the material of interest or allow the backscattered electrons to escape and reach the detector. Adequate signal for analysis may not be obtainable.

Farrer[20] used EBSD extensively to determine preferential migration of grain boundaries in alumina bicrystals. By using LPS to join single-crystal alumina with known boundary orientation to polycrystalline alumina, GBM rates could be determined. Stable boundary orientations could also be found by watching which grains disappeared during migration of the pressed boundary and which grains were not altered.

Previous studies[4, 21] have demonstrated AGG and single-crystal conversion by doping Al_2O_3 with MgO and CaO and annealing in vacuum. Dillon and Harmer[4] have reported 30 mm of polycrystalline alumina converted to single crystal. Scott, et al.[21] report a conversion rate of ~1.5 cm/h. In addition, a reduction in hardness has been found when grains grow at abnormally fast rates.[7]

Monahan and Halloran[11] calculated grain boundary mobilities and velocities of hot-pressed MgO-doped Al_2O_3. The two concluded that MgO retards grain growth and "A more realistic account of grain growth in the undoped alumina would take into account the size and volume fractions of the large lath-shaped grains in the fine-grained matrix." Several groups[22, 23] confirmed this observation at different thermal and atmospheric conditions. Bennison and Harmer[22] noted that the effect was enhanced when glassy films were absent from grain boundaries.

In another study, Dillon and Harmer[24] looked at the IGF in Nd_2O_3-doped Al_2O_3 grains. They found that the large Nd atoms align themselves along the grain in which the atoms were absorbed. However, they do not consider what affects the large ionic radius may have on the IGF; Nd_2O_3 is not a typical IGF and was used here for the high atomic-number contrast in high-resolution transmission electron microscopy (HRTEM).

6.3 Experimental

6.3.1 Sample Surface Preparation

Pure Al_2O_3 powder was isostatically cold-pressed and sintered for 1 h at 1500˚C to produce a dense compact with an average grain size of 3 μm, shown in the EBSD map in figure 6.2. Pellets were sliced into 1 mm thick disks and polished to 0.5-μm surface finish using diamond lapping films. Surfaces were cleaned by soaking them in acetone and methanol for 10 minutes, respectively, in an ultrasonic cleaner.

6.3.2 CAS Film Deposition

Amorphous CAS films were deposited onto the polished surfaces at room temperature using pulsed-laser deposition (PLD). The deposition chamber was backfilled with 20 mTorr of O_2, and the KrF excimer laser was pulsed at 10 Hz with 200 mJ/pulse. Disks were diced into samples approximately 2 x 2 x 1 mm^3 using a diamond-embedded wafering saw after deposition. Care was taken not to delaminate the films during cutting.

6.3.3 Specimen Annealing

Surfaces were cleaning in the same manner as described above prior to annealing. A box furnace was used to anneal the samples at 1650˚C in air. The heating rate was 20˚C/min and samples were allowed to cool naturally inside the box furnace. Total anneal times varied between 30 minutes and 80 hours. Some surfaces were annealed in a series of 10 or 20 h thermal treatments in order to monitor the extent of AGG.

Sets of specimens were processed together. After each anneal, one surface was kept as annealed, another was polished to a 0.5 μm surface finish with diamond lapping film and the rest were used to continue the annealing series. The polished samples were used to monitor grain growth in the bulk. Once polished, this surface was not annealed further.

6.3.4 Grain Growth Characterization

Surfaces were imaged before and after each anneal with VLM and SEM. Surfaces did not need carbon coating for SEM imaging; the fluorescent behavior of the CAS film was believed to provide suitable electron transport to limit charging under the electron beam. Annealing carbon-coated samples may also give skewed analysis, since the carbon may alter the surface and grain boundary tensions.

EBSD was used to determine surface orientations and accurately determine grain sizes. Orientation image maps were acquired by scanning the surface using 800-1200x magnification at a step size of 0.4 μm. EBSD requires a smooth surface in order to acquire the highest quality orientation maps. However, if annealed surfaces were polished, the surface information would be lost and EBSD would be pointless. Therefore, an as-annealed surface sample and a polished bulk sample from the same thermal series were always looked at together and compared with EBSD. The unpolished surfaces had poorer image quality (IQ), as expected, due to poor signal from electrons not being able to escape from pores, thermal grooves and other surface features. Again, surfaces were not carbon coated since charging was not an issue.

6.4: Results

After annealing for only 20 hrs in air at 1650˚C, exaggerated grain growth began. Grains as large as 200 μm form at the surface and can be easily seen in the VLM image shown in figure 6.3. The EBSD maps in figure 6.4 show the abnormal grains clearer. Large lath-like grains formed with the long side of the grain having a relationship to the basal plane of alumina. Grain boundary migration occurs so quickly that significant remnant grooves remain.

The exaggerated grain growth occurs within the bulk material as well as the surface, as shown in figure 6.4. This figure also proves that EBSD can be used to map rough sample surfaces, albeit difficultly. No conductive coating is needed during mapping. The CAS film fluoresces allowing enough charge to be dissipated from the surface. By

watching the Kikuchi patterns during EBSD collection, fluorescing of the surface can be monitored.

Figure 6.5 shows the evolution of the surface microstructure after a series of anneals. After annealing for 80 hours nearly all of the small normal grains have disappeared and only the large grains remain. When the 80 hr orientation map is compared to the as-received map in figure 6.2, AGG is obvious. Some grains begin to grow large after only 10 hr at temperature, but AGG can not be said to have for sure started until after 20 hr at temperature. Grain growth begins to behave normally after annealing for 80 hours.

Small, trapped grains were found within the abnormal grains, shown in figure 6.6, and appeared to be stationary. The remaining small grains are trapped at grain boundaries, rather than in the grain matrix. These small grains are shown to have a subsurface relationship at the grain boundary with the basal plane of alumina.

No second phases are found within the grain matrices. However, Ca and Si were found to sit at the triple pockets, as illustrated in the EDS mapping of Si in figure 6.7. Ca was also found in the same triple pockets, but printer resolution limited the ability to see the mapped points.

6.5 Discussion

The large grains seen in figures 6.3-5 are indicative of AGG. Figure 6.4 shows that the AGG was not just a surface effect; the bulk also underwent AGG. Undoped alumina hot-pressed at 1550˚C and annealed at 1672˚C has been reported to form lath-shaped grains[11], an indicator of AGG. In addition, small grains were found[4, 11] to be trapped within the large lath-shaped grains similar in manner to those observed in this study (figure 6.6). No orientation information was given in the previous study describing any special misorientations between the trapped grains. However, as shown with the overlayed alumina unit cell, a relationship exists at the grain boundary with the basal plane. Cross-section analysis should be done of these boundaries to determine the exact orientation relationships, since EBSD analysis software assumes that grain boundaries

only lie perpendicular to the free surface. Immobile grains have been previously found to not affect grain boundary mobility.[4] Lath-like grains have been reported[22] to have non-equilibrium dihedral angles at the grain boundary grooves, suggesting the presence of a wetting liquid phase. Growth of large grains has been attributed to the prism planes of alumina.[21]

With time, lath-like grains form and eventually consume all of the small grains, as seen in the series of EBSD orientation maps in figure 6.5. The formation of lath-like or columnar grains supports Mullins'[25] theory of grain boundary migration speed and the formation of a stable configuration consisting of 120˚ grain boundary angles during AGG. In addition, Mullins postulated that impurities, strain and changes in boundary density would create a non-ideal migration velocity, as is the case here. Normal grains in front of the growing single crystal in SCC studies had no intergranular thin-film containing Ca. Glass found at grain boundaries causes disorder at the grain boundary, creating mobilities twice as fast as intrinsic grain boundaries. This observation suggests that diffusional transport is promoted[4] and is related to Cahn's impurity-drag theorem.[2] However, a note should be made that impurity-drag would counter AGG.

Fluorescing at the grain boundaries supports the theory of CAS being only at the grain boundaries and the previous studies' observations of impurities present during AGG. EDS mapping of trapped grains between two abnormal grains in figure 6.7 show that Ca and Si are trapped at the triple pockets. No impurities were found in the grain matrix.

Silica impurities introduced just from processing conditions are often measured between a few ppm to as much as 30 ppm.[10] Silica in the absence of MgO creates small amounts of liquid phase responsible for AGG. In the presence of silica, MgO solubility can be increased. MgO solubility will increase with decreasing alumina grain size. MgO may evaporate from the compact, and thus, the initial dopant level may not be the resulting concentration. MgO is known to inhibit AGG when the alumina contains ~300-500 ppm MgO, but promotes AGG when the concentration is less than 50 ppm MgO.[21] Scott, et al.[21] found that codoping MgO with CaO, Cr_2O_3, La_2O_3 or ZrO_2 inhibited the AGG

behavior. However, no work was done on CaO codoped with SiO_2, not in the presence of MgO, as in this case. This groups' work also required a much higher temperature (1880˚C), while the AGG observed here only required a temperature of 1650˚C.

Two significant features may be found in the microstructure found here; the first being large remnant grooves in the large grains which have not had enough time to fully heal, and the second, being small grains trapped within the large abnormal grains. Scott, et al[21] observed microstructure identical to that observed here. In both cases, The trapped grains appear to have grown, exhibit hexagonal symmetry and are not a second phase. Rossi and Burke[26] noted in their experiments to find additives to impede grain growth in alumina, that grain growth occurred so quickly in some cases, that the pores and remnant grooves did not have time to shrink or heal. Their work agrees with the observations presented here.

As Carter[27] pointed out, misorientation rather than sigma number is responsible for low-index planes to be parallel to each other at grain boundaries. Using diffusion-bonded bicrystals and high-resolution transmission electron microscopy (HRTEM), Ikuhara, et al.[28] noted that the stacking fault length near grain boundaries decreased with increasing grain boundary misorientation. Even in deformed minerals,[29] low-index phase and grain boundaries are preferred rather than high-index ones. This behavior is attributed to the lower grain boundary energy of the low-index planes. The preliminary orientation data measured here agreed with this. However, as previously noted, EBSD software only assumes that grain boundaries lie perpendicular to the surface. Cross-section analysis must be done using TEM and/or FIB to confirm any orientation relationships.

Most orientation studies using EBSD are performed using highly polished surfaces. In this study, polishing the sample surfaces would have destroyed the data. Rough surfaces needed to be analyzed. Figures 6.4a, 6.5 and 6.6 are all rough surfaces. Figure 6.4b compares the difference between the quality of maps obtained when a sample is polished opposed to as-annealed. While the data gathered from rough samples is not as

good as from polished surfaces, a significant amount can be gathered and accurate conclusions can be made.

6.6 Summary and Future Work

AGG was found to occur in pure alumina compacts when exposed to anorthite glass. The behavior occurred at both the surface and within the bulk material. A series of heat treatments showed the evolution of the surface morphology. After 10 hr, grain growth has begun. After 20 hr, AGG is distinct. NGG has begun again after 80 hr at temperature. Trapped grains were found within abnormal grains and have a relationship with low-index planes at the interfaces. Finally, EDS mapping found that Ca and Si impurities exist at the triple pockets, but not in the grain matrix or at remnant grooves.

Atmosphere has been reported[4] to drastically influence grain boundary behavior. The structure of the grain boundaries has been found to be different went samples are quenched rather than slow-cooled. Both of these variables need to be carefully examined in future work.

Pore-boundary interactions may play a roll.[3, 22] Brook[3] measured mobility ratios and regimes for normal and abnormal grain growth based on pore interaction with the grain boundary. The effect of impurities is to increase the pore mobility ratio and promote a shift in critical grain size needed to begin AGG. These sintering additives will force AGG to begin at a larger grain size. Further work should be done on grain boundary migration and the interaction of pores and impurities with interfaces.

Monitoring the thermal grooves would be an interesting way to measure the differences between grains experiencing NGG and those under AGG. A difference in interfacial energy should exist between the two types of grains which may be estimated by measuring the groove dihedral angles and backing out the surface and interfacial energies using Young's equation.[9] In addition, seeing how Gottstein and Shvindlerman's[14] proposed model that larger grain size promotes grain growth with

respect to triple junction and grain boundary mobility should be considered and related to Mullins'[25] work.

Appendix 6.1: Exaggerated vs. Abnormal Grain Growth

The difference between "exaggerated" and "abnormal" grain growth is somewhat grey. A literature search using the Compendex Search Index between the years 1884 and 2008 came back with 170 hits for "exaggerated grain growth." The same search criteria for "abnormal grain growth" yielded 1043 hits. While most of the recent literature refers to the formation of large grains within a "normal" matrix as having grown "abnormally," is this the correct term to be using? Exaggerated growth implies that select grains are growing much faster than the majority of grains in the matrix. The grains still have an equiaxed form and appear to be the same as normal grains, but at a larger scale. However, the term "abnormal" implies that the increased growth occurs in an irregular manner. Hillert[5] described abnormal grain growth as discontinuous, which would agree with the given comparison. Hillert[5] was the first in 1965 to give a generalized theory on the difference between normal and abnormal grain growth. Anisotropic grain growth occurs in preferred directions causing grains to form lath-shaped grains. The chemistry surrounding the grain, such as impurities and second-phase grains can allow for greater grain boundary mobility along the interface. Precipitates, pores and dislocations can pin grain boundaries, causing the grain to grow into an abnormal shape. Little is understood on how the difference affects the overall microstructure and properties.

The difference is illustrated in Figure 6.8. Exaggerated grains in Lucalox™, MgO-doped alumina, have the expected shape for a grain, but are just much larger than the surrounding grains. However, by changing the dopant material, alumina grains can grow abnormally.

Appendix 6.2: Lath-Like Grains

Anisotropic grain growth occurs in most types of materials, especially ceramics. Crystals with different surface energies for different planes will grow anisotropically. Growth rates will be different in every direction, just because of space-charge effects and ease of forming the unit cell. Capillary effects will also depend on the anisotropy of the crystal.[30] By altering the chemistry, even isotropic crystals may begin to behave anisotropically.

Anisotropy within a material will also cause behavior that appears to be energetically unfavorable. On closer examination, one realizes that the total system's energy has been reduced. Faceting and grain boundary migration are two such behaviors. Faceting at a free surface or at a grain boundary will increase the surface area, which is usually energetically forbidden. However, the planes that form the facets have low surface energy compared to the original orientation. If the plane can reconstruct into two or more planes that together have a lower total surface tension, faceting will occur.[31] The same is true for grain boundary migration. An initially flat grain boundary will move, creating more interfacial area, if the overall energy of the system is lowered. While these behaviors occur in isotropic materials, anisotropic materials show these behaviors in a more pronounced way.[32]

Recently nanofibers have attracted a lot of interest. Single crystal fibers, no matter the length scale, utilize anisotropic grain growth to form. Growth is constricted in two directions but permitted in one. Catalysis and growth environment, such as in the vapor-liquid-solid (VLS) growth mechanism, can contribute to the anisotropy. Similar to dewetting, Young's equation governs the relationship at the triple-phase junction at the fiber-catalyst interface and determines the surface tension balances. The presence of impurities can hinder growth in one direction by altering the surface tension on growth plane in which the impurities are sitting. Of course, preferred surface orientations will be an important growth parameter. Some crystal planes require greater energy for ions to diffuse to because of high surface tensions or high Peierls' barriers in a particular

direction. Ions will migrate in the crystal direction that has the lowest energy barriers to overcome, thus causing preferred growth planes.

Appendix 6.3: Texture

Texture within a crystalline material is defined as a preferred orientation within the polycrystals, grains and/or second phases. Texture can be introduced via growth techniques, impurities or deformation. Material properties are extremely sensitive to any texture within the material. For example, strong texture can allow grain boundary sliding to occur more easily than in a randomly oriented polycrystalline material. Texture within a material can often eliminate a dimension for easier analysis, since all of the grains with respect to one another share a common direction.

Texture can be purposely induced with polycrystalline materials via the growth method. Columnar growth of films is well known. The film material being deposited aligns itself along a particular direction to form an epitactic relationship with the substrate. Rather than growing in three dimensions, the polycrystalline material grows only in one once the grains touch each other. The grain boundaries are aligned and have a special misorientation between the interfacial planes. The grains grow in the *z*-direction as the more material is deposited, creating long column-shaped grains. Tape-casting deposits films of polycrystalline material by using a slurry. A seed crystal is used to encourage crystallization of the slurry in a particular direction. This method is useful in magnetic recording media. Single-crystal multilayer stacks, grown by molecular-beam epitaxy, should be considered textured. Texture in thin-films is of particular interest in the microelectronics industry, where electrons may conduct faster in one direction or along aligned grain and phase boundaries. Nanoparticles can be aligned within films by using electrostatic forces between the particles and substrate.

Deformation of crystalline material is known to induce texture. Rolling is perhaps the most familiar type of texture-inducing process. Usually used in metals, rolling causes the grains to rotate and align a particular crystallographic direction with the rolling direction. A similar behavior occurs during tensile strength testing of materials. Wear

patterns during tribological testing can induce texture at the surface during scratching. This behavior has significance in MEMS technology where parts grind against each other. Using sensitive measurements collected with EBSD, the amount of strain within each grain needed to induce grain turning and texture formation can be measured.

Magnetic materials are particularly sensitive to texture. Magnetic domains are usually dependent on anisotropic crystal structures. Domains can be a single grain or a group of grains that are closely related in orientation. A material may be a hard magnetic in one direction, but not magnetic in another. Magnetic recording relies on the domain wall texture and the ability to change the texture quickly and easily.

Likewise, the piezoelectric effect depends on crystal texture. The ion that is responsible for shifting within the unit cell and inducing a current will usually only move in one particular direction. This direction will depend on the surrounding ionic charge and how closely packed the unit cell is.

Texture in polymers is harder to define. Polymers can be amorphous, semi-crystalline or crystalline, but not in the same sense as inorganic materials. Crystalline polymers have their molecule chains line-up via van der Waal's forces. Crystalline texture in a polymer can be important for tensile strength, absorption sites and fluidics. Liquid crystal displays rely heavily on polymer texture.

Appendix 6.4: Surface Preparation

Surfaces for grain growth studies can be prepared in a variety of ways. Initially, surfaces need to be completely flat in order to render any curvature effects negligible. This requires some method of polishing or milling. Mechanical, chemical and electro-polishing are the common methods for achieving a smooth surface. However, not only does the surface need to be smooth, surface damage during surface preparation also needs to be avoided.

Chemical and electropolishing are the best methods for avoiding surface damage. Chemical polishing typically uses strong acids to attack the surface of interest. The acids remove material by causing surface ions to leave the material and form a reaction with the acid. Care must be taken that the acid does not contaminate the surface and that preferential etching of grain boundaries, dislocations, precipitates, etc. is avoided. The acids used during chemical polishing can be dangerous to work with, so safety is a concern.

Electropolishing also uses acids as an electrolyte.[33] The sample is immersed in the electrolyte and a current is passed through the liquid. The combination of the charge and chemistry results in material removal from the sample. Again, preferential etching needs to be avoided and safety is a concern. Electropolishing is only useful for metals and some semiconductors; the samples need to be conductive.

Mechanical polishing uses slurries or lapping films to remove material. Surfaces are placed in contact with the polishing medium and friction is used to remove material. The polishing medium must be made from a material that is harder than the surface of interest or no material will be removed. Very little pressure is placed on the surface to avoid as much surface damage as possible. The damage layer thickness is roughly three times the grit size used. Successively smaller grit size is used to remove scratches and surface damage from the previous polishing step. However, not all of the surface damage can be removed and some other type of polishing needs to be used as a final step to remove the damage remaining after the final grit. Preferential etching needs to be watched out for. The advantages of mechanical polishing are that few hazardous chemicals are used and any type of material can be polished.

Milling is an alternative to polishing. Ion milling is a common final step to remove surface damage after mechanical polishing of TEM samples. An argon ion beam is operated between 0-5 kV and focused onto the sample surface. The ions knock off atoms in the lattice and cause a sputtering effect. Not all of the damage can be removed via this method and often, preferential etching occurs. In addition, argon atoms can be

implanted into the sample. The focused-ion beam (FIB) tool uses metal ions that are liquid at room temperature, usually gallium, to mill surfaces in the same manner and cut into the bulk material. Gallium can be easily implanted into the sample, since the beam is operated at 30 kV. Recently, manufacturers have been working on developing a FIB tool that mills at a much lower accelerating voltage to be used as a final cleaning/polishing step. FIB milling allows for much less pre-milling preparation and the ability to mill specific sites. Unfortunately, all types of milling must be done in vacuum, which limits the type of samples able to be prepared.

EBSD analysis requires a flat surface that is free of surface damage. Rough samples can be analyzed, but with difficulty. The backscattered electrons can be reabsorbed or shadowed by surface features and never reach the detector. Therefore, a highly polished surface is necessary to allow the most signal to reach the detector and maps with higher signal-to-noise ratios to be collected. In the studies presented here, mechanical polishing, using diamond-embedded lapping film, polished surfaces to a 0.5 μm finish. Syton™, a silica-based slurry with a high pH, was used for the final chemical-mechanical polish. Surfaces were inspected using VLM and AFM to confirm surface roughness.

Charging of surfaces under an electron beam is a problem for ceramics and some semiconductors. EBSD needs a high beam voltage and probe size in order to produce enough signal for the detector to analyze. These microscope parameters cause the beam to have a large probe current which needs to be dissipated in some manner. Insulating ceramics and poorly conducting semiconductors can not distribute the charge being dumped into the sample quick enough. The surfaces end-up accumulating a surface charge that is capable of repelling the beam. The charging makes imaging difficult and orientation and chemical mapping impossible.

Coating sample surfaces to prevent charging limits analysis, also, and should be avoided if possible. Conductive coatings are usually thin carbon or precious metal films. However, since the electron beam is only sensitive to the first 100 μm of the sample, a

coating would interfere with the signal produced. To get around coating a surface, several things can be tried. Use the lowest beam accelerating voltage and probe current needed to get adequate signal. A faster scan rate during imaging and mapping may prevent charge build-up. Tilting the sample causes the surface to intersect more of the interaction volume of the beam. A larger cross-section allows more electrons and X-rays to escape from the sample reducing the amount of charge left in the sample. Polymer-based epoxy pucks and fixatives are known to trap charge by not allowing a conductive path from the sample surface to the microscope's stage. (Not to mention, epoxy contaminates the microscope.) Silver epoxy or carbon paint or tape can be used to mount samples to metal stubs and allow conduction. Rather than coating the entire sample, carbon and silver paint can be used to draw a line from a spot close to the region of interest to the metal stub creating a conduction path.

Appendix 6.5: Grain Growth in 3D

Most studies in the literature only consider two-dimensional cases when referring to grain growth. However, by not considering the third dimension, the analysis of the research could be completely wrong. With out doing some sort of 3D sectioning, a surface grain could appear to be completely equiaxed and normal, but really be lath-like sub-surface.

Figure 6.9 illustrates this important point. Consider grains A and B; grain A appears to be smaller than grain B when viewed from the surface. In reality, grain A is larger by volume when you consider the entire grain and view the bulk. When performing grain growth studies, grain A is expected to shrink and grain B is expected to grow if the researcher only has the surface information. However, the opposite will happen.

Surface preparation can also be deceptive. Figure 6.10 shows how a completely normal, equiaxed grain may be considered lath-like. By polishing the grain at an angle, rather than perpendicular or parallel, the grain looks to be lath-like rather than symmetric at the surface. This artifact may skew grain size measurements.

Triple lines and quadruple junctions are 3D even if only the surface is being considered. Often composition gradients exist between these features, the grain boundaries and the grain matrix. However, if the gradient exists in a preferential direction sub-surface, traditional surface characterization techniques will not be adequate.

The development of two important tools has started to aid in understanding grain growth in 3D. The focused-ion beam (FIB) tool uses a liquid-metal source to form an electron beam. Often the ion column is mounted 52˚ to an SEM column, allowing simultaneous use of both. The FIB column can mill away material at site-specific regions to expose the bulk characteristics. SEM and TEM cross-sections can be milled and plucked from the bulk for future viewing. Software has recently been introduced to combine FIB with EBSD and EDS for tomography; a section is milled with the FIB, an EBSD and/or EDS map is collected from the newly exposed region, and milling resumes. While being time intensive and creating huge data sets, a true 3D picture can be formed.

The three-dimensional atom probe (3DAP) is the other recently developed tool. By using sharp needle-shaped specimens like the one shown in figure 6.11, less than 50 nm in tip radius, the specimen is exposed to high voltage to induce atom evaporation from the needle tip using the field effect. Individual atoms are monitored using a time-of-flight mass spectrometer and a traditional field ion microscope.[34] By combining the two, the needle can be reconstructed in 3D and include chemical data. The 3DAP does have limitations.[33] Because of the low collection efficiency, vacancies can not be studied. The technique is destructive, so data can not be collected using other techniques after evaporation. Currently, specimens are limited to being only metals or semiconductors capable of conducting electrons. The field effect does not easily occur in insulating ceramic materials. Imago Scientific Instruments, who developed the local electrode atom probe (LEAP), has recently released a 3DAP that is capable of heating the specimen with a laser to aid the field effect.[35] With laser-assistance, ceramics are starting to be analyzed.

By combining the FIB and 3DAP, site-specific needles can be made and specific features, such as triple junctions, can be analyzed. Since the 3DAP needles are electron transparent, the TEM can be used prior to evaporation to confirm or compare the 3DAP data collected.

Appendix 6.6: Composition of Liquid Phases

Grain boundaries can have a wide range of compositions. The dopants at the grain boundaries can be intentionally placed there, but unfortunately, impurities often show-up at interfaces on their own. Grain boundaries are somewhat like the "trash can" of the bulk material; the grain boundary has a more open structure than the bulk, and therefore, can accommodate the impurities. Many studies have been done on intentional doping to see how the bulk's properties are altered.

Greskovich and Brewer[10] showed that the amount of a dopant at the grain boundary can change the grain growth behavior. Abnormal grain growth of alumina was found to only occur in the presence of small MgO-doping levels or very large doping levels; an intermediate concentration range actually impeded grain growth. These results imply that grain boundary mobility is heavily dependent on the amount of impurities at the boundary. Similar results were found in another study that considered co-doping.[21] Co-doping of CaO, La_2O_3 or ZrO_2 with MgO was found to inhibit grain growth, but abnormal growth occurred when the co-dopant was Cr_2O_3.

Many more additives have been found to promote exaggerated grain growth rather than impede grain growth.[26, 36] Undoped alumina was found to grow in an exaggerated manner without any intentional doping.[26] Adding significant amounts of CaO, SrO, BaO, Y_2O_3 or ZrO_2 also allowed alumina grains to grow faster than normal. The addition of MgO was found to limit the grain growth and create a nearly pore-free compact. The same impedance occurred when MgO was co-doped with any of the previously mentioned additives. The MgO is believed to lower the grain boundary mobility. In all cases, an IGF was observed and the grain boundaries were proposed to

be sweeping the pores from the grain matrix. The IGF plays an important role in densification by aiding in pore coalescence and annhilation.

A significant amount of work has been done on understanding the role of MgO in sintering and grain boundary migration of alumina. This system is desirable for sodium-vapor lamp tubes. Coble[37] was one of the first to study how MgO promotes densification of alumina compacts. He noted that both continuous and abnormal grain growth occurred and depended on MgO concentration. In fact, Coble wrote a patent[38] on using MgO-doping to produce translucent alumina tubes now used for sodium-vapor lamps. Not surprisingly, Coble was doing this research while working for General Electric Companies.

Harmer's research group has done a significant amount of work on doping alumina. Alumina doped with 500 ppm MgO and annealed in N_2/H_2 atmosphere was found to grow grains as large as 30 mm.[4] A disordered IGF was found at the grain boundaries of the large grains that contained Ca; disorder at the grain boundary is thought to enhance diffusion. Large atoms with a high atomic number have been used as tracers to see how the boundary constructs in the presence of an impurity.[24] However, a large atom will change the grain boundary structure and is not entirely representative of small-atom doping typically found in industry.

Anorthite ($CaAl_2Si_2O_8$) is a dopant that is often used to simulate impurities found in industrial processing. Anorthite forms a liquid film at the grain boundaries of alumina.[16, 20] The boundaries are usually flat, but crystallography at the boundary can change the behavior somewhat.[20] When Cr is added to anorthite, the IGF behavior drastically changes. The liquid film forms finger-like structures perpendicular to the grain boundary, but parallel to the direction of migration.[16]

Potassium was also found to induce abnormal grain boundary migration.[39] Wavelength-dispersive spectroscopy (WDS) using an electron microprobe showed that the potassium only resides at the abnormal grain boundaries. Arias[36] found that columnar or lath-like grains formed in several types of oxides when ZrO_2 is added. In the same work

metal ions and boron-based compounds added to alumina were found to impede grain growth, with the exception of Ti and Mn additions.

Bulk alumina is not the only material that can have a different composition at the grain boundaries. When alumina is the dopant, UO_2 grains exhibit enhanced grain growth when a Al_2O_3-UO_2 liquid forms at the grain boundaries.[40] Various amounts of doping in Ni-alloys has been shown to change the grain boundary structure and the growth behavior.[6] Metal ions and boron-based compounds were added to ZrO_2, MgO and HfO_2 to determine the effect on grain growth.[36]

As with bulk crystalline material, grain boundaries can have local composition differences where grain boundaries meet surfaces due to oxygen partial pressure. A change in partial pressure can change the local defect structure, resulting in a composition change.[17] Similarly, point defects within grain boundaries will attract one another and alter the composition.

Thickness of IGFs at grain boundary curves is a critical parameter in knowing whether or not the system is in equilibrium.[17] The thickness may not be uniform along a curved interface, leading to composition variations. IGFs may be as thin as 1 nm, but also thicker than 1 μm. If a film is less than 1 nm thick, the film is referred to as an absorbate layer that can reach equilibrium easier than a thick IGF. Some researchers believe that an amorphous film exists at all grain boundaries, but the coincident-site lattice (CSL) model and reported observations[27] contradict this. Amorphous films indicate that the processing conditions introduced impurities.

Pores at grain boundaries can be considered a second phase or an additional composition. They have been found to play an important role in exaggerated grain growth.[12] The interaction between grain boundaries and pores is what ultimately limits the achievable density of the compact during sintering.

The composition at triple lines can be dramatically different from that at grain boundaries. Grain boundaries are on the order of only a few nanometers, while triple

lines or pockets are much larger. The larger volume is able to accommodate more impurities. Some large atoms, such as the rare earths, can not be stable in a grain boundary, but the triple junction can easily accommodate the large ionic radius. In addition, the differences in misorientation across grain boundaries can lead to different compositions within the grain boundaries. Grain boundaries can be larger or smaller depending on the crystallographic relationship between the interface planes. Therefore, the composition of IGFs is often not uniform in even small regions of a sample.

Quad junctions are not understood at all. A quad junction is a point where for triple lines meet. The only way to analyze these features is in 3D. So little is known about their structure that quad junctions are difficult to model. No one knows how the presence of a quad junction affects grain boundary migration and grain growth. One thing that is assumed about the junctions is that they are excellent diffusion paths for impurities and charge.

References

[1] W. D. Kingery, H. K. Bowen, D. R. Uhlmann, Introduction to Ceramics, John Wiley & Sons New York, (1960).

[2] J. W. Cahn, "The Impurity-Drag Effect in Grain Boundary Motion" Acta metall., **10** 789-798 (1962).

[3] R. J. Brook, "Pore-grain boundary interactions and grain growth" J. Am. Ceram. Soc., **52** [1] 56-57 (1969).

[4] S. J. Dillon, M. P. Harmer, "Mechanism of "solid-state" single-crystal conversion in alumina" Journal of the American Ceramic Society, **90** [3] 993-995 (2007).

[5] M. Hillert, "On the theory of normal and abnormal grain growth" Acta Metall., **13** [3] 238-238 (1965).

[6] S. B. Lee, D. Y. Yoon, M. F. Henry, "Abnormal Grain Growth and Grain Boundary Faceting in a Model Ni-Base Superalloy" Acta. mater., **48** 3071-3080 (2000).

[7] V. Randle, A. Brown, "The effects of strain on grain misorientation texture during the grain growth incubation period" Phil. Mag. A, **58** [5] 717-736 (1988).

[8] G. S. Rohrer, C. L. Rohrer, W. W. Mullins, "Coarsening of faceted crystals" J. Am. Ceram. Soc., **85** [3] 675-682 (2002).

[9] W. W. Mullins, "Effect of thermal grooving on grain boundary motion" Acta Metall., **6** [6] 414-424 (1958).

[10] C. Greskovich, J. A. Brewer, "Solubility of magnesia in polycrystalline alumina at high temperatures" J. Am. Ceram. Soc., **84** [2] 420-425 (2001).

[11] R. D. Monahan, J. W. Halloran, "Single-Crystal Boundary Migration in Hot-Pressed Aluminum Oxide" J. Am. Ceram. Soc., **62** [11-12] 564-567 (1979).

[12] J. E. Burke, "Role of grain boundaries in sintering" J. Am. Ceram. Soc., **40** [3] 80-85 (1957).

[13] A. D. Rollett, W. W. Mullins, "On the Growth of Abnormal Grains" Scripta Mater., **36** [9] 975-980 (1997).

[14] G. Gottstein, L. S. Shvindlerman, "Triple junction drag and grain growth in 2D polycrystals" Acta Mater., **50** 703-713 (2002).

[15] R. S. Hay, B. Evans, "Chemically induced grain boundary migration in calcite: temperature dependence, phenomenology, and possible applications to geologic systems" Contrib. Mineral. Petrol., **97** 127-141 (1987).

[16] J.-K. Park, D.-Y. Kim, H. Lee, -Y, J. E. Blendell, C. A. Handwerker, "Crystallographic-Orientation-Dependent Dissolution Behavior of Sapphire in Anorthite Liquid Containing Chromia" J. Am. Ceram. Soc., **86** [6] 1014-1018 (2003).

[17] C. B. Carter, M. G. Norton, Ceramic Materials: Science and Engineering, Springer New York, NY, (2007).

[18] S. Wu, E. Gilbart, R. J. Brook, in, Science of Ceramics, Italy, (1983), pp. 371-380.

[19] D. B. Williams, C. B. Carter, Transmission Electron Microscopy: A Textbook for Materials Science, Plenum New York, (1996).

[20] J. K. Farrer, C. B. Carter, N. Ravishankar, "The effects of crystallography on grain-boundary migration in alumina" J. Mats. Sci., **41** 661-674 (2006).

[21] C. Scott, M. Kaliszewski, C. Greskovich, L. Levinson, "Conversion of Polycrystalline Al2O3 into Single-Crystal Sapphire by Abnormal Grain Growth" J. Am. Ceram. Soc., **85** [5] 1275-1280 (2002).

[22] S. J. Bennison, M. P. Harmer, "Grain-growth kinetics for alumina in the absence of a liquid phase" J. Am. Ceram. Soc., **68** [1] C22-C24 (1985).

[23] M. Kinoshita, "Boundary Migration of Single Crystal in Polycrystalline Alumina" Yogyo-Kyokai-Shi, **82** [5] 63-64 (1974).

[24] S. J. Dillon, M. P. Harmer, "Direct observation of multilayer adsorption on alumina grain boundaries" J. Am. Ceram. Soc., **90** [3] 996-998 (2007).

[25] W. W. Mullins, "Two-Dimensional Motion of Idealized Grain Boundaries" J. Appl. Phys., **27** [8] 900-904 (1956).

[26] G. Rossi, J. E. Burke, "Influence of additives on the microstructure of sintered Al_2O_3" J. Am. Ceram. Soc., **56** [12] 654-659 (1973).

[27] C. B. Carter, "Σ=99 and Σ=41 Grain Boundaries" Acta metall., **36** [10] 2753-2760 (1988).

[28] Y. Ikuhara, H. Nishimura, A. Nakamura, K. Matsunaga, T. Yamamoto, "Dislocation Structures of Low-Angle and Near-S3 Grain Boundaries in Alumina Bicrystals" J. Am. Ceram. Soc., **86** [4] 595-602 (2003).

[29] T. Hiraga, T. Nagase, M. Akizuki, "The structure of grain boundaries in granite-origin ultramylonite studied by high-resolution electron microscopy" Phys. Chem. Minerals, **26** 617-623 (1999).

[30] M. K. Santala, A. M. Glaesar, "Surface-energy-anisotropy-induced orientation effects on Rayleigh instabilities in sapphire" Surf. Sci., **600** 782-792 (2006).

[31] W. W. Mullins, "Theory of Linear Facet Growth During Thermal Etching" Phil. Mag., **6** [71] 1313-1341 (1961).

[32] N. Ravishankar, C. B. Carter, "Migration of alumina grain boundaries containing a thin glass film" Acta Mater., **49** 1963-1969 (2001).

[33] M. K. Miller, Atom Probe Tomography: Analysis at the Atomic Level, Kluwer Academic/Plenum Publishers New York, (2000).

[34] M. K. Miller, "The Development of Atom Probe Field-Ion Microscopy" Mater. Charact., **44** 11-27 (2000).

[35] I. S. Instruments, Imago Products-Laser Pulsing, website, http://www.imago.com/imago/html/products/laserpulsing.jsp#, (12 January).

[36] A. Arias, "Effect of inclusions on grain growth of oxides" J. Am. Ceram. Soc., **19** [11] 621-624 (1966).

[37] R. L. Coble, "Sintering Crystalline Solids. II. Experimental Test of Diffusion Models in Powder Compacts" J. Appl. Phys., **32** [5] 793-799 (1961).

[38] R. Coble, Transparent Alumina and Method of Preparation, USA, 3026210, (1962).

[39] D. W. Susnitzky, C. B. Carter, "Localization of Potassium in Al_2O_3" J. Am. Ceram. Soc., **68** [11] 569-574 (1985).

[40] K. W. Lay, "Grain growth in UO_2-Al_2O_3 in the presence of a liquid phase" J. Am. Ceram. Soc., **51** [7] 373-376 (1968).

Chapter 6 Figures

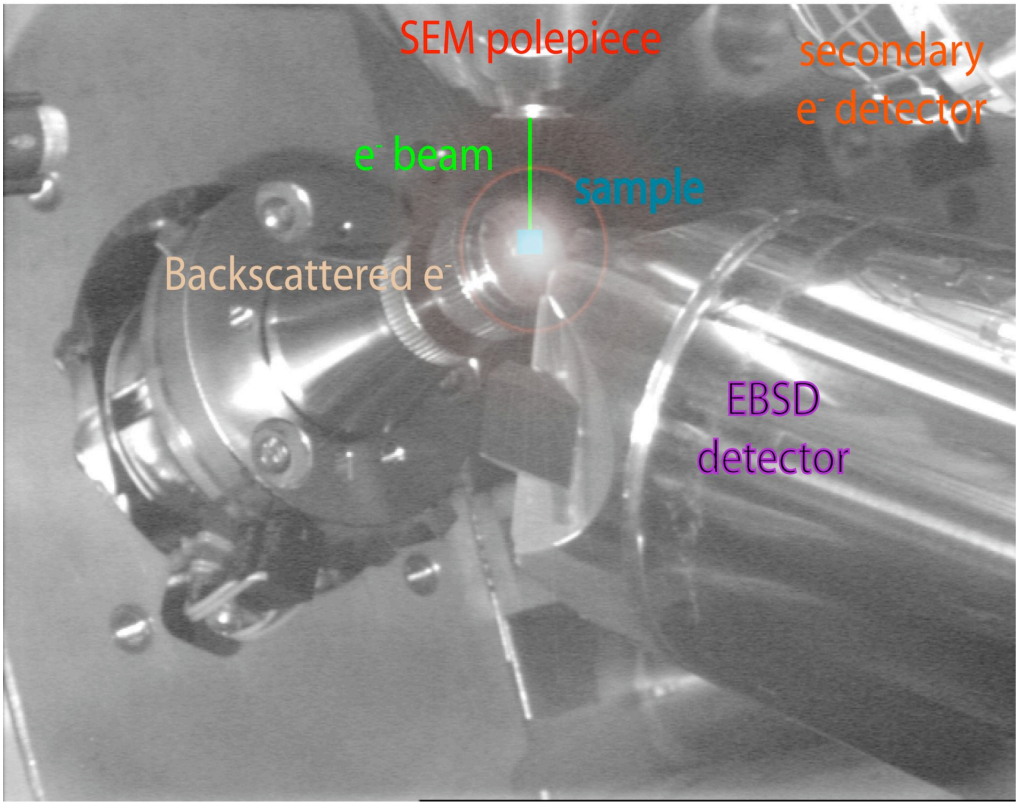

Figure 6.1: Phillips XL-30 SEM chamber showing how the EBSD detector is aligned with SEM column with respect to the sample.

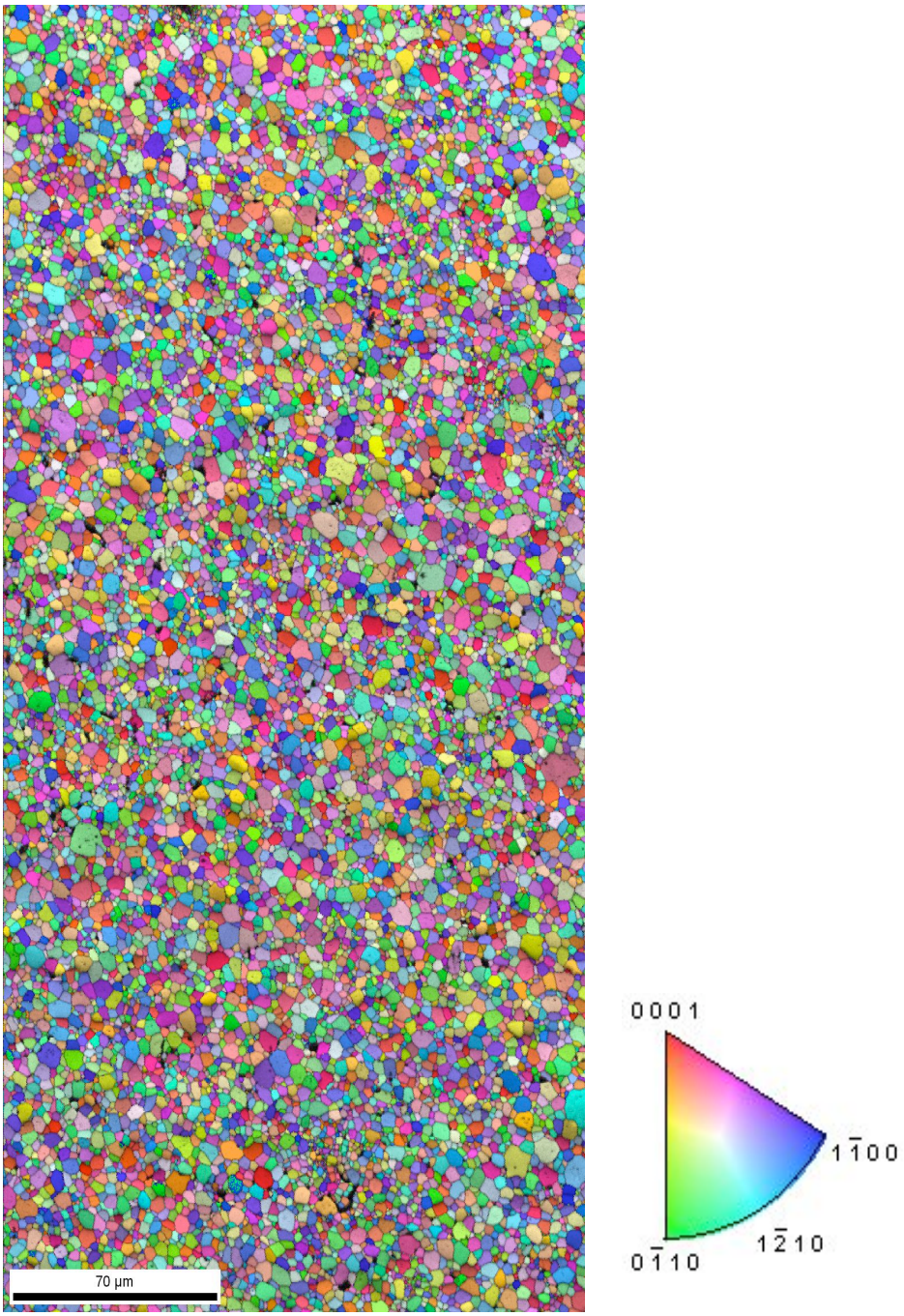

Figure 6.2: As-received pure alumina was polished to 0.5-µm finish for EBSD. Average grain size was measured to be ~3 µm.

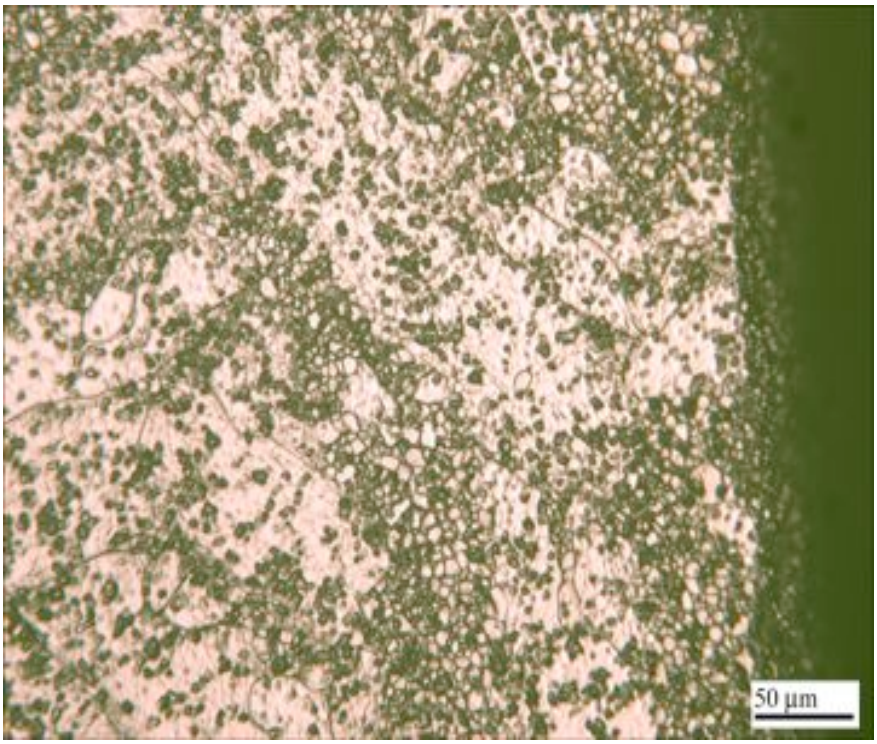

Figure 6.3: VLM shows large abnormal grains with small grains trapped at the grain boundaries and within the matrix. The surface is covered with remnant grooves.

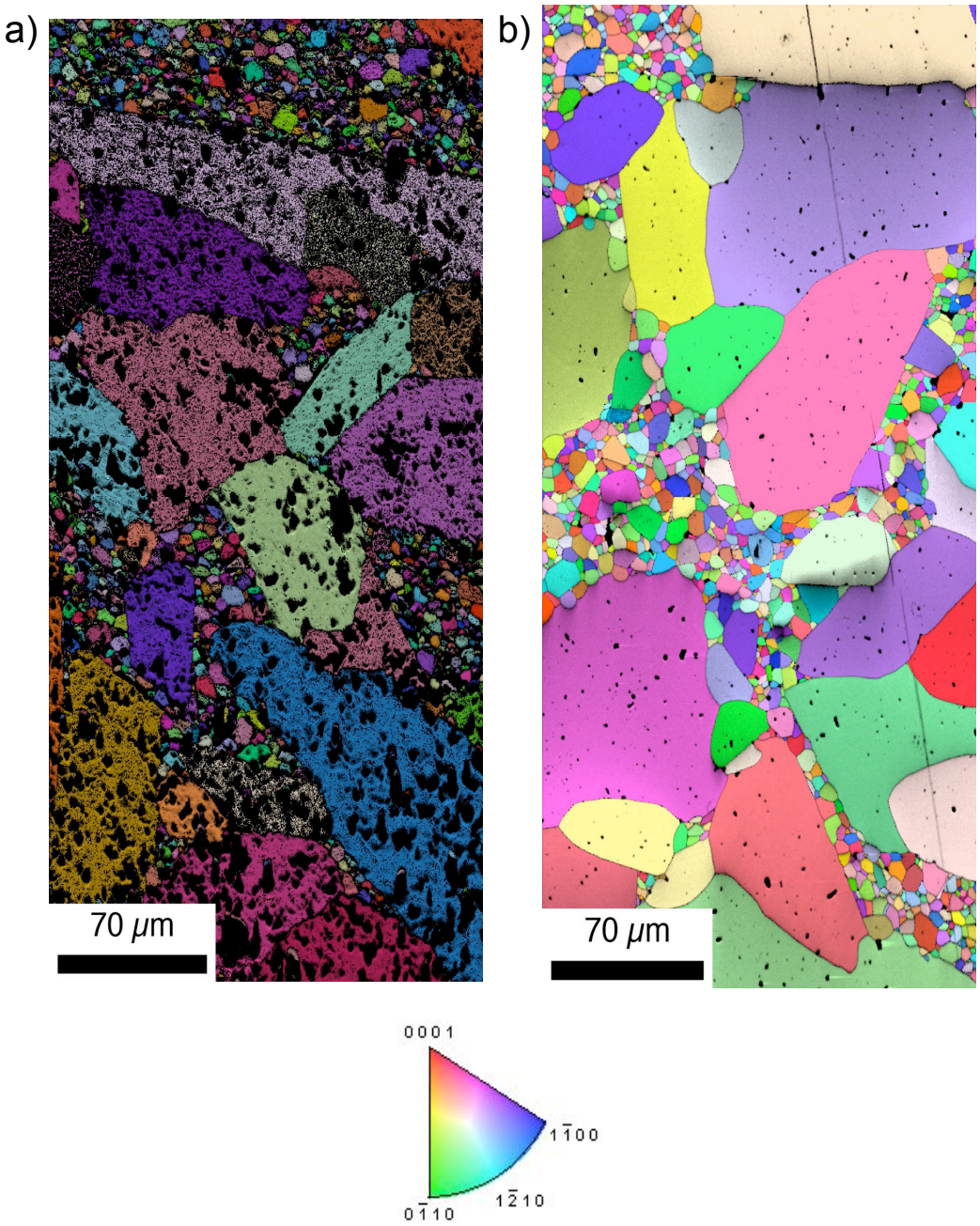

Figure 6.4: (a) EBSD maps of the surface are of poorer quality than (b) maps of polished bulk material.

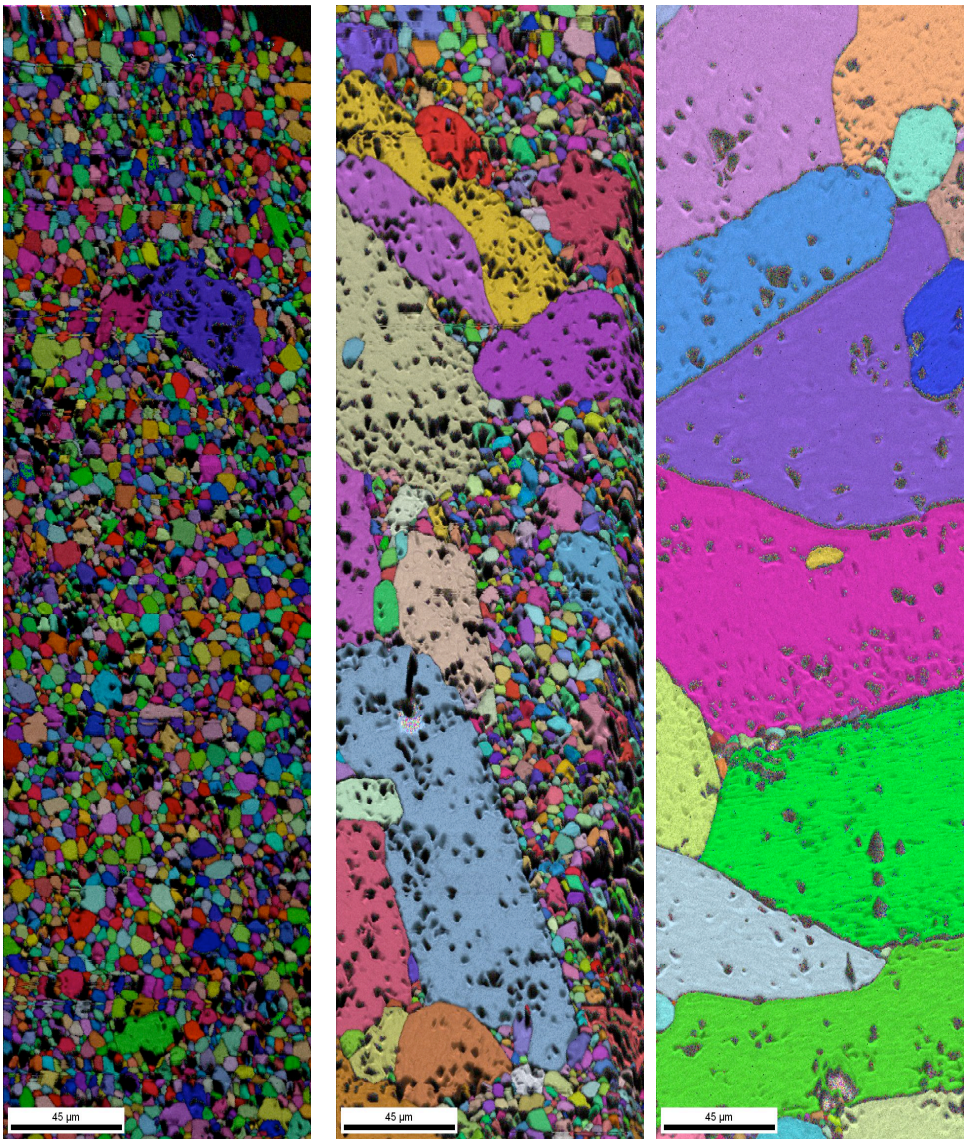

a) 10 hr surface b) 20 hr surface c) 80 hr surface

Figure 6.5: EBSD orientation maps show how the surface evolves from small 3 µm grains to large abnormal grains several hundred µm in size.

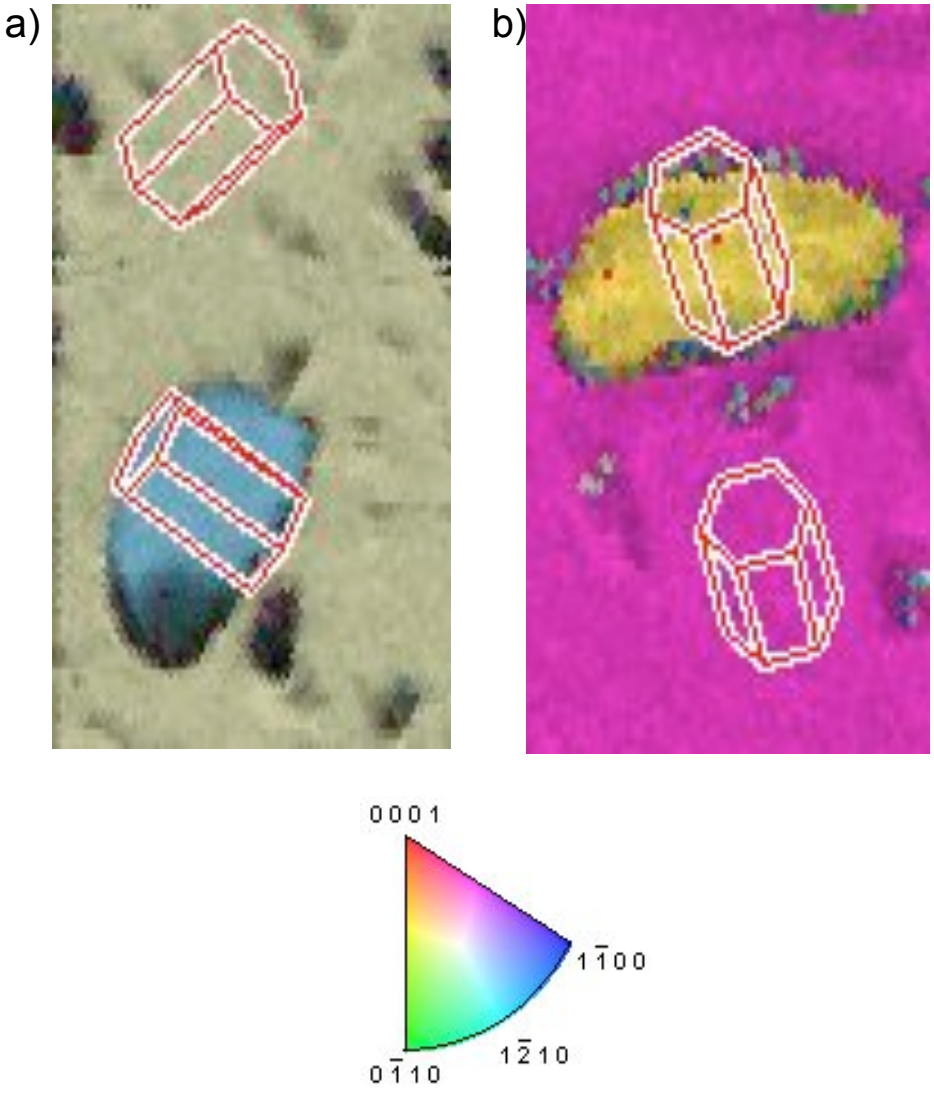

Figure 6.6: After (a) 20 hr and (b) 80 hr, smaller grains were found to be trapped with abnormal grains. The trapped grains have an interface relationship with the alumina (0001).

a)

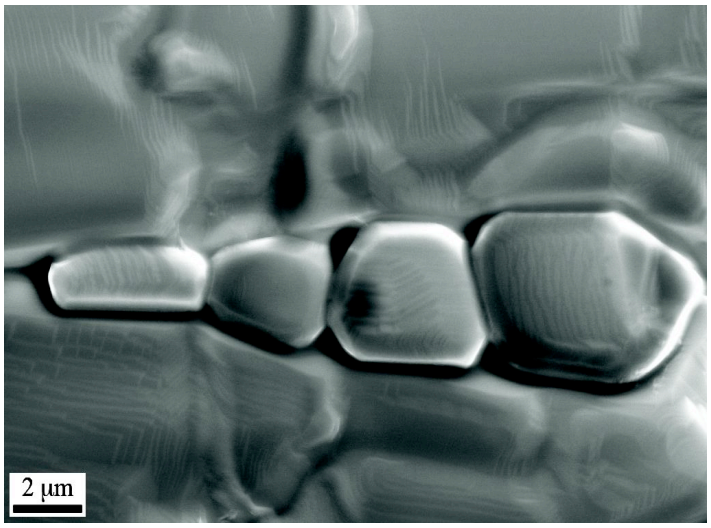

b)

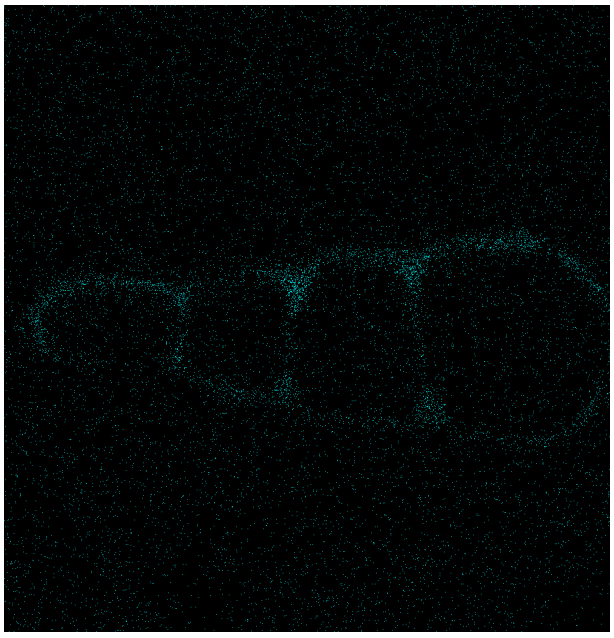

Figure 6.7: EDS of grains trapped in a grain boundary between two abnormal grains shows that Si resides at the triple pockets and not with in the matrix. Ca was also found, but due to printing resolution, is not shown here.

a)

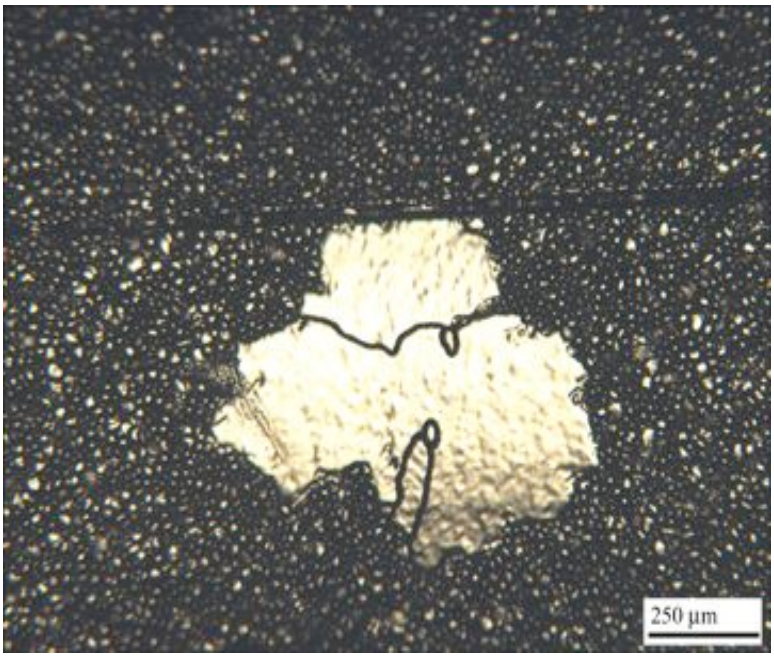

b)

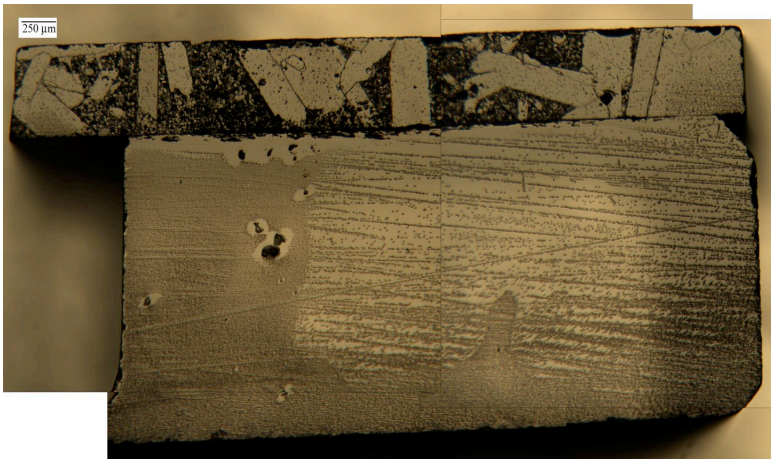

Figure 6.8: (a) An exaggerated grain in an alumina tube. The grain is fairly equiaxed. (b) Abnormal grains in alumina have a lath-like shape.

a) Plan-View

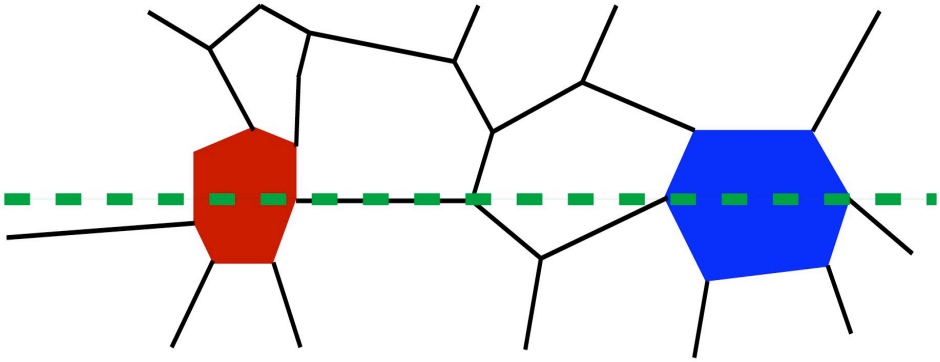

b) Cross-Section

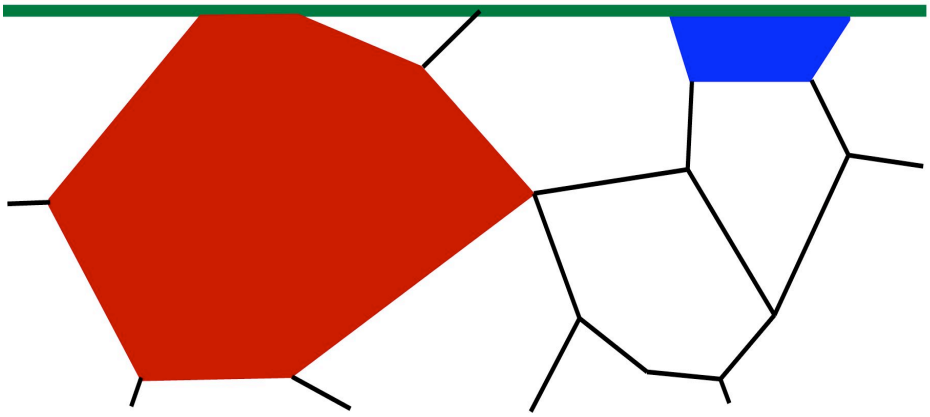

Figure 6.9: When looking at the sample in plan-view, the blue grain appears to be larger than the red grain. But if a cross-section is made along the green line, one can clearly see that the red grain is larger than the blue grain.

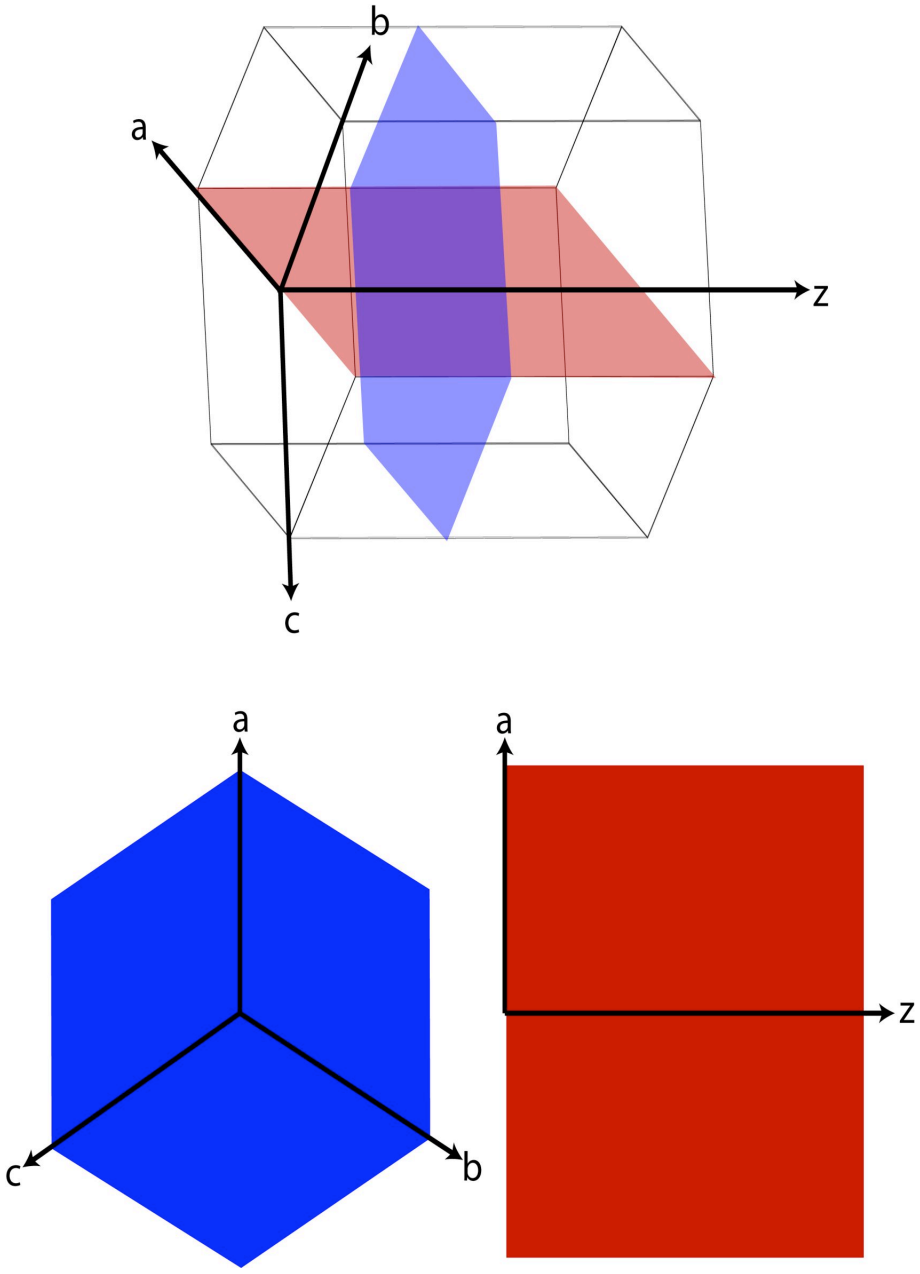

Figure 6.10: Depending on how the grain is diced, a misleading grain shape may result at the surface when polished. In this example, a hexagonal grain is diced in two different directions. When viewed from the new surfaces, the blue grain looks very different from the red one.

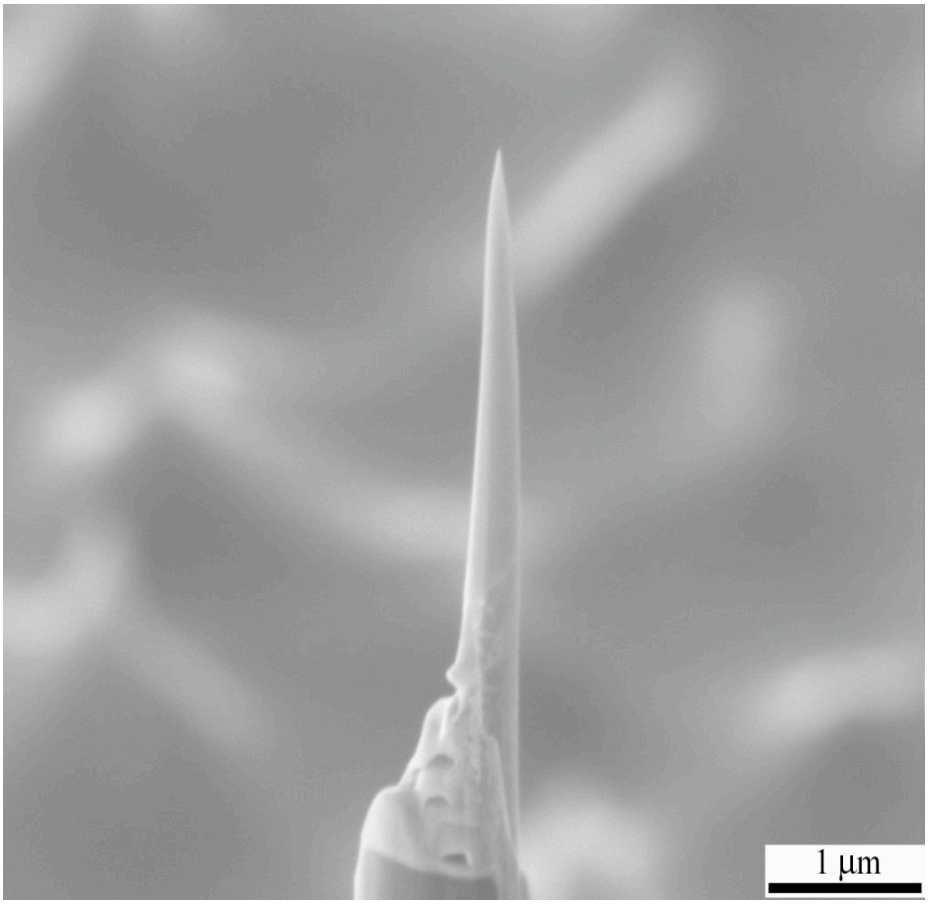

Figure 6.11: A FIB-prepared Cu atom-probe tomography (APT) needle has a radius of curvature of < 50 nm.

Chapter 7: Summary and Future Work

7.1 Conclusions and Summary of Work

7.1.1 Using AFM to Monitor Alumina Surface Facets

Fiducial markers were used to return to the exact same set of facets in the AFM. The markers unfortunately created accelerated surface reconstruction due to the subsurface damage near the indent. Faceting began near the indents in an attempt to heal the area.

A mechanism for facet coarsening/lengthening was proposed. Facet tips form kinks when they meet other facets. The kinks move in a way to wrap themselves around the adjacent facet. The facet continues to lengthen and coarsening occurs on the complex plane of the facet.

Vicinal surfaces must form first before surface reconstruction can begin. When surfaces are slightly miscut from a low-index plane, the low-index plane must form first and then facets can form. Surface energy balances must move through a minor energy cusp on the Wullf plot before reaching the final major energy cusp, or lowest energy state.

7.1.2 Thermal Grooving of Alumina

Thermal grooving at grain boundaries of alumina is a constant balance of forces at non-equilibrium conditions. Grain boundaries were observed to move ahead of their thermal grooves. The thermal groove caught-up to the grain boundary by forming bridges at the surface. The time that the surface is exposed to the dwell temperature during the anneal will change what extent the grooving has formed. Even after 16 hr at 1650˚C, the thermal grooves were still dynamic, indicating that a long time is needed to establish equilibrium.

When surfaces were exposed to glass at temperature, the thermal grooves were found to form at an accelerated rate. The ability for material to diffuse quicker through liquid is thought to be the contributing factor as to why the grooves form faster.

Remnant triple junctions were observed for the first time. The triple junction must move in tandem with two of its three grain boundaries. The adjacent grain boundaries also form remnant grooves. By monitoring the surface reconstruction, the degree of remnant groove healing can be monitored without any special analysis tools.

7.1.3 Dewetting of SiO_2 on TiO_2

Processing conditions were found to be an important parameter when investigating dewetting of glass films. When identical films were subjected to the same thermal treatment, but in different crucibles, the type of crucible was found to change what kind of dewetting occurred. Pt and Al_2O_3 crucibles were used. Films heated in Pt crucibles exhibited Marangoni convection, while those heated in Al_2O_3 crucibles disappeared and produced large etch pits and irregular surface facets.

The thickness was also confirmed to be an important variable. Very thin films were non-existent after annealing, but films 100 nm thick showed dewetting behavior indicative of Rayleigh convection. When the thickness was increased to 200 nm, the continuous film took longer to dewet into a regular array of droplets and cylinders seen in the 100 nm thick film.

7.1.4 Exudation and Penetration of Glass at Grain Boundaries

By using a unique dimpled sample geometry, anorthite glass was found to be able to penetrate grain boundaries on one surface and exude onto the opposite surface of polycrystalline alumina. Once exuded, the glass dewet into patterns on the grains' surfaces or completely wet the grain, depending on the grains' surface orientation. The wetting behavior was found to depend on the balance of surface tension and droplet patterns would change depending on the underlying bulk orientation.

Grain boundaries were observed to migrate, straighten and draw glass back into them with further heat treatment. Grain boundaries may become decorated with glass droplets, migrate and leave the droplets behind. The droplets along with the remnant groove mark exactly where the initial position of the boundary had been. Glass sitting at grain boundaries and triple junctions is able to pull back into the bulk in order to satisfy force balances. In addition, surface droplets can move on the surface and Ostwald ripen in an effort to lower the overall surface energy of the system.

7.1.5 GBM and AGG in Alumina with a Liquid Phase Present

Pure alumina compacts were found to undergo AGG when exposed to anorthite glass. Grains as large as several hundred microns formed from an initially 3-μm average grain-size compact in as little as 20 hr. The behavior was found to occur at the surface and within the bulk. A series of heat treatments showed that NGG began again after roughly 80 hr at 1650˚C.

EBSD was used to characterize and monitor morphology with time. While smooth samples are usually needed to get good data when using EBSD, polishing would destroy the data in this study. Rough samples were successfully mapped to gather significant amount of data in this study.

Preliminary orientation results indicate that the grain boundaries have a relationship with the basal plane of alumina. The long grain boundaries of the lath-like grains appear to have (0001) at the interface. Likewise, small grains completely trapped within abnormal grains have an orientation relationship with low-index planes.

7.2 Development of New Characterization Techniques

7.2.1 Atom-probe tomography for ceramic materials

A promising technique for 3D reconstruction and chemical analysis is atom-probe tomography (APT), also known as 3D atom probe (3DAP) or atom probe field ion microscopy (APFIM). The theory behind the instrument has been around for decades;

the basic part of the microscope is the same as a field-ion microscope (FIM).[1] In FIM fine needle-shaped specimens are made from the material of interest and are evaporated via the field effect. A bias is applied to the tip and a cathode such that the evaporated electrons will be accelerated towards the cathode. The cathode is also the detector and the position of where the electrons strike can be mapped. The 3DAP uses the same procedure, but is coupled with a time-of-flight mass spectrometer, allowing for the chemistry of each ion to be determined. Combining the two forms of data results in a 3D reconstruction of the needle.

As of now, the APT has its limitations.[1] The needle for evaporation must have a radius of curvature of less than 50 nm, making sample preparation difficult. In addition, the needles are usually prepared via electrochemical polishing using highly concentrated electrolyte acids. Safety becomes a concern. Unfortunately, the collection efficiency of APT is only 60% at best. Thus vacancies and low-concentration point defects can not be measured accurately. The main limitation is the type of materials that can be analyzed with the microscope. Currently, the materials must be conducting in order to use the field effect. Therefore, most ceramics can not be analyzed using the technique. However, the 3DAP manufacturer Imago has developed the local-electrode atom probe (LEAP) that uses a specially designed cathode to draw electrons with a higher work function off of the needle tip. Imago is currently developing a laser system to be inserted within the LEAP. The laser is directed at the needle and provides more energy for the electrons to break free from the needle, allowing for insulators to be evaporated. The new systems are still being perfected, but offer an interesting possibility for characterization in the future.

The transmission electron microscope (TEM) can be combined with APT to get an accurate reconstruction of the specimen. The needles are electron transparent and can be inserted into the TEM for traditional imaging. APT is a destructive technique, so TEM provides another record of the data after the needle has been evaporated. The focused-ion beam (FIB) tool has been proven to be a helpful technique for needle preparation. The FIB is used in a similar manner as when preparing TEM lamellae. Instead of using

rectangular thinning patterns, ring-shaped patterns are used to create needles. By decreasing the inner annulus of the ring, the needle can be milled to have a radius of curvature less than 50 nm. The needles can be mounted in situ to micromanipulator tips, silicon tower arrays or pre-prepared traditional APT sample mounts. The combination of APT, TEM and FIB allow for specific features to be analyzed with great accuracy.

7.2.2 Electron Tomography

Electron tomography is another promising new technique. Using a special holder, TEM samples are rotated and tilted within the TEM and a series of images are collected to produce a 3D reconstruction of the sample.

Limitations do exist and make the technique difficult to use. The same tedious sample preparation is needed, but the samples must be much more uniform in thickness to make the computer-reconstruction techniques work more correctly. A new holder and modifications to the microscope are very costly. A tomography experiment takes a long time to run in the microscope. Any sample drift in the microscope during image collection will form an inaccurate reconstruction. Samples that are beam sensitive may not be able to withstand the long exposure time. The collected images are still subject to the same aberrations as traditional TEM images. Each image must be carefully corrected for spherical and chromatic aberrations after collection. Hundreds of images may be collected in one series, making the reconstruction technique tedious.

7.3 Future Experiments

Several experiments have been identified during this work that should be performed in order to clarify the behaviors investigated further. Due to time constraints and access to instruments, the following experiments could not be performed, but should be considered for future work.

7.3.1 Ion-Beam Induced Grooving

Two experiments using ion beams can be used to create grooves in ceramics for studying. The technique used in chapter 3 uses a 30 min thermal etch to induce grain boundary grooving. However, the kinetics for healing the grooves and grain boundary migration have already started by the time the first AFM images have been collected. By creating the grooves in a manner that is not also coupled to these kinetics would give a better understanding of how the grooves behave.

The first experiment uses a standard ion mill for TEM sample preparation. The ceramic samples could be prepared in the same manner as described here and mounted to an ion mill holder after the final polish. The argon ion beam could then be used to preferentially etch the grain boundaries and produce grooves. The same experiments presented in chapter 3 could then be repeated to analyze the very first stages of grain boundary migration and remnant groove formation.

The second experiment uses the FIB tool. Specific groove geometries could be milled into single crystals, bicrystals and polycrystalline compacts to see how the material heals. By changing the beam parameters and milling angle, grooves can be made to have flat bottoms or have a range of groove angles with the surface. Using bicrystals would allow systematic monitoring of how the grain boundaries move and the grooves heal with orientation.

7.3.2 In situ *Grain Boundary Penetration of Liquid*

In situ TEM and SEM is becoming more available. While most of the temperatures used in this dissertation are much higher than what can be reached *in situ*, similar experiments using lower melting point materials could be used to begin to understand the behaviors, expecially those dealing with the liquid phase. For example, preparing cross-sections of bicrystals would begin to give an understanding of how liquid will penetrate grain boundaries and wet surfaces. A thin film of a metal could be deposited onto an alumina bicrystal and then heated to above the metal's melting point within the

microscope. The film's behavior at the grain boundary-surface intersection could be monitored in real time. *In situ* SEM would allow fewer complications with sample preparation and would be able to analyze a larger area at once, but may be limited in resolution.

7.3.3 3D Reconstruction

Recently, FIB tools have been combined with electron backscatter diffraction (EBSD) and energy dispersive spectroscopy (EDS). Combining milling with these techniques allows a 3D reconstruction of specific sites in the bulk material. Using this technique would be allow distinguishing of tilted grain boundaries, sub-surface pores and chemical inhomogeneities that traditional 2D characterization techniques can not provide. Samples would be milled with the FIB and then tilted to the correct detector(s). After chemical and/or orientation mapping concludes, the sample can be tilted back for further milling of a known amount. The mapping is then repeated and the resulting images and maps are combined to form a 3D image of what the material looked like.

Unfortunately, this technique has limitations that need to be considered. The FIB will create a damage layer within the material that may alter the data or reduce the map resolution. The stage motions are limited within a FIB tool with so many attachments, which may limit data collection. Finally, the entire process is extremely time consuming, especially for ceramics, and would require exclusive access to a FIB tool. Unfortunately, this scenario is highly unlikely.

7.3.4 Environmental Effects During Processing

Controlling atmosphere is a key point that has been ignored in this work. The changes in humidity from day to day can cause different amounts of hydroxyl groups to reside on the surface of ceramics and alter the surface tension. The change in surface tension would create slightly different behavior at the surface. Some sort of humidity control should be used when studying surfaces. Chandrasekharan, et al.[2] have recently shown that humidity levels during thermal treatment and drastically change the faceting

behavior of the *c*-, *r*- and *a*-planes of α–alumina. However, no work was done on understanding how hydroxylation of the m-plane alumina surface changes the surface reconstruction.

Characterizing materials in different humidity levels may change the analysis. Atomic-force microscopy (AFM) is sensitive to humidity and contact-mode AFM relies on a water meniscus to hold the tip in contact with the surface. If the humidity level is different from day-to-day, the tip's interaction with the surface will be different depending on the size of the water meniscus.

7.3.5 Alternative Sample Geometries for Interface Studies

Using alternative sample geometries would allow more information to be gathered in a systematic way for the study of thermal grooving, intergranular films and grain boundary migration. Bicrystals and multilayers would allow interfaces with known orientations to be used and eliminate a set of variables. Bicrystals hot-pressed together with a PLD deposited film between would allow a specific grain boundary type to be monitored. Likewise, growing a series of multilayers of different thicknesses and orientations would provide a model specimen where several parameters could be easily tailored. In addition, these geometries could be polished to form a wedge. The change in sample thickness would be measurable, and therefore, the effect of grain boundary length on migration and intergranular films could be monitored.

7.4 Review of How This Work Fits Together

Returning to the same feature over a series of experiments and 3D reconstruction is key for getting a full understanding of behaviors in ceramics. By doing research in the traditional way, a whole dimension or set of variables are completely ignored. The experimental set-up no longer resembles real life. With the future development of the techniques described here, completed representative experiments will be realized.

At first look, the work presented here seems unrelated. However, closer inspection reveals that each of the kinetic behaviors investigated effect one another. Surface energy and capillary forces tie everything together. Faceting, thermal grooving, film wetting, grain boundary migration and intergranular films all behave differently depending on orientation and chemistry. Capillary forces govern second-phases and sintering processes. While separating each driving force for study gives a good understanding that force, eventually all possible driving forces must be studied in combination. This work aimed to begin just that for traditional ceramic materials in a systematic manner.

References

[1] M. K. Miller, "The Development of Atom Probe Field-Ion Microscopy" Mater. Charact., **44** 11-27 (2000).

[2] R. Chandrasekharan, L. Zhang, V. Ostroverkhov, S. Prakash, Y. Wu, Y.-R. Shen, M. A. Shannon, "High-temperature hydroxylation of alumina crystalline surfaces" Surf. Sci., **602** 1466-1474 (2008).

Bibliography

[1] Science, community encyclopedia, http://en.wikipedia.org/wiki/Science, (May 30).
[2] B. L. Adams, D. Kinderlehrer, W. W. Mullins, A. D. Rollett, S. Ta'asan, "Extracting the relative grain boundary free energy and mobility functions from the geometry of microstructures" Scripta Mater., **38** [4] 531-536 (1998).
[3] M. D. Antonik, R. J. Lad, "Faceting, Reconstruction, and Defect Microstructure at Ceramic Surfaces Revealed by Atomic Force Microscopy" Journal of Vacuum Science & Technology a-Vacuum Surfaces and Films, **10** [4] 669-673 (1992).
[4] A. Arias, "Effect of inclusions on grain growth of oxides" J. Am. Ceram. Soc., **19** [11] 621-624 (1966).
[5] C. Barth, M. Reichling, "Imaging the atomic arrangements on the high-temperature reconstructed α-Al_2O_3(0001) surface" Nature, **414** 54-57 (2001).
[6] P. E. Batson, N. Dellby, O. L. Krivanek, "Sub-angstrom resolution using aberration corrected electron optics" Nature, **418** [6898] 617-620 (2002).
[7] D. Bäuerle, Laser Processing and Chemistry, Springer Berlin, (2000).
[8] M. W. Bench, P. G. Kotula, C. B. Carter, "Influence of the nature of the (0001) alumina surface on thin film growth" Surf. Sci., **391** 183-195 (1997).
[9] S. J. Bennison, M. P. Harmer, "Grain-growth kinetics for alumina in the absence of a liquid phase" J. Am. Ceram. Soc., **68** [1] C22-C24 (1985).
[10] B. M. Besancon, P. F. Green, "Moving fronts in entangled polymeric films" Phys. Rev. E, **70** (2004).
[11] S. Bhattacharyya, C. T. Koch, M. Rühle, "Projected potential profiles across intergranular glassy films" J. Ceram. Soc. Japan, **114** [11] 1005-1012 (2006).
[12] G. Bilalbegovic, F. Ercolessi, E. Tosatti, "High-temperature surface faceting" Surf. Sci. Let., **258** L676-L678 (1991).
[13] G. Binnig, C. F. Quate, C. Gerber, "Atomic Force Microscope" Phys. Rev. Lett., **56** [9] 930-933 (1986).
[14] B. S. Bokstein, L. M. Klinger, I. V. Apikhtina, "Liquid grooving at grain boundaries" Mater. Sci. Eng. A, **203** 373-376 (1995).
[15] M. P. Brada, D. R. Clarke, "A thermodynamic approach to the wetting and dewetting of grain boundaries" Acta Mater., **45** [6] 2501-2508 (1997).
[16] E. Brener, H. Müller-Krumbhaar, D. Temkin, T. Abel, "Structure formation in diffusional growth and dewetting" Solid State Ionics, **131** 23-33 (2000).
[17] J. Britt, The Complete Guide to High-Fire Glazes: Glazing & Firing at Cone 10, Lark Books New York, NY, (2004).
[18] J. Britt, The Complete Guide to High-Fire Glazes, Lark Books New York, (2004).
[19] R. J. Brook, "Pore-grain boundary interactions and grain growth" J. Am. Ceram. Soc., **52** [1] 56-57 (1969).
[20] R. J. Brook, "Obituary: W. David Kingery (1926-2000)" Nature, **406** [6796] 582 (2000).
[21] J. E. Burke, "Role of grain boundaries in sintering" J. Am. Ceram. Soc., **40** [3] 80-85 (1957).

[22] L. A. Bursill, P. J. Lin, D. J. Smith, "Surface Faceting and Polarity of Alumina" Ultramicroscopy, **23** 223-228 (1987).
[23] J. Burton, Glass: Philosophy and Method, Bonanza Books New York, (1967).
[24] X. Buttol, R. Dramais, G. Richez, J. Ruelle, "Silica refractories get a second life" Glass Ind., **82** [3] 12-14 (2001).
[25] J. W. Cahn, "The Impurity-Drag Effect in Grain Boundary Motion" Acta metall., **10** 789-798 (1962).
[26] G. Callegari, A. Calvo, J.-P. Hulin, F. Brochard-Wyart, "Dewetting versus Rayleigh Instability inside Capillaries" Langmuir, **18** 4795-4798 (2002).
[27] S. A. Campbell, The Science and Engineering of Microelectronic Fabrication, Oxford University Press New York, (2001).
[28] C. B. Carter, "S=99 and S=41 Grain Boundaries" Acta Metall., **36** [10] 2753-2760 (1988).
[29] C. B. Carter, M. G. Norton, Ceramic Materials: Science and Engineering, Springer New York, NY, (2007).
[30] B. Chalmers, R. King, R. Shuttleworth, "The thermal etching of silver" Proc. Roy. Soc. A, **193** [1035] 465-483 (1948).
[31] R. Chandrasekharan, L. Zhang, V. Ostroverkhov, S. Prakash, Y. Wu, Y.-R. Shen, M. A. Shannon, "High-temperature hydroxylation of alumina crystalline surfaces" Surf. Sci., **602** 1466-1474 (2008).
[32] C. W. Chesterman, K. E. Lowe, National Audubon Society Field Guide to Rocks and Minerals, Alfred A. Knopf, Inc. New York, (1979).
[33] R. Coble, Transparent Alumina and Method of Preparation, USA, 3026210, (1962).
[34] R. L. Coble, "Sintering Crystalline Solids. II. Experimental Test of Diffusion Models in Powder Compacts" J. Appl. Phys., **32** [5] 793-799 (1961).
[35] R. L. Coble, Transparent alumina and method of preparation, U. S. P. Office, United States, (1962).
[36] U. Czubayko, V. G. Sursaeva, G. Gottstein, L. S. Shvindlerman, "Influence of triple junctions on grain boundary motion" Acta Mater., **46** [16] 5863-5871 (1998).
[37] P. G. de Gennes, "Wetting: statics and dynamics" Rev. Mod. Phys., **57** [3] 827-863 (1985).
[38] R. C. DeVries, R. Roy, E. F. Osborn, "The system TiO_2-SiO_2" Trans. Brit. Ceram. Soc., **53** [9] 525-540 (1954).
[39] S. J. Dillon, M. P. Harmer, "Mechanism of "solid-state" single-crystal conversion in alumina" Journal of the American Ceramic Society, **90** [3] 993-995 (2007).
[40] S. J. Dillon, M. P. Harmer, "Direct observation of multilayer adsorption on alumina grain boundaries" J. Am. Ceram. Soc., **90** [3] 996-998 (2007).
[41] D. B. Dingwell, "The density of titanium (IV) oxide liquid" J. Am. Ceram. Soc., **74** [10] 2718-2719 (1991).
[42] P. Donnadieu, "TEM investigations of glide lines in amorphous silica below the glass transition" J. Non-Cryst. Solids, **111** 7-15 (1989).
[43] A. G. Evans, Y. Fu, in: W. D. Kingery (Ed.), Structure and Properties of MgO and Al_2O_3 Ceramics, Columbus, OH, (1984), pp. 697-719.
[44] J. K. Farrer, C. B. Carter, N. Ravishankar, "The effects of crystallography on grain-boundary migration in alumina" J. Mats. Sci., **41** 661-674 (2006).

[45] Z. Feng, L. Kaiming, W. Guoliang, S. Hua, H. Anmin, "Crystallizaton behavior of Li^+-doped SiO_2-TiO_2 films prepared by sol-gel dip coating" J. Cryst. Growth, **264** 297-301 (2004).
[46] G. S. Ferguson, G. M. Whitesides, in: M. E. Schrader, G. Loeb (Eds.), Modern Approach to Wettability: Theory and Applications, New York, (1991), pp. 143-177.
[47] M. Ferrario, D. U. Hernández-Becerril, I. Garibotti, "Morphological study of the marin planktonic diatom Chaetoceros castranei Karsten (Bacillariophyceae) from Antarctic waters, with a discussion on its possible taxonomic relationships" Botanica Marina, **47** 349-355 (2004).
[48] P. Fortier, G. Palumbo, G. D. Bruce, W. A. Miller, K. T. Aust, "Triple line energy determination by scanning tunneling microscopy" Scripta Metall. Mater., **25** 177-182 (1991).
[49] H. Friedman, Geode, webpage, http://www.minerals.net/mineral/silicate/tecto/quartz/images/geode4.htm, (20 January).
[50] M. Fujimoto, T. Ohno, H. Suzuki, H. Koyama, J. Tanaka, "Nanostructure of TiO_2 nano-coated SiO_2 particles" J. Am. Ceram. Soc., **88** [11] 3264-3266 (2005).
[51] A. R. Gaddipati, W. D. Scott, "Surface mass transport of alumina" J. Mater. Sci., **21** 419-423 (1986).
[52] Z. Gai, J. Y. Howe, D. A. Blom, E. W. Plummer, J. Shen, "Self-assembled FePt nanodot arrays with mono-dispersion and -orientation" Appl. Phys. Lett., **86** 1-3 (2005).
[53] R. Gehlhaar, M. Swoboda, M. Sudzius, M. Hoffmann, h. Fröb, H. Wendrock, "Polarization splitting and terahertz oscillations from a single planar Fabry-Pérot microcavity" Appl. Phys. Lett., **88** (2006).
[54] R. M. German, P. Suri, S. J. Park, "Review: liquid phase sintering" J. Mater. Sci., **44** [1] 1-39 (2009).
[55] L. A. Giannuzzi, F. A. Stevie, Introduction to Focused Ion Beams: Instrumentations, Theory, Techniques and Practice, Springer New York, (2005).
[56] S. R. Gilliss, Ceramic Oxides: Surfaces and Amorphous/Crystalline Interfaces, Minneapolis, MN, University of Minnesota, 261 (2004).
[57] J. J. Gilman, W. G. Johnston, "Observations of dislocation glide and climb in lithium fluoride crystals" J. Appl. Phys., **27** [9] 1018-1022 (1956).
[58] J. J. Gilman, W. G. Johnston, G. W. Sears, "Dislocation etch pit formation in lithium fluoride" J. Appl. Phys., **29** [5] 747-754 (1958).
[59] J. Goldstein, D. Newbury, D. Joy, C. Lyman, P. Echlin, E. Lifshin, L. Sawyer, J. Michael, Scanning Electron Microscopy and X-ray Microanalysis, Kluwer Academic/Plenum Publishers New York, (2003).
[60] R. J. Good, C. J. van Oss, in: M. E. Schrader, G. Loeb (Eds.), Modern Approach to Wettability: Theory and Applications, New York, (1991), pp. 1-27.
[61] G. Gottstein, L. S. Shvindlerman, "Triple junction drag and grain growth in 2D polycrystals" Acta Mater., **50** 703-713 (2002).
[62] C. Greskovich, J. A. Brewer, "Solubility of magnesia in polycrystalline alumina at high temperatures" J. Am. Ceram. Soc., **84** [2] 420-425 (2001).

[63] H. Gu, R. M. Cannon, I. Tanaka, M. Rühle, "Calcia partition in phase-separated intergranular glass and interfaces in doped silicon nitride produced by hot isostatic pressing" Mater. Sci. Eng. A, **422** 51-65 (2006).
[64] C. A. Handwerker, R. M. Cannon, R. H. French, "Robert L Coble: A retrospective" J. Am. Ceram. Soc., **77** [2] 293-297 (1994).
[65] P. Hartman, "The attachment energy as a habit controlling factor III. Application to Corundum" J. Crys. Growth, **49** 166-170 (1980).
[66] R. S. Hay, B. Evans, "Chemically induced grain boundary migration in calcite: temperature dependence, phenomenology, and possible applications to geologic systems" Contrib. Mineral. Petrol., **97** 127-141 (1987).
[67] J. R. Heffelfinger, M. W. Bench, C. B. Carter, "On the faceting of ceramic surfaces" Surf. Sci. Let., **343** L1161-L1166 (1995).
[68] J. R. Heffelfinger, M. W. Bench, C. B. Carter, "Steps and the structure of the (0001) a-alumina surface" Surf. Sci., **370** L168-L172 (1997).
[69] J. R. Heffelfinger, C. B. Carter, "The effect of surface structure on the growth of ceramic thin films" Phil. Mag. Lett., **76** [3] 223-232 (1997).
[70] J. R. Heffelfinger, C. B. Carter, "Mechansms of surface faceting and coarsening" Surf. Sci., **389** 188-200 (1997).
[71] C. Herring, "Some Theorems on the Free Energies of Crystal Surfaces" Phys. Rev., **82** [1] 87-93 (1951).
[72] C. Hess, K. Wight, Looking at Glass: A Guide to Terms, Styles and Techniques, The J. Paul Getty Museum Los Angelos, (2005).
[73] M. Hillert, "On the theory of normal and abnormal grain growth" Acta metall., **13** [3] 238-238 (1965).
[74] T. Hiraga, T. Nagase, M. Akizuki, "The structure of grain boundaries in granite-origin ultramylonite studied by high-resolution electron microscopy" Phys. Chem. Minerals, **26** 617-623 (1999).
[75] H. Hirota, M. Itoh, M. Oguma, Y. Hibino, "Temperature coefficients of refractive indices of TiO_2-SiO_2 films" Jap. J. Appl. Phys., **44** [2] 1009-1010 (2005).
[76] M. F. Hocella Jr, C. M. Eggleston, V. B. Elings, M. S. Thompson, "Atomic structure and morphology of the albite {010} surface: An atomic-force microscope and electron diffraction study" Amer. Miner., **75** 723-730 (1990).
[77] K. Horrocks, E. Masuoka, Cloud vortex streets off the Cape Verde Islands, website, http://images.google.com/imgres?imgurl=http://rapidfire.sci.gsfc.nasa.gov/gallery/2005005-
0105/CapeVerde.A2005005.1225.150x115.jpg&imgrefurl=http://rapidfire.sci.gsfc.nasa.gov/gallery/%3F2005005-
0105&h=115&w=150&sz=3&tbnid=jfe0dPQ1L2oJ:&tbnh=69&tbnw=90&hl=en&start=33&prev=/images%3Fq%3DNASA%2Bcloud%2Bstreets%26start%3D20%26svnum%3D10%26hl%3Den%26lr%3D%26client%3Dfirefox-a%26rls%3Dorg.mozilla:en-US:official%26sa%3DN
, (4 October 2005).
[78] R. Hosemann, A. M. Hindeleh, R. Brueckner, "Paracrystalline lattice structure of silica glass, α- and β-crystobalite" Phys. Status Solidi A, **126** [2] 313-324 (1991).

[79] R. Howland, L. Benatar, A Practical Guide to Scanning Probe Microscopy, Park Scientific Instruments Sunnyvale, CA, (1993).
[80] M. Hu, S. Noda, H. Komiyama, "A new insight into the growth mode of metals on TiO_2(110)" Surf. Sci., **513** 530-538 (2002).
[81] Y. Huang, M. Liu, Y. Zeng, C. Li, "The effect of secondary phases on electrical properties of ZnO-based ceramic films prepared by a sol-gel method" J. Mater. Sci., **15** 549-553 (2004).
[82] D. Hull, D. J. Bacon, Introduction to Dislocations, Butterworth Heinemann Oxford, (1965).
[83] Y. Ikuhara, H. Nishimura, A. Nakamura, K. Matsunaga, T. Yamamoto, "Dislocation Structures of Low-Angle and Near-S3 Grain Boundaries in Alumina Bicrystals" J. Am. Ceram. Soc., **86** [4] 595-602 (2003).
[84] Y. Ikuhara, N. Shibata, T. Watanabe, F. Oba, T. Yamamoto, T. Sakuma, "Grain boundary characters and structures in structural ceramics" Ann. Chim. Sci. Mat., **27** [1] S21-S30 (2002).
[85] O. A. Inc., Olympus Microscopy Resource Center, webpage, http://www.olympusmicro.com/, (20 January).
[86] I. S. Instruments, Imago Products-Laser Pulsing, website, http://www.imago.com/imago/html/products/laserpulsing.jsp#, (12 January).
[87] M. J. J. Jak, A. van Kreuningen, J. Verhoeven, J. W. M. Frenken, "The effect of stoichiometry on the stability of stes on TiO_2 (110)" Appl. Surf. Sci., **201** 161-170 (2002).
[88] M. Jin, E. Shimada, Y. Ikuma, "Atomic force microscopy study of surface diffusion in polycrystalline CeO_2 via grain boundary grooving" J. Ceram. Soc. JPN, **108** [5] 456-461 (2000).
[89] R. E. Johnson Jr., "Conflicts between Gibbsian Thermodynamics and Recent Treatments of Interfacial Energies in Solid-Liquid-Vapor Systems" J. Phys. Chem., **63** [10] 1655-1658 (1959).
[90] B. S. Kang, F. Ren, B. S. Jeong, Y. W. Kwon, K. H. Baik, D. P. Norton, S. J. Pearton, "Use of 370 nm UV light for selective-area fibroblast cell growth" J. Vac. Sci. Technol. B, **23** [1] 57-60 (2005).
[91] W. D. Kingery, H. K. Bowen, D. R. Uhlmann, Introduction to Ceramics, John Wiley & Sons New York, (1960).
[92] M. Kinoshita, "Boundary Migration of Single Crystal in Polycrystalline Alumina" Yogyo-Kyokai-Shi, **82** [5] 63-64 (1974).
[93] E. L. Koschmieder, in, Bénard Cells and Taylor Vortices, Cambridge, (1993), pp. 4-10.
[94] E. L. Koschmieder, Bénard Cells and Taylor Vortices, University of Cambridge Cambridge, UK, (1993).
[95] M. L. Kronberg, "Plastic Deformation of single Crystals of Sapphire: Basal Slip and Twinning" Acta Metall., **5** 507-524 (1957).
[96] O. Kurnosikov, L. Pham Van, J. Cousty, "High-Temperature transformation of vicinal (0001) Al_2O_3-α Surfaces: an AFM Study" Surf. Interface Anal., **29** 608-613 (2000).

[97] K. W. Lay, "Grain growth in UO_2-Al_2O_3 in the presence of a liquid phase" J. Am. Ceram. Soc., **51** [7] 373-376 (1968).
[98] S. B. Lee, D. Y. Yoon, M. F. Henry, "Abnormal Grain Growth and Grain Boundary Faceting in a Model Ni-Base Superalloy" Acta. mater., **48** 3071-3080 (2000).
[99] W. E. Lee, K. P. D. Lagerlof, "Structural and Electron Diffraction Data for (a-Al_2O_3)" J. Elect. Microsc. Techn., **2** 247-285 (1985).
[100] E. M. Levin, C. R. Robbins, H. F. McMurdie (Eds.), Phase Diagrams for Ceramists, The American Ceramic Society, Inc., Columbus, Ohio, p. 601, (1964).
[101] M. Li, W. Hebenstreit, U. Diebold, "Oxygen-induced restructuring of the rutile TiO_2 (110)(1x1) surface" Surf. Sci., **414** L951-L956 (1998).
[102] S.-Y. Lien, D.-S. Wuu, W.-C. Yeh, J.-C. Liu, "Tri-layer antireflection coatings (SiO_2/SiO_2-TiO_2/TiO_2) for silicon solar cells using a sol-gel technique" Sol. Energ. Mater. Sol. C., **90** 2710-2719 (2006).
[103] W. L. Ling, N. C. Bartelt, K. F. McCarty, C. B. Carter, "Twin boundaries can be moved by step edges during film growth" Phys. Rev. Lett., **95** (2005).
[104] Z. Lødziana, J. K. Norskov, "Interaction of Pd with steps on a-Al_2O_3 (0001)" Surface Science Letters, **518** L577-L582 (2002).
[105] W. Ludwig, E. Pereiro-López, D. Bellet, "In situ investigation of liquid Ga penetration in Al bicrystal grain boundaries: grain boundary wetting or liquid metal embrittlement?" Acta Mater., **53** 151-162 (2005).
[106] A. Marmur, in: M. E. Schrader, G. Loeb (Eds.), Modern Approach to Wettability: Theory and Applications, New York, (1991), pp. 327-358.
[107] D. B. Marshall, J. R. Waldrop, P. E. D. Morgan, "Thermal grooving at the interface between alumina and monazite" Acta Mater., **48** [18-19] 4471-4474 (2000).
[108] R. L. Meeks, Federal R&D funding by budget function: Fiscal years 2003-2005, (2004).
[109] F. Mei, C. Liu, L. Zhang, F. Ren, L. Zhou, W. K. Zhao, Y. L. Fang, "Microstructural study of binary TiO2:SiO2 nanocrystalline thin films" J. Cryst. Growth, **292** 87-91 (2006).
[110] R. A. Metzler, M. Abrecht, R. M. Olabisi, D. Ariosa, C. J. Johnson, B. H. Frazer, S. N. Coppersmith, P. U. P. A. Bilbert, "Architecture of Columnar Nacre, and Implications for Its Formation Mechanism" Phys. Rev. Lett., **98** (2007).
[111] Microbus, History of the Microscope, web page, www.microscope-microscope.org/basic/microscope-history.htm, (August 15).
[112] L. Microsystems, Camera Systems, webpage, http://www.leica-microsystems.com/website/products.nsf?open&path=/website/products.nsf/(allids)/89d748f7e7a47026c12574560026bd89, (20 January).
[113] M. K. Miller, Atom Probe Tomography: Analysis at the Atomic Level, Kluwer Academic/Plenum Publishers New York, (2000).
[114] M. K. Miller, "The Development of Atom Probe Field-Ion Microscopy" Mater. Charact., **44** 11-27 (2000).
[115] R. D. Monahan, J. W. Halloran, "Single-Crystal Boundary Migration in Hot-Pressed Aluminum Oxide" J. Am. Ceram. Soc., **62** [11-12] 564-567 (1979).
[116] R. Monti, R. Savino, G. Alterio, "Pushing of liquid drops by Marangoni force" Acta Astro., **51** [11] 789-796 (2002).

[117] A. J. W. Moore, "The Influence of Surface Energy on Thermal Etching" Acta metall. mater., **6** 293-304 (1958).
[118] K. J. Morrissey, C. B. Carter, "Surface steps on α-alumina films" Journal, **41** [Issue] 137-142 (Year).
[119] C. A. M. Mulder, G. van Leeuwen-Stienstra, J. G. van Lierop, J. P. Woerdman, "Chain-like structure of ultra-low density SiO_2 sol-gel glass observed by TEM" J. Non-Cryst. Solids, **82** 148-153 (1986).
[120] K. Müller, M. von Heimendahl, "TEM investigation of crystallization phenomena in the metallic glass Vitrovac® 0040 ($Fe_{40}Ni_{40}B_{20}$)" J. Mater. Sci., **17** 2525-2532 (1982).
[121] W. W. Mullins, "Two-dimensional motion of idealized grain boundaries" J. Appl. Phys., **27** [8] 900-904 (1956).
[122] W. W. Mullins, "Theory of thermal grooving" J. Appl. Phys., **28** [3] 333-339 (1957).
[123] W. W. Mullins, "Effect of thermal grooving on grain boundary motion" Acta Metall., **6** [6] 414-424 (1958).
[124] W. W. Mullins, "Flattening of a nearly plane solid surface due to capillarity" J. Appl. Phys., **30** [1] 77-83 (1959).
[125] W. W. Mullins, "Theory of Linear Facet Growth During Thermal Etching" Phil. Mag., **6** [71] 1313-1341 (1961).
[126] W. W. Mullins, "Stochastic theory of particle flow under gravity" J. Appl. Phys., **43** [2] 665-677 (1972).
[127] W. W. Mullins, R. F. Sekerka, "Morphological stability of a particle growing by diffusion or heat flow" J. Appl. Phys., **34** [2] 323-329 (1963).
[128] J. D. Mun, A. P. Sutton, B. Derby, "Grain growth and texture changes in a Ni foil during diffusion bonding to ZrO2" Phil. Mag. A, **76** [2] 289-305 (1997).
[129] N. E. Munoz, S. R. Gilliss, C. B. Carter, "The monitoring of grain-boundary grooves in alumina" Phil. Mag. Lett., **84** [1] 21-26 (2004).
[130] N. E. Munoz, S. R. Gilliss, C. B. Carter, "Remnant grooves on alumina surfaces" Surf. Sci., **573** [3] 391-402 (2004).
[131] J. Muscat, N. M. Harrison, "The physical and electronic structure of the rutile (001) surface" Surf. Sci., **446** 119-127 (2000).
[132] H. Nakano, K. Watari, K. Urabe, "Grain boundary phase in AlN ceramics fired under reducing N_2 atomosphere with carbon" J. Euro. Ceram. Soc., **23** 1761-1768 (2003).
[133] C. Noguera, Physics and Chemistry at Oxide Surfaces, Cambridge University Press Cambridge, UK, (1996).
[134] P. Nozières, F. Gallet, "The roughening transition of crystal surfaces. I. Static and dynamic renormalization theory, crystal shape and facet growth" J. Physique, **48** [3] 353-367 (1987).
[135] M. A. O'Keeffe, "News and Views: Edge effects" Nat. Mater., **419** 28-29 (2002).
[136] M. A. O'Keeffe, E. C. Nelson, Y. C. Wang, A. Thust, "Sub-angstrom resolution of atomistic structures below 0.8 A" Phil. Mag. B, **81** [11 SPEC] 1861-1878 (2001).
[137] J. Oster, M. Huth, L. Wiehl, H. Adrian, "Growth of Fe nanostructures" J. Magn. Magn. Mater., **272-276** 1588-1589 (2004).
[138] J.-K. Park, D.-Y. Kim, H. Lee, -Y, J. E. Blendell, C. A. Handwerker, "Crystallographic-Orientation-Dependent Dissolution Behavior of Sapphire in Anorthite Liquid Containing Chromia" J. Am. Ceram. Soc., **86** [6] 1014-1018 (2003).

[139] L. Pauling, "The Principles Determining the Structure of Complex Ionic Crystals" J. Amer. Ceram. Soc., **51** 1010-1026 (1929).
[140] G. Pezzotti, A. Nakahira, M. Tajika, "Effect of extended annealing cycles on the thermal conductivity of AlN/Y_2O_3 ceramics" J. Euro. Ceram. Soc., **20** 1319-1325 (2000).
[141] M. W. Phaneuf, "Applications of focused ion beam microscopy to materials science specimens" Micron, **30** 277-288 (1999).
[142] E. Pouget, E. Dujardin, A. Cavalier, A. Moreac, C. Valéry, V. Marchi-Artzner, T. Weiss, A. Renault, M. Paternostre, F. Artzner, "Hierarchial architectures by synergy between dynamical template self-assembly and biomineralization" Nat. Mater., **6** 434-439 (2007).
[143] S. Prestipino, E. A. Jagla, E. Tosatti, "Can one have preroughening of vicinal surfaces?" Surface Science, **454** 652-656 (2000).
[144] M. N. Rahaman, Ceramic Processing, Taylor & Francis Boca Raton, (2007).
[145] S. Ramamurthy, M. P. Mallamaci, C. B. Carter, "Initial stages of solid-liquid interactions in the MgO-$CaMgSiO_4$ system" Scripta Mater., **34** [11] 1779-1783 (1996).
[146] S. Ramamurthy, H. Schmalzried, C. B. Carter, "Interaction of Silicate Liquid with a Sapphire Surface" Phil. Mag. A, **80** [11] 2651-2674 (2000).
[147] V. Randle, A. Brown, "The effects of strain on grain misorientation texture during the grain growth incubation period" Phil. Mag. A, **58** [5] 717-736 (1988).
[148] D. R. Rasmussen, Y. K. Simpson, R. Kilaas, C. B. Carter, "Contrast Effects at Grooved Interfaces" Ultramicroscopy, **30** 52-57 (1989).
[149] N. Ravishankar, C. B. Carter, "Glass/Crystal Interfaces in Liquid-Phase Sintered Materials" Inter. Sci., **8** 295-304 (2000).
[150] N. Ravishankar, C. B. Carter, "Migration of alumina grain boundaries containing a thin glass film" Acta Mater., **49** 1963-1969 (2001).
[151] N. Ravishankar, C. B. Carter, "Ordered nanostructures by site-specific heterogeneous nucleation" Phil. Mag. Lett., **85** [10] 523-531 (2005).
[152] N. Ravishankar, S. R. Gilliss, C. B. Carter, "Dewetting of liquids on ceramic surfaces at high temperature" Microsc. Microanal., **8** 257-267 (2002).
[153] N. Ravishankar, S. R. Gilliss, C. B. Carter, "Glass and metals on crystalline oxides" J. Euro. Ceram. Soc., **23** 2777-2785 (2003).
[154] N. Ravishankar, V. B. Shenoy, C. B. Carter, "Electric Field Singularity Assisted Nanopatterning" Adv. Mater., **16** [1] 76-80 (2004).
[155] L. Rayleigh, "On the Instability of Jets" Proc. Lon. Math. Soc., **10** 4-13 (1878).
[156] S. J. B. Reed, Electron Microprobe Analysis and Scanning Electron Microscopy in Geology, Cambridge University Press Cambridge, Great Britain, (1996).
[157] R. E. Reed-Hill, R. Abbaschian, Physical Metallurgy Principles, PWS Publishing Company Boston, (1973).
[158] I. E. Reimanis, "Pore Removal During Diffusion Bonding of Nb-Al2o3 Interfaces" Acta Metall. Mater., **40** S67-S74 (1992).
[159] J. L. Riesterer, Combining FIB, AFM and EBSD for Analysis of Dynamic Processes on Ceramic Surfaces, Minneapolis, MN, University of Minnesota (2005).
[160] G. S. Rohrer, C. L. Rohrer, W. W. Mullins, "Coarsening of faceted crystals" J. Am. Ceram. Soc., **85** [3] 675-682 (2002).

[161] A. D. Rollett, W. W. Mullins, "On the Growth of Abnormal Grains" Scripta Mater., **36** [9] 975-980 (1997).
[162] A. R. Roosen, R. P. McCormack, C. W. Carter, "Wulffman: A tool for the calculation and display of crystal shapes" Comp. Mater. Sci., **11** 16-26 (1998).
[163] G. Rossi, J. E. Burke, "Influence of additives on the microstructure of sintered Al_2O_3" J. Am. Ceram. Soc., **56** [12] 654-659 (1973).
[164] M. K. Santala, A. M. Glaesar, "Surface-energy-anisotropy-induced orientation effects on Rayleigh instabilities in sapphire" Surf. Sci., **600** 782-792 (2006).
[165] T. Sata, T. Sasamoto, in: W. D. Kingery (Ed.), Structure and Properties of MgO and Al_2O_3 Ceramics, Columbus, OH, (1984), pp. 541-552.
[166] T. V. Savina, A. A. Golovin, S. H. Davis, A. A. Nepomnyashchy, P. W. Voorhees, "Faceting of a growing crystal surface by surface diffusion" Phys. Rev. E, **67** [21] (2003).
[167] K. G. Saw, "Surface reconstruction of α-(0001) sapphire: An AFM, XPS, AES and EELS investigation" J. Mater. Sci., **39** 2911-2914 (2004).
[168] M. E. Schrader, in: M. E. Schrader, G. Loeb (Eds.), Modern Approach to Wettability: Theory and Applications, New York, (1991), pp. 53-71.
[169] J. Schultz, M. Nardin, in: M. E. Schrader, G. Loeb (Eds.), Modern Approach to Wettability: Theory and Applications, New York, (1991), pp. 73-100.
[170] A. J. Schwartz, M. Kumar, B. L. Adams (Eds.), Electron Backscatter Diffraction in Materials Science, Kluwer Academic/Plenum Publishers, New York, p. 339, (2000).
[171] C. Scott, M. Kaliszewski, C. Greskovich, L. Levinson, "Conversion of Polycrystalline Al2O3 into Single-Crystal Sapphire by Abnormal Grain Growth" J. Am. Ceram. Soc., **85** [5] 1275-1280 (2002).
[172] R. F. Sekerka, "Analytical criteria for missing orientations on three-dimensional equilibrium shapes" J. Crys. Growth, **275** 77-82 (2005).
[173] K. Seshan (Ed.) Handbook of Thin-Film Depositin Processes and Techniques, Noyes Publications/William Andrew Publishing, Norwich, NY, p. 629, (2002).
[174] P. Shewmon, Diffusion in Solids, The Minerals, Metals & Materials Society Warrendale, Pennsylvania, (1989).
[175] W. Shin, W. Seo, K. Koumoto, "Grain-boundary grooves and surface diffusion in polycrystalline alumina measured by atomic force microscope" J. Eur. Ceram. Soc., **18** [6] 595-600 (1998).
[176] W. Sigle, G. Richter, M. Rühle, S. Schmidt, "Insight into the atomic-scale mechanism of liquid metal embrittlement" Appl. Phys. Lett., **89** (2006).
[177] j. K. Spelt, D. Li, A. W. Neumann, in: M. E. Schrader, G. Loeb (Eds.), Modern Approach to Wettability: Theory and Applications, New York, (1991), pp. 101-142.
[178] D. Srinivasan, P. R. Subramanian, "Kirkendall porosity during thermal treatment of Mo-Cu nanomultilayers" Mater. Sci. Eng. A-Struct., **459** [1-2] 145-150 (2007).
[179] C. E. Stickley, J. Pike, A. Leventer, "Productivity events of the marine diatom *Thalassiosira tumida* (Janisch) Hasle recorded in deglacial varves from the East Antarctic Margin" Mar. Micropaleontol., **59** 184-196 (2006).
[180] B. B. Straumal, V. G. Sursaeva, S. A. Polyakov, "Faceting and Roughening of the Asymmetric Twin Grain Boundaries in Zinc" Interface Sci., **9** 275-279 (2002).

[181] A. Subramaniam, C. T. Koch, R. M. Cannon, M. Rühle, "Intergranular glassy films: An overview" Mater. Sci. Eng. A, **422** 3-18 (2006).
[182] R. C. Sun, C. L. Bauer, "Measurement of grain boundary mobilities through magnification of capillary forces" Acta Metall., **18** 635-638 (1970).
[183] D. W. Susnitzky, C. B. Carter, "Localization of Potassium in Al_2O_3" J. Am. Ceram. Soc., **68** [11] 569-574 (1985).
[184] D. W. Susnitzky, C. B. Carter, "Identification of α-alumina surface structures by electron diffraction" J. Am. Ceram. Soc., **69** [9] C217-C220 (1986).
[185] D. W. Susnitzky, C. B. Carter, "Surface Morphology of Heat-Treated Ceramic Thin Films" J. Am. Ceram. Soc., **75** [9] 2463-2478 (1992).
[186] D. W. Susnitzky, Y. Kouh Simpson, B. C. DeCooman, C. B. Carter, "The structure of surface steps on low-index planes of oxides" Journal, **60** [Issue] 219-226 (Year).
[187] P. W. Tasker, in: W. D. Kingery (Ed.), Structure and Properties of MgO and Al_2O_3 Ceramics, Columbus, OH, (1984), pp. 176-189.
[188] A. Thomas, The Gemstones Handbook: Properties, Identification and Use, Barnes & Noble New York, (2008).
[189] J. Thomson, "On certain curious Motions observable at the Surfaces of Wine and other Alcoholic Liquors" Phil. Mag., **10** 330-333 (1855).
[190] T. T. To, D. Bougeard, K. S. Smirnov, "Molecular dynamics study of the vibrational pattern of ring structures in the Raman spectra of vitreous silica" J. Raman Spectrosc., **39** 1869-1877 (2008).
[191] W. Uytenbogaardt, E. A. J. Burke, Tables for Microscopic Indentification of Ore Minerals, Dover Publications, Inc. New York, (1985).
[192] D. J. Vaughan, R. A. D. Pattrick (Eds.), Mineral Surfaces, Chapman & Hall, London, p. 370, (1995).
[193] M. G. Velarde, in: E. D. Hondros *et al.* (Eds.), Marangoni and Interfacial Phenomena in Materials Processing, London, (1998), pp. 15-30.
[194] W. Vogel, in, Leipzig, Germany, (1965), pp. 134-202.
[195] J. Weertman, J. R. Weertman, Elementary Dislocation Theory, Oxford University Press New York, (1964).
[196] L. Wiehl, J. Oster, M. Huth, "High-resolution transmission electron microscopic investigations of molybdenum thin films on faceted α-Al_2O_3" J. Appl. Cryst., **38** 260-265 (2005).
[197] D. B. Williams, C. B. Carter, Transmission Electron Microscopy: A Textbook for Materials Science, Plenum New York, (1996).
[198] E. D. Williams, "Surface steps and surface morphology: understanding macroscopic phenomena from atomic observations" Surf. Sci., **299/300** 502-524 (1994).
[199] E. D. Williams, N. C. Bartelt, "Surface Faceting and the Equilibrium Crystal Shape" Ultramicroscopy, **31** 36-48 (1989).
[200] A. F. Wright, J. Talbot, B. E. F. Fender, "Nucleation and growth studies by small angle neutron scattering and results for a glass ceramic" Nature, **277** 366-368 (1979).
[201] S. Wu, E. Gilbart, R. J. Brook, in, Science of Ceramics, Italy, (1983), pp. 371-380.
[202] G. Wulff, "Regarding the question of the speed at which crystals grow and shrink" Z. Krist., **34** 449-530 (1901).

[203] J.-Q. Xi, M. Ojha, J. L. Plawsky, W. N. Gill, J. K. Kim, E. F. Schubert, "Internal high-reflectivity omni-directional reflectors" Appl. Phys. Lett., **87** (2005).
[204] R. J. Young, P. A. Lovell, Introduction to Polymers, Stanley Thornes (Publishers) Ltd. Cheltenham, UK, (1981).
[205] T. Young, "An Essay on the Cohesion of Fluids" Phil. Trans. R. Soc. Lon. 65-87 (1805).
[206] M. S. Zei, Y. Nakai, G. Lehmpfuhl, D. Kolb, "The structure of gold and silver films evaporate on glass" J. Electroanal. Chem., **150** 201-206 (1983).
[207] A. Ziegler, M. K. Cinibulk, C. Kisieloski, R. O. Ritchie, "Atomic-scale observation of the grain-boundary structure of Yb-doped and heat-treate silicon nitride ceramics" Appl. Phys. Lett., **91** [14] 141906 (2007).